Feasibility of Tissue Differentiation with Multi-energy Computed Tomography: A Monte Carlo Breast Phantom study

By

Déte van Eeden

Thesis submitted to comply with the requirements for the Ph.D. (Medical Physics) degree in the Faculty of Health Sciences at the University of the Free State

Promoter: Dr. F.C.P. du Plessis

Department of Medical Physics, University of the Free State

March, 2017

DECLARATION

I, Déte van Eeden, declare that the doctoral research thesis that I herewith submit at the University of the Free State, is my independent effort and that I have not previously submitted it for a qualification at another institution of higher education.

I furthermore declare that I am aware that the copyright is vested in the University of the Free State.

Signature: Déte van Eeden

If you want something you have never had, you must be willing to do something you have never done.

-Thomas Jefferson

Table of Contents

List of Abbreviations

AAPM	The American Association of Physicists in Medicine
Al	aluminium
ASCII	American Standard Code for Information Interchange
BCA	boundary cross algorithm
BI-RADS	The Breast Imaging Reporting and Data System
Ca	calcium
$CaCO_3$	calcium carbonate
CBCT	cone beam CT
CdTe	cadmium telluride
CdZnTe	cadmium zinc telluride
CT	Computed Tomography
CMs	component modules
CNR	contrast-to-noise ratio
CTDI	CT dose index
Cu	copper
ECUT	electron cut-off energy
EGSnrc	Electron Gamma Shower

EIT	efficiency improving techniques
EJMP	European Journal of Medical Physics
FDA	Food and Drug Administration
FDK	Feldkamp-Davis-Kress
Fe	iron
FOV	field of view
GdOS	gadolinium oxysulfide
GEANT4	GEometry ANd Tracking
GUI	Graphical User Interface
HUs	Hounsfield units
HVL	half-value layer
ICRU	The International Commission on Radiation Units and Measurements
IDL	Interactive Data Language
KBCT	Koning Breast Computed Tomography
keV	kiloelectron volt
kV	kilovoltage
kVp	peak kilovoltage
LB	large bore
MC	Monte Carlo

MeV	mega electron volt
MFPTR	path length stretching technique
MRE	mean relative error
MRI	Magnetic Resonance Imaging
Ni	nickel
NIST	National Institute of Standards and Technology
OSCaR	Open Source Cone-beam Reconstructor
P	phosphorus
PCUT	photon cut-off energy
PEGS	Preprocessor for EGS
PRESTA	The Parameter Reduced Electron-Step Transport Algorithm
Rb	rubidium
ROI	region-of-interest
RT	rekenaar tomografie
S	sulphur
SAD	source-to-axis distance
Se	selenium
Si	silicon
SNR	signal-to-noise ratio

SSD	source-to-surface distance
VRTs	variance reduction techniques
3D	3-dimensional
ρe	electron density

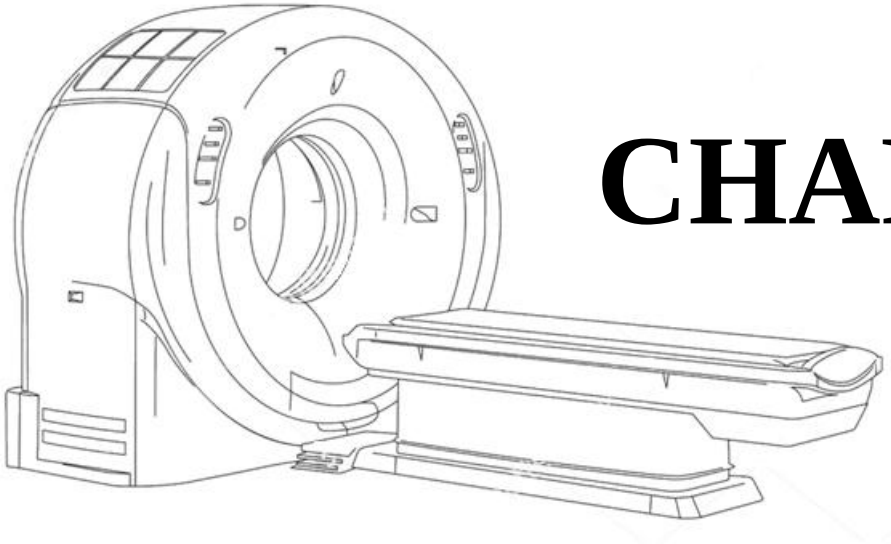

CHAPTER 1

Introduction

Table of Contents

1.1 Background

The first record of breast cancer dates back to 3000 years before Christ. Various Greek and Roman physicians have documented breast lumps that progress into tumours over the decades. The primary form of treatment was surgery that included mastectomies, removal of chest muscles, and even the removal of the oestrogen-producing ovaries. In the mid-'90s, it was suggested that breast cancer is a systemic disease and is capable of metastasizing. A different approach was used to treat breast cancer with the aid of surgeries and the use of radiation therapy and chemotherapy.[1,2]

It was also the start of using general X-rays and film to detect suspicious lesions in uncompressed breast tissue. Mammography is the golden standard for early detection of breast cancer and is attributed to the recent reduction in breast cancer mortality.[3-5] It is especially useful for the detection of microcalcifications, which is an early indicator of cancer formation. It has the advantage of high spatial resolution and by using digital mammography one can adjust the viewing parameters. This leads to better detection of suspicious lesions.

Whether mammography screening is justifiable or not is a controversial subject. Some experts and articles state that screening leads to over diagnoses and overtreatment.[6] Some state that screening will result in some women getting a cancer diagnosis even though their cancer would not have led to death or sickness. Although there is no proof that the treated disease would not have had a detrimental outcome if left untreated. The American Cancer Society states that the 5-year survival rate for women with stage 0 or stage I breast cancer is close to 100%. These are cancers that have been detected in the early stages by methods such as mammography screening. For women with stage II and stage III cancers, the 5-year survival rate drops to 93 % and 72 % respectively. For breast cancers that have gone undetected and spread to other parts of the body the 5-year survival rate is only 22%.[7] This shows that breast

cancer treatment works best when it is detected in the early stages before spreading outside the breast to other parts of the body. In a recent study by Weedon-Fekaer *et al.* it was shown that screening mammography reduced the mortality rate of a population of woman with 28% in comparison with those who had not undergone any screening.[8]

Despite the popularity of this imaging technique, it still has its pitfalls due to the superposition of structures. This is in particular for women with dense breasts that consist mainly of glandular tissue.[9, 10] This superposition leads to a low positive predictive value and studies have shown that between 70% - 90% of biopsies turn out to be negative.[11]

1.1.1 Imaging modalities for breast cancer detection

A mammogram usually consists of two X-ray projection views of a compressed breast in the coronal and sagittal planes. It is hard to detect small lesions or abnormalities when projecting a three-dimensional image onto a two-dimensional plane, especially if overlapped with dense breast tissue.[11-13] Multiple studies have shown that magnetic resonance imaging (MRI) may be useful in detecting breast cancer[14-17] but is not a replacement for mammography. Contrast-enhanced MRI is sensitive enough to detect breast cancer, but the specificity ranges from 37% to 96%.[18] This limits the use of MRI for early breast cancer detection.

An alternative imaging technique is needed that overcomes the limitations of mammography. Dedicated breast computed tomography (CT) is a new technique and eliminates the superposition of different structures as seen with mammography.

1.1.2 Breast Computed Tomography

The idea of breast computed tomography developed shortly after the development of computed tomography in the late ‘70s.[19-22] Since the technology was not as advanced as today, a body scanner had to be used to perform a chest scan for breast imaging. This

included the thoracic cavity and a significant amount of non-breast tissue. This leads to an increase in the dose that the patient receives and breathing artifacts. The idea of a breast CT was set aside until the early 2000s when the improved technology allowed for a dedicated breast CT scanner.[23]

In 2001 Boone *et al*. investigated the feasibility of using a breast CT regarding radiation dose and image quality.[24] A patient would lay in a prone position with the breast hanging through an opening. This geometry would avoid exposing any thoracic tissue resulting in coronal images of the breast. They found that the breast CT resulted in lower doses than mammography with breasts thicker than 5 cm. Breast CT led to a higher photon penetration and better X-ray energy penetration that compensate for the high fluence requirements of the CT. The higher contrast-to-noise ratio (CNR) and signal-to-noise ratio (SNR) and reasonable doses make this technique quite impressive. In a pilot study conducted in 2004, they found that breast CT was superior to mammography for the visualisation of masses and also more comfortable for the patient.[25] A further study found that visibility of malignant masses was better with contrast-enhanced CT than with unenhanced CT or mammography and it is also possible to distinguish between benign and malignant lesions.[26] The large number of projections needed for accurate reconstruction posed a concern regarding the necessary dose required during a dedicated breast CT acquisition to acquire good image quality. This concern was addressed by Boone *et al.* that showed that the dose needed is comparable to that of a standard mammogram.[24]

The Koning Corporation, a leading developer of advanced imaging systems, announced on 4 February 2015 that the Food and Drug Administration (FDA) approved their Koning Breast CT (KBCT) system. This is the first commercially available three-dimensional (3D) breast CT that can image the entire breast without compression. The KBCT system operates at a maximum voltage of 49 kVp and consists of a flat panel detector.

Conventional CT systems like the KBCT are usually referred to as single energy CT because of the single polychromatic source that is used. The difference in material contrast that is seen depends on the properties of the materials being imaged and the photon energy. Different attenuation coefficients will result in different contrasts. Also, the difference between the energy being used and the K-edge of the material will have an effect on the resulting contrast.[27] Materials with the same photon attenuation but different elemental composition or mass densities cannot be distinguished with single energy CT.[28] When using single energy CT the cumulative attenuation coefficient is measured over the entire energy range in the energy spectrum. [29-31] Different materials are expressed in terms of Hounsfield units (HUs) and are displayed in shades of grey. Certain concentrations of calcium and iodine may have similar CT numbers and will not be distinguishable from one another on a single energy CT.[31]

The CT number presented by any material is caused by a combination of the photoelectric effect and Compton effect. The photoelectric effect usually occurs at low energies, is very dependent on the energy, and is related to high atomic number materials. The Compton effect occurs at energies above 30 kV and depends on the total number of electrons in an absorber. Therefore, it depends on the density of a material and not the atomic number.[32]

This different response of materials at different energies can be used to differentiate between the materials. This idea gave rise to dual-energy CT and multi-energy CT.

1.1.3 Dual- and Multi-energy CT

In dual-energy CT, two different energy spectra are used to acquire two CT datasets. This can be achieved either by switching the kV of one tube or by using two tubes with different voltages. By using this technique, differences in material composition can be detected due to the differences in the photoelectric and Compton effects of the materials at different energies.

Dual-energy has resolved multiple issues such as image co-registration problems caused by temporal changes.[31,33,34] Other applications include the differentiation or quantification of materials with a large difference in atomic numbers. This can be used for the differentiation of bone and iodine in post-processing techniques [35-37] and also for the analysis of urinary stones.[38-42]. A virtual non-enhanced image is obtained when the iodine content is subtracted from the contrast-enhanced image. [33-34] The non-contrast CT acquisition can be eliminated by replacing the non-contrast-enhanced image with the virtual non-contrast-enhanced image. This will limit the dose the patient receives.

In Figure 1.1 below the difference in the attenuation coefficients for the iodine and bone at 80 kV and 140 kV can be seen. The difference is much more pronounced for the iodine in comparison with the bone.

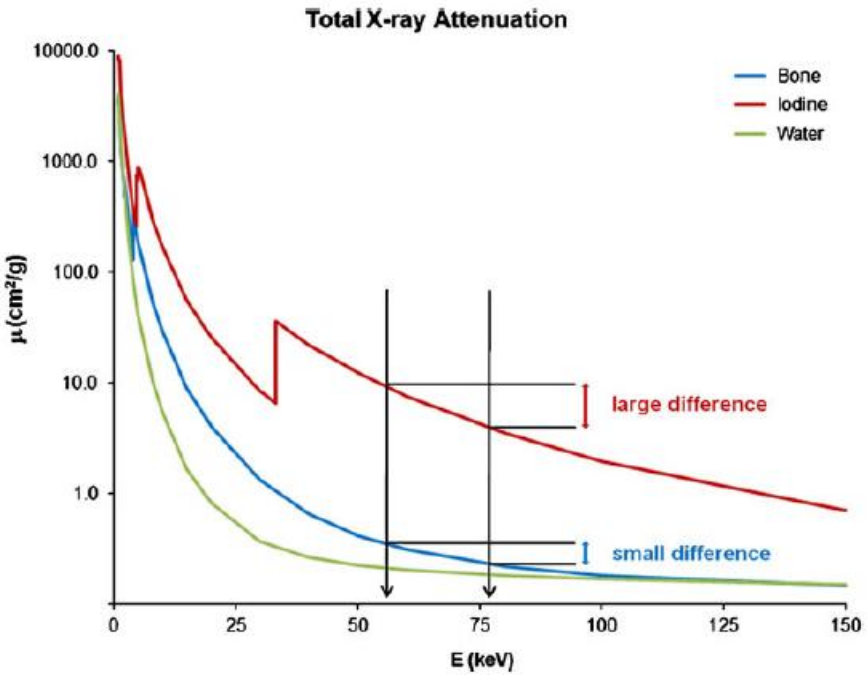

Figure 1.1: Attenuation coefficients for a range of energies for bone, iodine and water. The large difference in attenuation coefficient for the iodine and small difference for the bone can be seen clearly.[43]

These responses at different energies can exploit information regarding the elemental composition as long as the atomic number and/or mass densities are different.[44] Some of the

disadvantages of dual-energy CT is that materials with similar attenuation coefficients cannot be distinguished from one another. It lacks soft tissue classification and high dose levels are required.[45] Iodine is often used as contrast agent, but this can lead to an increase in dose in organs and tissues.[46]

The future of CT techniques lies within the additional information that is present in the energy spectrum. By utilising the different energies much richer images can be obtained that contains additional information regarding the tissue under investigation. This imaging technique produces such vivid images that it is referred to as "true-colour CT" in a study conducted by Gao *et al*.[47]

Multi-energy CT has been used for small animal imaging[48], whole-body clinical systems[49] and breast CT.[50] This technique refers to the utilisation of spectral data that is used for differentiation and classification of different tissues within images.[30] In conventional CT techniques, energy-integrating detectors are used where the X-ray interactions are accumulated over the entire energy spectrum.[51] The detector forms a vital part of the imaging process, and a newly developed photon-counting detector has been developed for use in multi-energy CT.[52,53]

These detectors can count the number of X-ray photons within a specific energy range. These energy ranges are referred to as bins, and there can be up to eight different bins in one detector. All of the energies are acquired at the same time eliminating registration problems between the different images. The energies are within narrow energy ranges[53,55,56] and the tube output usually consists of a single energy spectrum since the separation of energies happens in the detector. This new method of detection provides more optimal weighting than intensity integrating, resulting in lower noise and better contrast.[57] These detectors have been considered instead of the conventional X-ray detectors to increase contrast and reduce the

dose. When using multiple-energy in CT, the impact on patient dose must be considered. The dose is actually reduced due to only using a single energy per exposure and the lack of contrast agents. Multi-energy scanning is based on the basic concept of predictable differences in attenuation when substances are imaged with different X-ray energies of known spectra. It is, therefore, worthwhile to explore the opportunities that can exist for the use of multiple energies.

Several studies have been conducted with multi-energy CT[58-60] and include K-edge imaging of multiple contrast agents.[56,48] More than one high atomic number can be distinguished due to the range of energies available in multi-energy CT. Some of these contrast agents include iodine, barium, gadolinium and gold. There exists an increase in attenuation above the binding energies of these K-shell electrons due to photoelectric absorption. This K-edge imaging with multiple contrast agents has been demonstrated in mice.[53] The study showed that contrast agents could be given at different time points but imaged simultaneously. This can be used for triple renal or liver studies in a single examination, which would lead to a reduction in dose and elimination of patient movement.

Multi-energy CT has led to the development of new contrast agents such as gold-labelled nano-particles.[61] This can be used for functional imaging as the particles can be targeted to specific cells or enzymes.

1.1.4 Tissue differentiation

Another use of dual- and multi-energy CT is the determination of the chemical composition of tissues. This is referred to as tissue decomposition and can be used to determine the chemical composition of soft tissues. In previous studies, it has also been used to identify calcifications[62], glandular tissue, adipose tissue[63-65] and atherosclerotic plaque.[45] This

compositional method has also been used for determining the density of breast tissue by calculating the amounts of protein, water and lipid present.[66]

The possibility exists to differentiate between normal and malignant tissues in terms of their composition. Previous studies have found that malignant tissues have significantly higher water and reduced lipid content compared to healthy tissue.[67-70] Elemental concentrations of phosphorus (P), sulphur (S), potassium (K), calcium (Ca), iron (Fe), nickel (Ni), selenium (Se) and rubidium (Rb) are also different in malignant tissues.[71-75] Different methods of tissue differentiation are seen in the literature, Ding *et al*. use a two-step process consisting of a calibration phantom.[76] Le and Molloi use a decomposition algorithm that first identifies the material and then computes the concentration.[50]

The linear attenuation coefficient is a valuable parameter that can be used to distinguish between different tissues. The glandular tissue has a much higher attenuation coefficient than fatty tissue at all energies. There exists a significant difference between the attenuation coefficients of glandular tissue and carcinomas at energies below 31 keV as seen in Figure 1.2 below.[77]

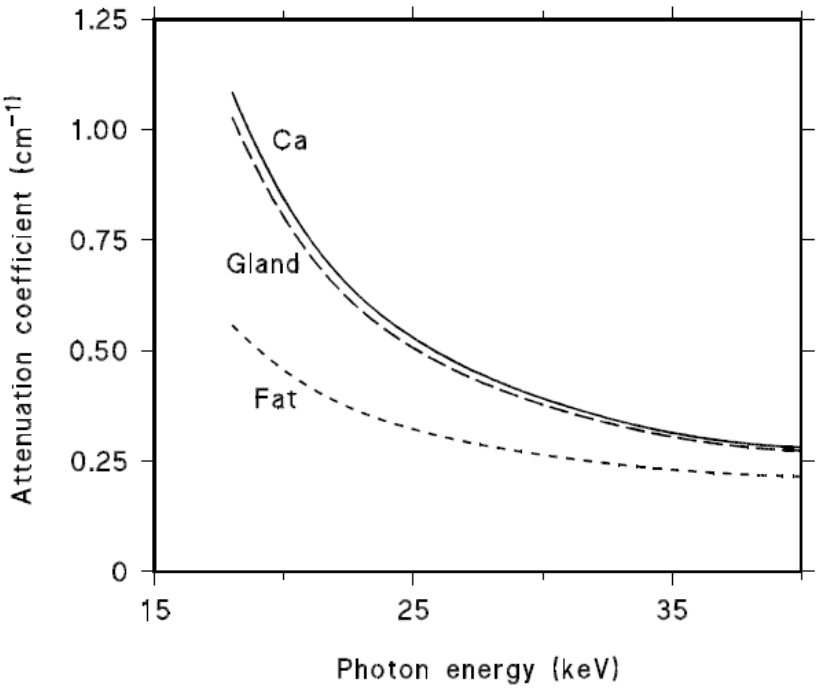

Figure 1.2: Variation in the attenuation coefficient for different breast tissues and energies.[77]

1.1.5 Energy weighting imaging

Although the current dedicated breast CT systems operate at 49 keV, it is of great importance to explore lower energies, in particular with the development of the photon-counting detectors. In a previous study by Schmidt *et al.*[78], a method was investigated for reconstructing images from different energy bins using projection-based and image-based optimal energy weighting. Le *et al.*[79] also investigated these two types of energy weighting modes with a cadmium zinc telluride (CdZnTe) detector. In both studies, an increase in the CNR was seen, but specific parameters like the length of tissue or tissue thicknesses need to be known. These parameters are easy to calculate in phantoms with known dimensions but not in the case for phantoms based on clinical data with varying tumour sizes.

In this dissertation, the feasibility for differentiating between different breast tissues is explored through the Monte Carlo (MC) simulation of a virtual multi-energy CT unit.

In Chapter 2 the energy spectrum of the Toshiba Aquilion Large Bore (LB) 16 CT is approximated by means of BEAMnrc simulations and half-value layer (HVL) comparisons. Different component modules (CM's) are used to model the beam-defining components of the virtual CT.

In Chapter 3 the HUs of the virtual CT is compared to that of the Toshiba Aquilion LB 16 CT. It is shown that the MC and reconstruction methods used can accurately model a CT unit and some of the results were published in the European Journal of Medical Physics (EJMP).

In Chapter 4 the possibility of differentiating between different tissues are explored by using a range of energies. Different breast phantoms are modelled and simulated with the egs_cbct code. The Feldkamp-Davis-Kress (FDK) algorithm is used for the reconstruction of the projection images. The CNR for each energy bin is calculated and compared with one another.

In Chapter 5 an alternative image-based energy weighting method is developed that does not require prior knowledge information of the effective attenuation coefficient. The method also shows that there is a possibility of using multi-energy CT without the use of contrast agents like iodine.

In Chapter 6 a new method for tissue differentiation is explored based on the mass attenuation coefficients of different breast tissues. The sum of the least squares method is used together with an in-house developed Interactive Data Language (IDL) program.

1.2 References

1. Early History of Cancer | American Cancer Society [Internet]. [cited 2017 Jan 20]. Available from: https://www.cancer.org/cancer/cancer-basics/history-of-cancer/what-is-cancer.html

2. Medical Therapy of Breast Cancer [Internet]. Cambridge University Press. [cited 2017 Jan 20]. Available from: http://www.cambridge.org/za/academic/subjects/medicine/oncology/medical-therapy-breast-cancer?format=PB

3. Tabár L, Chen H-H, Fagerberg G, Duffy SW, Smith TC. Recent Results From the Swedish Two-County Trial: The Effects of Age, Histologic Type, and Mode of Detection on the Efficacy of Breast Cancer Screening. JNCI Monogr. 1997 Jan 1;1997(22):43–7.

4. Larsson LG, Andersson I, Bjurstam N, Fagerberg G, Frisell J, Tabár L, et al. Updated overview of the Swedish Randomized Trials on Breast Cancer Screening with Mammography: age group 40-49 at randomization. J Natl Cancer Inst Monogr. 1997;(22):57–61.

5. The Swedish Randomised Mammography Screening Trials: Analysis of Their Effect on the Breast Cancer Related Excess Mortality [Internet]. PubMed Journals. [cited 2016 Dec 26]. Available from: https://ncbi.nlm.nih.gov/labs/articles/8946307/

6. Gøtzsche PC, Olsen O. Is screening for breast cancer with mammography justifiable? Lancet Lond Engl. 2000 Jan 8;355(9198):129–34.

7. Cancer Facts and Statistics | American Cancer Society [Internet]. [cited 2017 Jun 28]. Available from: https://www.cancer.org/research/cancer-facts-statistics.html

8. Weedon-Fekjær H, Romundstad PR, Vatten LJ. Modern mammography screening and breast cancer mortality: population study. BMJ. 2014 Jun 17;348:g3701.

9. Bird RE, Wallace TW, Yankaskas BC. Analysis of cancers missed at screening mammography. Radiology. 1992 Sep;184(3):613–7.

10. Buist DSM, Porter PL, Lehman C, Taplin SH, White E. Factors contributing to mammography failure in women aged 40-49 years. J Natl Cancer Inst. 2004 Oct 6;96(19):1432–40.

11. Glick SJ. Breast CT. Annu Rev Biomed Eng. 2007;9(1):501–26.

12. Lai C-J, Shaw CC, Chen L, Altunbas MC, Liu X, Han T, et al. Visibility of microcalcification in cone beam breast CT: effects of X-ray tube voltage and radiation dose. Med Phys. 2007 Jul;34(7):2995–3004.

13. Chen B, Ning R. Cone-beam volume CT breast imaging: Feasibility study. Med Phys. 2002 May 1;29(5):755–70.

14. Lord SJ, Lei W, Craft P, Cawson JN, Morris I, Walleser S, et al. A systematic review of the effectiveness of magnetic resonance imaging (MRI) as an addition to mammography and ultrasound in screening young women at high risk of breast cancer. Eur J Cancer Oxf Engl 1990. 2007 Sep;43(13):1905–17.

15. Freitas V, Scaranelo A, Menezes R, Kulkarni S, Hodgson D, Crystal P. Added cancer yield of breast magnetic resonance imaging screening in women with a prior history of chest radiation therapy. Cancer. 2013 Feb 1;119(3):495–503.

16. Warner E. The role of magnetic resonance imaging in screening women at high risk of breast cancer. Top Magn Reson Imaging TMRI. 2008 Jun;19(3):163–9.

17. Warner E, Hill K, Causer P, Plewes D, Jong R, Yaffe M, et al. Prospective Study of Breast Cancer Incidence in Women With a BRCA1 or BRCA2 Mutation Under Surveillance With and Without Magnetic Resonance Imaging. J Clin Oncol. 2011 May 1;29(13):1664–9.

18. The Application of Breast MRI in Staging and Screening for Breast Cancer | Cancer Network [Internet]. 2005 [cited 2016 Dec 26]. Available from: http://www.cancernetwork.com/oncology-journal/application-breast-mri-staging-and-screening-breast-cancer

19. Chang CHJ, Sibala JL, Gallagher JH, Riley RC, Templeton AW, Beasley PV, et al. Computed Tomography of the Breast. Radiology. 1977 Sep 1;124(3):827–9.

20. Chang CHJ, Sibala JL, Fritz SL, Gallagher JH, Dwyer SJ, Templeton AW. Computed tomographic evaluation of the breast. ResearchGate. 1978 Oct 1;131(3):459–64.

21. Chang CHJ, Sibala JL, Fritz SL, Dwyer SJ, Templeton AW. Specific Value of Computed Tomographic Breast Scanner (CT/M) in Diagnosis of Breast Diseases. Radiology. 1979 Sep 1;132(3):647–52.

22. Rittenberg GM. Clinical evaluation of computerized tomographic mammography. J Comput Tomogr. 1977 Jun 1;1(2):156.

23. Physics of Mammographic Imaging [Internet]. CRC Press. 2012 [cited 2016 Dec 26]. Available from: https://www.crcpress.com/Physics-of-Mammographic-Imaging/Markey/p/book/9781439875445

24. Boone JM, Nelson TR, Lindfors KK, Seibert JA. Dedicated breast CT: radiation dose and image quality evaluation. Radiology. 2001 Dec;221(3):657–67.

25. Lindfors KK, Boone JM, Nelson TR, Yang K, Kwan ALC, Miller DF. Dedicated breast CT: initial clinical experience. Radiology. 2008 Mar;246(3):725–33.

26. Prionas ND, Lindfors KK, Ray S, Huang S-Y, Beckett LA, Monsky WL, et al. Contrast-enhanced Dedicated Breast CT: Initial Clinical Experience. Radiology. 2010 Sep 1;256(3):714–23.

27. Dual-energy CT in practice: Basic principles and applications [Internet]. [cited 2016 Nov 21]. Available from: http://appliedradiology.com/articles/dual-energy-ct-in-practice-basic-principles-and-applications

28. Hünemohr N, Paganetti H, Greilich S, Jäkel O, Seco J. Tissue decomposition from dual energy CT data for MC-based dose calculation in particle therapy. Med Phys. 2014 Jun 1;41(6):061714.

29. Avrin DE, Macovski A, Zatz LE. Clinical application of Compton and photo-electric reconstruction in computed tomography: preliminary results. Invest Radiol. 1978 Jun;13(3):217–22.

30. Alvarez RE, Macovski A. Energy-selective reconstructions in X-ray computerised tomography. Phys Med Biol. 1976 Sep 1;21(5):733.

31. Johnson TRC, Krauss B, Sedlmair M, Grasruck M, Bruder H, Morhard D, et al. Material differentiation by dual energy CT: initial experience. Eur Radiol. 2007 Jun;17(6):1510–7.

32. Curry, III TS, Dowdey JE, Murray, JR. RC. Christensen's Physics of Diagnostic Radiology. Fourth edition. Philadelphia, London: Lea & Febiger; 1990. 522 p.

33. Fletcher JG, Takahashi N, Hartman R, Guimaraes L, Huprich JE, Hough DM, et al. Dual-energy and dual-source CT: is there a role in the abdomen and pelvis? Radiol Clin North Am. 2009 Jan;47(1):41–57.

34. Graser A, Johnson TRC, Chandarana H, Macari M. Dual energy CT: preliminary observations and potential clinical applications in the abdomen. Eur Radiol. 2009 Jan;19(1):13–23.

35. Uotani K, Watanabe Y, Higashi M, Nakazawa T, Kono AK, Hori Y, et al. Dual-energy CT head bone and hard plaque removal for quantification of calcified carotid stenosis: utility and comparison with digital subtraction angiography. Eur Radiol. 2009 Aug;19(8):2060–5.

36. Watanabe Y, Uotani K, Nakazawa T, Higashi M, Yamada N, Hori Y, et al. Dual-energy direct bone removal CT angiography for evaluation of intracranial aneurysm or stenosis: comparison with conventional digital subtraction angiography. Eur Radiol. 2009 Apr;19(4):1019–24.

37. Yamamoto S, McWilliams J, Arellano C, Marfori W, Cheng W, Mcnamara T, et al. Dual-energy CT angiography of pelvic and lower extremity arteries: dual-energy bone subtraction versus manual bone subtraction. Clin Radiol. 2009 Nov;64(11):1088–96.

38. Stolzmann P, Kozomara M, Chuck N, Müntener M, Leschka S, Scheffel H, et al. In vivo identification of uric acid stones with dual-energy CT: diagnostic performance evaluation in patients. Abdom Imaging. 2010 Oct;35(5):629–35.

39. Stolzmann P, Leschka S, Scheffel H, Rentsch K, Baumüller S, Desbiolles L, et al. Characterization of urinary stones with dual-energy CT: improved differentiation using a tin filter. Invest Radiol. 2010 Jan;45(1):1–6.

40. Stolzmann P, Scheffel H, Rentsch K, Schertler T, Frauenfelder T, Leschka S, et al. Dual-energy computed tomography for the differentiation of uric acid stones: ex vivo performance evaluation. Urol Res. 2008 Aug;36(3–4):133–8.

41. Thomas C, Patschan O, Ketelsen D, Tsiflikas I, Reimann A, Brodoefel H, et al. Dual-energy CT for the characterization of urinary calculi: In vitro and in vivo evaluation of a low-dose scanning protocol. Eur Radiol. 2009 Jun;19(6):1553–9.

42. Graser A, Johnson TRC, Bader M, Staehler M, Haseke N, Nikolaou K, et al. Dual energy CT characterization of urinary calculi: initial in vitro and clinical experience. Invest Radiol. 2008 Feb;43(2):112–9.

43. Material-specific attenuation curves of bone, iodine and water plotted.. - Figure 1 of 8 [Internet]. [cited 2017 Jan 23]. Available from: https://www.researchgate.net/Figure/221845330_fig1_Material-specific-attenuation-curves-of-bone-iodine-and-water-plotted-versus-photon

44. Fornaro J, Leschka S, Hibbeln D, Butler A, Anderson N, Pache G, et al. Dual- and multi-energy CT: approach to functional imaging. Insights Imaging. 2011 Jan 19;2(2):149–59.

45. Barreto M, Schoenhagen P, Nair A, Amatangelo S, Milite M, Obuchowski NA, et al. Potential of dual-energy computed tomography to characterize atherosclerotic plaque: ex vivo assessment of human coronary arteries in comparison to histology. J Cardiovasc Comput Tomogr. 2008 Aug;2(4):234–42.

46. Amato E, Lizio D, Settineri N, Pasquale AD, Salamone I, Pandolfo I. A method to evaluate the dose increase in CT with iodinated contrast medium. Med Phys. 2010 Aug 1;37(8):4249–56.

47. Gao H, Yu H, Osher S, Wang G. Multi-energy CT based on a prior rank, intensity and sparsity model (PRISM). Inverse Probl. 2011 Nov 1;27(11):115012.

48. Schlomka JP, Roessl E, Dorscheid R, Dill S, Martens G, Istel T, et al. Experimental feasibility of multi-energy photon-counting K-edge imaging in pre-clinical computed tomography. Phys Med Biol. 2008 Aug 7;53(15):4031.

49. Taguchi K, Zhang M, Frey EC, Wang X, Iwanczyk JS, Nygard E, et al. Modeling the performance of a photon counting x-ray detector for CT: Energy response and pulse pileup effects. Med Phys. 2011 Feb 1;38(2):1089–102.

50. Le HQ, Molloi S. Segmentation and quantification of materials with energy discriminating computed tomography: A phantom study. Med Phys. 2011 Jan 1;38(1):228–37.

51. Lasio GM, Whiting BR, Williamson JF. Statistical reconstruction for x-ray computed tomography using energy-integrating detectors. Phys Med Biol. 2007 Apr 21;52(8):2247–66.

52. Yu H, Xu Q, He P, Bennett J, Amir R, Dobbs B, et al. Medipix-based Spectral Micro-CT. CT Li Lun Yu Ying Yong Yan Jiu. 2012 Dec;21(4):583.

53. Anderson NG, Butler AP, Scott NJA, Cook NJ, Butzer JS, Schleich N, et al. Spectroscopic (multi-energy) CT distinguishes iodine and barium contrast material in MICE. Eur Radiol. 2010 Mar 23;20(9):2126–34.

54. Boll DT, Hoffmann MH, Huber N, Bossert AS, Aschoff AJ, Fleiter TR. Spectral coronary multidetector computed tomography angiography: dual benefit by facilitating plaque characterization and enhancing lumen depiction. J Comput Assist Tomogr. 2006 Oct;30(5):804–11.

55. Boll DT, Patil NA, Paulson EK, Merkle EM, Nelson RC, Schindera ST, et al. Focal Cystic High-Attenuation Lesions: Characterization in Renal Phantom by Using Photon-counting Spectral CT—Improved Differentiation of Lesion Composition [1]. Radiology. 2010 Jan;254(1):270–6.

56. Roessl E, Proksa R. K-edge imaging in x-ray computed tomography using multi-bin photon counting detectors. Phys Med Biol. 2007;52(15):4679.

57. Wang X, Meier D, Mikkelsen S, Maehlum GE, Wagenaar DJ, Tsui B, et al. MicroCT with energy-resolved photon-counting detectors. Phys Med Biol. 2011 May 7;56(9):2791–816.

58. Masetti S, Fiaschetti M, Turco A, Roma L, Rossi PL, Mariselli M, et al. Development of a Multi-Energy CT for Small Animals: Characterization of the Quasi-Monochromatic X-Ray Source. IEEE Trans Nucl Sci. 2009 Feb;56(1):29–35.

59. Yang Q, Cong W, Wang G. Superiorization-based multi-energy CT image reconstruction. Inverse Probl. 2017;33(4):044014.

60. Yu L, Leng S, McCollough CH. Dual-Source Multi-Energy CT with Triple or Quadruple X-ray Beams. Proc SPIE-- Int Soc Opt Eng [Internet]. 2016 Feb [cited 2017 Mar 26];9783. Available from: /pmcc/articles/PMC4912217/?report=abstract

61. Cormode DP, Skajaa T, Fayad ZA, Mulder WJM. Nanotechnology in medical imaging: probe design and applications. Arterioscler Thromb Vasc Biol. 2009 Jul;29(7):992–1000.

62. Lemacks MR, Kappadath SC, Shaw CC, Liu X, Whitman GJ. A dual-energy subtraction technique for microcalcification imaging in digital mammography--a signal-to-noise analysis. Med Phys. 2002 Aug;29(8):1739–51.

63. Shepherd JA, Kerlikowske KM, Smith-Bindman R, Genant HK, Cummings SR. Measurement of breast density with dual X-ray absorptiometry: feasibility. Radiology. 2002 May;223(2):554–7.

64. Ducote JL, Molloi S. Quantification of breast density with dual energy mammography: a simulation study. Med Phys. 2008 Dec;35(12):5411–8.

65. Ducote JL, Molloi S. Quantification of breast density with dual energy mammography: an experimental feasibility study. Med Phys. 2010 Feb;37(2):793–801.

66. Laidevant AD, Malkov S, Flowers CI, Kerlikowske K, Shepherd JA. Compositional breast imaging using a dual-energy mammography protocol. Med Phys. 2010 Jan 1;37(1):164–74.

67. Chung SH, Cerussi AE, Klifa C, Baek HM, Birgul O, Gulsen G, et al. In vivo water state measurements in breast cancer using broadband diffuse optical spectroscopy. Phys Med Biol. 2008 Dec 7;53(23):6713–27.

68. Tromberg BJ, Cerussi A, Shah N, Compton M, Durkin A, Hsiang D, et al. Imaging in breast cancer: Diffuse optics in breast cancer: detecting tumors in pre-menopausal women and monitoring neoadjuvant chemotherapy. Breast Cancer Res. 2005 Nov 28;7(6):279.

69. Cerussi A, Shah N, Hsiang D, Durkin A, Butler J, Tromberg BJ. In vivo absorption, scattering, and physiologic properties of 58 malignant breast tumors determined by broadband diffuse optical spectroscopy. J Biomed Opt. 2006 Aug;11(4):044005.

70. Haka AS, Shafer-Peltier KE, Fitzmaurice M, Crowe J, Dasari RR, Feld MS. Diagnosing breast cancer by using Raman spectroscopy. Proc Natl Acad Sci U S A. 2005 Aug 30;102(35):12371–6.

71. U Majewska JB. Some aspects of statistical distribution of trace element concentrations in biomedical samples. Nucl Instrum Methods Phys Res Sect B Beam Interact Mater At. 1999;254–9.

72. Kubala-Kukuś A, Kuternoga E, Braziewicz J, Pajek M. Log-stable concentration distributions of trace elements in biomedical samples. Spectrochim Acta Part B At Spectrosc. 2004 Oct 8;59(10–11):1711–6.

73. Mulay IL, Roy R, Knox BE, Suhr NH, Delaney WE. Trace-metal analysis of cancerous and noncancerous human tissues. J Natl Cancer Inst. 1971 Jul;47(1):1–13.

74. Ebrahim AM, Eltayeb M a. H, Shaat MK, Mohmed NMA, Eltayeb EA, Ahmed AY. Study of selected trace elements in cancerous and non-cancerous human breast tissues from Sudanese subjects using instrumental neutron activation analysis. Sci Total Environ. 2007 Sep 20;383(1–3):52–8.

75. Piacenti da Silva M, Zucchi OLAD, Ribeiro-Silva A, Poletti ME. Discriminant analysis of trace elements in normal, benign and malignant breast tissues measured by total reflection X-ray fluorescence. Spectrochim Acta. 2009 Jun 1;64:587–92.

76. Ding H, Zhao B, Baturin P, Behroozi F, Molloi S. Breast tissue decomposition with spectral distortion correction: A postmortem study. Med Phys. 2014 Oct 1;41(10):101901.

77. Johns PC, Yaffe MJ. X-ray characterisation of normal and neoplastic breast tissues. Phys Med Biol. 1987 Jun 1;32(6):675–95.

78. Schmidt TG. Optimal “image-based” weighting for energy-resolved CT. Med Phys. 2009 Jul;36(7):3018–27.

79. Le HQ, Ducote JL, Molloi S. Radiation dose reduction using a CdZnTe-based computed tomography system: Comparison to flat-panel detectors. Med Phys. 2010 Mar;37(3):1225–36.

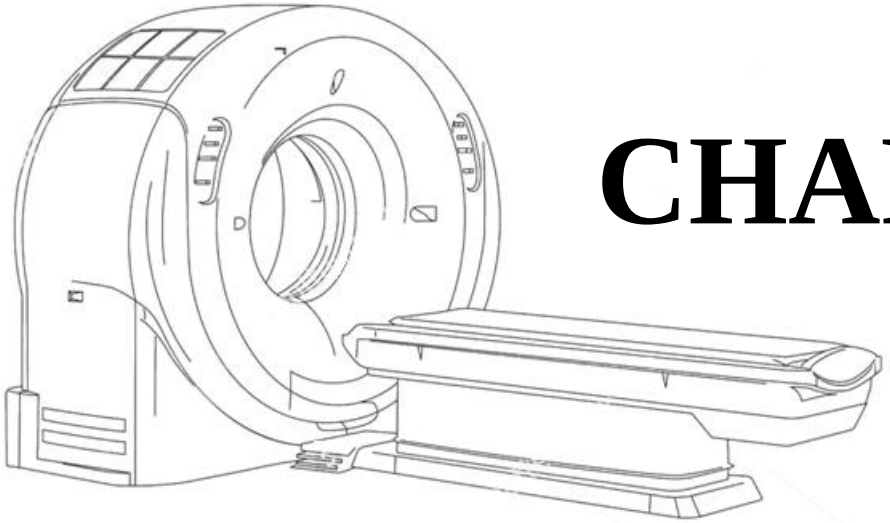

CHAPTER 2

CT modelling in BEAMnrc to characterise cone beam properties

Table of Contents

2.1 Introduction

BEAMnrc is part of the OMEGA project and is used for the simulation of the radiation beam of radiotherapy units.[1] The code consists of multiple CM's that can be used to make up the different components of the unit being simulated.

If X-rays are directed towards an object, they can either be absorbed, scattered or penetrate the object completely. The penetration abilities of a specific beam of X-rays depend on the energy of the photons and the density, atomic number and thickness of the object. The most common way to express the penetrating ability of a beam is by means of the HVL. The HVL is the absorber thickness required to reduce the intensity of the incident beam by one-half. A beam with a high HVL is more penetrating than a beam with a low HVL.[2]

The penetration abilities of a beam through a particular material depend on the energy of the incident beam. A beam containing a spectrum of energies is usually referred to as a polychromatic beam. Each of the energies in this spectrum will have different penetrating abilities. The penetrability of a polychromatic beam will increase as it moves through an attenuator since the lower energies are removed and the average energy of the beam changes. The effective attenuation coefficient, u_{eff}, of a polychromatic beam can be determined by using the HVL and is given by $u_{eff} = \frac{0.693}{HVL}$. The equivalent energy is a term that describes the energy of a monoenergetic beam that will have an attenuation coefficient similar to u_{eff}.[3]

In Figure 2.1 is a plot of the linear attenuation coefficient as a function of photon energy. If we have a 100 kV beam with a HVL of 4.5 mm then the linear attenuation coefficient would be as follows:

$$\mu = \frac{0.693}{HVL} = 1.54\,cm^{-1} \qquad 2.1$$

Bremsstrahlung X-rays are formed from a Coulomb interaction between an incident electron and the nucleus of the target material. It is caused by the sudden slowing down of the incident electron due to the strong electric fields of atomic nuclei. These electrons will be influenced and deflected by the electric field and will lose part of their energy.[3-5] This energy is bremsstrahlung radiation as seen in Figure 2.1.

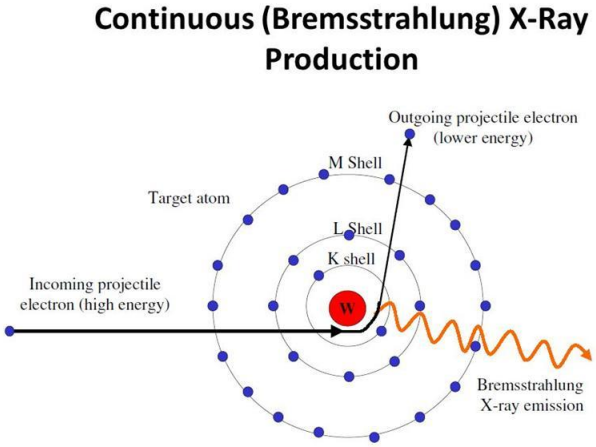

Figure 2.1: Interaction between an incoming electron and a nucleus. The electron is deflected and loses energy in the form of Bremsstrahlung.[6]

The spectrum of energies can range from zero to the kinetic energy of the incident electron. The spectrum produced will depend on the kinetic energy of the incident electron and the characteristics of the target material.[7,8] The intensity of the bremsstrahlung is proportional to the square of the target atomic number and inversely with the mass of the incident particle. A light particle such as an electron will therefore be more efficient in producing bremsstrahlung than a heavier particle. The 'peak' of the spectrum will occur at approximately one-third of the maximum energy. A spectrum of 120 kV will therefore have a peak at approximately 40 kV. An energy spectrum of 100 kVp can be seen below in Figure 2.2. The photons below the low energy cut-off are so easily attenuated by the anode and added filtration that the

emerging energy from them is negligible. The maximum energy depends on the energy of the incoming electron that loses all of its energy during a collision.

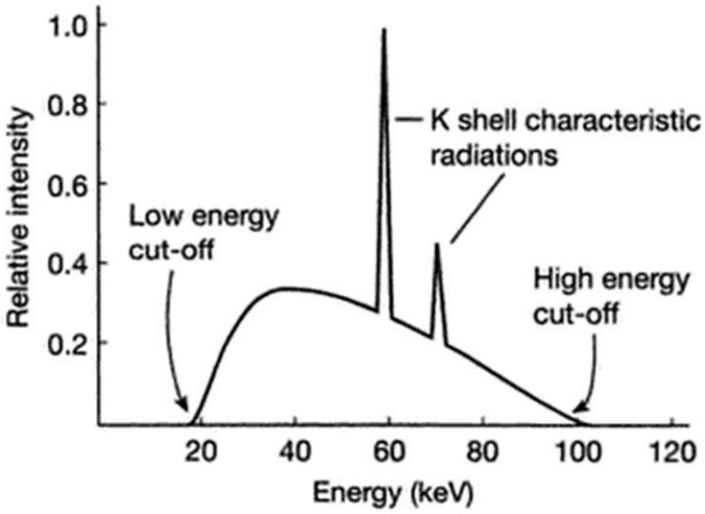

Figure 2.2: Energy spectrum from an X-ray tube operating at 100 kVp with 2.5 mm aluminium filtration.[9]

Low energy photons are absorbed more easily as they mostly undergo photoelectric interactions. This can pose a problem when imaging a patient with a spectrum consisting of low energies. Energies below 10 keV will be completely absorbed by the patient and will add to the dose the patient receives. This can be avoided by filtering the beam with a metal sheet, usually aluminium (Al). The filtration material will increase the ratio of the higher photons that can penetrate the patient and add to the radiographic image. Aluminium has an atomic number of 13 and is a good absorber of low energies. It produces characteristic X-rays of 1.5 keV that is easily absorbed in the air before reaching the patient. A copper (Cu) filter can also be used for higher energies and has an atomic number of 29. It is used in conjunction with an Al filter to filter out the characteristic radiation of the Cu at 8 keV. The Cu filter will be the closest to the tube and the Al filter closest to the patient.[10]

If a collision occurs between the incident electron and a bound orbital electron of the target material, characteristic X-rays are formed. If the incoming electron has sufficient energy, the

orbital electron is ejected from its shell, and an electron from a higher level shell fills the resulting vacancy. The energy difference between the two shells is emitted as characteristic X-rays, or it can be passed on to another orbital electron that is ejected as an Auger electron as seen in Figure 2.3.

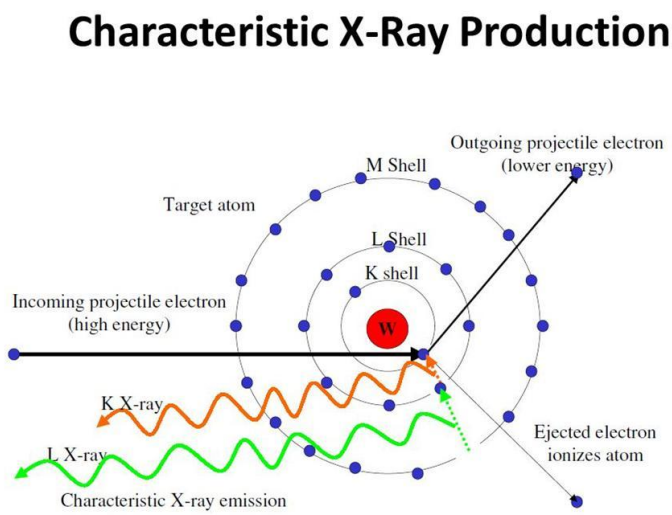

Figure 2.3: Interaction between an incoming electron and an orbital electron. The electron is ejected, the vacancy is filled by another electron from a higher shell, and characteristic X-rays are formed.[6]

As seen in Figure 2.4 above, an atom consists of different core shells denoted by K, L, M etc. Each of these shells has their own binding energy that needs to be exceeded in order to eject an electron. For aluminium the K shell has a binding energy of 1.6 keV and copper (Cu) 8.98 keV. An X-ray absorption spectrum for lead (Pb) can be seen below in Figure 2.4

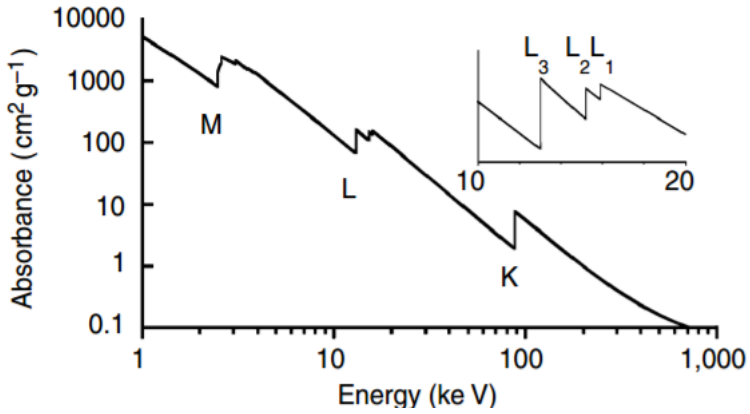

Figure 2.4: The X-ray absorption spectrum for Pb. Three major transitions are seen (K, L, and M edges), corresponding to excitation of an electron from n = 1, 2, and 3 shells, respectively.[4]

The increase in the cross-section at the specific edges is due to additional contributions when the energy is sufficient to eject an inner shell electron.[4]

The tube current and exposure time will alter the flux of X-rays, but the X-ray spectrum will stay unchanged. By increasing the tube voltage, the quality of the X-rays will increase and therefore the spectrum will have a higher HVL.

In this chapter, an energy spectrum was generated by simulating an X-ray tube and filters in BEAMnrc. The HVL of this spectrum was benchmarked against that of the Aquilion LB 16 CT available at our hospital. The anode angle was chosen in such a way to produce a small focal spot size, and the appropriate amount of filtration was determined through calculations. The resulting energy spectrum was used in the next chapter for the matching of the simulated HUs to that of the Toshiba Aquilion LB 16 CT.

2.2 Methods & Materials

The following steps were taken to compare the measured HVL value with the simulated HVL by using MC simulations.

2.2.1: Step1: HVL measurements for the Toshiba Aquilion LB 16 CT scanner

The X-ray tube exit window of the CT was parked in a 12 o'clock position, and the HVL was determined for 80, 100, 120 and 140 kV with technical support from Tecmed Africa (Pty) Ltd. A Magic-MaX M Rad/Flu/Dent ionisation chamber from IBA Dosimetry was used for the determination of the HVL. The chamber has built-in filtration of 1.5 mm to 30 mm of Al equivalent and also the necessary backscatter. The Magic-MaX M Rad/Flu/Dent was placed on the couch of the CT, and the resulting HVL for the different energies was determined.

2.2.2 Step 2: X-ray tube simulation in BEAMnrc

The MC code, BEAMnrc, was used for the simulation of the X-ray tube. The set-up consisted of a target at an angle of 7 degrees and a filter composed of various materials as seen in Figure 2.5 below.

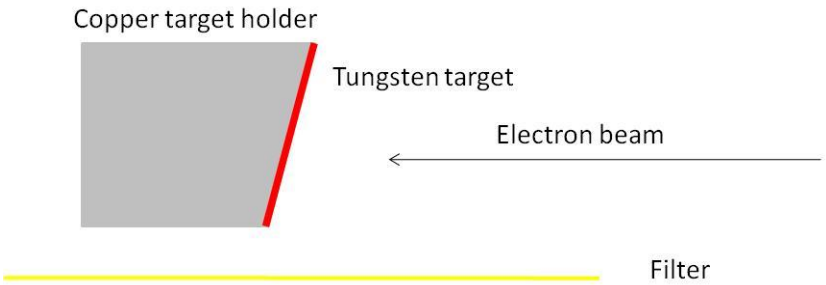

Figure 2.5: Schematic of the set-up in BEAMnrc for the simulation of the X-ray tube. (The image is not to scale)

Beryllium windows are often added to an X-ray tube to hold a perfect vacuum. Beryllium only has 4 electrons for the interaction with X-rays and a low density of 1.85 g/cm^3. It is therefore virtually transparent to X-rays and was not included in the X-ray tube simulation.[12] The simulation efficiency was improved by modifying the default parameters in the macro file beamnrc_user_macros.mortran. The BDY_TOL parameter is used to avoid round-off errors by shifting the boundaries between different regions in the geometry by a small

distance. In the kilovoltage range the charged particle step size is of the same order of magnitude as the default value of 10^{-5} cm and will affect the backscatter correction.[9] The value of boundary tolerance BDY_TOL was modified to 5×10^{-7} cm to limit the deviations in the total backscatter coefficient. The maximum directional bremsstrahlung split number was set to 2×10^{4} as suggested by Ali and Rogers.[13] Variance reduction techniques (VRTs) such as Rayleigh scattering, atomic relaxations, bound Compton scattering, electron impact ionisation and spin effects were implemented as recommended for low-energy simulations. The XCOM database was used for photon cross-sections. The global electron cut-off energy (ECUT) and photon cut-off energy (PCUT) were set to 0.512 MeV and 0.001 MeV respectively. The electron-step algorithm and boundary cross algorithm (BCA) was PRESTA-II and EXACT, respectively. The skin depth for the BCA was set to three elastic mean free paths.

2.2.3 Step 3: HVL simulations in DOSXYZnrc

The simulated HVL value was determined in DOSXYZnrc by using the resulting phase space of step 2.

The HVL was verified with the help of the DOSXYZnrc code. The resulting phase space file from BEAMnrc was used as input for the DOSXYZnrc simulation. The X-ray source was placed a distance of 100 cm from a semi-infinite slab of aluminium. The slab thickness was increased in small increments, and the dose was scored in a water phantom 150 cm from the source. The central voxel was used for scoring with a dimension of 1 x 1 cm to improve the dose statistics. To satisfy the conditions of narrow-beam geometry, a small parallel source was used to ensure no scattered photons are recorded. The same simulation parameters were used as in the case of the BEAMnrc simulation.

The simulation set-up can be seen in Figure 2.6 below.

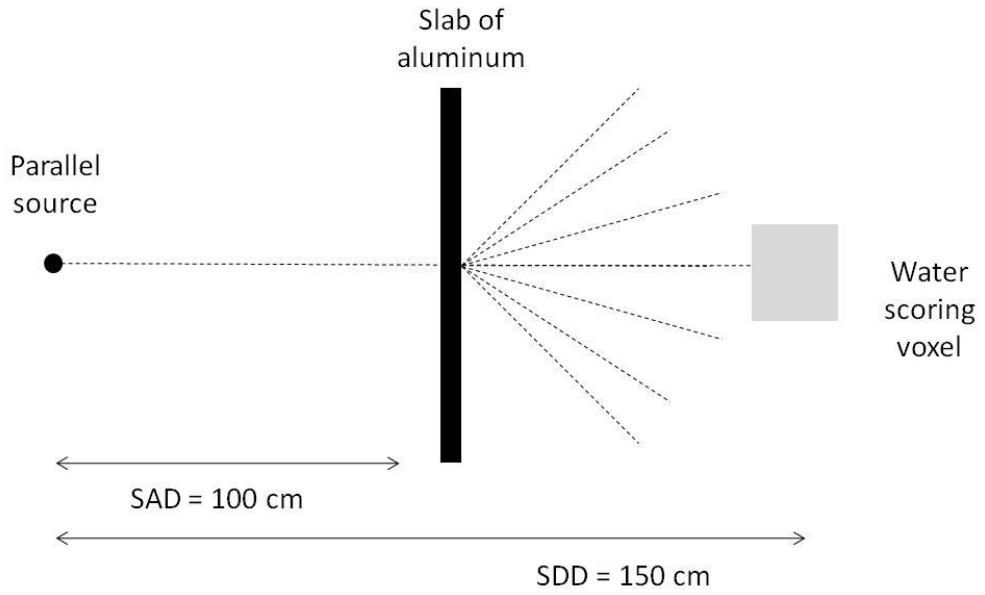

Figure 2.6: Simulation set-up in DOSXYZnrc for the determination of the HVL.

The HVL was determined as the thickness of material that reduces the dose to one-half of the initial value when there is no material (aluminium) in the beam path. This was done for phase space files with various amounts of Al filtration and filters consisting of a combination of Cu and Al.

2.2.4 Step 4: Berlin cavity theory correction

The Toshiba Aquilion LB 16 CT HVL was determined with in-air measurements and the simulated HVL was done in water. The simulated values obtained in water were converted to in-air measurements to compare the two values with one another. The linear attenuation coefficient was derived from the HVL by using Equation 2.1. The effective energy of the beam was obtained from the NIST database[10] by using the calculated linear attenuation coefficient of the X-ray beam. The mass energy-absorption coefficient for water and air at the effective energy was then used. It was assumed that only photon interactions would occur since no build-up is needed for such a low energy and that charged particle equilibrium exists.

The Berlin (Burlin) cavity theory and the ratio of the mass energy-absorption coefficients were used to convert the simulated water measurements to in-air measurements as shown below.

$$\frac{D_{water}}{D_{air}} = \left(\frac{\mu_{en}}{\rho} \right)_{air}^{water} \tag{2.2}$$

2.2.5 Step 5: HVL determination

The corrected dose values from step 4 versus the thickness of Al were plotted and an exponential curve was fitted to the data. The equation of the fitted curve was used for the determination of the HVL as seen below.

$$y = z\, e^{-\mu x} \tag{2.3}$$

Where y equals the dose values on the y-axis, z is the y-intercept, μ is the slope of the exponential curve and x is the thickness of Al on the x-axis in mm. The HVL will reduce the initial intensity on the y-axis, without any Al present, I_0, to half of its value as shown below.

$$\frac{I_0}{2} = z\, e^{-\mu x} \tag{2.4}$$

To obtain the value of x, that represents the HVL value, Equation 2.3 is rearranged to give the following:

$$\ln\left(\frac{I_0}{2} \Big/ z \right) \Big/ \mu = x \tag{2.5}$$

The HVL is expressed in mm of Al. The two HVL values were compared with one another.

2.3 Results & Discussion

2.3.1 HVL measurements for the Toshiba Aquilion LB 16 CT scanner

The Toshiba Aquilion LB 16 CT scanner had an HVL of 5.3 mm of Al and was measured as explained in Section 2.2.1.

2.3.2 Spectral distributions from BEAMnrc simulations

The spectral distribution of the phase space file without filtration and with various amounts of filtration can be seen in the figures below. The number of particles incident from the original source was 20 million, resulting in an uncertainty below 1%.

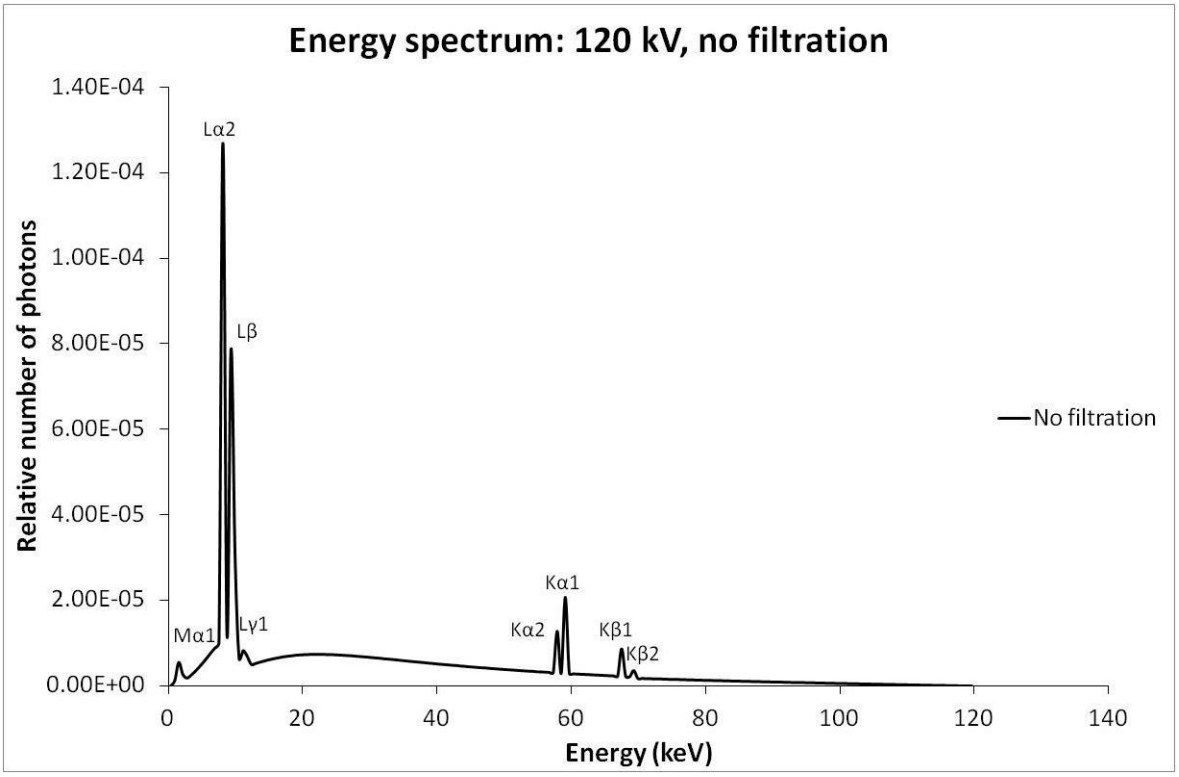

Figure 2.7: Energy spectrum of the phase space file resulting from the BEAMnrc simulation. No filtration was added. The prominent peaks at the low energies will increase the patient dose without contributing to the image.

The characteristic K, L and M X-ray line energies are seen in Figure 2.7 above. The K-line energies are a result of the ejection of a K-shell electron that is then filled with an electron

from the L-shell (K_α) or the M-shell (K_β). The different transitions that give rise to the emission lines can be seen below in Figure 2.8.

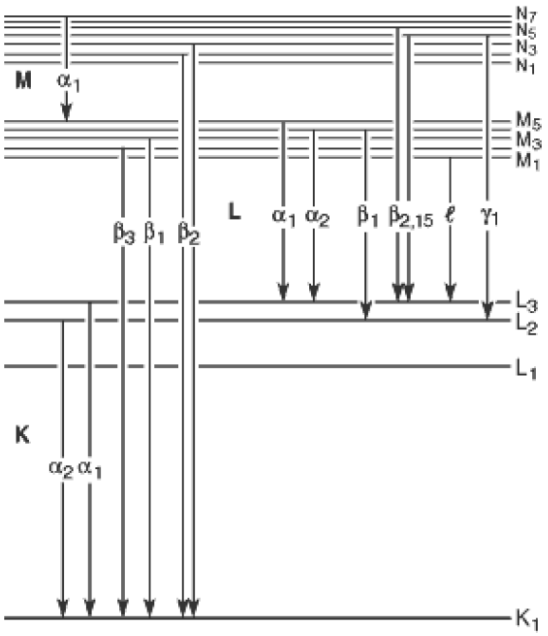

Figure 2.8: Different emission lines due to transitions between the shells. [14]

The mass attenuation coefficient for aluminium can be seen in Figure 2.9 as taken from the NIST database.[11] The mass absorption coefficient is, $\frac{\mu}{\rho}$ and the mass energy-absorption coefficient is $\frac{\mu_{en}}{\rho}$.

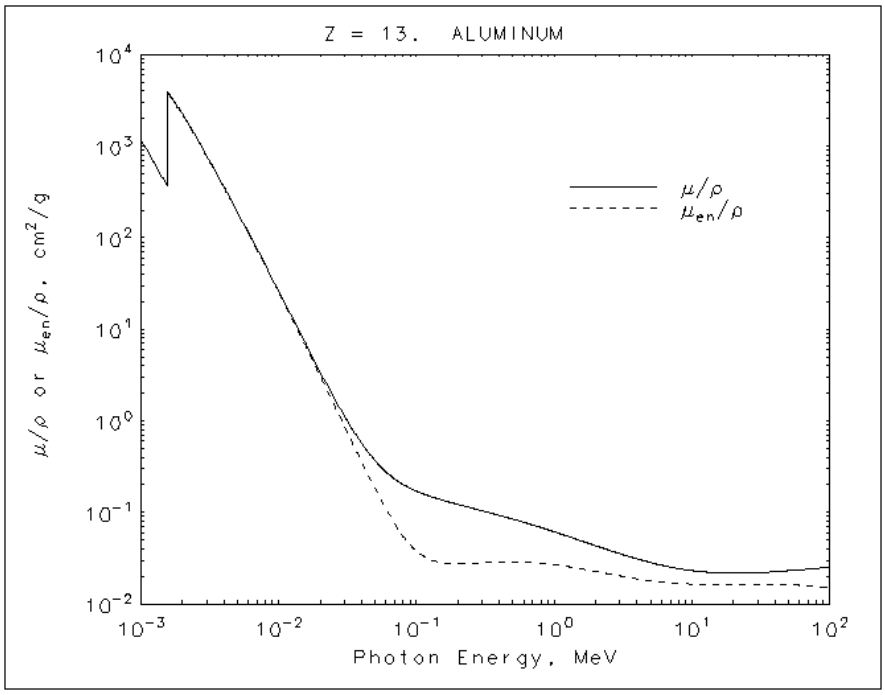

Figure 2.9: The mass attenuation coefficient and mass energy-absorption coefficient for aluminium. A sharp increase is visible at the K-edge of 1.6 keV.[15]

As seen below in Figure 2.10, aluminium filtration of 2 mm absorbs almost all the energies below 20 keV.

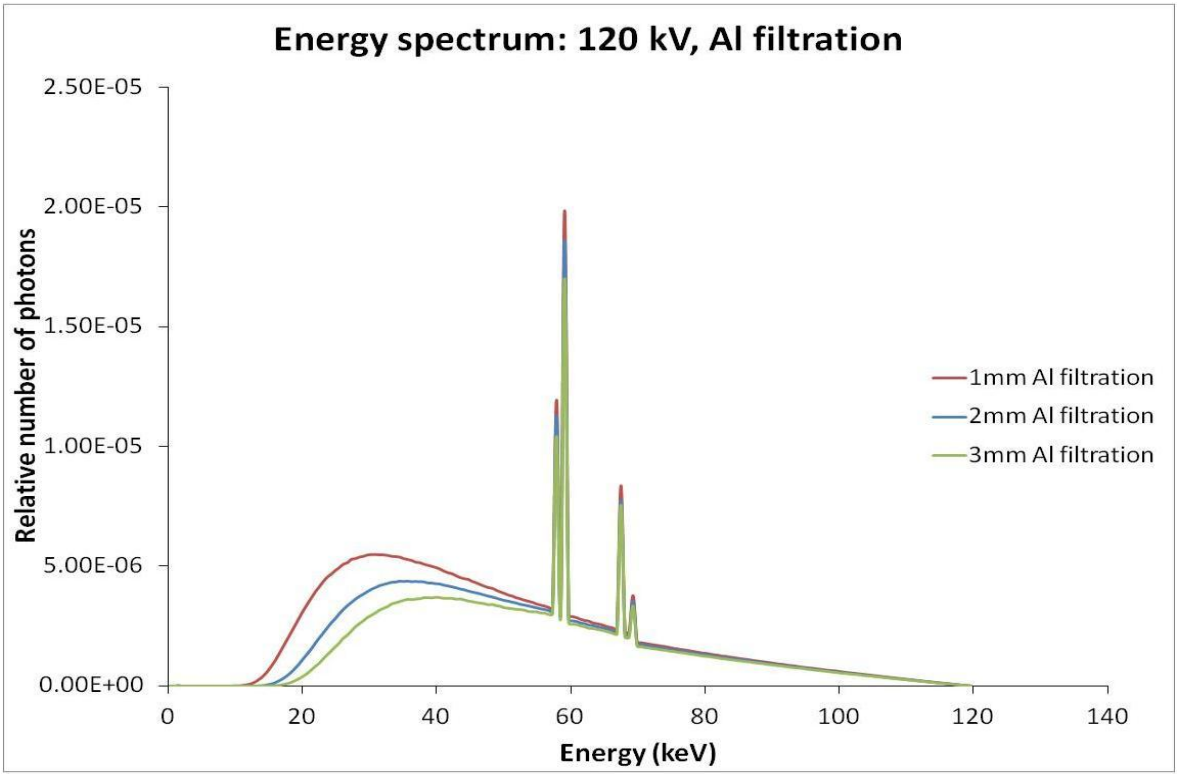

Figure 2.10: Energy spectrum of the phase space file resulting from the BEAMnrc simulation. Different amounts of filtration were added. The Al filters out the lower energies and increases the mean energy of the energy spectrum.

In Figure 2.11 below the effect of a compound filter consisting of Cu and Al can be seen. The Cu filter causes excessive filtration and absorbs almost all of the photons below 40 keV. An overall attenuation of the photon beam can be seen. The characteristic X-rays at 8 keV that is produced by the Cu are filtered out by using an Al filter.

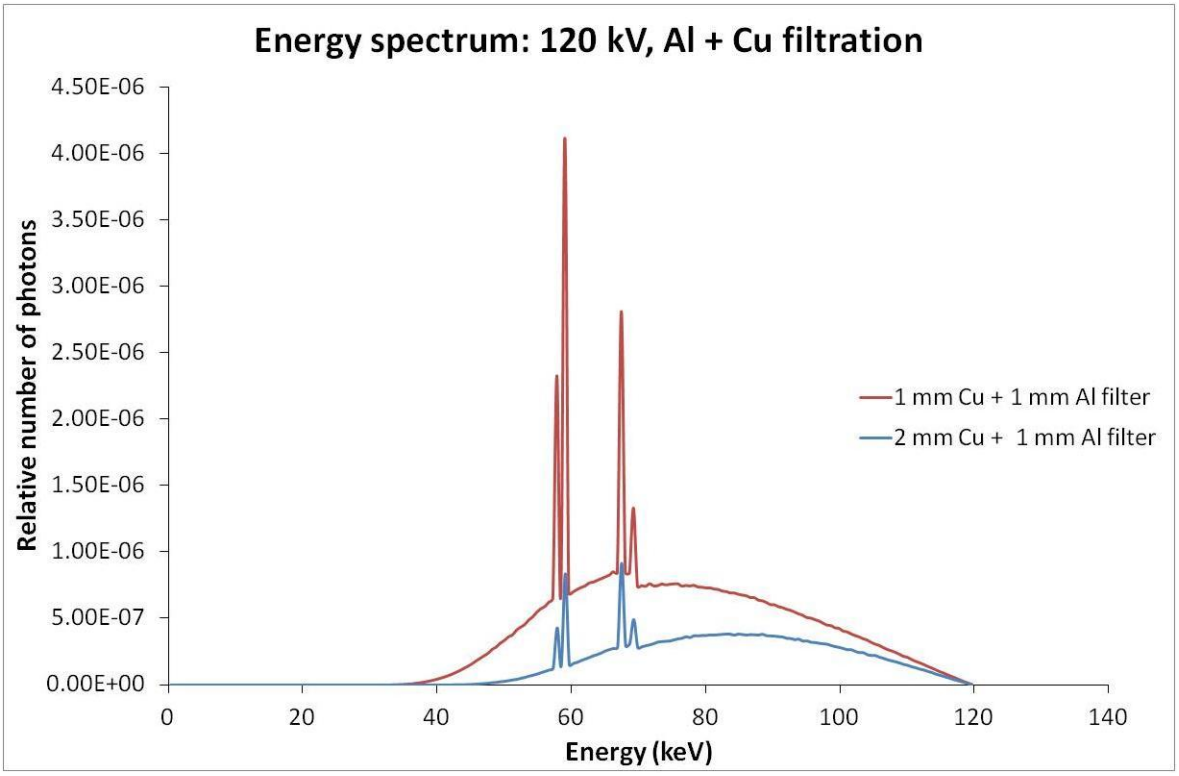

Figure 2.11: Energy spectrum of the phase space file resulting from the BEAMnrc simulation. Different amounts of Cu and Al filtration were added. Almost all the energies below 40 keV are filtered out. The Al filter absorbs the characteristic radiation of the Cu at 8 keV.

2.3.3 HVL verification

The following section shows results obtained by using an energy spectrum with 3 mm of Al filtration.

The dose values from the DOSXYZnrc simulation in water versus the thickness of Al absorption material can be seen for a filtered energy spectrum of 120 kV in Figure 2.11 below, by using the set-up shown in Figure 2.6. The dose decreases exponentially as the thickness of Al increases. As the beam passes through the first piece of Al, the lower energy photons have been eliminated and the remaining higher energy photons produce a beam which has a higher effective energy leading to an exponential curve. The uncertainties in the dose values are below 0.5 %.

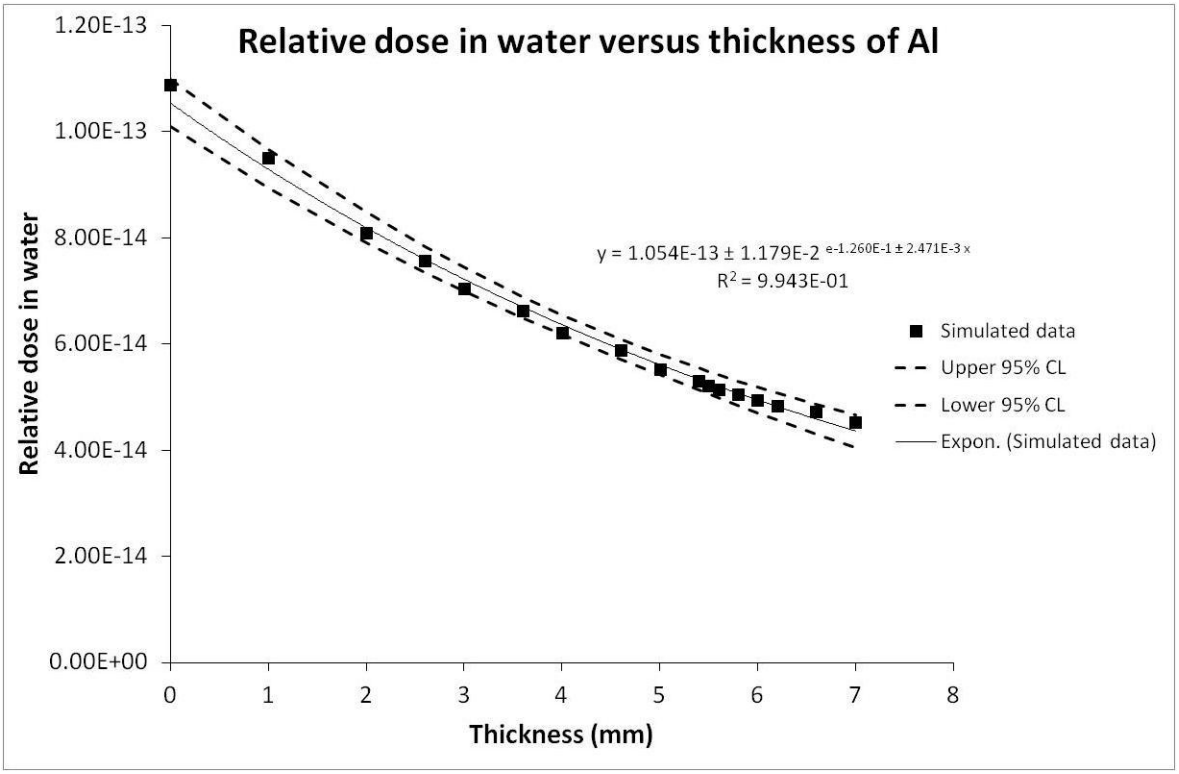

Figure 2.12: Exponential decrease in dose in water as a function of Al thickness. The uncertainties in the dose values are smaller than the symbol size and below 0.5 %. The 95% confidence levels are indicated.

The simulated water data were converted to in-air measurements by the following mass energy-absorption coefficient ratios.

$$D_{air} = D_{water}\left(\frac{\mu_{en}}{\rho}\right)_{water}^{air} = D_{water}\left(\frac{0.075}{0.086}\right) \qquad 2.6$$

The resulting dose values for the air are shown below.

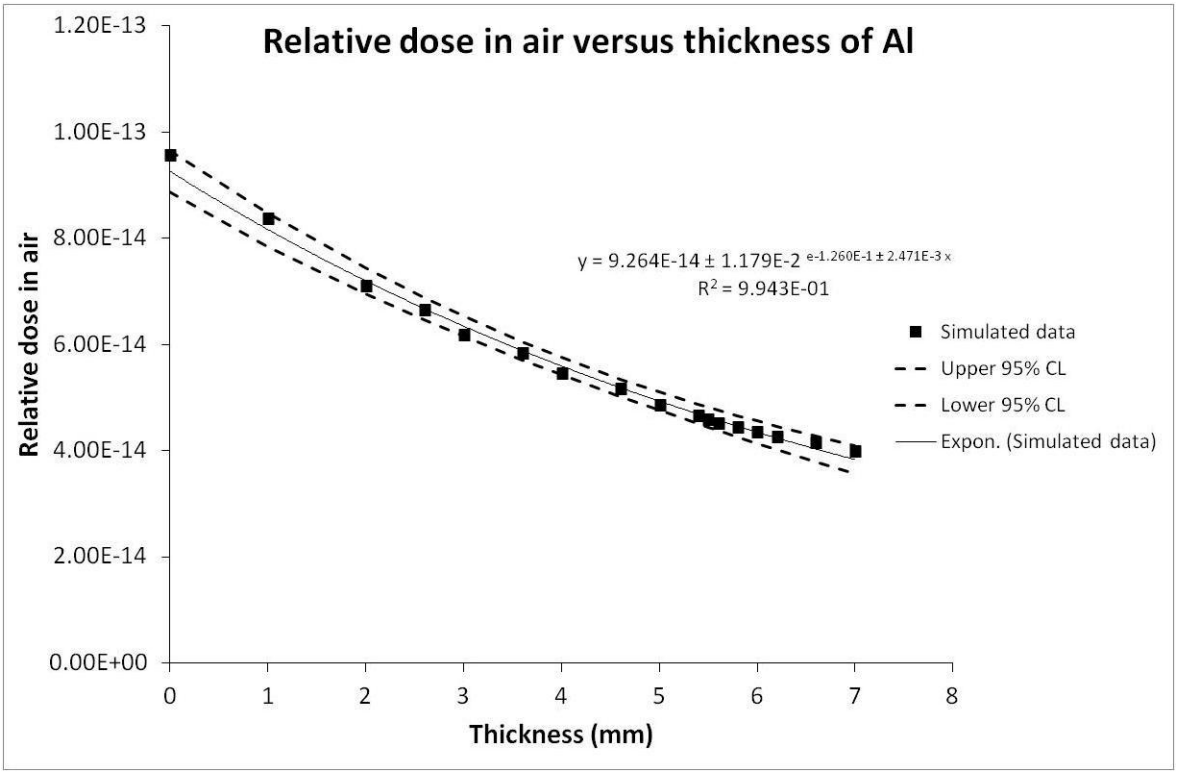

Figure 2.13: Exponential decrease in dose in the air as a function of Al thickness. The uncertainties in the dose values are smaller than the symbol size and below 0.5 %. The 95% confidence levels are indicated.

The HVL from the in-air dose values is calculated by using equation 2.4 as seen below.

$$\ln\left(\frac{9.564\text{E-}14}{2}\Big/9.264\text{E-}14\right)\Big/-0.126 = 5.25 \text{ mm} \qquad 2.7$$

The calculated HVL from the simulated data, 5.25 mm of Al, was within 1% of the measured value of 5.3 mm of Al for the Toshiba Aquilion LB 16 CT scanner.

2.4 Conclusion

In this chapter, it was shown that the energy spectrum of the Toshiba Aquilion LB 16 CT could be approximated with the aid of MC simulations. The BEAMnrc code successfully modelled the X-ray tube, and the simulated HVL could be matched with the measured HVL. An aluminium filter absorbs all the low energies and increases the mean energy of the X-ray

beam. The output could then be used for the further simulation of the RMI phantom for HU verification in the next chapter.

2.5 References

1. Rogers DWO, Faddegon BA, Ding GX, Ma C-M, We J, Mackie TR. BEAM: A Monte Carlo code to simulate radiotherapy treatment units. Med Phys. 1995 May 1;22(5):503–24.

2. Radiation Penetration [Internet]. [cited 2017 Jan 20]. Available from: http://www.sprawls.org/ppmi2/RADPEN/

3. Pawlicki T, Scanderbeg DJ, Starkschall G. Hendee's Radiation Therapy Physics. John Wiley & Sons; 2016. 349 p.

4. Dowsett D, Kenny PA, Johnston RE. The Physics of Diagnostic Imaging Second Edition. CRC Press; 2006. 706 p.

5. Allisy-Roberts P, Williams J. Farr's Physics for Medical Imaging. W.B. Saunders Company. (2007) ISBN:0702028444

6. X-Ray Technology By: PROF. Dr. Moustafa Moustafa Mohamed Faculty of Allied Medical Science Pharos University in Alexandria. - ppt download [Internet]. [cited 2017 Jan 25]. Available from: http://slideplayer.com/slide/6188331/

7. Khan FM. The Physics of Radiation Therapy. Fourth edition. Philadelphia: LWW; 2009. 592 p.

8. Podgorsak E. IAEA Review of Radiation Oncology Physics - A HAndbook for Teachers and Students. Vienna: International Atomic Energy Agency; 2005.

9. Dendy PP, Heaton B. Physics for Diagnostic Radiology, Third Edition. CRC Press; 1999. 470 p.

10. Curry, III TS, Dowdey JE, Murray, JR. RC. Christensen's Physics of Diagnostic Radiology. Fourth edition. Philadelphia, London: Lea & Febiger; 1990. 522 p.

11. Penner-Hahn JE. 2.13 - X-ray Absorption Spectroscopy. In: McCleverty JA, Meyer TJ, editors. Comprehensive Coordination Chemistry II [Internet]. Oxford: Pergamon; 2003. p. 159–86. Available from: http://www.sciencedirect.com/science/article/pii/B008043748601063X

12. Carlton RR, Adler AM. Principles of Radiographic Imaging: An Art and A Science. 5 edition. Clifton Park, NY: Delmar Cengage Learning; 2012. 832 p.

13. Benchmarking EGSnrc in the kilovoltage energy range against experimental measurements of charged particle backscatter coefficients - MedicalPhysicsWeb [Internet]. [cited 2016 Dec 29]. Available from: http://medicalphysicsweb.org/cws/article/journals/33025

14. BEARDEN JA. X-Ray Wavelengths. Rev Mod Phys. 1967 Jan 1;39(1):78–124.

15. NIST: X-Ray Mass Attenuation Coefficients - Aluminum [Internet]. [cited 2017 Mar 17]. Available from: http://physics.nist.gov/PhysRefData/XrayMassCoef/ElemTab/z13.html

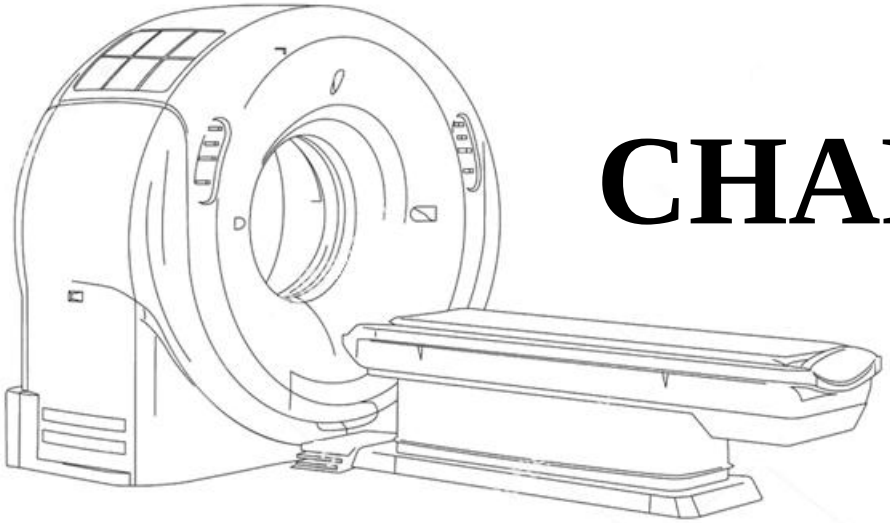

CHAPTER 3

RMI phantom simulation in egs_cbct

This chapter includes work published by the author – Appendix I (van Eeden *et al.* Phys Medica Eur J Med Phys. 2016 Oct 1; 32(10))

Table of Contents

3.1 Introduction

The specifications of a CT scanner usually depict all the information needed to perform an accurate simulation of the X-ray tube and beam modifying parameters. This includes the geometry of the scanner, anode angle, focus-isocentre distance, focus-detector distance, filtration and specifics regarding the collimators. This information is not always available, and other methods have been used in previous studies. Most recent studies use transmission measurements[1,2] and MC simulations[3-5] to estimate the X-ray spectrum. Older methods include nonlinear least-square fits to experimental data[6,7] and empirical methods.[8-11]

Other beam modifiers such as bowtie filters are used in multislice and cone beam CT (CBCT) to ensure a more uniform fluence reaches the detector.[12-16] There exist differences in the X-ray beam path length as it passes through an object. A polychromatic beam consists of photons with different energies. As this beam passes through an object, the lower energies are absorbed, and only the higher energies remain. This leads to an increase in the mean energy of the beam. The path length of the beam is longer through the centre of a cylindrical phantom (indicated by the red line) as seen below in Figure 3.1. This will result in more low energies being removed, and the beam will become ‘harder'. The path length at the periphery of the phantom is much shorter (indicated by the blue line below), and less beam hardening occurs.

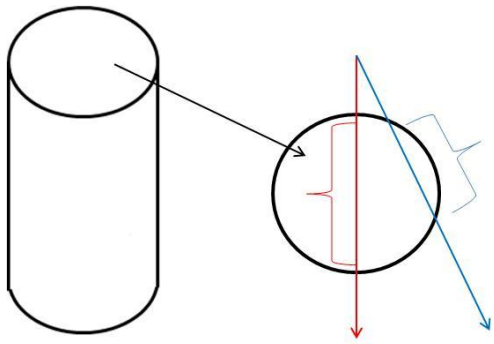

Figure 3.1: A cylindrical phantom seen from the side and the front. The path length through the centre of the phantom indicated by the red line is longer than the path length through the periphery of the phantom indicated by the blue line.

This altering in the attenuation profile for a polychromatic beam across the phantom from the centre to the periphery causes a cupping artifact.[17] This does not happen for a monoenergetic beam since the quality of the beam doesn't change as it passes through a phantom.[19] Compensator materials such as bowtie filters can be used to reduce beam-hardening and eliminate artifacts.[18] A bowtie filter has two-sided symmetry and an increase in thickness as a function of an increasing angle from the centre ray. This leads to a reduction in the radiation dose at the periphery of the field of view (FOV).[16] The design of the bowtie filter differs between the different CT scanners and is dependent on the linear attenuation coefficient and the size of the object being imaged. One of the methods to determine the bowtie filter design is through measurements.[16,20-22] This is not always possible in a busy department with a heavy workflow, and technical support is sometimes needed.

MC has been used previously in CT dosimetry studies and is regarded as the most accurate dose calculation code.[23] Previous studies include patient-specific dose calculations,[24,25] validation for complex geometries[26] and industrial applications[27,28]. In the field of breast CT imaging, the GEANT4-based simulation package was used for scatter distribution determination[29] and organ dose calculations.[30] Recent studies include the influence of monoenergetic and polyenergetic glandular dose coefficients[31] and mean glandular dose evaluations.[32] As stated in a study by McMillian *et al.*[33], most CT simulations lack validation beyond CT dose index (CTDI) measurements[34] and mostly include dose calculations.[35-37]

A reason for this can be the inefficiency of CT simulations with the currently available MC codes.[38] The user code egs_cbct was used which is an EGSnrc user code written in C++ by Ernesto Mainegra-Hing and Iwan Kawrakow.[39,40] EGSnrc[41] is the most frequently used MC application in medical physics[23] and include many user codes that can be used for the simulation of various geometries. With the egs_cbct user code, it is possible to set up a CBCT imaging system without knowledge of the C++ programming code. It is mainly used

for the fast estimation of scatter contribution in CBCT but can be used for other applications as well.

The egs_cbct code uses several VRTs together with a denoising algorithm to improve the scatter simulation efficiency. Since its release in March 2013, it has already been used for several studies.[42-45] One of the original papers describes how these VRTs can improve the efficiency of scatter calculations for a chest phantom by three orders of magnitude.[39] In a further paper by Thing *et al.* [46], the specific optimisation for different geometries is explored.

The detector detects the air-kerma after passing through a phantom at a specific angle. To do a full CT simulation, one has to submit each angle separately and obtain projection images around the phantom. In order to measure the attenuation along the beam path accurately, one needs first to run a simulation without a phantom to produce a 'blank' scan. The resulting file from the blank scan, I_0, is used to compute the final signal as seen in Equation 3.1 below.

$$-\ln\left(\frac{I}{I_0}\right) = \mu t \tag{3.1}$$

I is the projection measurement with a phantom, μ is the linear attenuation coefficient (cm^{-1}) and t is the thickness of the phantom in cm.

The resulting projections are then backprojected to reconstruct the original image. During backprojection, the projections are 'smeared back' across the image from the angle it originally came from. This results in a blurry version of the correct image. This can be accounted for by using filtered backprojection where each projection is filtered before it is backprojected as seen below in Figure 3.2.[47]

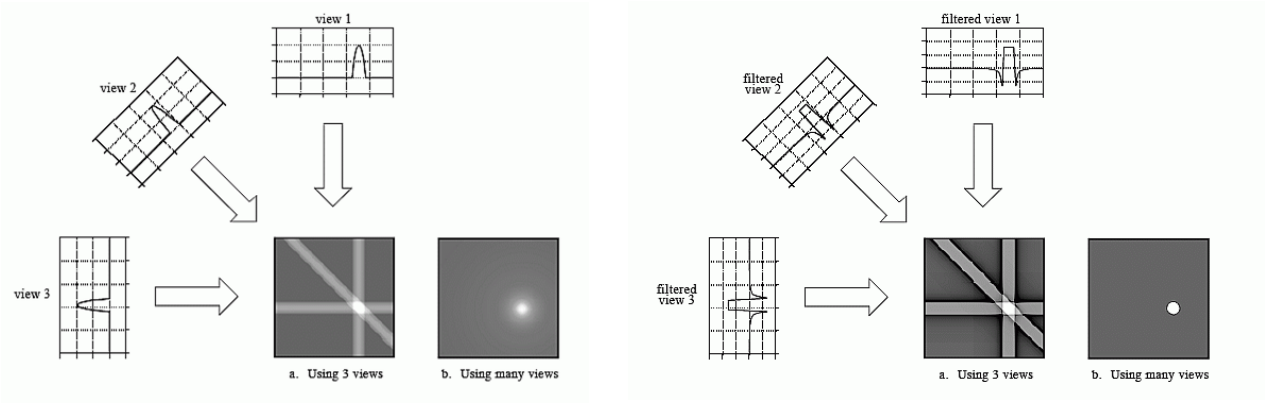

b)

Figure 3.2: a) Simple backprojection where each profile is smeared along its original path. b) Filtered backprojected where each profile is filtered before it is backprojected.[47]

There are high-pass filters and low-pass filters that can be used for the filtering of the projection data. The Ram-Lak filter is a high-pass filter and will sharpen parts of the image where there is a sudden change in signal, e.g. at the edges. A downfall of this filter is that it amplifies statistical noise and therefore it is always used in combination with a low-pass filter.[48] These combination filters smooth the image and reduces the amplification of the noise of the Ram-Lak filter, but results in a decrease in resolution. There exists a trade-off between the high-pass filters to sharpen the image and low-pass filters to reduce the noise. The Shepp-Logan filter is obtained by multiplying the Ram-Lak filter by a sinc function. The reconstructed images will have a reduction in noise but with some edge sharpness. A Cosine filter is obtained by multiplying the Ram-Lak filter by a cosine function. Similarly, Hamming and Hann filters are obtained by multiplying Ram-Lak filter by Hamming and Hann windows respectively. Ram-Lak and Shepp-Logan filters are high pass filters which keep the edges information intact, whereas Cosine, Hamming and Hann filters are band pass filters. They are used to smooth the image and remove extra edges from the image.[49]

In this chapter, the egs_cbct user code was used to simulate a fan beam CT to benchmark the simulated HUs against the measured ones. This was done for a Toshiba Aquilion LB 16 CT unit and the RMI 465 Electron Density CT phantom from Gammex. Using this phantom in

conjunction with CT simulations one can establish the relationship between the electron density (ρe) of various tissues and their corresponding HUs.

3.2 Methods & Materials

The phase space file generated by the BEAMnrc simulation from Chapter 2 was used in the next step of the simulations as input together with a bowtie filter. The RMI phantom was modelled in IDL and profile information around the phantom was obtained through egs_cbct simulations. These profiles were then used for reconstruction with a filtered backprojection algorithm. The HUs were extracted and used for verification of the commissioning values from the Toshiba Aquilion LB 16 CT.

In this chapter, it was decided to deviate from the original paper by adding the bowtie filter in the egs_cbct simulations instead of BEAMnrc. This will lead to more accurate results since there is no component module in BEAMnrc for bowtie modelling.

3.2.1 Modelling of the RMI phantom

The Gammex 465 consists of a 33 cm diameter Solid Water® disk approximating the size of an average pelvis. It has 20 inserts of 2.8 cm diameter, each of various tissue and water substitutes (Figure 3.3). The physical density (g/cm^3) and electron density relative to water of the insert materials is listed in Table 3.1

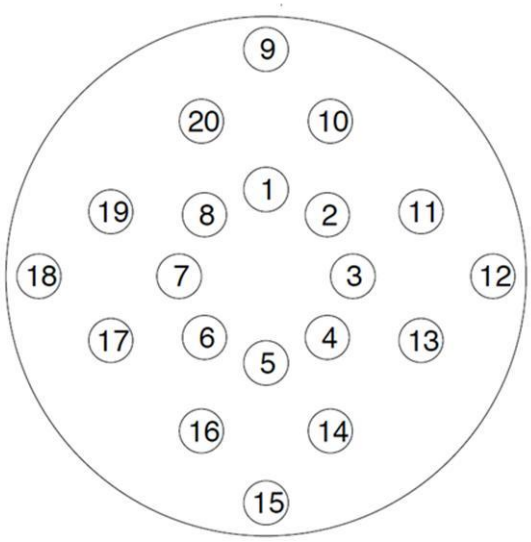

Figure 3.3: The RMI 465 phantom configuration with 20 inserts at various positions. Detail regarding each insert is found in Table 3.1 below.

Table 3.1: RMI-465 inserts material data.

Material	Tissue type	Density (g cm^{-3})	Electron density relative to water
LN-300	Lung	0.300	0.292
LN-450	Lung	0.450	0.438
AP6	Adipose	0.920	0.895
Polyethylene	-	0.920	0.945
Breast	Breast	0.990	0.980
Water	-	1.000	1.000
CT solid water	-	1.015	1.000
CB3 resin mix	-	1.020	1.020
Brain	Brain	1.045	1.039
Liver	Liver	1.080	1.050
IB1	Inner bone	1.120	1.081
B200	Bone mineral	1.145	1.099
CB4 resin mix	-	1.150	1.116
CB2-10% $CaCO_3$	Bone	1.170	1.142
Acrylic	-	1.180	1.147
CB2-30% $CaCO_3$	Bone	1.340	1.285
CB2-50% $CaCO_3$	Bone	1.560	1.473
SB3	Cortical bone	1.840	1.707

The relationship between the HUs and electron densities for all the inserts is seen below in Figure 3.4. These values were obtained during the commissioning of the Toshiba Aquilion LB 16 CT scanner.

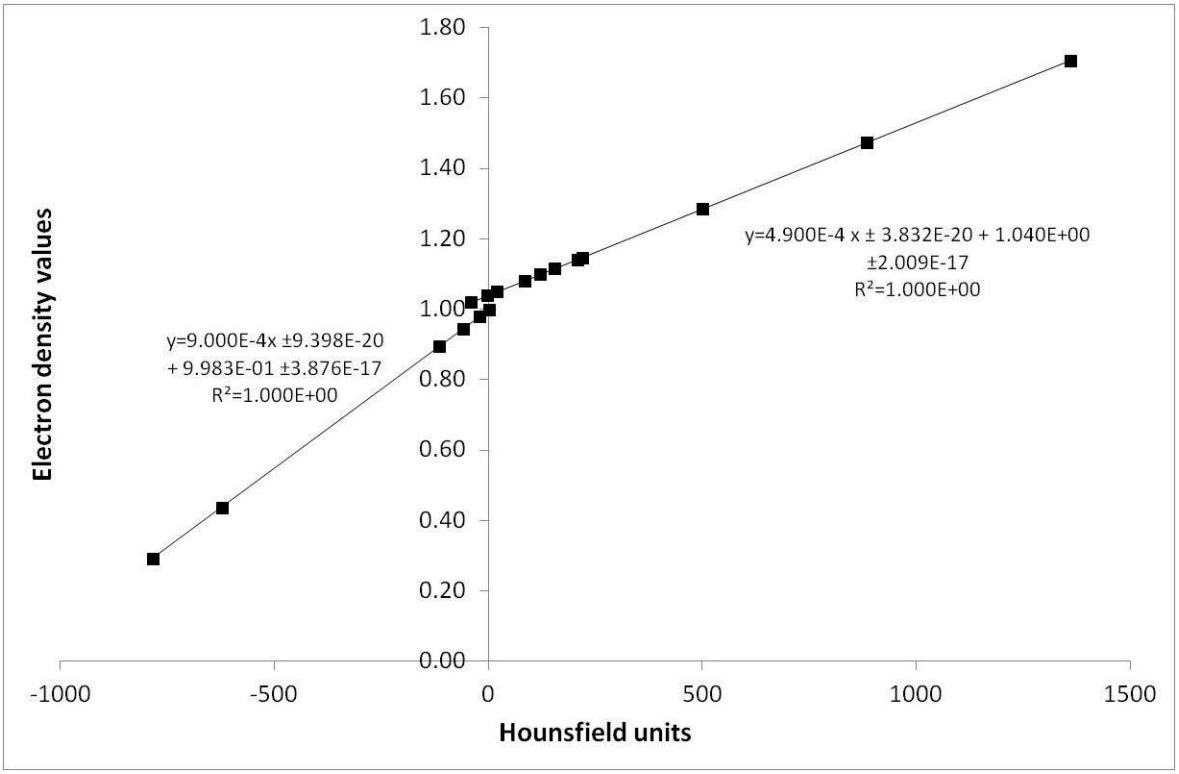

Figure 3.4: The electron density to Hounsfield unit conversion for the Toshiba Aquilion LB 16 CT scanner. The uncertainties in the Hounsfield units are smaller than the symbol size.

The RMI phantom was modelled with an IDL program (Appendix II) and written out in an *.egsphant file format.[50] It was then converted to a *.ramp and *.density file that is used by the egs_cbct code for simulation.[51] The phantom inserts were divided into three separate simulations because of the limitations of the *.egsphant file format. All the inserts were placed in the middle of the phantom for simplicity. Diagrams of the phantoms can be seen in Figure 3.5.

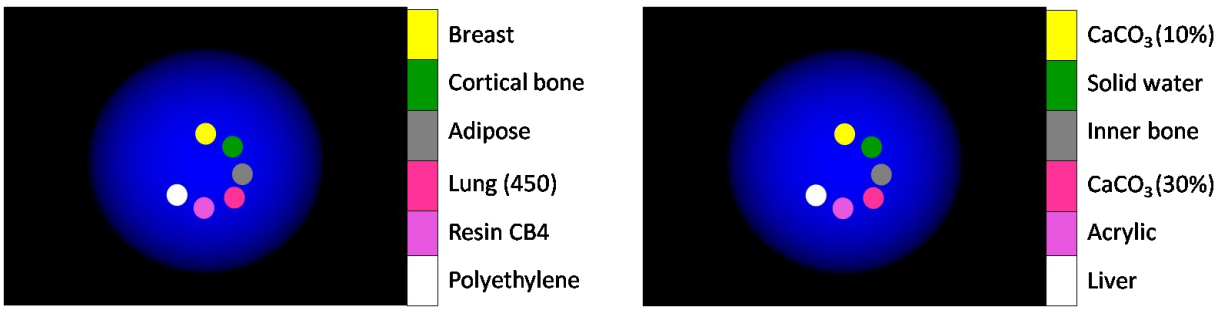

Figure 3.5: 3D view of the phantoms used to simulate the RMI phantom with 20 inserts.

3.2.1.1 Egsphant file format and conversion

The *.egsphant file is an ASCII file that contains information necessary for DOSXYZnrc to run a simulation with a phantom. It contains information regarding the number of media in the phantom and their names, voxel numbers and sizes and material density information. In Figure 3.6 below a slice of a head phantom can be seen. Each number represents a different material with a specific density.

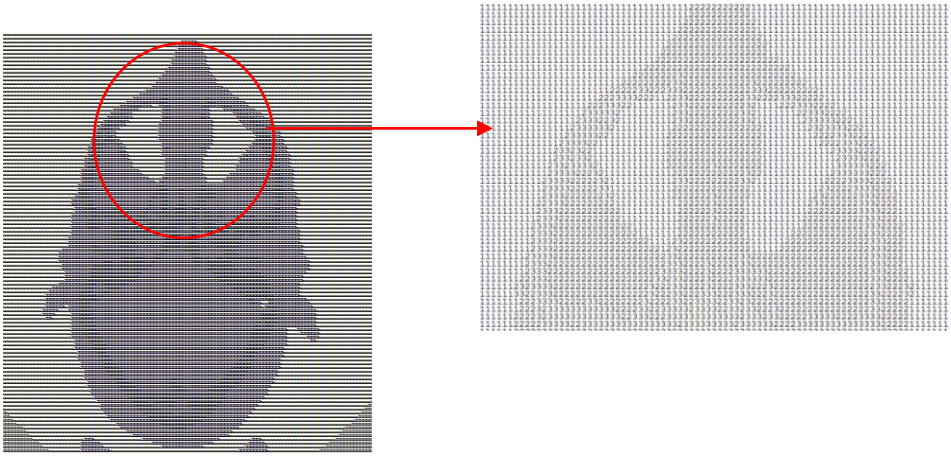

Figure 3.6: The egsphant file consisting of numbers representing the different materials present.[52]

To use the *.egsphant file in egs_cbct, it has to be converted to a *.density and *.ramp file. The *.density file is a binary file that contains the specifications of the phantom dimensions and the density in each voxel. A *.ramp file is also needed to convert the densities to the correct interaction cross-sections for simulation.

The CT unit was simulated in two steps. The first step consists of the BEAMnrc simulation as discussed in Chapter 2 and the second step includes the RMI phantom and bowtie filter simulation in egs_cbct.

3.2.1.2 RMI phantom simulation

The RMI phantoms seen in Figure 3.5 were simulated in egs_cbct, and the set-up without the bowtie filter can be seen in Figure 3.7 below. A collimated point source was used with a

field size of 30 cm x 0.2 cm, source-to-axis distance (SAD) of 71.2 cm and source-to-surface distance (SSD) of 127.5 cm. The values for the SAD and SSD were found in the specifications of the Toshiba Aquilion LB 16 CT. A gadolinium oxysulfide (GdOS) detector was used with a resolution of 2 mm.

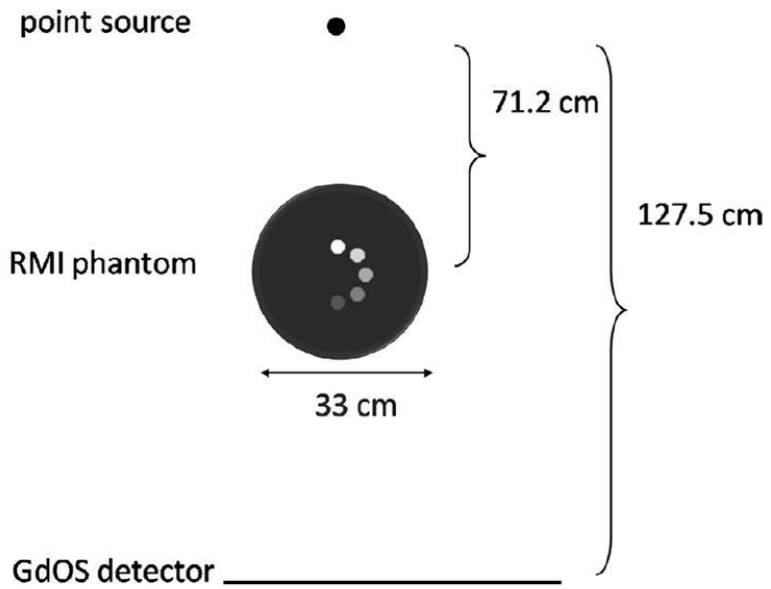

Figure 3.7: The simulation set-up for the RMI phantom with a SAD of 71.2 cm and SSD of 127.5 cm.[53]

The output files from egs_cbct were then used for the reconstruction of the images. The output file of egs_cbct is a binary file containing the detector signal from the primary photons, scattered photons or the combined signal from the primary and scattered photons (total signal). The file can be opened with a program like ImageJ where the projection images can be viewed.

3.2.1.3 Monte Carlo transport parameters in egs_cbct

The XCOM photon cross-section compilation[54] was used during the simulations. Rayleigh scattering and Compton scattering with binding corrections were implemented. The PCUT and ECUT values were 0.001 MeV and 1.000 MeV, respectively. Electron transport was avoided by choosing a very high value for ECUT. The efficiency of the primary signal

simulation was improved by using efficiency improving techniques (EIT) available in egs_cbct. Since the EITs are aimed at improving scatter simulation efficiency, it was unclear if it would be suitable for primary signal simulations. Forced detection, delta transport, denoising algorithm and path length transformation, as seen in the study by Thing *et al.*, [46] were explored. Equation 3.2 was used to determine the mean relative error (MRE) to see if the techniques used introduced a biased result.

$$MRE = \frac{1}{N}\sum_{i=1}^{N}\frac{x_i - x_i^0}{x_i^0} \qquad 3.2$$

N is the number of detector pixels, x_i is the signal from pixel i using the EITs and x_i^0 is the signal without any EITs. If the MRE value is smaller than the statistical uncertainty, the result is considered to be unbiased.

The simulation is done with a ray-tracing algorithm that determines the attenuation through the phantom. It is recommended that forced detection is implemented for all simulations in egs_cbct. Delta transport is used for photons not aimed at the detector. These photons are transported directly to the next interaction step by using the maximum interaction cross-section provided by the user. No boundary checks are needed for these photons as their contribution to the detector is assumed to be small. The denoising algorithm uses a Savitzky-Golay filter and three user-defined input values. The first two are the maximum allowed denoising window size in one direction and two dimensions respectively. The third value is the threshold for the χ^2-test performed.[51] A path length stretching technique is implemented in egs_cbct denoted by MFPTR. This technique focuses on scattered photons but was added to see the effect on the primary signal.

3.2.1.4 Bowtie filter determination

The bowtie was modelled using the method proposed by Zhang *et al*.[55] A brief description of the method is given below. The method aims for uniform flux intensity on the detector by reducing the dynamic range.

The minimum thickness of the filter, t_0, was taken to be 1 mm. The change in intensity as an X-ray beam passes through an object with diameter D, can be expressed by the Beer-Lambert law:

$$\frac{I(\theta)}{I(0)} = \exp\left[\mu_{Obj} D - \mu_{Obj} L_{Obj}(\theta)\right] \tag{3.3}$$

Where $I(0)$ is the initial intensity of the beam and $I(\theta)$ the intensity after passing through the object at an angle θ.

To obtain a complete 3D reconstruction of an object, projections need to be acquired over an angular range of at least 180° plus the fan angle. Where the fan angle is calculated with:

$$\theta_{fan} = 2\tan^{-1}\left[\frac{\text{Detector width}}{2\,\text{SDD}}\right] = 2\tan^{-1}\left[\frac{30cm}{2\times 127.5cm}\right] = x \tag{3.4}$$

The SSD is the source-to-detector-distance of 127.5 cm. The total arc used in this study was 194 degrees. L_{Obj} is the length of the beam path as it crossed the object as in Figure 3.8, determined by:

$$L_{Obj}(\theta) = 2\sqrt{\left(\frac{D}{2}\right)^2 - \left(FAD\sin\theta\right)^2} \tag{3.5}$$

Where FAD is the focal spot to rotation axis distance. This leads to $L_{Obj}(0) = D$ and the distance is corrected for the variance of the photon fluence using the inverse square law. Equation 3.3 becomes

$$\frac{I(\theta)}{I(0)} = \exp\left[\mu_{Obj} D - \mu_{Obj} L_{Obj}(\theta)\right] \frac{d^2(0)}{d^2(\theta)} \qquad 3.6$$

Where $d(\theta)$ is the total path length at θ. Equation 3.6 becomes

$$\frac{I(\theta)}{I(0)} = \exp\left[\mu_{Obj} D - \mu_{Obj} L_{Obj}(\theta)\right] \cos^2\theta \qquad 3.7$$

The attenuation profile should be equalised by the bowtie filter such that $I(\theta)$ is equal to $I(0)$. This requires that

$$\exp\left[\left(\mu_{Obj} D + \mu_{BT} t_0\right) - \left(\mu_{Obj} L_{Obj}(\theta) + \mu_{BT} L_{BT}(\theta)\right)\right] \cos^2\theta = 1 \qquad 3.8$$

Where L_{BT} is the angular length of filtration and the linear attenuation coefficient of the bowtie is μ_{BT}. By assuming $L_{BT}(0) = t_0$, Equation 3.8 can be rearranged to

$$L_{BT}(\theta) = t_0 + \frac{\mu_{Obj}}{\mu_{BT}}\left[D - L_{Obj}(\theta)\right] + \frac{2\ln(\cos\theta)}{\mu_{BT}} \qquad 3.9$$

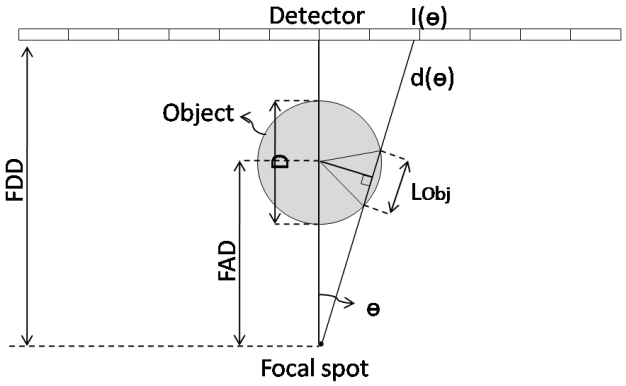

Figure 3.8: Path length through an object

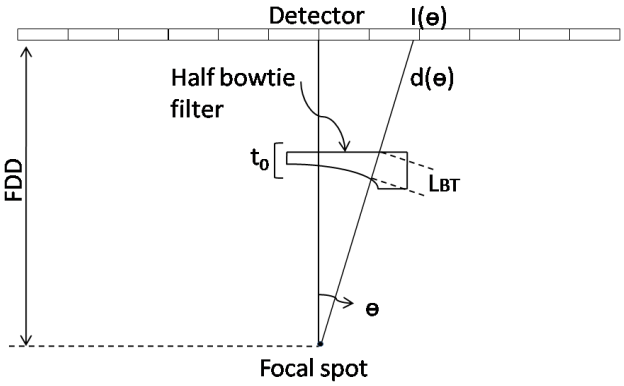

Figure 3.8: Angular length of filtration

The coordinates of the bowtie surface are determined with:

$$\begin{aligned} x(\theta) &= y_2 \tan\theta - L_{BT}(\theta)\sin\theta \\ y(\theta) &= y_2 - L_{BT}(\theta)\cos\theta \end{aligned} \qquad 3.7$$

The bowtie was modelled by using Equation 3.3 to 3.9 and consisted of aluminium, and the diameter of the RMI phantom was taken as 8.25 cm. The dimensions of the phantom were reduced as part of a variance reduction technique.

A semi-infinite slab was varied in thickness from 1 to 10 cm consisting of water and aluminium to determine the linear attenuation coefficients μ_{BT} and μ_{Obj} in DOSXYZnrc. A parallel source from the energy spectrum falls in on the slab of material, and the dose is scored in water. The simulation set-up is similar to the one used in Chapter 2 for the determination of the HVL. The HVL for each material was determined with the same method as explained in Chapter 2.

Forced detection was used and a ray-tracing calculation type to improve the efficiency of the primary signal simulation. Efficiency improving techniques were used to further increase the efficiency as described by Thing *et al.*[46] and $1x10^8$ histories were used for the simulation of the blank scan and attenuation scan of the phantom. This resulted in a statistical uncertainty of 0.2%. The complete simulation set-up of BEAMnrc and egs_cbct is seen below in Figure 3.9.

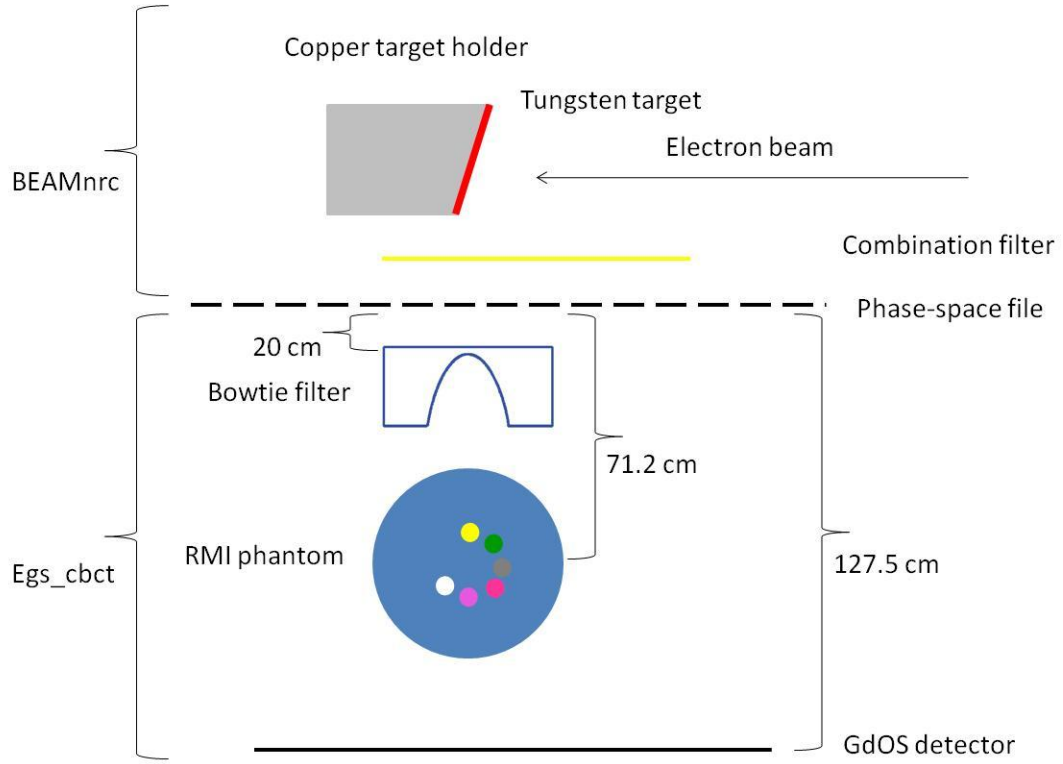

Figure 3.9: Simulation set-up for the complete CT simulation.

3.2.1.5 Reconstruction algorithm software

An FDK filtered backprojection reconstruction method was used to obtain reconstructed images from the simulated profiles by using the Open Source Cone-beam Reconstructor (OSCaR) software from the American Association of Physicists in Medicine (AAPM).[56] It is a software package that is developed for computing three-dimensional reconstructions for projection image data obtained from cone-beam CT geometries. The software includes a Graphical User Interface (GUI), and the MATLAB codes can be customised for your executions. A few modifications were made to make it more suitable for the reconstruction of the RMI phantom by using the profile data from the fan beam configuration. The software was then used for the reconstruction of the RMI phantom with different filters.

3.2.1.6 HU determination

A region-of-interest (ROI) was drawn on each of the inserts on the reconstructed images, and the resulting pixel value was obtained. The pixel value was then linked to the pre-known electron density of each insert. The HUs versus electron density data from the commissioning of the Toshiba Aquilion LB 16 CT was available and is displayed in Figure 3.3.

3.3 Results & Discussion

3.3.1 RMI phantom and bowtie filter modelling

In Figure 3.10 below, the RMI phantom can be seen as displayed by egs_view in egs_cbct. IDL accurately modelled the phantom and the *.egsphant file. All the inserts can be seen in egs_view that shows that the egsphant file was successfully converted to a *.ramp and *.density file.

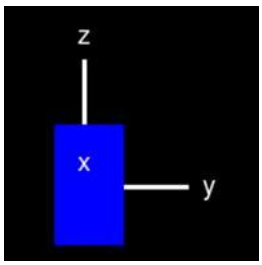

a)

b)

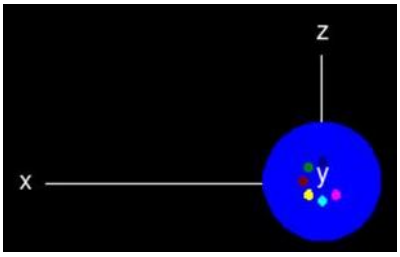

c)

Figure 3.10: The RMI phantom with some of the inserts viewed from the a) x-axis b) z-axis and c) y-axis.

The calculated linear attenuation coefficients for aluminium and water was 2.554 cm^{-1} and 0.402 cm^{-1} respectively and are in agreement with the values from the XCOM database for an average energy between 20 and 30 keV.[57] These values for the average energy correlates with what is expected from the 120 kV energy spectrum derived in Chapter 2. The linear attenuation values were used to model the bowtie filter that can be seen below in Figure 3.11.

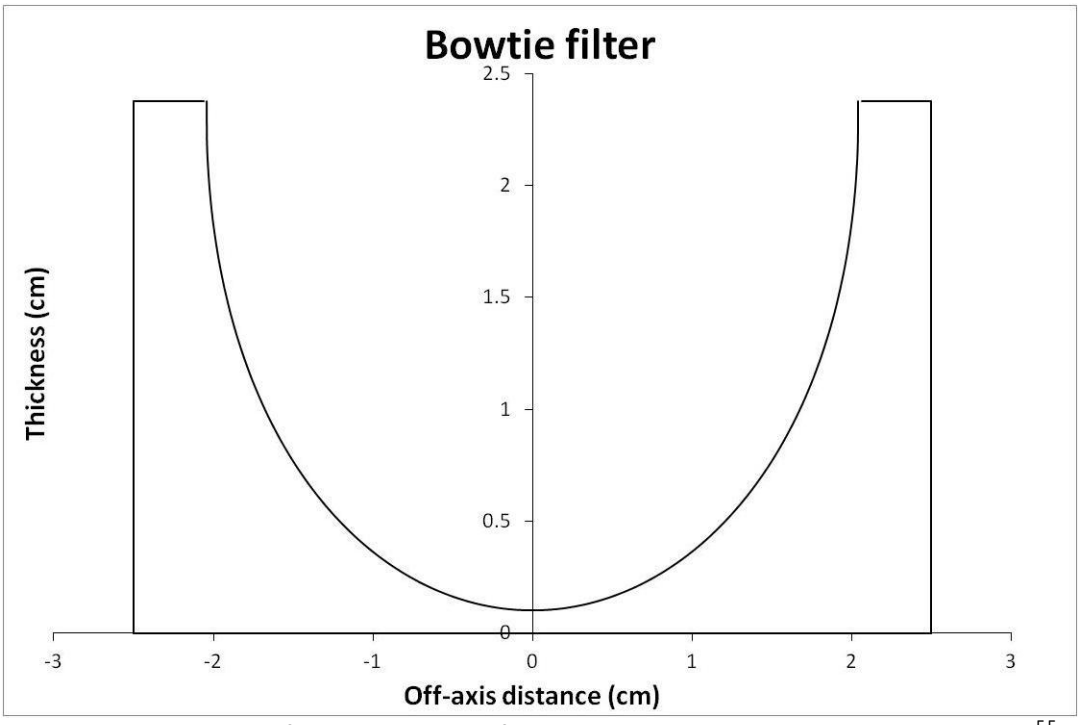

Figure 3.11: Bowtie filter modelled for a phantom with an 8.25 cm radius. [55]

The central part of the filter is 1 mm and increases in thickness from the central axis.

3.3.2 Efficiency improving techniques

The following results were obtained for the different efficiency improving techniques. The statistical uncertainties are calculated and given by the egs_cbct code.

Table 3.2: Results from the different efficiency improvement techniques. Statistical uncertainty (σ) and mean relative error (MRE)

Phantom	Technique used	Number of histories	Computation time (h)	σ (%)	Efficiency estimate	MRE (%)
RMI	Baseline without any techniques	1×10^8	0.965	0.214	62.563	0.0
	Forced detection	1×10^8	0.871	0.214	69.319	0.04
	Forced detection Delta transport	1×10^8	0.540	0.214	111.798	3×10^{-3}
	Forced detection Delta transport MFPTR = 6.0	1×10^8	0.520	0.214	116.104	1×10^{-3}
	Forced detection Delta transport MFPTR = 6.0 Denoising algorithm	1×10^8	0.493	0.214	122.295	1×10^{-3}

The statistical uncertainty for all the techniques was the same, but there was a difference between the simulation time and the efficiency. The most efficient simulation with the shortest simulation time and without any bias result was with forced detection, delta transport, an MFPTR value of 6 and the denoising algorithm. By using these improving techniques the simulation time decreased from 0.965 hours to 0.493 hours resulting in a 49% decrease in simulation time.

3.3.3 Reconstructed RMI phantoms

In the images below the RMI phantom with the bowtie filter can be seen reconstructed with various filters.

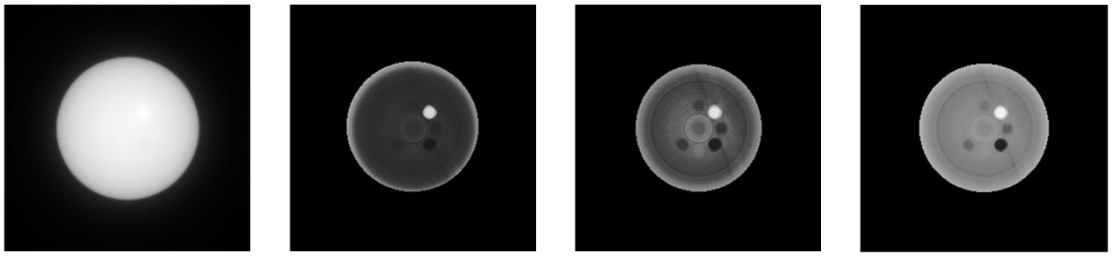

Figure 3.12: The RMI phantom in Figure 3.10 reconstructed with (a) no filter, (b) Ram-Lak filter, (c) Shepp-Logan filter, and (d) a low pass filter. All of the images are shown with the same display settings.[53]

All of the inserts ranging from a density of 0.450 g/cm^3 to 1.870 g/cm^3 can clearly be seen. The inserts that appear black have a density smaller than water, and those appearing white have a density larger than water. The Ram-Lak filter suppresses the low-frequency components, but amplifies the high frequencies and, as a result, amplifies the statistical noise in the simulated data. The ring artifacts, especially in the middle of the phantom, can be due to some periodic noise that is present in each projection profile used for the reconstruction. The number of histories influences the statistical noise which in turn influences the image quality. A small statistical variance is needed to obtain accurate signal-to-noise ratios. High noise levels in the image will result in wrong pixel values which will influence the HU correlation. Similar results were obtained for the other inserts.

In Figure 3.13 below a profile through the RMI phantom can be seen that shows the performance of the bowtie filter. The bowtie filter reduced the dynamic range on the detector and no cupping artifact is visible as seen below in Figure 3.13.

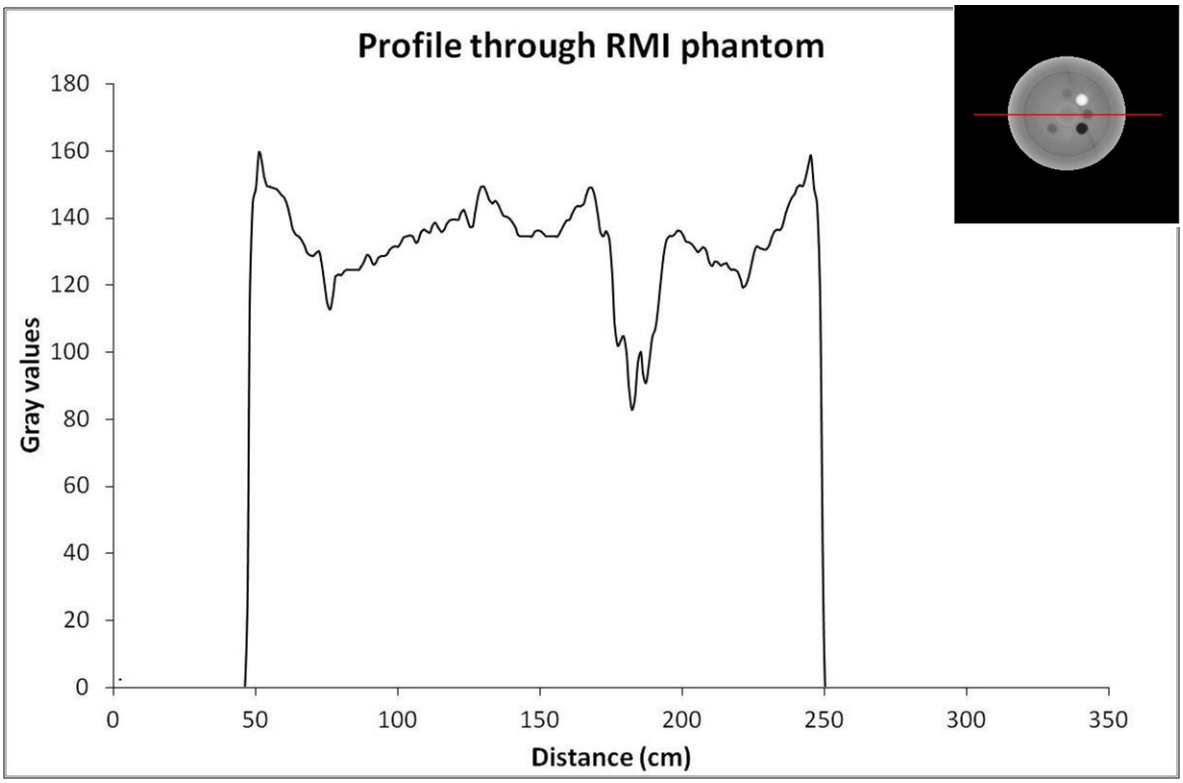

Figure 3.13: Profile through the RMI phantom reconstructed with a low pass filter. No cupping-effect can be seen after the use of the bowtie filter.

Some inserts can be seen better than others as displayed in Figure 3.14 below. The $CaCO_3$ (10 %) and $CaCO_3$ (30 %) appears white and is clearly visible. Inserts like the solid water (density of 1.02 g/cm3) is barely visible, corresponding to the true CT image of the RMI phantom.

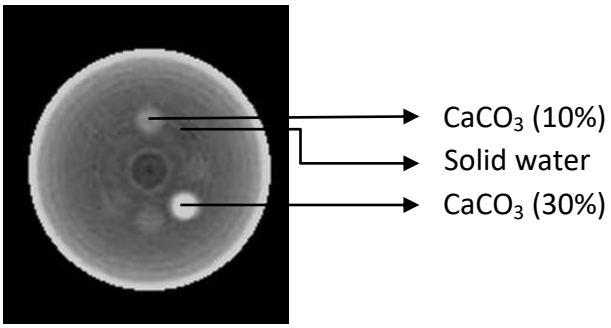

Figure 3.14: The second RMI phantom reconstructed with a Shepp-Logan filter. (The display parameters differ from those used in Figure 3.12)

The correlation between the pixel values of the simulated data and the measured HUs from the Toshiba Aquilion LB 16 CT can be seen below in Figure 3.15. The linear fit can be used to convert the pixel values to HUs. The errors in the pixel values are indicated.

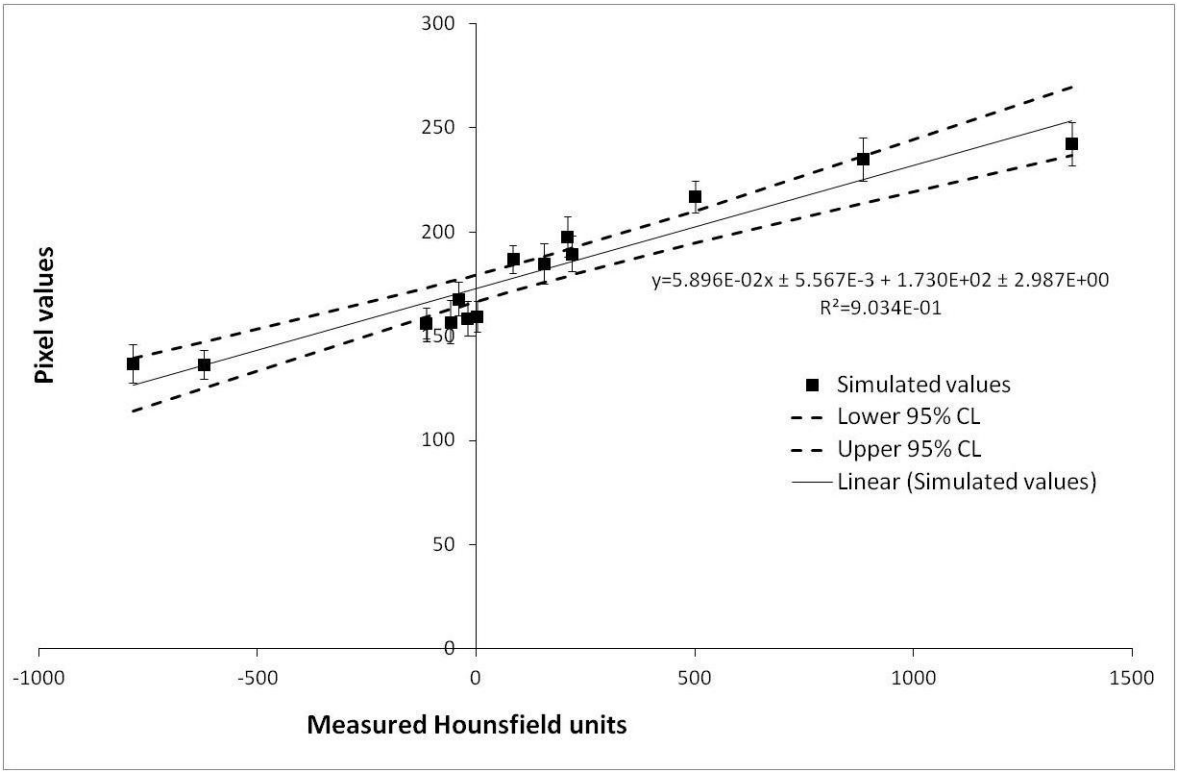

Figure 3.15: Correlation between the simulated pixel values and the measured HU numbers. The errors in the pixel values are indicated. The 95% confidence levels are indicated by dashed lines. The linear fit can be used to convert the simulated pixel values to HU numbers.

The linear fit seen in Figure 3.15 above is used to convert the simulated pixel values to HU.

In Figure 3.16, the correlation between the calculated HUs and the known relative electron density can be seen as well as the measured HUs and the known relative electron density values.

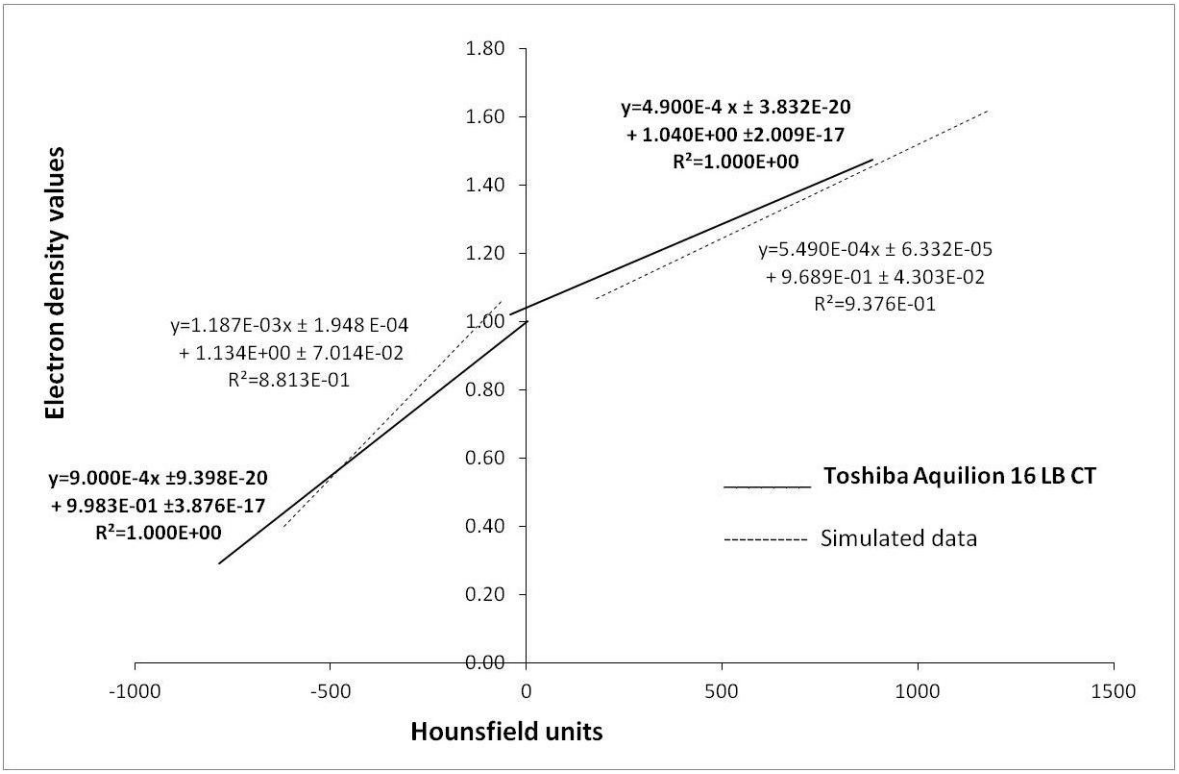

Figure 3.16: The conversion curve for electron density to Hounsfield units for the Toshiba Aquilion LB 16 CT (solid line) and the simulated CT (dashed line).[53]

3.4 Conclusion

MC simulations can lead to long computing hours, especially when a low statistical variance and high resolution is needed. Advances in technology and the availability of high-performance computers have made it possible to achieve such results. This chapter shows that the egs_cbct code can effectively simulate fan beam projection data although it is designed for scatter calculations in a CBCT set-up.

The in-house developed IDL program used can successfully generate *.egsphant files that can be used for simulations. The bowtie filter was modelled successfully and no cupping artifact was seen. Inserts with small density differences in comparison to water could be seen e.g. breast with a density of 0.98 g/cm^3. Good correlation was observed between the measured HUs and the calculated HUs from the simulated data. The results from this chapter show that it is feasible to simulate a virtual CT and that it can be extended to further studies.

3.5 References

1. Duan X, Wang J, Yu L, Leng S, McCollough CH. CT scanner x-ray spectrum estimation from transmission measurements. Med Phys. 2011 Feb;38(2):993–7.

2. Zhao W, Niu K, Schafer S, Royalty K. An indirect transmission measurement-based spectrum estimation method for computed tomography. Phys Med Biol. 2015 Jan 7;60(1):339–57.

3. Ay MR, Shahriari M, Sarkar S, Adib M, Zaidi H. Monte Carlo simulation of x-ray spectra in diagnostic radiology and mammography using MCNP4C. Phys Med Biol. 2004;49(21):4897.

4. Ng KP, Kwok CS, Ng KP, Tang FH. Monte Carlo simulation of x-ray spectra in mammography. Phys Med Biol. 2000;45(5):1309.

5. Qamhiyeh S, Wysocka-Rabin A, Jakel O. Monte Carlo calculated CT numbers for improved heavy ion treatment planning. NUKLEONIKA 2014;59(1):15−23

6. Tucker DM, Barnes GT, Wu X. Molybdenum target x-ray spectra: A semiempirical model. Med Phys. 1991 May 1;18(3):402–7.

7. Tucker DM, Barnes GT, Chakraborty DP. Semiempirical model for generating tungsten target x-ray spectra. Med Phys. 1991 Mar 1;18(2):211–8.

8. Blough MM, Waggener RG, Payne WH, Terry JA. Calculated mammographic spectra confirmed with attenuation curves for molybdenum, rhodium, and tungsten targets. Med Phys. 1998 Sep 1;25(9):1605–12.

9. Archer BR, Wagner LK. Determination of diagnostic x-ray spectra with characteristic radiation using attenuation analysis. Med Phys. 1988 Jul 1;15(4):637–41.

10. Boone JM, Seibert JA. An accurate method for computer-generating tungsten anode x-ray spectra from 30 to 140 kV. Med Phys. 1997 Nov 1;24(11):1661–70.

11. Waggener RG, Blough MM, Terry JA, Chen D, Lee NE, Zhang S, et al. X-ray spectra estimation using attenuation measurements from 25 kVp to 18 MV. Med Phys. 1999 Jul 1;26(7):1269–78.

12. Graham SA, Moseley DJ, Siewerdsen JH, Jaffray DA. Compensators for dose and scatter management in cone-beam computed tomography. Med Phys. 2007 Jul;34(7):2691–703.

13. Ding GX, Duggan DM, Coffey CW. Characteristics of kilovoltage x-ray beams used for cone-beam computed tomography in radiation therapy. Phys Med Biol. 2007 Mar 21;52(6):1595–615.

14. Mail N, Moseley DJ, Siewerdsen JH, Jaffray DA. The influence of bowtie filtration on cone-beam CT image quality. Med Phys. 2009 Jan 1;36(1):22–32.

15. Menser B, Wiegert J, Wiesner S, Bertram M. Use of beam shapers for cone-beam CT with off-centered flat detector. *Proc. SPIE* 7622, Medical Imaging 2010: Physics of Medical Imaging, 762233 (March 22, 2010); doi:10.1117/12.844437

16. Boone JM. Method for evaluating bow tie filter angle-dependent attenuation in CT: theory and simulation results. Med Phys. 2010 Jan;37(1):40–8.

17. Blessing M, Bhagwat MS, Lyatskaya Y, Bellon JR, Hesser J, Zygmanski P. Kilovoltage beam model for flat panel imaging system with bow-tie filter for scatter prediction and correction. Phys Medica Eur J Med Phys. 2012 Apr 1;28(2):134–43.

18. Bootsma GJ, Verhaegen F, Jaffray DA. The effects of compensator and imaging geometry on the distribution of x-ray scatter in CBCT. Med Phys. 2011 Feb;38(2):897–914.

19. Curry, III TS, Dowdey JE, Murray, JR. RC. Christensen's Physics of Diagnostic Radiology. Fourth edition. Philadelphia, London: Lea & Febiger; 1990. 522 p.

20. McKenney SE, Nosratieh A, Gelskey D, Yang K, Huang S-Y, Chen L, et al. Experimental validation of a method characterizing bow tie filters in CT scanners using a real-time dose probe. Med Phys. 2011 Mar;38(3):1406–15.

21. Whiting BR, Dohatcu A. Method for measuring the intensity profile of a CT fan-beam filter. *Proc. SPIE* 9033, Medical Imaging 2014: Physics of Medical Imaging, 903322 (March 19, 2014); doi:10.1117/12.2043246

22. Whiting BR, Evans JD, Dohatcu AC, Williamson JF, Politte DG. Measurement of bow tie profiles in CT scanners using a real-time dosimeter. Med Phys. 2014 Oct;41(10):101915.

23. Rogers DWO. Fifty years of Monte Carlo simulations for medical physics. Phys Med Biol. 2006 Jul 7;51(13):R287–301.

24. Jia X, Yan H, Gu X, Jiang SB. Fast Monte Carlo simulation for patient-specific CT/CBCT imaging dose calculation. Phys Med Biol. 2012 Feb 7;57(3):577–90.

25. Salvadó M, López M, Morant JJ, Calzado A. Monte Carlo calculation of radiation dose in CT examinations using phantom and patient tomographic models. Radiat Prot Dosimetry. 2005;114(1–3):364–8.

26. Ay MR, Zaidi H. Development and validation of MCNP4C-based Monte Carlo simulator for fan- and cone-beam x-ray CT. Phys Med Biol. 2005 Oct 21;50(20):4863–85.

27. Miceli A, Thierry R, Flisch A, Hofmann J, Sennhauser U, Casali F. Monte Carlo simulation of a cone-beam CT system for industrial applications. ResearchGate [Internet]. 2007 Jan 1 [cited 2017 Jan 4];(2007). Available from: https://www.researchgate.net/publication/289682916_Monte_Carlo_simulation_of_a_cone-beam_CT_system_for_industrial_applications

28. Miceli A, Thierry R, Flisch A, Sennhauser U, Casali F, Simon M. Monte Carlo simulations of a high-resolution X-ray CT system for industrial applications. Nucl

Instrum Methods Phys Res Sect Accel Spectrometers Detect Assoc Equip. 2007 Dec 21;583(2–3):313–23.

29. Chen Y, Liu B, O'Connor JM, Didier CS, Glick SJ. Characterization of scatter in cone-beam CT breast imaging: Comparison of experimental measurements and Monte Carlo simulation. Med Phys. 2009 Mar 1;36(3):857–69.

30. Sechopoulos I, Vedantham S, Suryanarayanan S, D'Orsi CJ, Karellas A. Monte Carlo and Phantom Study of the Radiation Dose to the Body from Dedicated CT of the Breast. Radiology. 2008 Apr 1;247(1):98–105.

31. Sarno A, Mettivier G, Lillo FD, Russo P. A Monte Carlo study of monoenergetic and polyenergetic normalized glandular dose (DgN) coefficients in mammography. Phys Med Biol. 2017;62(1):306.

32. Mettivier G, Fedon C, Lillo FD, Longo R, Sarno A, Tromba G, et al. Glandular dose in breast computed tomography with synchrotron radiation. Phys Med Biol. 2016;61(2):569.

33. McMillan K, Khatonabadi M, McNitt-Gray M. SU-E-I-47: A Classification of Validation Tasks for Monte Carlo Simulations of CT Scanners: From Simple to Complex Source Models and Geometries. Med Phys. 2013 Jun 1;40(6):135–6.

34. Abuhaimed A, Martin CJ, MarimuthuSankaralingam, Gentle DJ, McJury M. An assessment of the efficiency of methods for measurement of the computed tomography dose index (CTDI) for cone beam (CBCT) dosimetry by Monte Carlo simulation. Phys Med Biol. 2014;59(21):6307.

35. Gao Y, Ding A, Zhang D, Liu B, Caracappa P, Xu X. TU-G-103-01: Monte Carlo Simulation and Dose Calculation of Chest CT Scan with Tube Current Modulation. Med Phys. 2013 Jun 1;40(6):458–458.

36. Bretin F, Bahri MA, Luxen A, Phillips C, Plenevaux A, Seret A. Monte Carlo simulations of the dose from imaging with GE eXplore 120 micro-CT using gate. Med Phys. 2015 Oct 1;42(10):5711–9.

37. Fujii K, Nomura K, Muramatsu Y, Takahashi K, Obara S, Akahane K, et al. Evaluation of organ doses in adult and paediatric CT examinations based on Monte Carlo simulations and in-phantom dosimetry. Radiat Prot Dosimetry. 2015 Jul;165(1–4):166–71.

38. Jarry G, Graham SA, Moseley DJ, Jaffray DJ, Siewerdsen JH, Verhaegen F. Characterization of scattered radiation in kV CBCT images using Monte Carlo simulations. Med Phys. 2006 Nov 1;33(11):4320–9.

39. Mainegra-Hing E, Kawrakow I. Variance reduction techniques for fast Monte Carlo CBCT scatter correction calculations. Phys Med Biol. 2010 Aug 21;55(16):4495–507.

40. Mainegra-Hing E, Kawrakow I. Fast Monte Carlo calculation of scatter corrections for CBCT images. J Phys Conf Ser. 2008;102(1):012017.

41. Kawrakov I, Mainegra-Hing E, Rogers DWO. The EGSnrc Code System: Monte Carlo Simulation of Electron and Photon Transport. 2010. Report No.: NRCC Reports PIRS-701.

42. Chang J, Zhou L, Wang S, Clifford Chao KS. Panoramic cone beam computed tomography. Med Phys. 2012 May 1;39(5):2930–46.

43. Watson P, Mainegra-Hing E, Soisson E, Naqa IE, Seuntjens J. SU-E-I-04: Implementation of a Fast Monte Carlo Scatter Correction for Cone- Beam Computed Tomography. Med Phys. 2012 Jun 1;39(6):3625–3625.

44. Watson P, Mainegra-Hing E, Soisson E, Naqa IE, Seuntjens J. Sci—Fri PM: Delivery — 12: Scatter-B-Gon: Implementing a fast Monte Carlo cone-beam computed tomography scatter correction on real data. Med Phys. 2012 Jul 1;39(7):4644–4644.

45. Thing RS, Bernchou U, Mainegra-Hing E, Brink C. Patient-specific scatter correction in clinical cone beam computed tomography imaging made possible by the combination of Monte Carlo simulations and a ray tracing algorithm. Acta Oncol. 2013 Oct 1;52(7):1477–83.

46. Thing RS, Mainegra-Hing E. Optimizing cone beam CT scatter estimation in egs_cbct for a clinical and virtual chest phantom. Med Phys. 2014 Jul 1;41(7):071902.

47. Smith SW. The Scientist & Engineer's Guide to Digital Signal Processing. 1st edition. San Diego, Calif: California Technical Pub; 1997. 626 p.

48. Lyra M, Ploussi A. Filtering in SPECT Image Reconstruction. Int J Biomed Imaging. 2011 Jun 23;2011:e693795.

49. Bushberg JT, Seibert JA, Jr EML, Boone JM. The Essential Physics of Medical Imaging, Third Edition. 3 edition. Philadelphia: LWW; 2011. 1048 p.

50. Ma CM, Rogers DWO, Walters BRB. DOSXYZnrc users manual. Ottawa: National Research Council of Canada; 2011. Report No.: NRCC Report PIRS-749revB.

51. EGSnrc C++ class library: Main Page [Internet]. [cited 2016 Aug 4]. Available from: http://nrc-cnrc.github.io/EGSnrc/doc/pirs898/index.html

52. Van Eeden D. Development of a particle source model for a synergy linear accelerator to be used in Monte Carlo radiation dose calculations for cancer therapy. 2014 May [cited 2017 Mar 27]; Available from: http://scholar.ufs.ac.za:8080/xmlui/handle/11660/2082

53. van Eeden D, du Plessis F. EGS_cbct: Simulation of a fan beam CT and RMI phantom for measured HU verification. Phys Medica Eur J Med Phys. 2016 Oct 1;32(10):1375–80.

54. Berger MJ, Hubbell JH. XCOM: Photon cross-sections on a personal computer [Internet]. 1987 Jul [cited 2016 Aug 2]. Report No.: NBSIR-87-3597, 6016002. Available from: http://www.osti.gov/servlets/purl/6016002-Jgm0Fa/

55. Zhang G, Marshall N, Jacobs R, Liu Q, Bosmans H. Bowtie filtration for dedicated cone beam CT of the head and neck: a simulation study. Br J Radiol. 2013 Aug;86(1028):20130002.

56. N. Rezvani DA. OSCaR: An open-source cone-beam CT reconstruction tool for imaging research. Med Phys - MED PHYS. 2007;34(6).

57. NIST: X-Ray Mass Attenuation Coefficients - Aluminum [Internet]. [cited 2016 Aug 2]. Available from: http://physics.nist.gov/PhysRefData/XrayMassCoef/ElemTab/z13.html

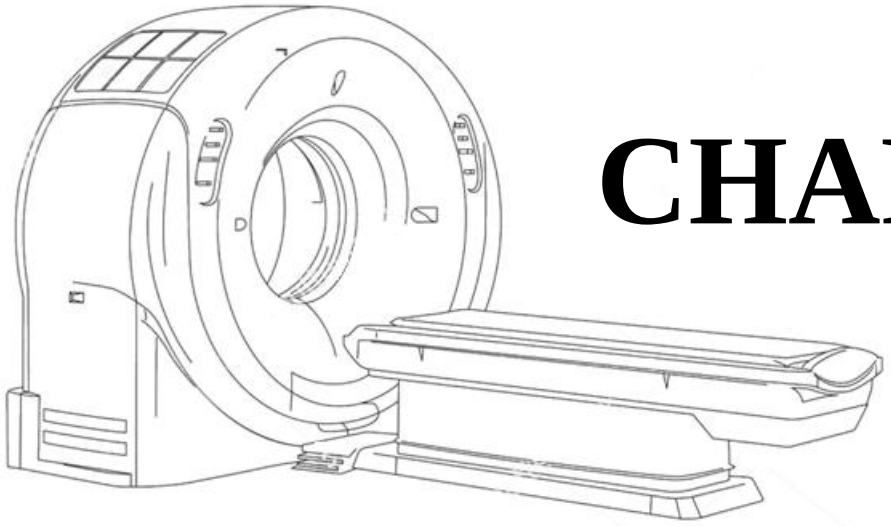

CHAPTER 4

Breast tissue simulation in egs_cbct

Table of Contents

4.1 Introduction

The breast is a modified sweat gland with its purpose being milk production. By understanding its basic anatomy, it is easier to interpret mammography and dedicated breast CT images.[1, 2]

The breast consists of three main structures: the skin, the subcutaneous fat and the breast tissue.[3] Underneath the breast is the pectoral muscle, which is also imaged during a mammogram. The breast tissue consists of Cooper's ligaments and fibrous strands that support the breast.[4] This parenchyma or functional part of the breast consists of multiple segments, drained by lactiferous ducts. The lactiferous ducts are concentrated beneath the nipple with a few major ducts draining into the nipple. Each of these ducts drains a lobe that consists of multiple lobules.[5]

The Breast Imaging Reporting and Data System (BI-RADS) were established by the American College of Radiology in the mid-1990s. This system consists of multiple categories which aid in the assessment of mammogram images.[6,7] The description of tissue composition is based on the volume of glandular tissue relative to fat and is divided into four categories. These range from almost purely fat to extremely dense and mainly glandular tissue.[8]

Modelling and simulation are valuable tools for research purposes in the field of medical imaging. They offer the possibility of exploring new techniques without the need for expensive equipment or patients. In order to have accurate results, it is important to have realistic models that depict the true breast. Simple mathematical models are commonly used for dosimetry simulations in breast phantoms.[9-12] These phantoms usually consist of homogeneous material and lack the detail of real breast tissue. Realistic 3D breast models have been developed[13-17] for use in digital mammography and breast tomosynthesis

applications.[18-20] Although these models can produce realistic mammograms, some of them are not suitable for more complex image modalities such as dedicated breast CT. One of the options is to produce breast phantoms from real breast CT data[21-23], but this leads to a single breast composition without the flexibility to alter it.

In 2003 a methodology for 3D breast modelling was reported by Bliznakova *et al.* using a combination of 3D geometrical primitives and voxel matrices.[17] In a further study, a general approach was presented for the simulation of compressed soft tissue.[24] This software was used by multiple research organisations and led to a further development of a breast simulation software package to be used for research in the field of breast X-ray imaging.[25] The software is capable of generating a 3D breast model, compress the model, model the X-ray transport through the breast, produce and visualise the projection images. Different breast components can be modelled such as the external shape, glandular tissue, adipose tissue, abnormalities and other components.

Several studies have reported on the simulation of a dedicated breast CT with the MC codes.[26-28] Over the past few years, there have been significant advances in detector technology and energy resolving or photon counting detectors are now a reality. These detectors together with breast CT have been an active area of research and are worth exploring further.[29-31]

Energy-resolving photon-counting detectors are capable of discriminating between different energies and producing multiple monoenergetic images from a single exposure. These detectors rely on direct conversion sensors based on semiconductors such as silicon (Si)[32-36] and cadmium telluride (CdTe).[37-41] CdTe is a promising semiconductor material for the use of detecting X-rays and gamma-rays. It has a high atomic number and high quantum efficiency.

The difference between a conventional detector and a CdTe detector can be seen below in Figure 4.1.

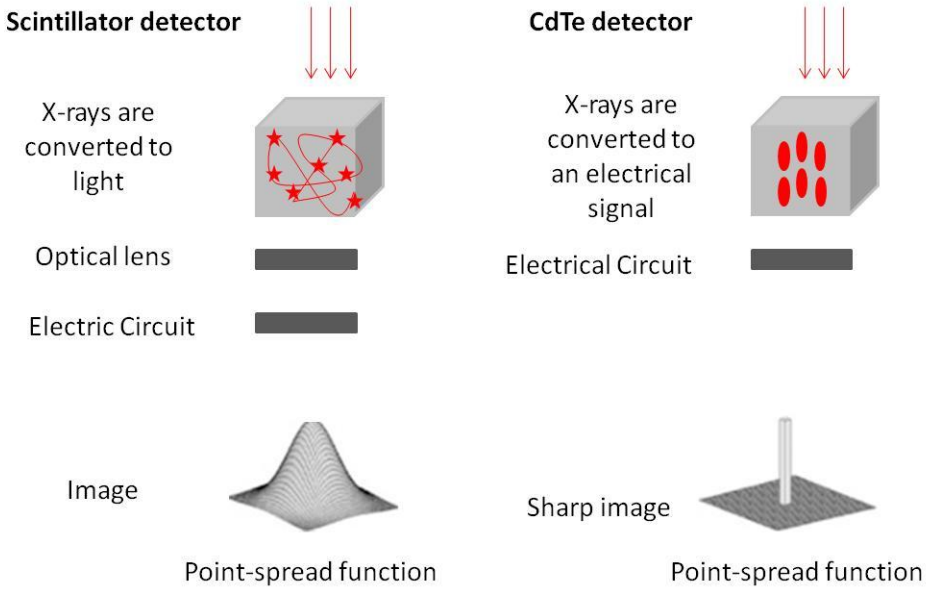

Figure 4.1: The detection mechanisms of a conventional detector and a CdTe detector.[42]

In a conventional detector, the X-rays are first converted into light that diffuses and spreads. In the CdTe detector, the X-rays move in a narrow path through the semiconductor leading to a sharp point-spread function and image.[42]

Contrast agents such as iodine are often used to increase the contrast that aids in specific radiological based diagnosis.[43-46] This increase, in contrast, exists when the contrast agents absorb the X-rays more efficiently. The maximum contrast will be achieved when the energy of the X-rays are slightly above the K-edge peak of the contrast agent. For iodine, this peak occurs at approximately 33.2 keV, and an energy bin at a slightly higher energy will receive a stronger signal.

In this chapter, the feasibility of breast tissue differentiation will be explored when using a range of energies. The BreastSimulator software[14,17,25] is used to generate three breast models with varying tumour sizes and composition. The models are then converted to a

format compatible with the egs_cbct code for the simulation of the projection images. The FDK reconstruction algorithm is then used for the reconstruction of the different images.

4.2 Methods and Materials

The pre-processor code for EGS (PEGS) generates cross-section data for the EGS code[47] by using the selection of materials, their densities and energy cut-offs.[48]

4.2.1 The PEGS file

The elemental composition of the glandular and adipose tissue was taken from The International Commission on Radiation Units and Measurements (ICRU) Report 44[49] and can be seen in Table 4.1 below. It was used to calculate the PEGS photon interaction cross section data for the energy range between 1 keV and 200 keV to accurately simulate photon transport through the breast phantom. The malignant tissue consisted of pork muscle as described in Section 4.2.3.

Table 4.1: Elemental composition of materials present in the breast phantoms

Material	H	C	N	O	Elements with Z>8
Adipose tissue	11.4	59.8	0.7	27.8	Na(0.1), S(0.1), Cl(0.1)
Glandular tissue	10.6	33.2	3.0	52.7	Na(0.1), P(0.1), S(0.2), Cl(0.1)
Skin	10.0	20.4	4.2	64.5	Na(0.2), P(0.1), S(0.2), Cl(0.3), K(0.1)
Malignant tissue	10.0	10.7	2.75	75	Cl(0.078)

Adipose tissue consists of a protein matrix of supporting cells for the storage of lipid. These lipids are a mixture of triglycerides and long-chain fatty acids. Glandular tissue contains specialised fat and data are taken from post-menopausal women. The skin consists of 2 distinct layers and a connective-tissue layer. A wide range of compositions are reported since it's so difficult to distinguish between the different layers.[50]

4.2.2 Linear attenuation coefficient determination for the different tissues

The linear attenuation coefficients are dependent on the tissue type and the energy. The linear attenuation coefficients for all the different tissues in the breast phantom were calculated with egs_cbct simulations. This was done to see if the linear attenuation coefficients of the different breast tissues used in this study correlate with that of the literature as seen below in Figure 4.2.

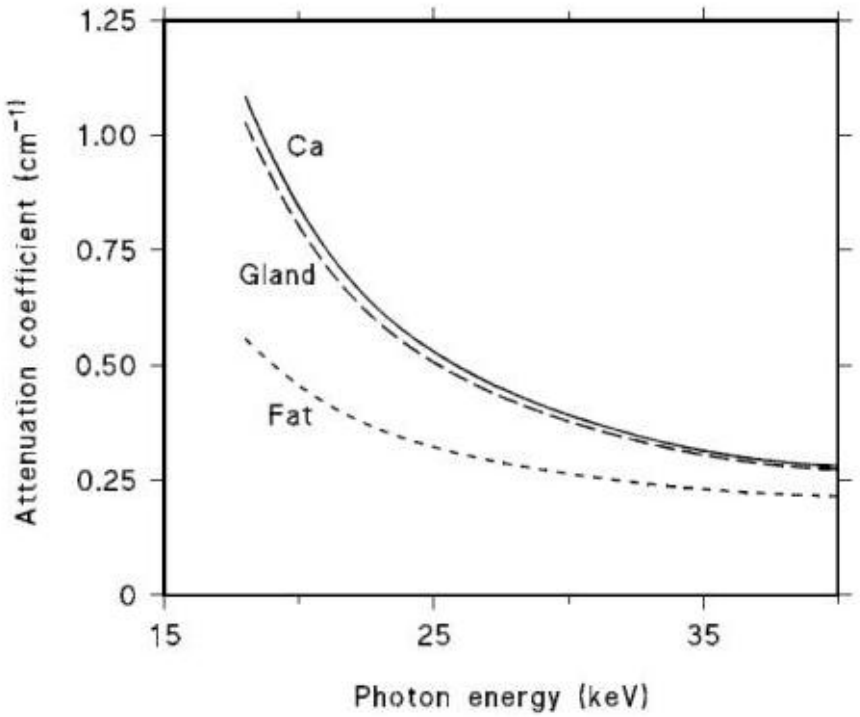

Figure 4.2: Variation of attenuation coefficient with tissue type and energy.[51]

The thickness of the material was varied, and the resulting signal for energies 20 keV to 65 keV was scored with a CdTe detector. The set-up is similar to that of the HVL in Chapter 2 and can be seen below in Figure 4.3. It was done in egs_cbct with a collimated source, a narrow-beam geometry and monoenergetic photons.

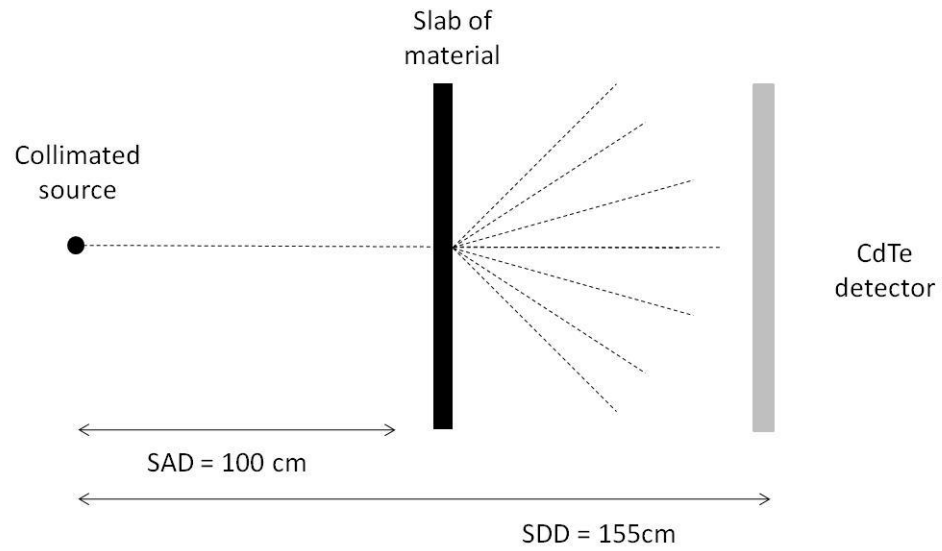

Figure 4.3: Simulation set-up in egs_cbct for the determination of the linear attenuation coefficients.

The *.att.scan output file of egs_cbct contains the primary signal which is log-transformed and normalised to the incident flux of X-rays from the source and is given by Equation 4.1.

$$\text{Primary signal in detector element} = -\ln\left(\frac{I_p}{I_0}\right) = \mu.x \qquad 4.1$$

Where I_p is the detector signal from the primary photons and I_0 is the detector signal from the source without any attenuating material in the beam path.[52]

The linear attenuation coefficient can, therefore, be determined by plotting the output signal from the *.att.scan file versus the thickness of material. The slope of the straight line represents the linear attenuation coefficient of the particular tissue. An example of the graph is seen below in Figure 4.4.

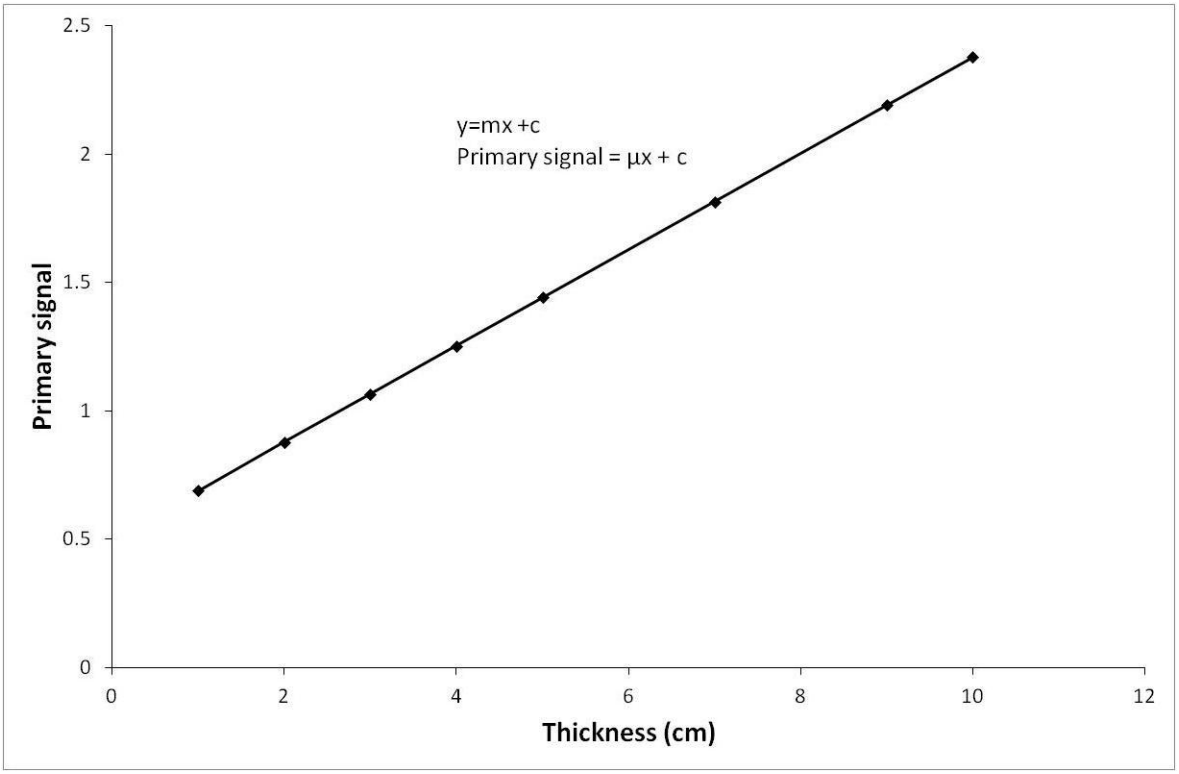

Figure 4.4: An example of the calculation of the linear attenuation coefficient from the simulation output of egs_cbct.

The linear attenuation coefficients are also used in Chapter 6 for the tissue differentiation of the different breast tissues.

4.2.3 Breast phantom modelling

All the breast phantoms were simulated with the BreastSimulator software package. All the phantoms were based on a small sized breast to reduce the radiation field needed for the simulations. The external shape consisted of a semi-ellipsoid as seen below in Figure 4.5.

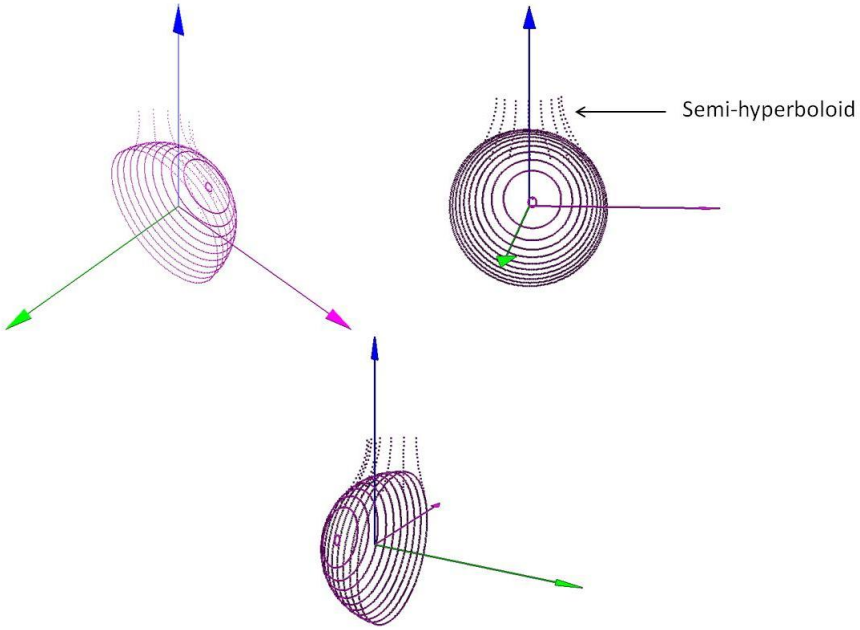

Figure 4.5: External shape preview as seen in the BreastSimulator software.

The semi-hyperboloid part is excluded when used for cone beam breast CT techniques. The duct system consists of an arrangement of cylinders to form a tree with branches consisting of lactiferous ducts. The duct configuration is arbitrary for each breast phantom simulation. The background texture usually consists of adipose, fibrous and connective tissues. In this study, the background was taken to be adipose tissue since the compositional information regarding other non-glandular tissues is not available. The Cooper's ligaments are ellipsoid shells that are placed randomly in the breast. The abnormalities were not modelled inside the BreastSimulator software but were placed at specific positions via an in-house developed IDL code. The matrix sizes were 256 x 256 x 256, and the pixel size was 1 mm in all three main directions. Dedicated breast CT is specifically aimed at the denser breast and therefore three phantoms were modelled, each with their own breast composition. The composition of adipose- and glandular breast tissue were found in the ICRU 44.[49] Pork muscle with a density of 1.066 g/cm^3 was used as a substitute for breast cancer tissue as reported by previous studies.[53-56] Each phantom consisted of Cooper's ligaments, major ducts and lactiferous

ducts. Three tumours were included ranging approximately from 4 mm to 8 mm in diameter and a fourth irregular shaped tumour.

The breast configuration is written out in a binary file and read out with a MATLAB code. IDL was used to insert the tumours in various positions and write out the *.egsphant file. Some difficulties were found with the conversion of the tumour data from the binary file to the *.egsphant file, and therefore it was inserted manually in IDL. The positions and the sizes of the different tumours can be chosen by the user. A detailed explanation of the *.egsphant file format can be found in Chapter 3. The *.egsphant file was then converted to a *.ramp and *.density file as discussed in Chapter 3 Section 3.2.1.1. One of the malignant masses contained iodine contrast agent of 8 mg/mL as used in a previous study.[57] The elemental information of the contrast agent was used to calculate the density for the generation of the PEGS file as shown below:

$$0.008 \times 4.93\ g.cm^{-3} + 0.992 \times 1\ g.cm^{-3} = 1.03144\ g.cm^{-3}$$

Where 0.8 and 99.2 represent the percentage iodine and water present respectively. The density of the iodine was taken as 4.93 g/cm^{3,} and that of water is 1 g/cm^{3}. The contrast agent consists of 0.8 % iodine and 99.2 % water.

4.2.3.1 Phantom 1

The first phantom consisted of 89% glandular tissue and 11% adipose tissue with five major ducts, five lactiferous ducts and ellipsoid structures with a radius of 3 mm, which represents the Cooper's ligaments. A visualisation of the breast model can be seen below in Figure 4.6.

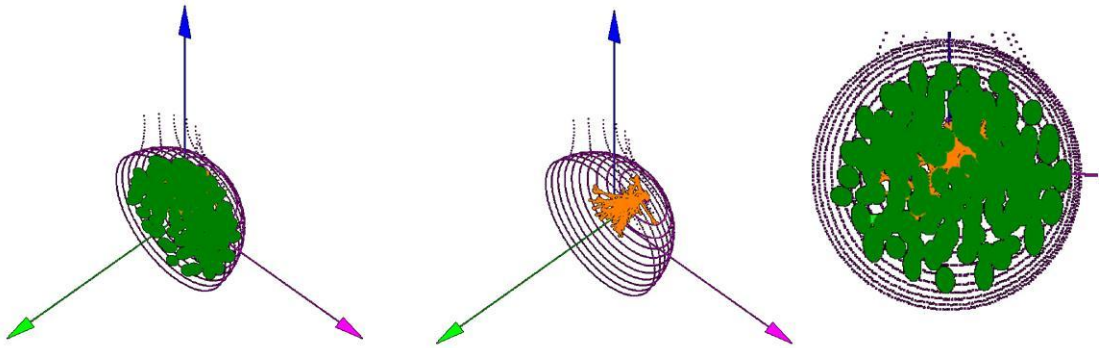

a) b) c)

Figure 4.6: Advanced visualisation of the breast phantom a) with Cooper's ligaments and b) without Cooper's ligaments. (The green structures represent the Cooper's ligaments, and the orange structures represent the ducts) c) The front view of the breast displaying all the glandular tissue present.

The phantom is seen in Figure 4.7 below.

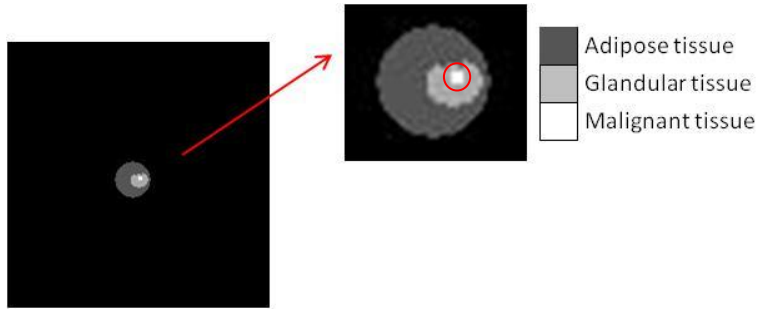

a)

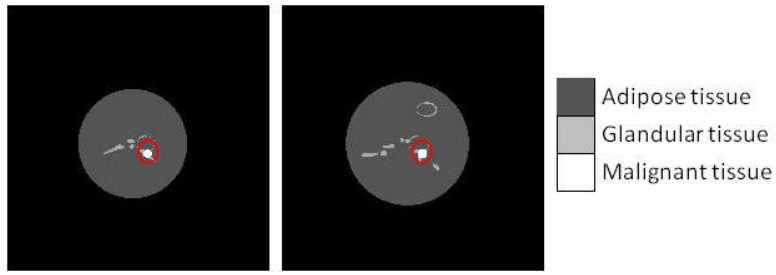

b)

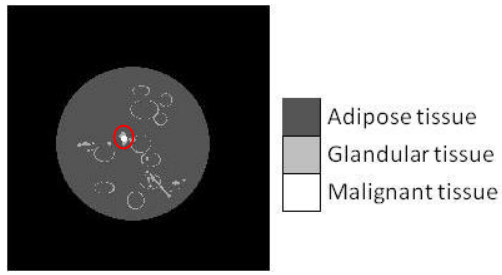

c)

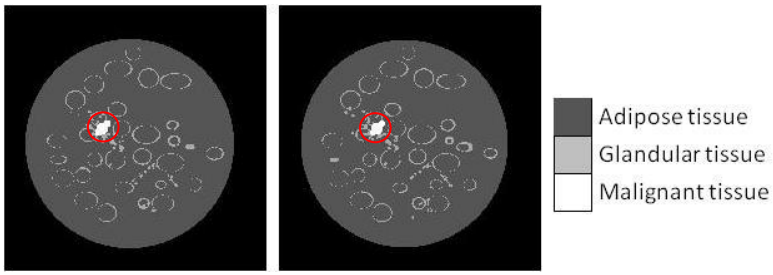

d)

Figure 4.7: Slices through the breast phantom matrix. Malignant masses are indicated by a red circle. a) A small mass is seen inside some glandular tissue. b) Two slices also consisting of malignant tissue and glandular tissue. c) The third mass inside the glandular tissue. d) An irregular sized mass surrounded by Cooper's ligaments.

4.2.3.2 Phantom 2

The second phantom consisted of 71% glandular tissue and 29% adipose tissue with six major ducts, six lactiferous ducts and ellipsoid structures with a radius of 3 mm which represents the Cooper's ligaments. A visualisation of the breast model can be seen below in Figure 4.8.

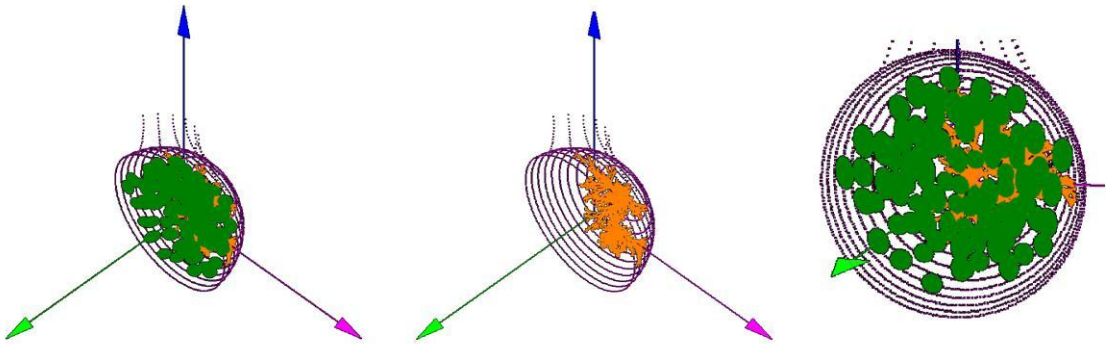

a) b)

Figure 4.8: Advanced visualisation of the breast phantom a) with Cooper's ligaments and b) without Cooper's ligaments. (The green structures represent the Cooper's ligaments, and the orange structures represent the ducts). c) It is clear that less ductal tissue is present in comparison with the first phantom in Figure 4.6.

The phantom is seen in Figure 4.9 below.

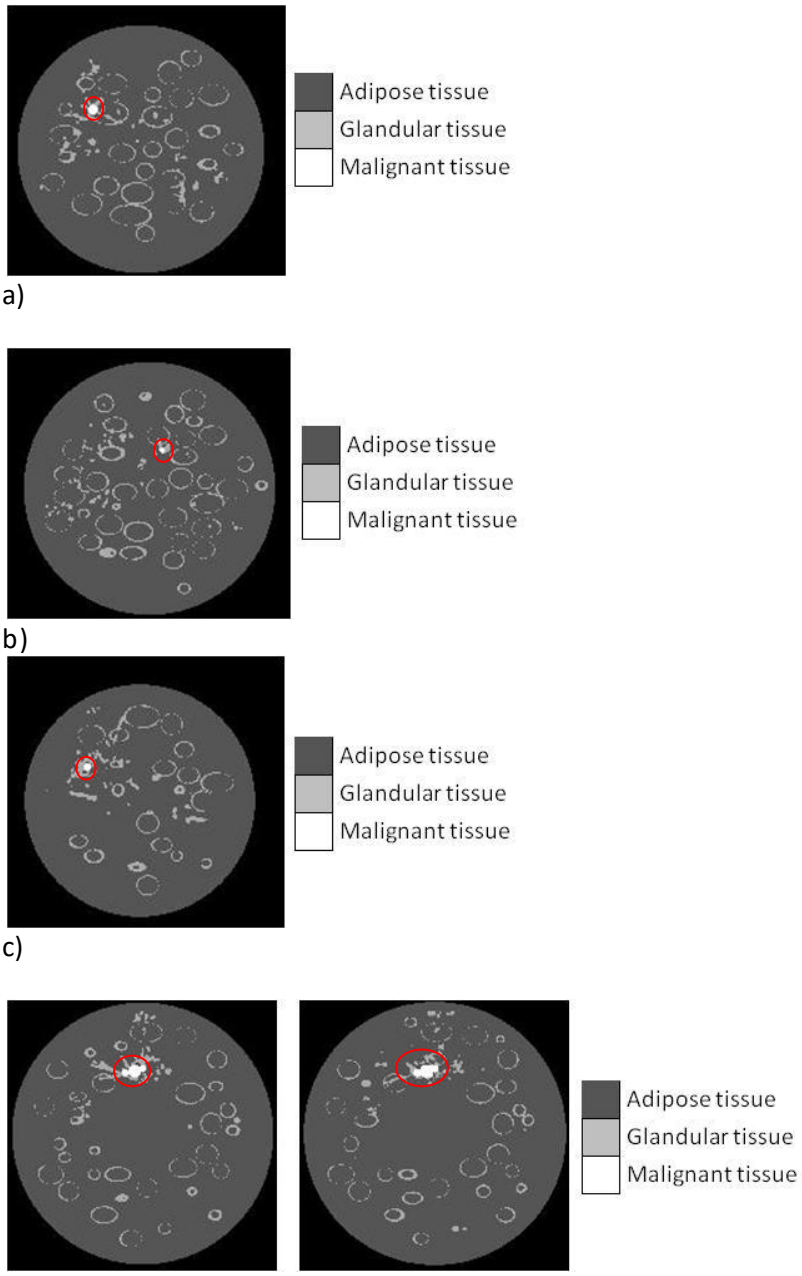

Figure 4.9: Slices through the breast phantom matrix. Malignant masses are indicated by a red circle. a,b,c) Masses of different sizes present in the glandular tissue. d) Irregular mass present on two different slices of the breast.

4.2.3.3 Phantom 3

The third phantom consisted of 58% glandular tissue and 42% adipose tissue with six major ducts, six lactiferous ducts and ellipsoid structures with a radius of 5 mm which represents the Cooper's ligaments. A visualisation of the breast model can be seen below in Figure 4.10.

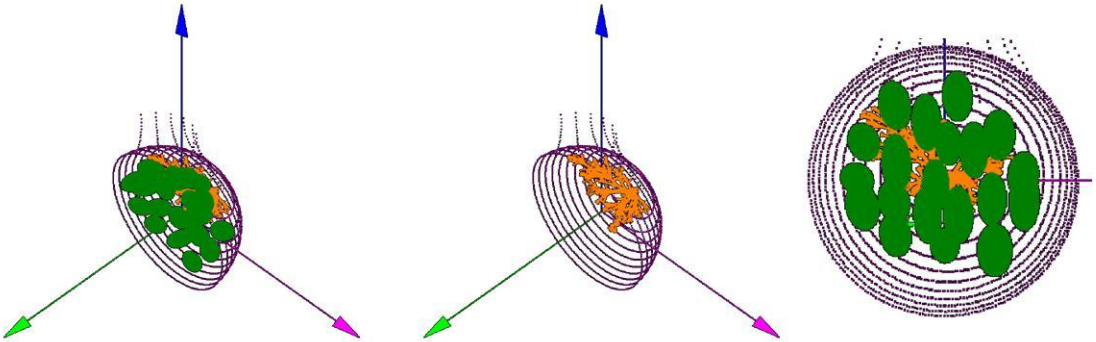

a) b)

Figure 4.10: Advanced visualisation of the breast phantom a) with Cooper's ligaments and b) without Cooper's ligaments. (The green structures represent the Cooper's ligaments, and the orange structures represent the ducts) c) This is the least dense breast with less glandular tissue than the breast compositions in Figure 4.6 and Figure 4.8.

The phantom is seen in Figure 4.11 below.

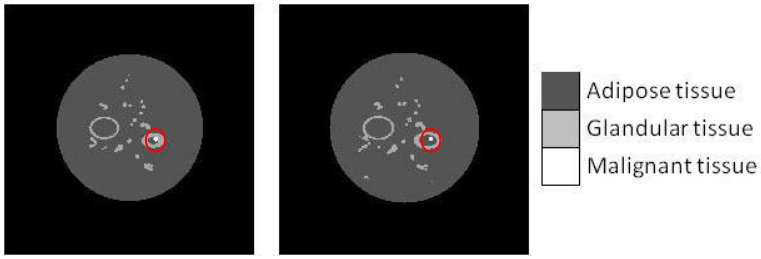

a)

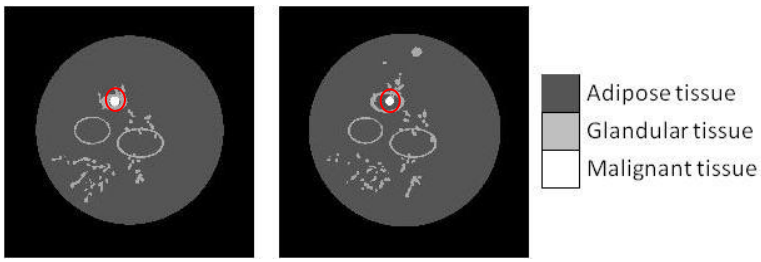

b)

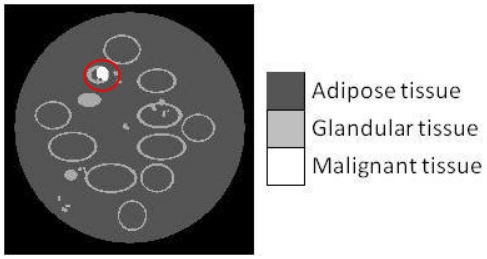

c)

d)

Figure 4.11: Slices through the dense breast phantom matrix. Malignant masses are indicated by a red circle. a,b,c) Masses of different sizes present in the glandular tissue. d) Irregular mass. It can be seen that the Cooper's ligaments are bigger than those present in the other two breast phantom.

All the breast phantoms were simulated with monoenergetic energies ranging from 20 keV to 65 keV in 5 keV increments. The SAD was 55 cm, and the SSD was chosen so that the whole breast could be projected on a detector with voxel sizes of 0.08 cm. The simulation set-up can be seen below in Figure 4.12.

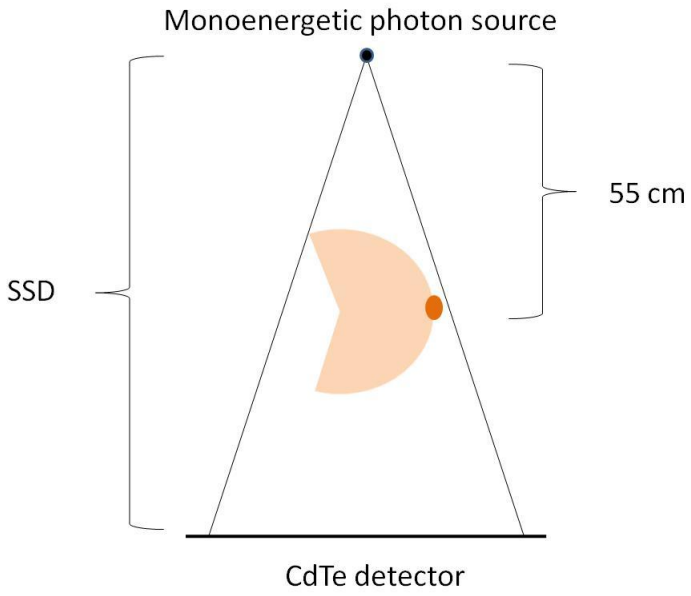

Figure 4.12: The simulation set-up for the simulation of the three breast phantoms.

A CdTe detector with a pixel size of 0.08 cm was used for the acquisition of the images.

4.2.4 Reconstruction of the images

The same OSCaR software was used for the reconstruction as in Chapter 3 Section 3.2.1.5.

Projection images over a 360-degree arc were taken with 1 billion histories and a statistical variance below 1%. The projection images were reconstructed with the BreastSimulator software described in Section 4.2.3 of this chapter. The OSCaR reconstruction software[58] was used for all the reconstructions with a Shepp-Logan filter and reconstruction voxels of 0.05 cm. The reconstructed images were then saved in binary format and read out with a MATLAB code. Ring artifacts were present in the images and obscured the structures present. This would lead to inaccurate results for the CNR. The same blank (air) scan is used for each projection and noise at a specific position in the blank (air) scan will be backprojected in each projection leading to rings on the reconstructed image. This is because the projection signal was divided by the air scan to get the final signal as seen in Equation 4.1. This cause for the ring artifacts was eliminated by using a different blank scan for each projection view and thereby adding statistical noise on the profiles opposed to systematic noise, which cancels out over a large number of projections. This resulted in 360 projection views, each one normalised by its own blank (air) scan. The ring artifacts were still present after the reconstruction, and it was concluded that it was not caused by the noise in the blank (air) scan. Sinograms were constructed for each slice through the phantom to see if the origin of the artifacts can be seen. An example of a sinogram can be seen below in Figure 4.13.

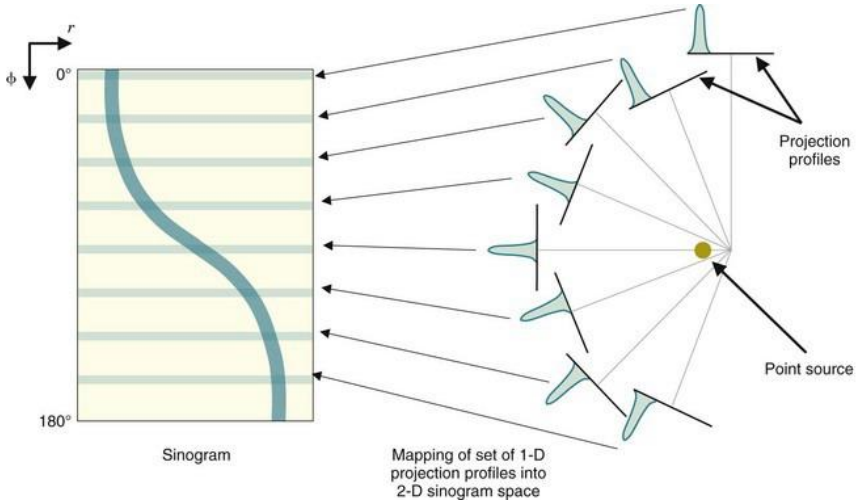

Figure 4.13: As the X-ray beam rotates around the object, different 1D projection profiles are obtained. The profiles of the same slice for each angle can be placed in a

2D space to form a sinogram. Each row represent the same projection profile of the image but at a different angle.[59]

In Figure 4.14 the sinogram of a phantom consisting of two inserts can be seen. As the X-ray beam rotates around the phantom, the inserts will move in a sinusoidal pattern in the sinogram.

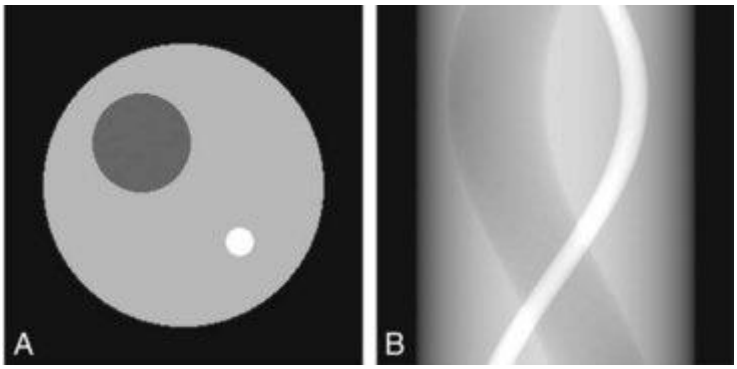

Figure 4.14: A) A phantom with two round inserts.B) The resulting sinogram with the two inserts clearly visible.[59]

According to a tutorial by Mark Rivers[60], a vertical stripe on the sinogram will be backprojected as a half cylinder centred on the rotation axis.

The method proposed by Mark Rivers[60] was used to suppress the ring artifacts. The method, as seen in the tutorial, is explained below and was done with an in-house developed IDL program (see Appendix III).

1. The columns, which represent a specific point on the projection profile, were summed and divided by the number of rows (represents the degrees). Very little high frequencies should be present as a real object will move in the sinogram as seen in Figure 4.14 above.

2. A smooth version of the average row values was then subtracted from the raw average row values.

3. The result from step 2 was then subtracted from each row, and the information from the resulting sinogram was used for the reconstruction. This results in a sinogram with much less vertical striping.

The final images were then used for the determination of the CNR.

4.2.5 CNR determination for all the images

An in-house developed IDL code was used to determine the CNR of the images acquired at the different photon energies. The breast phantoms were used as a reference to ensure the ROIs were drawn in at the correct positions. The Canny edge detection algorithm in MATLAB was used to determine exactly where the structures were situated in the phantoms. The edge detection image was then superimposed onto the reconstructed image, and the ROIs positions were determined for each phantom as seen in Figure 4.15.

a)

b)

Figure 4.15: Left) Reconstructed image. Middle) image with edge detection. Right) edge detection superimposed onto the reconstructed image. a) A section of the reconstructed image of phantom 1. From the first image, it is unclear where the border of the glandular tissue is. With the blended image on the right, the border is clearly visible. b) A section of the reconstructed image of phantom 3. The blended image clearly indicates the outline of the glandular structure.

The Canny edge detection algorithm was developed by John F. Canny in 1986 and is considered as one of the most strictly defined methods for structural detection.[61] In some cases, the noise in the background was also detected, and the Sobel method[62] was used instead as seen in Figure 4.16.

a) b) c)

Figure 4.16: a) The reconstructed image from the breast phantom with noise present in the central region of the image. b) Canny edge detection algorithm is detecting all the noise and non-uniformities in the background of the image. c) Sobel edge detection method is only detecting the structural parts of the phantom that is used for the ROI determination.

The most common equation for CNR in digital imaging is given by Equation 4.2 below.

$$CNR = \frac{|S_T - S_b|}{\sigma_b} \qquad 4.2$$

Where S_T represents the signal in the tissue, in this case, the malignant tissue and S_b denotes the background signal, in this case, the glandular tissue. The standard deviation in the background signal is given by σ_b. If Equation 4.2 is used for the CNR calculation with irregular tissue being the background, it will lead to large standard deviations in its ROI pixel counts. The malignant tissue, on the other hand, consists of spheres and the signal can be accurately determined through certain ROI regions. In Figure 4.17 below the variation in the glandular signal can be seen.

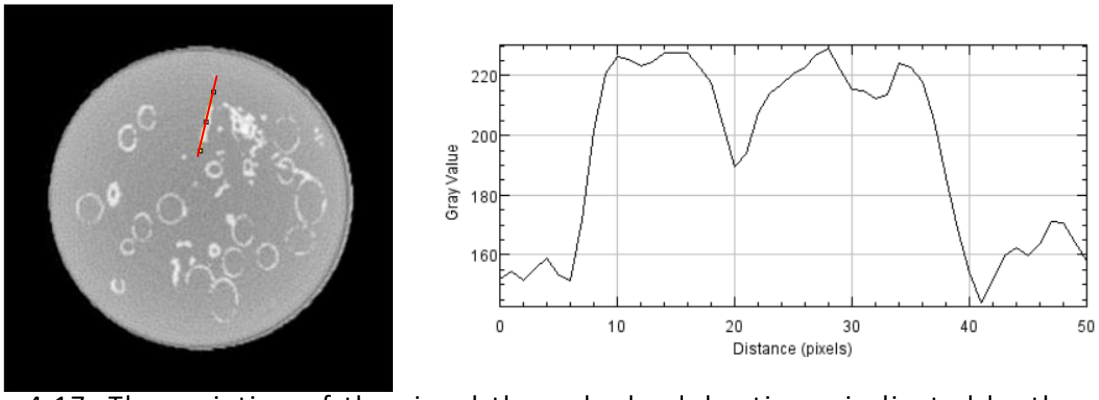

Figure 4.17: The variation of the signal through glandular tissue indicated by the red line.

It was decided to use Equation 4.3 below to determine the CNR.[63]

$$CNR = \frac{|S_T - S_b|}{\sigma_o} \qquad 4.3$$

S_T and S_b still represent the signal in the two tissues being compared but the standard deviation is taken in a uniform background region, in this case, the adipose tissue as seen below in Figure 4.18.

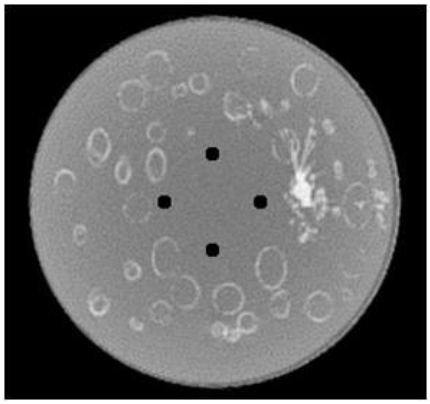

Figure 4.18: Positions of the background ROI in uniform adipose tissue.

Standard deviation values as large as 100 were found for the glandular tissue using Equation 4.2. The standard deviation for background regions used in Equation 4.3 had values ranging from 2 to 5.

An in-house developed IDL code was used to determine the mean pixel values in the ROIs. The program was completely automatic without any user input or inconsistency between the different energies. The program consisted of the following steps:

1) ROI position determination using edge detection to ensure the regions were in the correct position.
2) A mask was constructed that has a value of 1 inside the specific structure and 0 outside the structure. A for-loop was used to record the pixel values in the areas with a number of 1.
3) The mean pixel values were determined for the two ROIs.
4) The background region as described with Equation 4.3, consisted of 4 ROIs in uniform background areas. The standard deviation was taken as the average standard deviation in the four regions. The background regions were placed in areas not too close to the periphery or areas with pronounced ring artifacts.

The CNR for the same phantom and slice position were compared with one another at different energies.

4.2.6 Image correlation between the breast phantom and reconstructed image

The reconstructed images were compared to the breast phantom to determine the accuracy of the simulation and reconstruction process. The pixel size and resolution of the two datasets differ, and therefore the comparison could not be done on a pixel by pixel basis. An alternative method was used where the structures in the phantom were compared with those in the reconstructed images.

Automatic feature matching in MATLAB was used to ensure the two datasets, the phantom and the reconstructed image, were the same size before comparing them. The method is shown in the Figure 4.19 below.

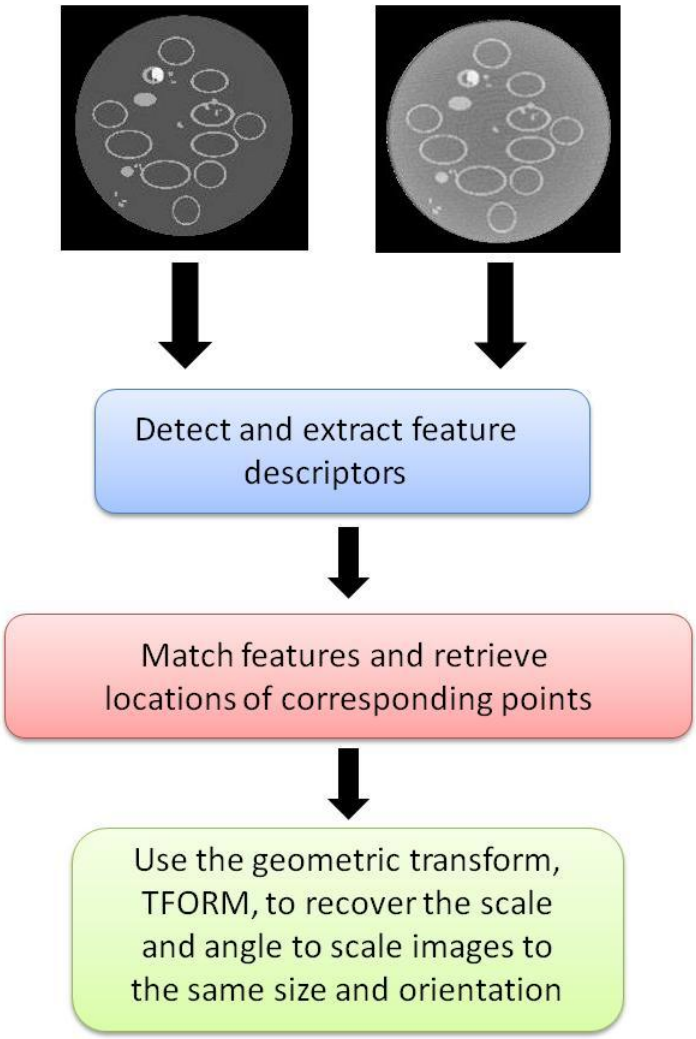

Figure 4.19: The method used to scale both datasets to the same size and orientation.

A composite image of the breast phantom and scaled reconstructed image was made to see if the structures in the images correlate with one another.

4.3 Results and Discussion

4.3.1 Linear attenuation coefficients for the different tissues

The linear attenuation coefficients for all the tissues can be seen below in Figure 4.20. The shape of the graph correlates well with the one seen in Figure 4.2. When looking at the graph, it is expected that the maximum CNR will be seen for a low energy of 20 keV and that it will decrease as the energy increases. This is by assuming that the noise levels for all the energies are the same. At energies 40 keV up to 65 keV, the decrease in the CNR should be more gradually as depicted in Figure 4.23. The maximum CNR for the iodine contrast should be seen just above the K-edge peak at 34-35 keV. When looking at the Figure below it is seen that the difference between the iodine contrast and glandular tissue increases from 20 keV and upwards.

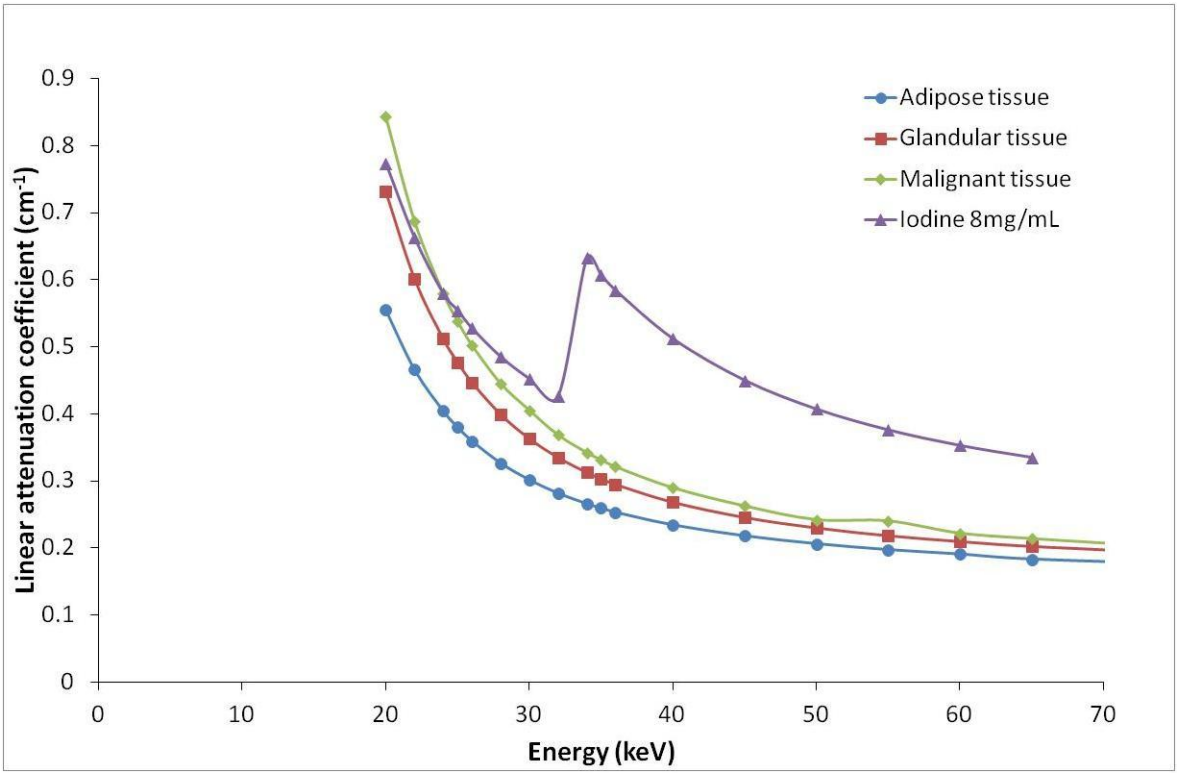

Figure 4.20: The linear attenuation coefficients for the different tissues for energies from 20 keV. The K-absorption edge of iodine can be seen at 33 keV.

4.3.2 Reconstruction and ring artifact correction

Some of the projection images obtained through the simulations of the egs_cbct code are seen below in Figure 4.21.

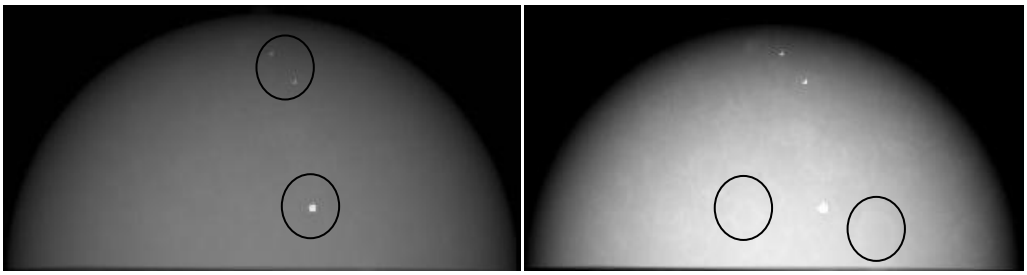

Figure 4.21: Left) The projection image for a gantry angle of 0°. (The white spots encircled in black are markers used for orientation purposes.) Right) By changing the display parameters the Cooper's ligaments can be seen as oval structures encircled in red.

The reconstructed images and their sinograms without the ring artifact correction are seen below in Figure 4.22. Vertical lines on the sinograms that result in the rings are indicated by red arrows. Both of the sinograms are shown with the same display parameters.

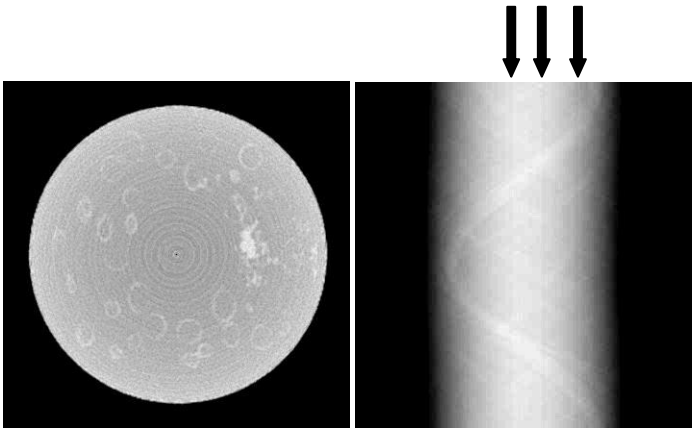

Figure 4.22: Reconstructed image with ring artifacts and a sinogram of the specific slice.

Images of the same slices as in Figure 4.22 are seen below with the ring artifact correction.

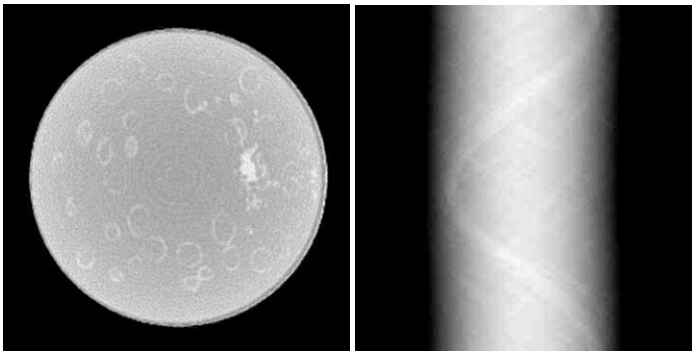

Figure 4.23: Reconstructed image with a ring artifact correction and a sinogram where the vertical lines are less pronounced.

When comparing the two sinograms, it can be seen that the vertical lines present are suppressed by the correction method.

4.3.2.1 Phantom 1

The following images were obtained after FDK reconstruction with voxel sizes of 0.05 cm and a Shepp-Logan filter. All of the images are shown with the same display parameters.

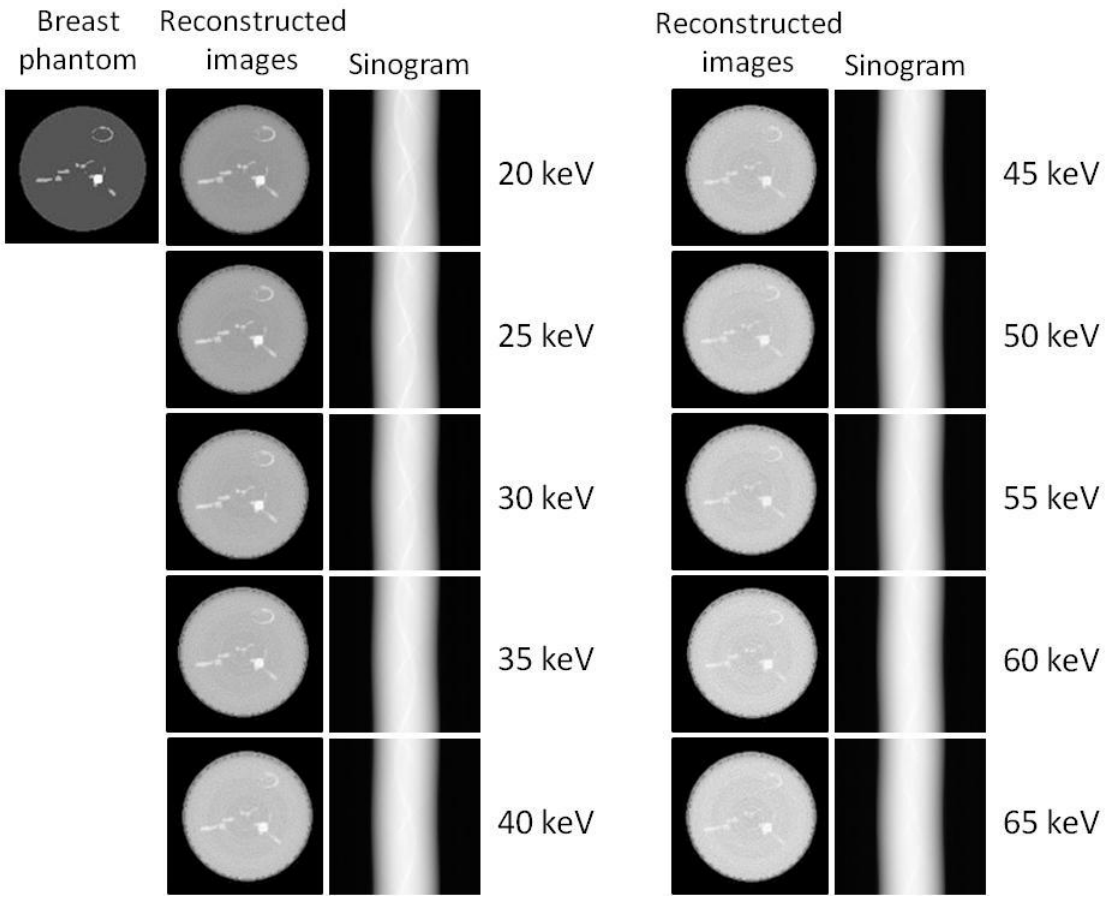

Figure 4.24: A reconstructed slice through phantom 1 consisting of glandular and malignant tissue (see Figure 4.7 b) for energies 20 keV to 65 keV. The contrast is better for the lower energies, and the structures are also seen in the sinograms.

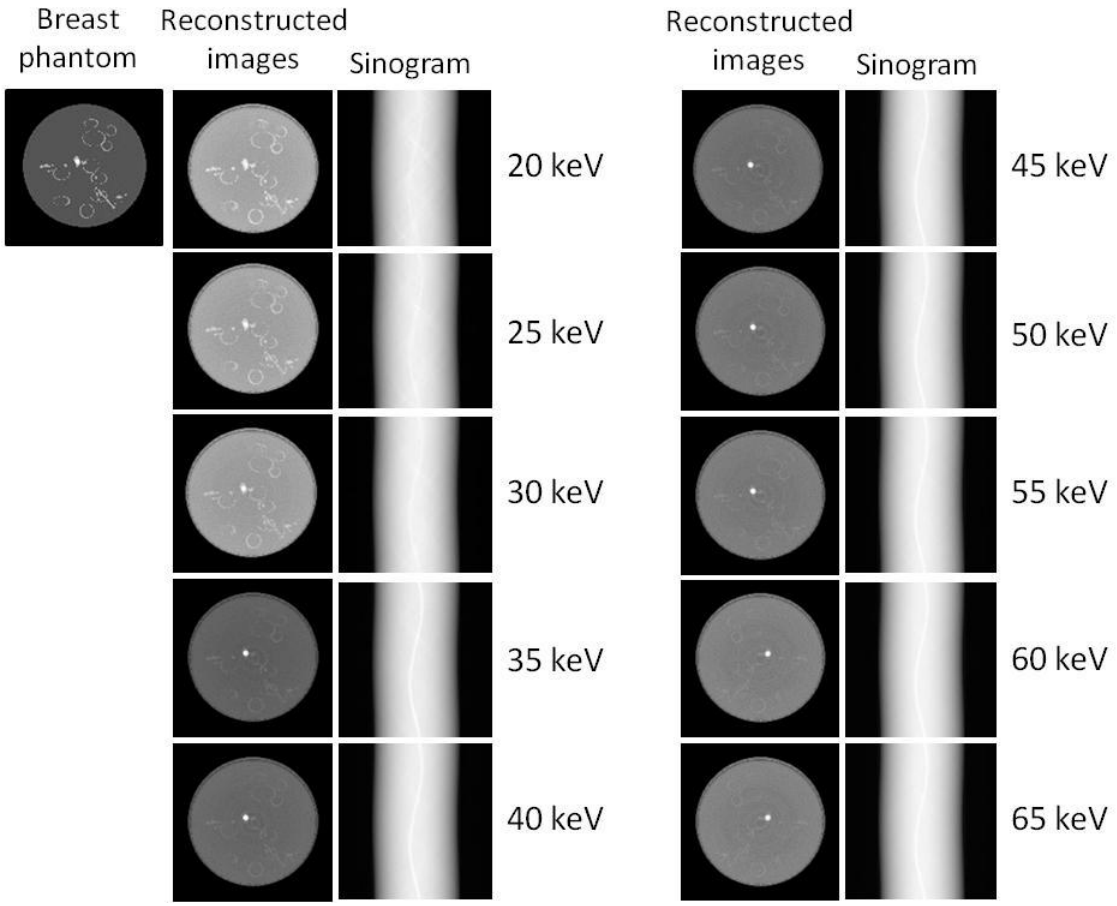

Figure 4.25: A reconstructed slice through phantom 1 consisting of glandular and malignant tissue containing 8mg/mL iodine (see Figure 4.7 c) for energies 20 keV to 65 keV. There occurs a sharp increase in the contrast between the iodinated malignant and glandular tissue slightly above the absorption edge of iodine.

4.3.2.2 Phantom 2

The following images were obtained after FDK reconstruction with voxel sizes of 0.05 cm and a Shepp-Logan filter. All of the images are shown with the same display parameters

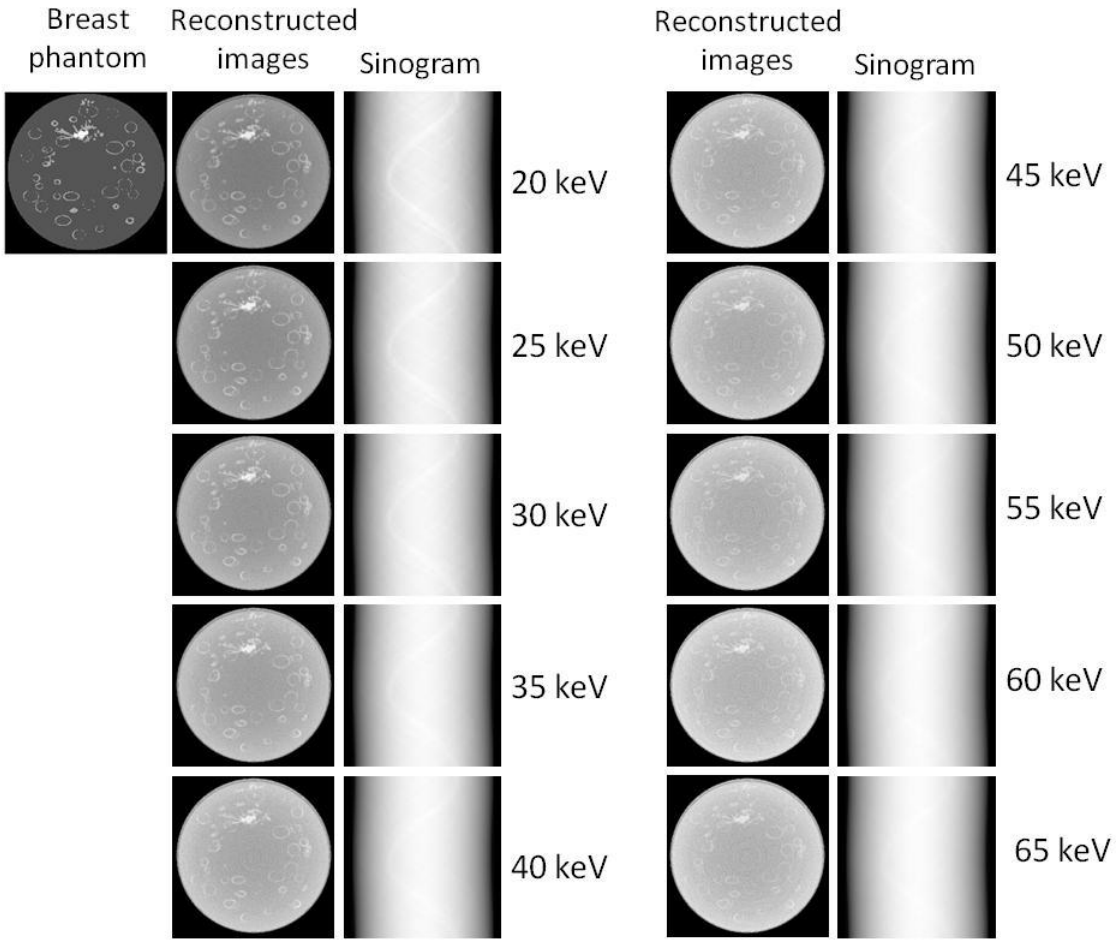

Figure 4.26: A reconstructed slice through phantom 2 consisting of glandular and malignant tissue (see Figure 4.9 d) for energies 20 keV to 65 keV. The contrast is better for the lower energies, and the structures are also seen in the sinograms. All of the Cooper's ligaments are clearly visible at the lower energies but from 55 keV and upwards it is hard to distinguish them from the surrounding structures.

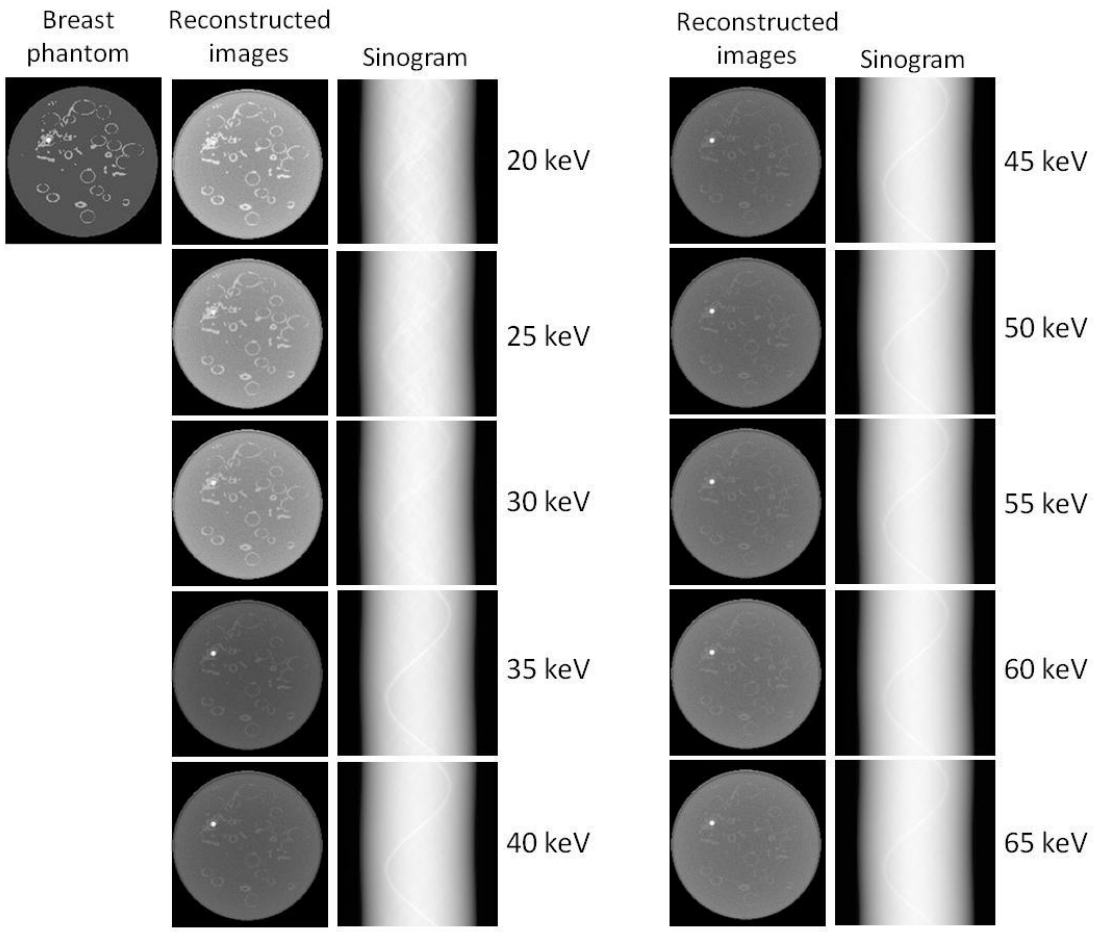

Figure 4.27: A reconstructed slice through phantom 2 consisting of glandular and malignant tissue containing 8mg/mL iodine (see Figure 4.9 c) for energies 20 keV to 65 keV. There occurs a sharp increase in the contrast between the iodinated malignant and glandular tissue slightly above the absorption edge of iodine. The malignant tissue with iodine produces a pronounced sinusoidal wave above 35 keV and is clearly visible.

4.3.2.3 Phantom 3

The following images were obtained after FDK reconstruction with voxel sizes of 0.05 cm and a Shepp-Logan filter. All of the images are shown with the same display parameters.

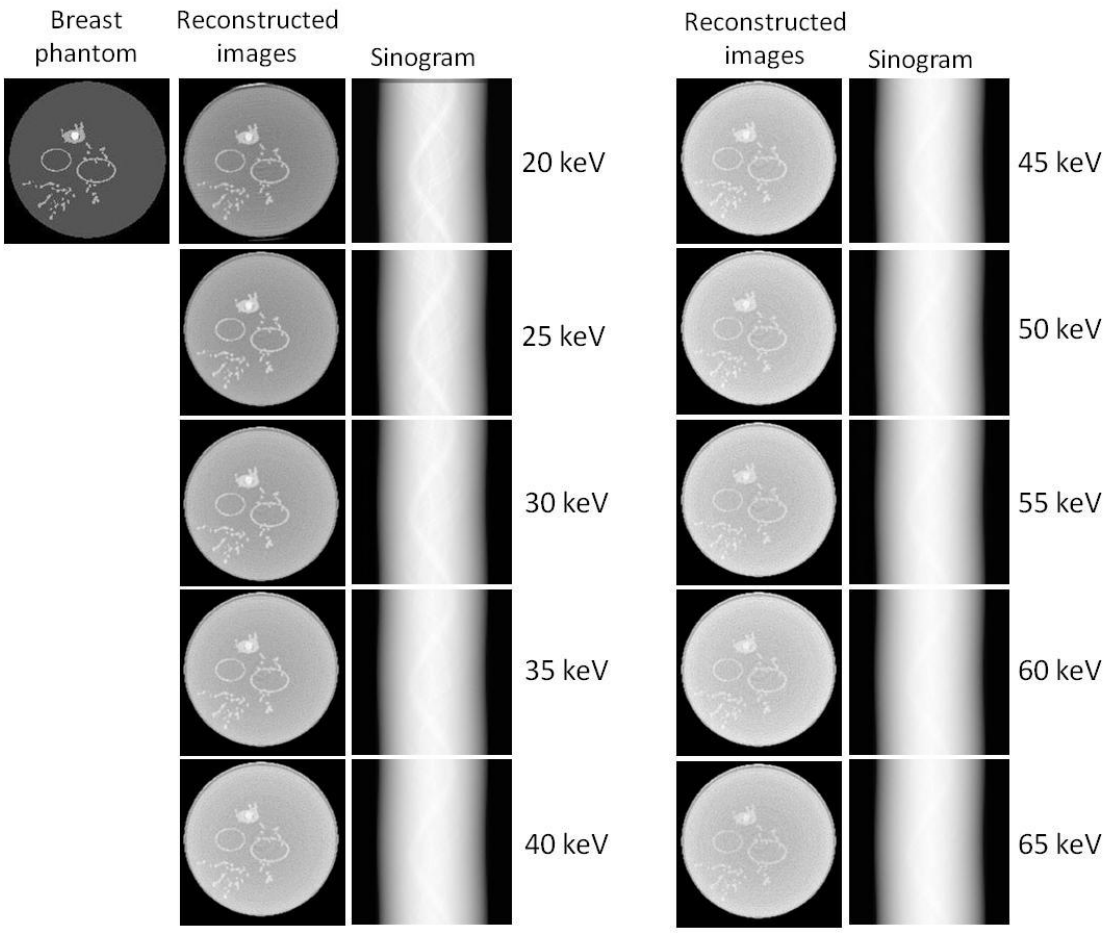

Figure 4.28: A reconstructed slice through phantom 3 consisting of glandular and malignant tissue (see Figure 4.11 b) for energies 20 keV to 65 keV. The contrast is better for the lower energies, and the structures are also seen in the sinograms. At the lower energies the malignant mass in clearly visible inside a Cooper's ligament.

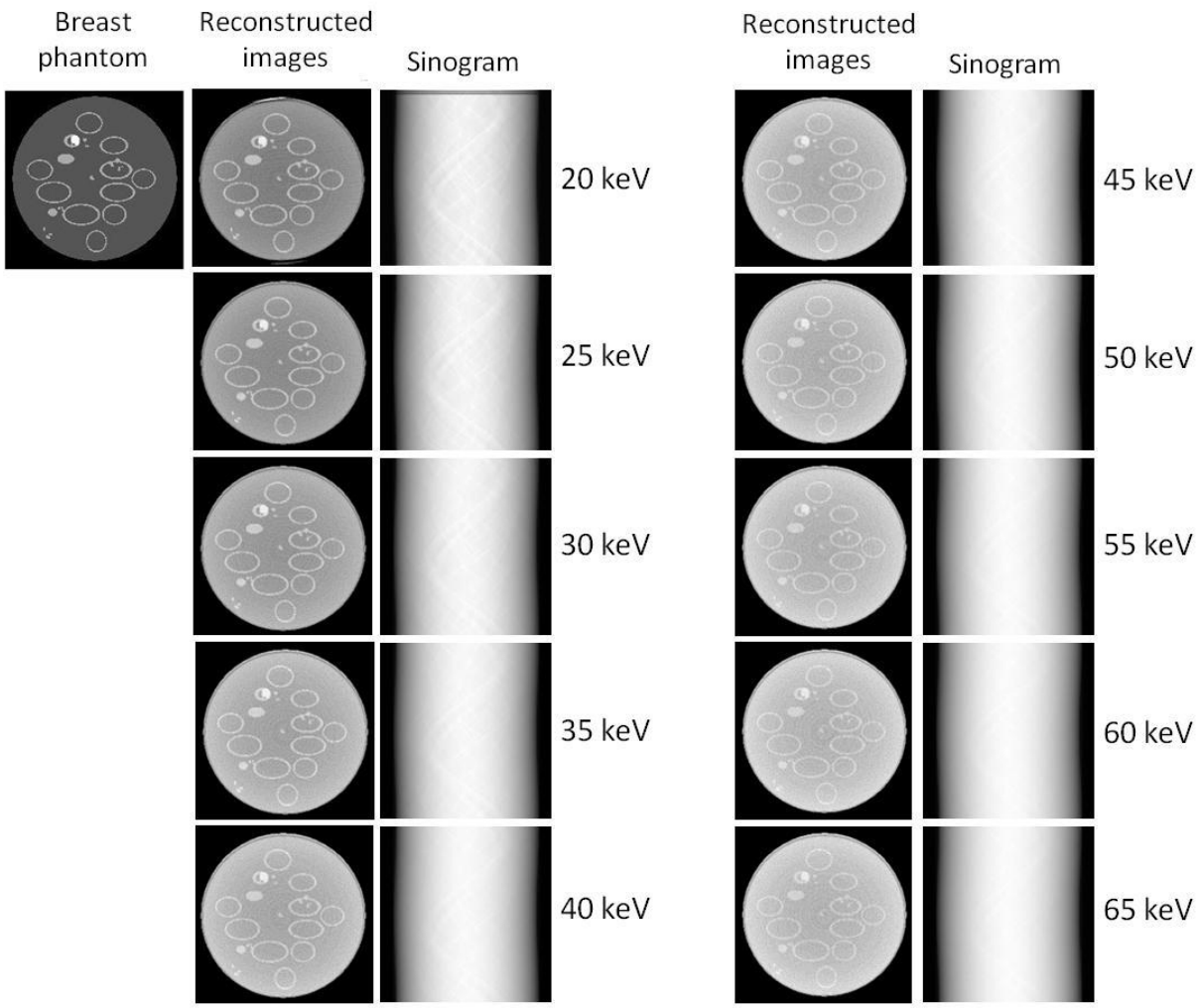

Figure 4.29: A reconstructed slice through phantom 3 consisting of glandular and malignant tissue (see Figure 4.11 c) for energies 20 keV to 65 keV. The contrast is better for the lower energies, and the structures are also seen in the sinograms. At the lower energies the malignant mass in clearly visible inside a Cooper's ligament.

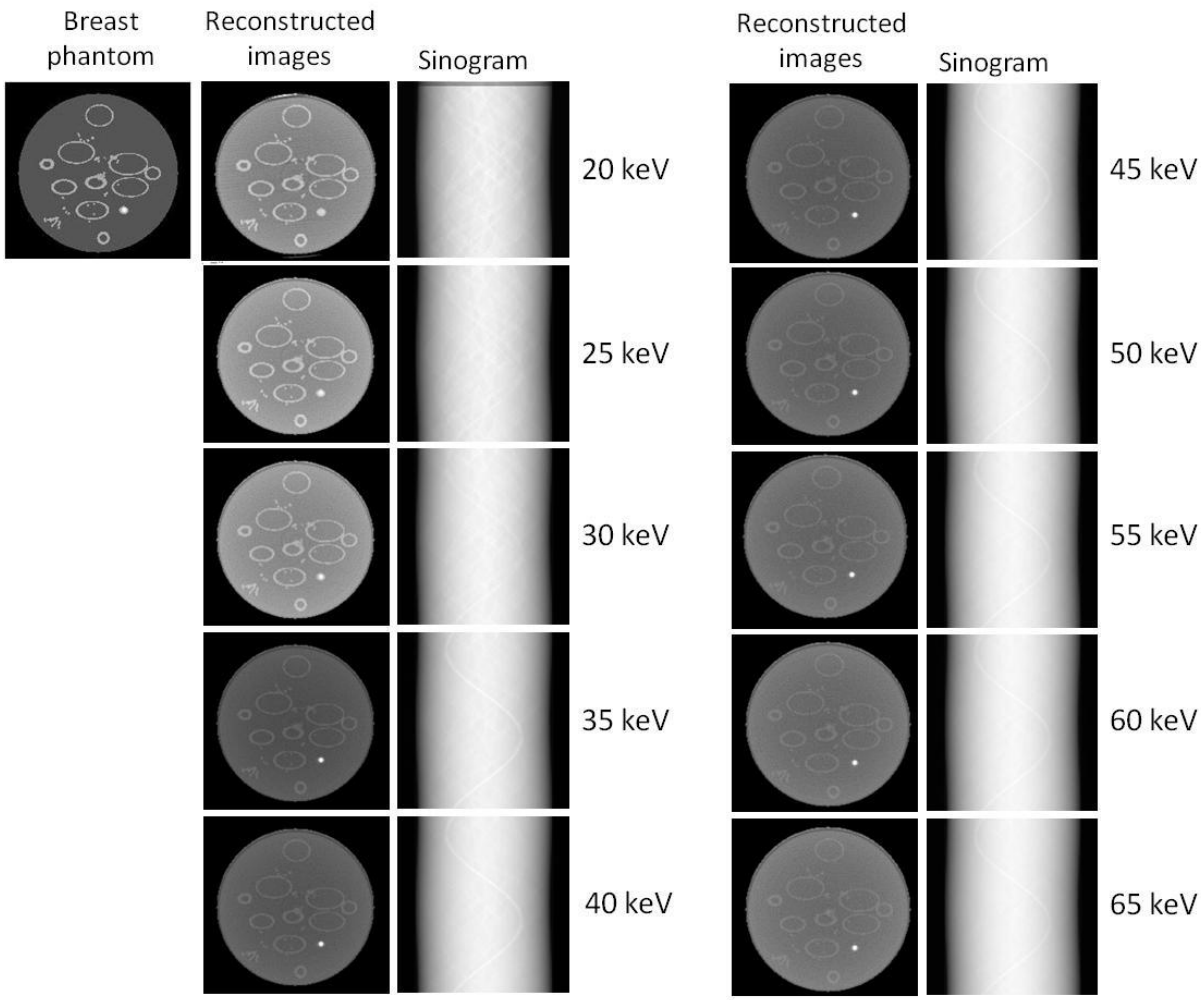

Figure 4.30: A reconstructed slice through phantom 3 consisting of glandular and malignant tissue containing 8mg/mL iodine (see Figure 4.11 d) for energies 20 keV to 65 keV. There occurs a sharp increase in the contrast between the iodinated malignant and glandular tissue slightly above the absorption edge of iodine. At 20 keV the small malignant mass cannot be distinguished from the background structures and is also not visible in the sinogram.

The CNRs were calculated for all the images displayed from Figure 4.24 to 4.30 by using the method explained in Section 4.2.5. The CNRs for phantom 1 to 3 without any contrast agent is seen below (information regarding the phantom glandularities can be seen in Section 4.2.3.1 to 4.2.3.3. above).

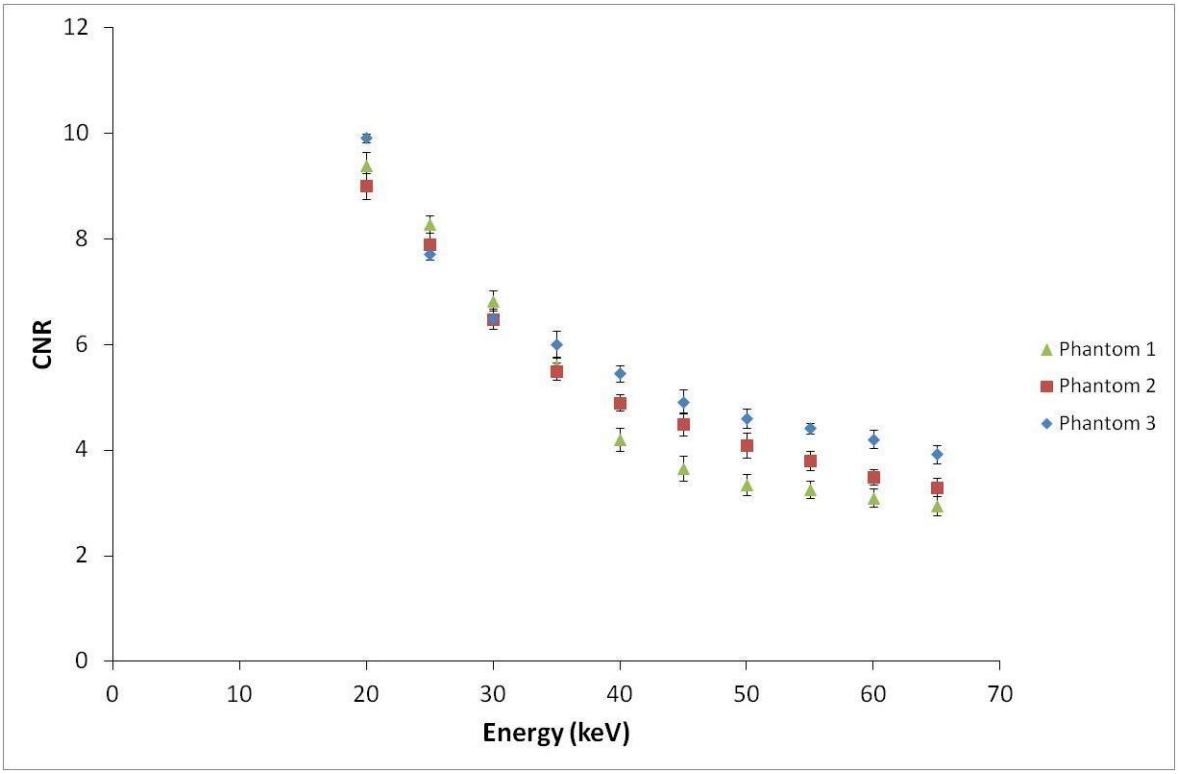

Figure 4.31: The CNRs for the malignant and glandular tissue for all three the phantoms without any contrast agent. The energies range from 20 keV to 65 keV. The uncertainties in the CNR values are indicated.

The differences seen between the different phantoms in Figure 4.31 depict that the glandularity of the phantoms have an effect on the resulting CNRs. This can be caused by the structures and amount of tissue that has to be transversed by the X-ray beam in each phantom. Phantom 1 represents a dense breast and the X-ray beam has to transverse dense glandular tissue, leading to low CNR's. The opposite happens for phantom 3 consisting of a large amount of fatty tissue. In Figure 4.32 below the CNRs for all three phantoms can be seen with contrast agents.

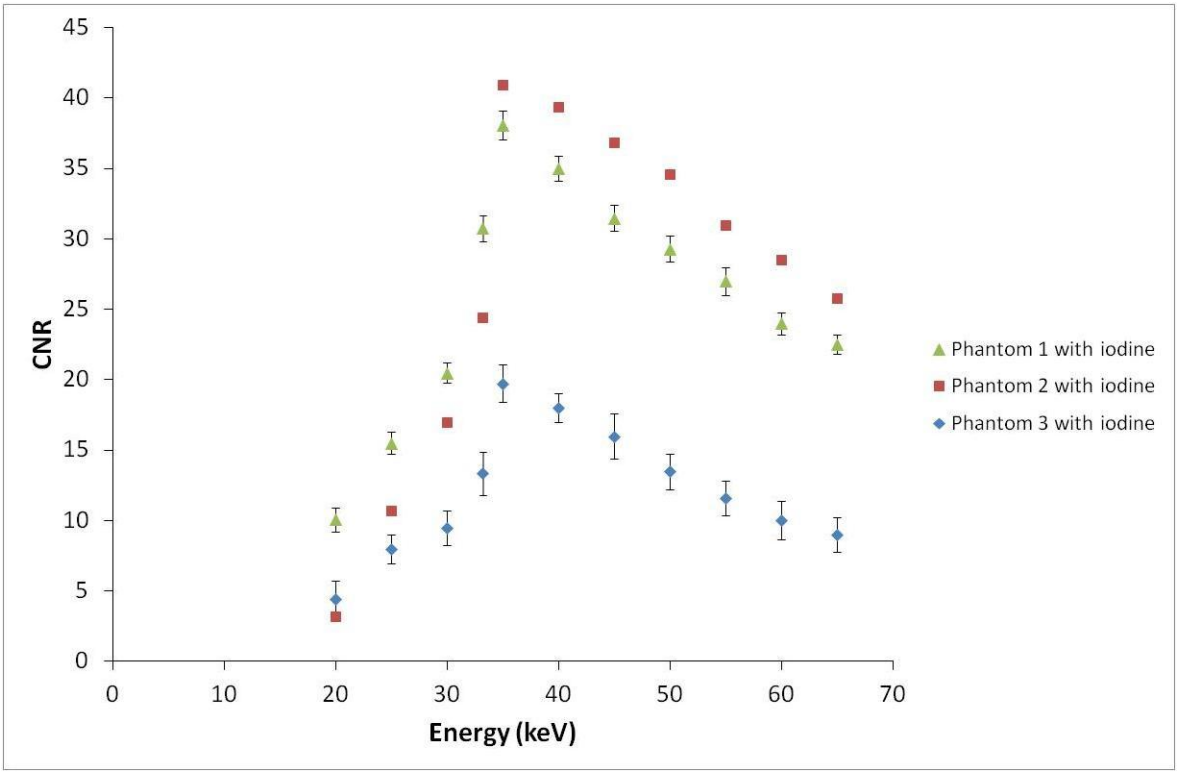

Figure 4.32: The CNRs for the malignant and glandular tissue for all three the phantoms with contrast agent. The energies range from 20 keV to 65 keV. The uncertainties in the CNR values are indicated. The error bars for phantom 2 is smaller than the symbol size.

The lowest CNRs are seen for phantom 3 which is the least dense phantom. This result contradicts the results found in Figure 4.31. A possible reason could be that the location of the malignant mass makes it difficult to get an accurate ROI. In Figure 4.33 below it can be seen that very little glandular tissue surrounds the mass and it could be that there was an error in the ROI's. This could lead to inaccurate ROI values and a CNR that is lower than expected.

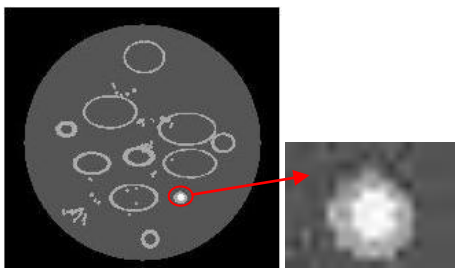

Figure 4.33: The position of the malignant mass with iodine contrast.

The reason for the increase in the CNR at 35 keV is due to the sharp increase in absorption just above the K-edge energy of 33.17 keV. The CNRs obtained in Figure 4.32 correlate well with what is seen for the linear attenuation coefficients seen in Figure 4.23.

4.3.3 Image correlation between the breast phantom and reconstructed image.

Image matching was done before image correlation to ensure the two data sets are the same size. It was done with the help of an in-house developed MATLAB code as described in Section 4.2.6. The breast phantom had voxel sizes of 0.1 cm, and the detector had pixel sizes of 0.08 cm. The reconstruction was done with a resolution of 0.05 cm, so some discrepancies were expected. Below the image of the breast phantom can be seen next to the reconstructed slice.

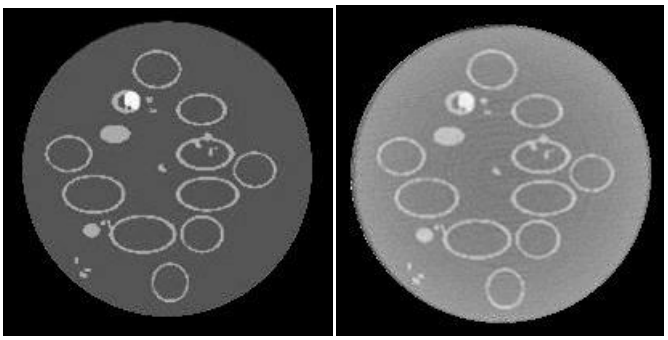

Figure 4.34: Left) Breast phantom slice. Right) Reconstructed slice

It seems like the two images are the same size but an offset can be seen when superimposing them into one image. The one data set is displayed with green and the other one with red. The yellow parts indicate where there is a match between the two dataset structures.

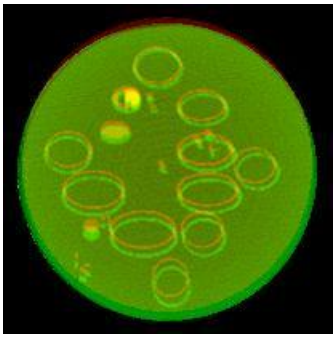

Figure 4.35: Superimposition of the two images. An offset can be seen between them in the vertical direction.

Locations of corresponding points between the two images were detected.

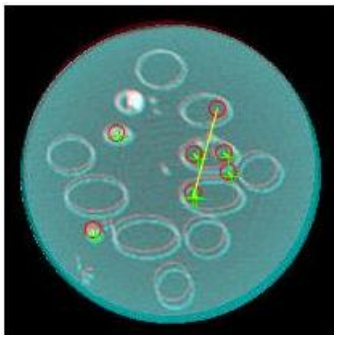

Figure 4.36: Points of matching features between the two image data sets.

The inverse transformation matrix was calculated, and the reconstructed image was transformed to match the size of the breast phantom slice image. The difference in scale was 1.0229, and a slight difference in rotation of 0.0252 degrees was detected. The two images after the transformation can be seen below.

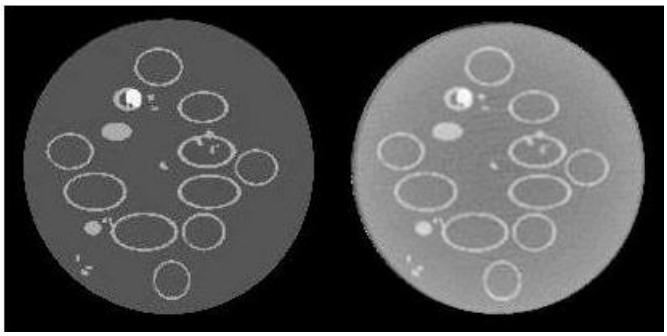

Figure 4.37: Left) Breast phantom slice. Right) Transformed reconstructed slice.

Even though they are the same size and some features correlate between them it does not mean that all the structures seen in the breast phantom slice are present after the simulation

and reconstruction process. The breast phantom slice and the reconstructed image were superimposed once again to see if all the structures overlap.

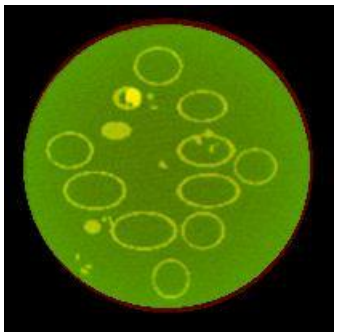

Figure 4.38: The superimposition of the breast phantom slice and the transformed reconstructed slice. It can be seen that there is a good correlation between the structures present in both images.

From the image above it can be seen that all the glandular and malignant tissue are present in the reconstructed image. The same was done for two other slices, and the results are seen below.

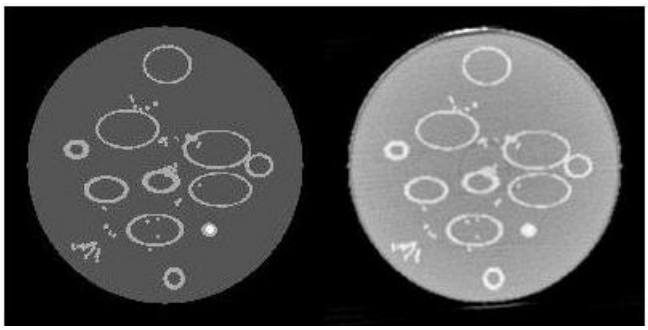

Figure 4.39: Left) Breast phantom slice. Right) Reconstructed slice

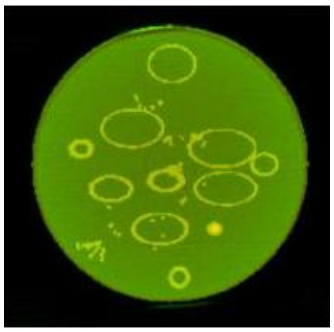

Figure 4.40: Superimposition of the two images shows that there is a good correlation between the structures in the two image data sets.

There are, however, discrepancies between some of the breast phantom slices and the corresponding reconstructed images. The reason for this is that the resolution of the breast

phantom and the reconstructed image are different and there can exist a slight offset in the slice position. In Figure 4.41 below there are some glandular tissue differences between the two images indicated by red circles. This shows that the slice position for the two data sets is not at the same position.

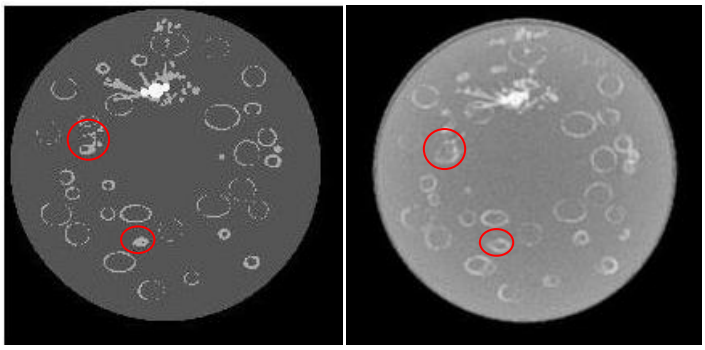

Figure 4.41: Left) Breast phantom slice. Right) Reconstructed image slice. Some small differences can be seen in the glandular tissue. This can be because the two images are not at the same slice position.

4.4 Conclusion

It was shown that a better contrast is seen between the malignant tissue and glandular tissue at lower energies. For phantom 1 the contrast difference between 20 keV and 65 keV was 6.43, phantom 2 was 5.7, and phantom 3 was 5.99. The decrease in CNR as the energy increases correlate well with the linear attenuation coefficient values obtained for the different tissue types at different energies. The BreastSimulator Software is a valuable tool for modelling breast phantoms based on clinical data. The OSCaR reconstruction software can accurately reconstruct the projection data obtained from egs_cbct simulations since good correlation was found between the breast phantom and the reconstructed images. Small glandular structures that were in the phantoms were also visible in the reconstructed images. Small discrepancies exist due to the differences in resolution for the two datasets. The ring artifacts present in the reconstructed images can obscure the ROI and lead to inaccurate results for the CNR. The rings in the images can lead to higher or lower ROI values and the subsequent CNR calculated will not represent the true CNR of the image. The method

proposed by Mark Rivers to remove the ring artifacts is easy to implement and sufficient in most cases. The CNR for the lower energies were at the least 2.5 times higher as for, the higher energies. This leads to better tumour detection and makes the idea of multiple-energy CT feasible. In multiple-energy CT a range of images can be obtained with a single image acquisition. The patient can be exposed to a single energy spectrum that will result in an acceptable dose while acquiring low energy images with high CNRs. If a single low energy is used for image acquisition to achieve a high CNR, the dose to the patient will be unacceptably high. Therefore multiple-energy CT is a promising technique that can lead to high CNRs within acceptable dose ranges. If contrast agents are not available for use, then multiple-energy CT will still result in 2.5-3 times better CNRs that the conventional methods currently used. A high CNR was still achieved for the breast consisting of 89 % glandular tissue and the tumours were still clearly visible.

4.5 References

1. O'Connell AM, Karellas A, Vedantham S. The potential role of dedicated 3D breast CT as a diagnostic tool: Review and early clinical examples. Breast J. 2014 Nov;20(6):592–605.

2. Metheany KG, Abbey CK, Packard N, Boone JM. Characterizing anatomical variability in breast CT images. Med Phys. 2008 Oct 1;35(10):4685–94.

3. Textbook of Anatomy Upper Limb and Thorax; Volume 1 - 2nd Edition [Internet]. [cited 2017 Jun 18]. Available from: https://www.elsevier.com/books/textbook-of-anatomy-upper-limb-and-thorax-volume-1/singh/978-81-312-3729-8

4. Breast Ultrasound: 9780397516247: Medicine & Health Science Books @ Amazon.com [Internet]. [cited 2017 Jun 18]. Available from: https://www.amazon.com/Breast-Ultrasound-Thomas-Stavros-FACR/dp/039751624X

5. MD ES deParedes. Atlas of Mammography. Third edition. Philadelphia: LWW; 2007. 704 p.

6. ACR BI-RADS Atlas. AMER COLLEGE OF RADIOLOGY. ISBN:155903016X

7. BI-RADS Classification for Management of Abnormal Mammograms. J Am Board Fam Med. 2006;19(2):161-164.

8. Boyd NF, Martin LJ, Bronskill M, Yaffe MJ, Duric N, Minkin S. Breast Tissue Composition and Susceptibility to Breast Cancer. JNCI J Natl Cancer Inst. 2010 Aug 18;102(16):1224–37.

9. Sechopoulos I, Suryanarayanan S, Vedantham S, D'Orsi C, Karellas A. Computation of the glandular radiation dose in digital tomosynthesis of the breast. Med Phys. 2007 Jan;34(1):221–32.

10. Dance DR. Monte Carlo calculation of conversion factors for the estimation of mean glandular breast dose. Phys Med Biol. 1990 Sep;35(9):1211–9.

11. Thacker SC, Glick SJ. Normalized glandular dose (DgN) coefficients for flat-panel CT breast imaging. Phys Med Biol. 2004 Dec 21;49(24):5433–44.

12. Sechopoulos I, Feng SSJ, D'Orsi CJ. Dosimetric characterization of a dedicated breast computed tomography clinical prototype. Med Phys. 2010 Aug;37(8):4110–20.

13. Bakic PR, Zhang C, Maidment ADA. Development and characterization of an anthropomorphic breast software phantom based upon region-growing algorithm. Med Phys. 2011 Jun;38(6):3165–76.

14. Bliznakova K, Suryanarayanan S, Karellas A, Pallikarakis N. Evaluation of an improved algorithm for producing realistic 3D breast software phantoms: application for mammography. Med Phys. 2010 Nov;37(11):5604–17.

15. Chen B, Shorey J, Saunders RS, Richard S, Thompson J, Nolte LW, et al. An anthropomorphic breast model for breast imaging simulation and optimization. Acad Radiol. 2011 May;18(5):536–46.

16. Ma AKW, Gunn S, Darambara DG. Introducing DeBRa: a detailed breast model for radiological studies. Phys Med Biol. 2009;54(14):4533.

17. Bliznakova K, Bliznakov Z, Bravou V, Kolitsi Z, Pallikarakis N. A three-dimensional breast software phantom for mammography simulation. Phys Med Biol. 2003 Nov 21;48(22):3699–719.

18. Dance DR, Hunt RA, Bakic PR, Maidment ADA, Sandborg M, Ullman G, et al. Breast dosimetry using high-resolution voxel phantoms. Radiat Prot Dosimetry. 2005;114(1–3):359–63.

19. Hunt RA, Dance DR, Bakic PR, Maidment ADA, Sandborg M, Ullman G, et al. Calculation of the properties of digital mammograms using a computer simulation. Radiat Prot Dosimetry. 2005;114(1–3):395–8.

20. Kontos D, Ikejimba LC, Bakic PR, Troxel AB, Conant EF, Maidment ADA. Analysis of parenchymal texture with digital breast tomosynthesis: comparison with digital mammography and implications for cancer risk assessment. Radiology. 2011 Oct;261(1):80–91.

21. Huang S-Y, Boone JM, Yang K, Packard NJ, McKenney SE, Prionas ND, et al. The characterization of breast anatomical metrics using dedicated breast CT. Med Phys. 2011 Apr 1;38(4):2180–91.

22. Li CM, Segars WP, Tourassi GD, Boone JM, Dobbins JT. Methodology for generating a 3D computerized breast phantom from empirical data. Med Phys. 2009 Jul;36(7):3122–31.

23. Yang X, Sechopoulos I, Fei B. Automatic Tissue Classification for High-resolution Breast CT Images Based on Bilateral Filtering. Proc SPIE. 2011 Mar 14;7962:79623H.

24. Zyganitidis C, Bliznakova K, Pallikarakis N. A novel simulation algorithm for soft tissue compression. Med Biol Eng Comput. 2007 Jul;45(7):661–9.

25. Bliznakova K, Sechopoulos I, Buliev I, Pallikarakis N. BreastSimulator: A software platform for breast x-ray imaging research. J Biomed Graph Comput. 2012 Mar 29;2(1):1.

26. Sechopoulos I, Vedantham S, Suryanarayanan S, D'Orsi CJ, Karellas A. Monte Carlo and Phantom Study of the Radiation Dose to the Body from Dedicated CT of the Breast. Radiology. 2008 Apr 1;247(1):98–105.

27. Lai C-J, Zhong Y, Yi Y, Wang T, Shaw CC. Radiation doses in volume-of-interest breast computed tomography--A Monte Carlo simulation study. Med Phys. 2015 Jun;42(6):3063–75.

28. Boone JM, Nelson TR, Lindfors KK, Seibert JA. Dedicated Breast CT: Radiation Dose and Image Quality Evaluation. Radiology. 2001 Dec 1;221(3):657–67.

29. Barber WC, Wessel JC, Malakhov N, Wawrzyniak G, Hartsough NE, Nœss-Ulseth E, et al. Photon counting systems for breast imaging. In: 2015 IEEE Nuclear Science Symposium and Medical Imaging Conference (NSS/MIC). 2015. p. 1–3.

30. Cho H-M, Barber WC, Ding H, Iwanczyk JS, Molloi S. Characteristic performance evaluation of a photon counting Si strip detector for low dose spectral breast CT imaging. Med Phys. 2014 Sep;41(9):091903.

31. Ding H, Klopfer MJ, Ducote JL, Masaki F, Molloi S. Breast Tissue Characterization with Photon-counting Spectral CT Imaging: A Postmortem Breast Study. Radiology. 2014 May 7;272(3):731–8.

32. Frallicciardi PM, Jakubek J, Vavrik D, Dammer J. Comparison of single-photon counting and charge-integrating detectors for X-ray high-resolution imaging of small biological objects. Nucl Instrum Methods Phys Res Sect Accel Spectrometers Detect Assoc Equip. 2009 Aug 1;607(1):221–2.

33. Bert C, Niederlöhner D, Giersch J, Pfeiffer K-F, Anton G. Computed tomography using the Medipix1 chip. Nucl Instrum Methods Phys Res Sect Accel Spectrometers Detect Assoc Equip. 2003 Aug 21;509(1–3):240–50.

34. Bisogni MG, Del Guerra A, Lanconelli N, Lauria A, Mettivier G, Montesi MC, et al. Experimental study of beam hardening artifacts in photon counting breast computed tomography. Nucl Instrum Methods Phys Res Sect Accel Spectrometers Detect Assoc Equip. 2007 Oct 21;581(1–2):94–8.

35. Chmeissani M, Frojdh C, Gal O, Llopart X, Ludwig J, Maiorino M, et al. First experimental tests with a CdTe photon counting pixel detector hybridized with a Medipix2 readout chip. IEEE Trans Nucl Sci. 2004 Oct;51(5):2379–85.

36. Ding H, Cho H-M, Barber WC, Iwanczyk JS, Molloi S. Characterization of energy response for photon-counting detectors using x-ray fluorescence. Med Phys 2014 Dec; 41(12): 121902.

37. Wang X, Meier D, Mikkelsen S, Maehlum GE, Wagenaar DJ, Tsui B, et al. MicroCT with energy-resolved photon-counting detectors. Phys Med Biol. 2011 May 7;56(9):2791–816.

38. Roessl E, Proksa R. K-edge imaging in x-ray computed tomography using multi-bin photon counting detectors. Phys Med Biol. 2007;52(15):4679.

39. Wagenaar DJ, Chowdhury S, Engdahl JC, Burckhardt DD. Planar image quality comparison between a CdZnTe prototype and a standard NaI(Tl) gamma camera. Nucl Instrum Methods Phys Res Sect Accel Spectrometers Detect Assoc Equip. 2003 Jun 1;505(1–2):586–9.

40. Barber WC, Nygard E, Iwanczyk JS, Zhang M, Frey EC, Tsui BMW, et al. Characterization of a novel photon counting detector for clinical CT: count rate, energy resolution, and noise performance. *Proc. SPIE* 7258, Medical Imaging 2009: Physics of Medical Imaging, 725824 (March 12, 2009); doi:10.1117/12.813915

41. Pan D, Roessl E, Schlomka J-P, Caruthers SD, Senpan A, Scott MJ, et al. Computed tomography in color: NanoK-enhanced spectral CT molecular imaging. Angew Chem Int Ed Engl. 2010 Dec 10;49(50):9635–9.

42. ISCT: New CT detectors promise sharper images [Internet]. AuntMinnie.com. [cited 2017 Mar 5]. Available from: http://www.auntminnie.com/index.aspx?sec=ser&sub=def&pag=dis&itemid=114488

43. Winkler SS, Sackett JF, Holden JE, Flemming DC, Alexander SC, Madsen M, et al. Xenon inhalation as an adjunct to computerized tomography of the brain: preliminary study. Invest Radiol. 1977 Feb;12(1):15–8.

44. Drayer BP, Wolfson SK, Reinmuth OM, Dujovny M, Boehnke M, Cook EE. Xenon enhanced CT for analysis of cerebral integrity, perfusion, and blood flow. Stroke. 1978 Apr;9(2):123–30.

45. Feuerlein S, Roessl E, Proksa R, Martens G, Klass O, Jeltsch M, et al. Multienergy Photon-counting K-edge Imaging: Potential for Improved Luminal Depiction in Vascular Imaging. Radiology. 2008 Dec 1;249(3):1010–6.

46. Abudurexiti A, Kameda M, Sato E, Abderyim P, Enomoto T, Watanabe M, et al. Demonstration of iodine K-edge imaging by use of an energy-discrimination X-ray computed tomography system with a cadmium telluride detector. Radiol Phys Technol. 2010 Jul 1;3(2):127–35.

47. PEGS4 User Manual [Internet]. [cited 2017 Mar 18]. Available from: http://www.fnal.gov/docs/products/egs4/pegs4.html

48. *173, 1.333 MeV. The latest collisional and radiative stopping powers of ICRU 37 (ICRU, 1984;* Duane et al., 1999*; Rogers et al., 1989*

49. International Commission on Radiation Units & Measurements. Tissue Substitutes in Radiation Dosimetry and Measurement (Report 44). Report No.: 44.

50. Woodard HQ, White DR. The composition of body tissues. Br J Radiol. 1986 Dec;59(708):1209–18.

51. Johns PC, Yaffe MJ. X-ray characterisation of normal and neoplastic breast tissues. Phys Med Biol. 1987 Jun 1;32(6):675–95.

52. EGSnrc C++ class library: Main Page [Internet]. [cited 2016 Aug 4]. Available from: http://nrc-cnrc.github.io/EGSnrc/doc/pirs898/index.html

53. Bohndiek SE, Cook EJ, Arvanitis CD, Olivo A, Royle GJ, Clark AT, et al. A CMOS active pixel sensor system for laboratory- based x-ray diffraction studies of biological tissue. Phys Med Biol. 2008 Feb 7;53(3):655.

54. Elshemey WM, Elsharkawy WB. Monte Carlo simulation of x-ray scattering for quantitative characterization of breast cancer. Phys Med Biol. 2009 Jun 21;54(12):3773.

55. Peplow DE, Verghese K. Measured molecular coherent scattering form factors of animal tissues, plastics and human breast tissue. Phys Med Biol. 1998 Sep 1;43(9):2431.

56. Griffiths JA, Royle GJ, Hanby AM, Horrocks JA, Bohndiek SE, Speller RD. Correlation of energy dispersive diffraction signatures and microCT of small breast tissue samples with pathological analysis. Phys Med Biol. 2007 Oct 21;52(20):6151.

57. Zhao W, Wan L, Zhang B, Zhang Q, Niu T. Energy Spectrum Extraction and Optimal Imaging via Dual-Energy Material Decomposition. ArXiv151207356 Phys. 2015 Oct;1–4.

58. N. Rezvani DA. OSCaR: An open-source cone-beam CT reconstruction tool for imaging research. Med Phys - MED PHYS. 2007;34(6).

59 Themes UFO. Tomographic Reconstruction in Nuclear Medicine | Radiology Key [Internet]. [cited 2017 Mar 6]. Available from: http://radiologykey.com/tomographic-reconstruction-in-nuclear-medicine/

60. Rivers M. Tutorial Introduction to X-ray Computed Microtomography [Internet]. [cited 2017 Mar 6]. Available from: http://www.mcs.anl.gov/research/projects/X-ray-cmt/rivers/tutorial.html

61. Canny J. A Computational Approach to Edge Detection. IEEE Trans Pattern Anal Mach Intell. 1986 Nov;PAMI-8(6):679–98.

62. R. Fisher, S. Perkins, A. Walker, E.Wolfart. Feature Detectors - Sobel Edge Detector [Internet]. [cited 2017 Mar 6]. Available from: http://homepages.inf.ed.ac.uk/rbf/HIPR2/sobel.htm

63. Magnotta VA, Friedman L. Measurement of Signal-to-Noise and Contrast-to-Noise in the fBIRN Multicenter Imaging Study. J Digit Imaging. 2006 Jun;19(2):140–7.

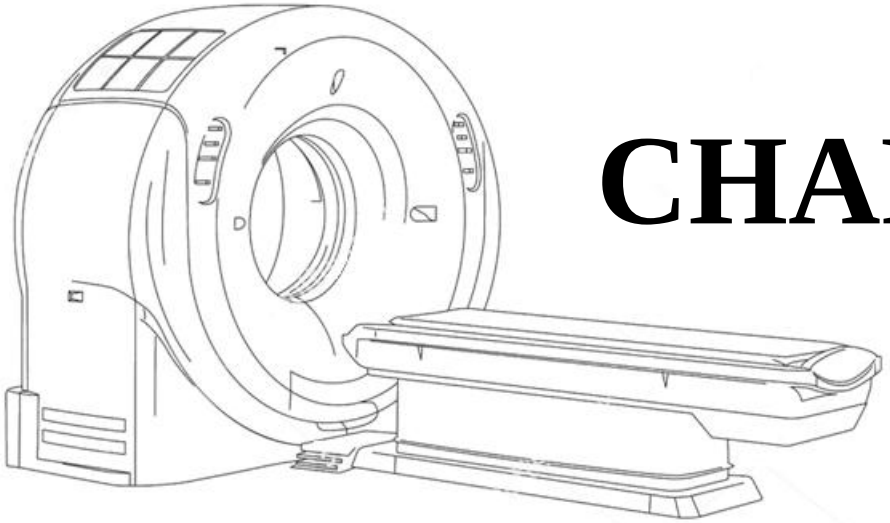

CHAPTER 5

Energy weighting to improve image quality

Table of Contents

5.1 Introduction

Photon counting detectors have been investigated for lesion detection in breast CT over the past few years.[1-5] One of the advantages is that this detector assigns equal weight to all the photons and optimal weighting schemes can be developed to maximise the CNR. These weighting schemes involve giving different energy bins different weights producing a combined image with a maximum CNR. Two methods can be employed and involve either weighting of the projection data in each energy bin before image reconstruction or weighting the images obtained at each energy bin interval and then combining them. In previous studies, projection-based energy weighting schemes have been applied to CT data.[6-10] The energy bins are weighted and combined before log normalisation and reconstruction. The signal from the detector is log normalised with a blank air scan as discussed in Chapter 4 Section 4.2.2. A CNR increase was found in these studies by assigning a higher weight to the images obtained from projection data for photons of lower energies.

Niederholder *et al*. first proposed an image-based energy weighting scheme with results comparable to projection-based energy weighting. They found a reduction in the cupping effect by applying the weighting after reconstruction and also an increase in the image quality.[11] The weighting is done after the first step of reconstruction by using the Downhill-Simplex method which is a trial algorithm that finds the optimum weighting function.[12] In image-based energy weighting, the weights are applied to the reconstructed images and then combined. In another study by Schmidt *et al*.[13] the weights are calculated analytically to maximise the CNR for a combined image obtained by a summation of individually weighted images obtained from multiple energy bins. Specific data regarding the projections or images are needed that is not always feasible to acquire. For example, the length of the contrast material in the phantom is needed for the projection-based weighting,[13] which is easy to obtain when dealing with a simple phantom with known inserts. It is however quite difficult

to obtain this length when looking at a breast phantom based on clinical data. The structures have random shapes, and the length will vary for each projection. For the currently proposed image-based optimal energy weighting method the reconstructed linear attenuation coefficients are needed for the material for which the CNR is calculated and for the background. These values are used to define the absolute contrast between the two materials mentioned. Depending on the reconstruction algorithm used and the processing of the images, the pixel values in the images may not represent the attenuation coefficients at all. In another study by Le *et al*.,[14] a spectral model was used for the calculation of the weighting factors for projection-based energy weighting. For the image-based energy weighting method, the effective linear attenuation coefficients were used that were calculated by using the material thicknesses. Both these studies are limited to phantom studies with simple geometries but are difficult to apply to other more complex geometries, such as the breast phantoms found in this study.

In this chapter an alternative method was explored that may be applicable to more complex cases. The first approach is a trial method without needing any prior information such as the effective attenuation coefficient or length of the contrast material. It is an image-based energy weighting method that uses random weights and the images from several energy bins to optimise the CNR. This method is further improved by using the weights based on the CNRs of the different energies used. Weighted energy-resolved data is a further improvement on photon-counting detectors and aids in constructing an image with the highest CNR achievable.[6,15]

5.2 Methods & Materials

Multiple reconstructed images were obtained for energies ranging from 20 keV to 65 keV as seen in Chapter 4.

Two alternative methods of image-based energy weighting were explored to improve the CNRs found in Chapter 4.

5.2.1 Method 1: Trial method

The first method is based on a trial method in IDL. The lack of requiring additional information such as the effective linear attenuation coefficients or length of structures may make this method more applicable to complex phantoms. No user input is required during the calculation of the weighting factors and the time of computation depends on the number of trials. A typical number of trials could be 1000.

For a series of images in the breast phantom, the first step is to determine random weights for each image and their associated energy bin. Each image is then multiplied by its own random weight factor, and all of them are summed to form a combined image. These weight factors are arbitrary numbers between 0 and 1 and are calculated with the RANDOMU function in IDL.[16] The ROIs values are then determined as explained in Chapter 4, and the CNRs are calculated with Equation 4.3. The CNR of the combined image calculated with Equation 5.1[14] is seen below.

$$CNR_{tot} = \frac{\sum_{e=1}^{t} w_e C_e}{\left(\sum_{e=1}^{t} w_e^2 \sigma_b^2\right)^{1/2}} \qquad 5.1$$

Where C_e is the absolute contrast between the malignant, ROI_m, and glandular tissue, ROI_g for each image for all the different energies.

$$C_e = ROI_m - ROI_g \qquad 5.2$$

The standard deviation in the background of each of these images is given by σ_b, and the weighting factor for each energy is w_e. An example of the background ROI positions is seen below and also in Chapter 4.

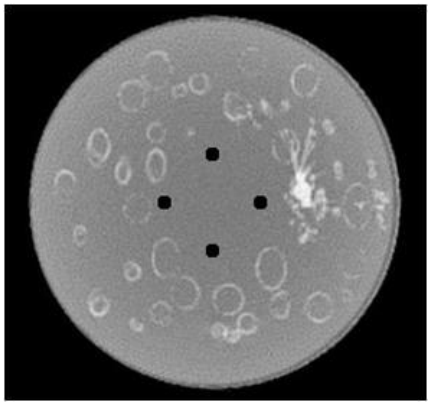

Figure 4.18: Positions of the background ROI in uniform adipose tissue.

A schematic of the process is given in Figure 5.1 below. The CNR_{tot} was calculated, and the maximum value was saved, $CNR_{\max(tot)}$. The corresponding weighting factors of the final $CNR_{\max(tot)}$ were considered as being the most optimal for the specific set of images. The number of trials depends on the user and the computation power available. This is considered as a post-processing procedure and does not affect the time the patient needs to be imaged. On a standard computer with a 2.4 GHz processor, it can take up to a few hours. This time can be reduced with the use of a supercomputer with parallel processing that has a high level of computing performance.

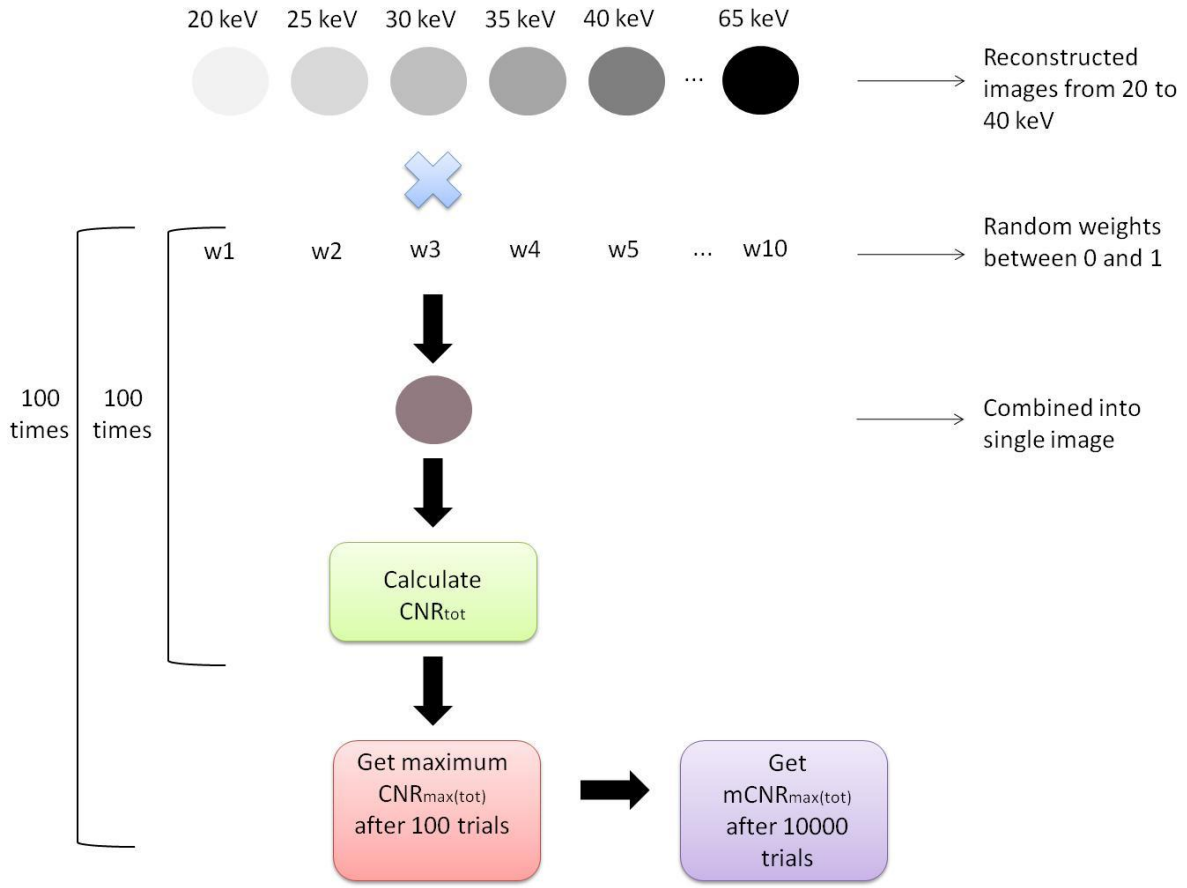

Figure 5.1: Schematic of the iterative process of maximising the CNR for a set of images acquired at different energies.

This weighting scheme was applied to all the images acquired in Chapter 4, and the results are seen in the next section. The combined CNR was calculated with weighting factors of 1 for each energy and then compared to that with weighting factors calculated with the iterative method

5.2.2 Method 2: CNR based constraints

As seen in Chapter 4, the lower energies have higher CNRs than the higher energies. This concept has been used in previous studies to determine weighting factors as discussed in the introduction of this chapter. An improvement on the method explored in Section 5.1 was done by also utilising the CNRs but without needing any prior information regarding the images.

The weighting factors for the different energy bins were devised from the CNRs acquired in Chapter 4. This ensured that the lower energies obtain high weighting factors that decrease as the energy increases. The energy with the highest CNR gets a weighting factor of 1 and the rest of the weighting factors are determined with Equation 5.3 below.

$$w_i = \left(\frac{CNR_i}{CNR_{\max}} \right) \times 1 \qquad 5.3$$

Where w_i is the weighting factor for energy bin *i*, CNR_i is the CNR for energy bin *i* and $CNR_{\max}$ is the maximum CNR out of all the energies. If bin *i* has a CNR value, CNR_i, of e.g 5.2 and the maximum CNR, $CNR_{\max}$, for all the bins is 8 then the weighting factor for bin *i* will be:

$$w_i = \left(\frac{5.2}{8} \right) \times 1 = 0.65 \qquad 5.4$$

The same method was followed for the images containing the iodine contrast.

5.3 Results & Discussion

The following results up to Figure 5.4 show the distribution of the CNRs found with different amounts of trials. This was done to determine the effect of the number of trials on the CNR.

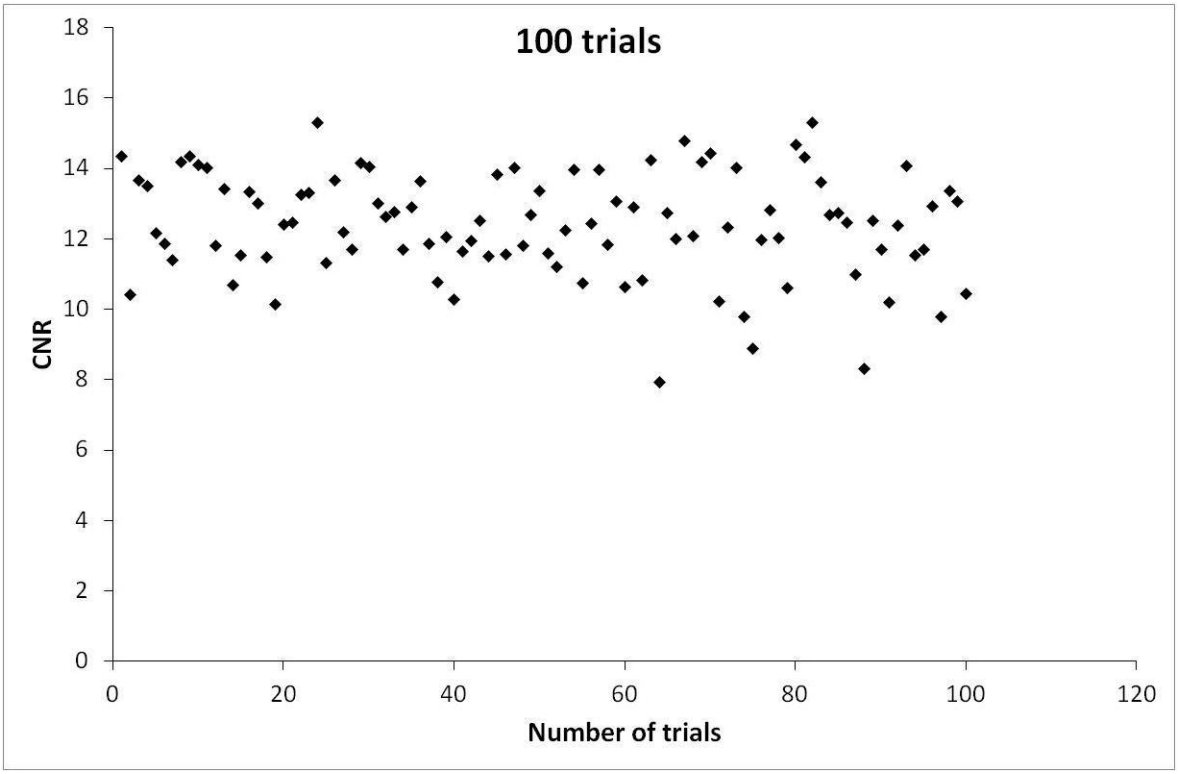

Figure 5.2: The CNR distribution after 100 trials.

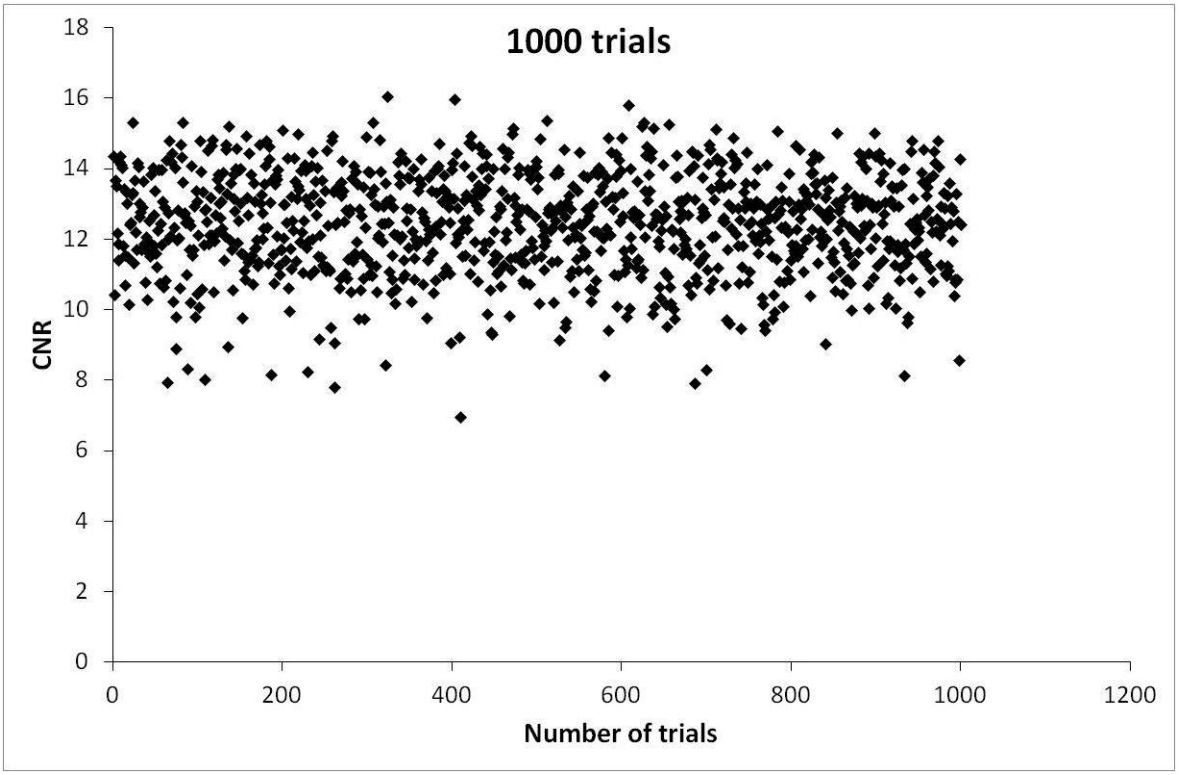

Figure 5.3: The CNR distribution after 1000 trials.

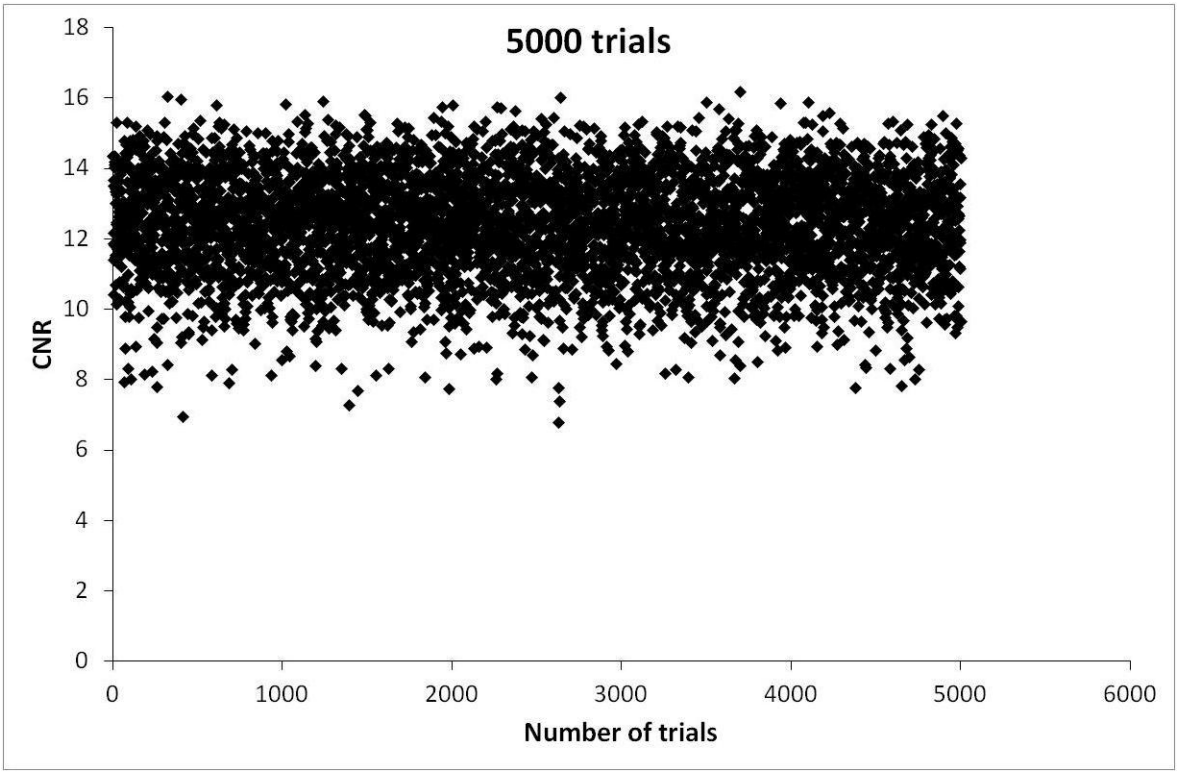

Figure 5.4: The CNR distribution after 5000 trials.

It can be seen from the figures above that the resulting CNRs are completely random and that no number of trials will result in an optimal solution. As seen in Figure 5.5 below, more trials will increase the frequency of CNRs between 7 and 17 but will not necessarily result in a higher CNR.

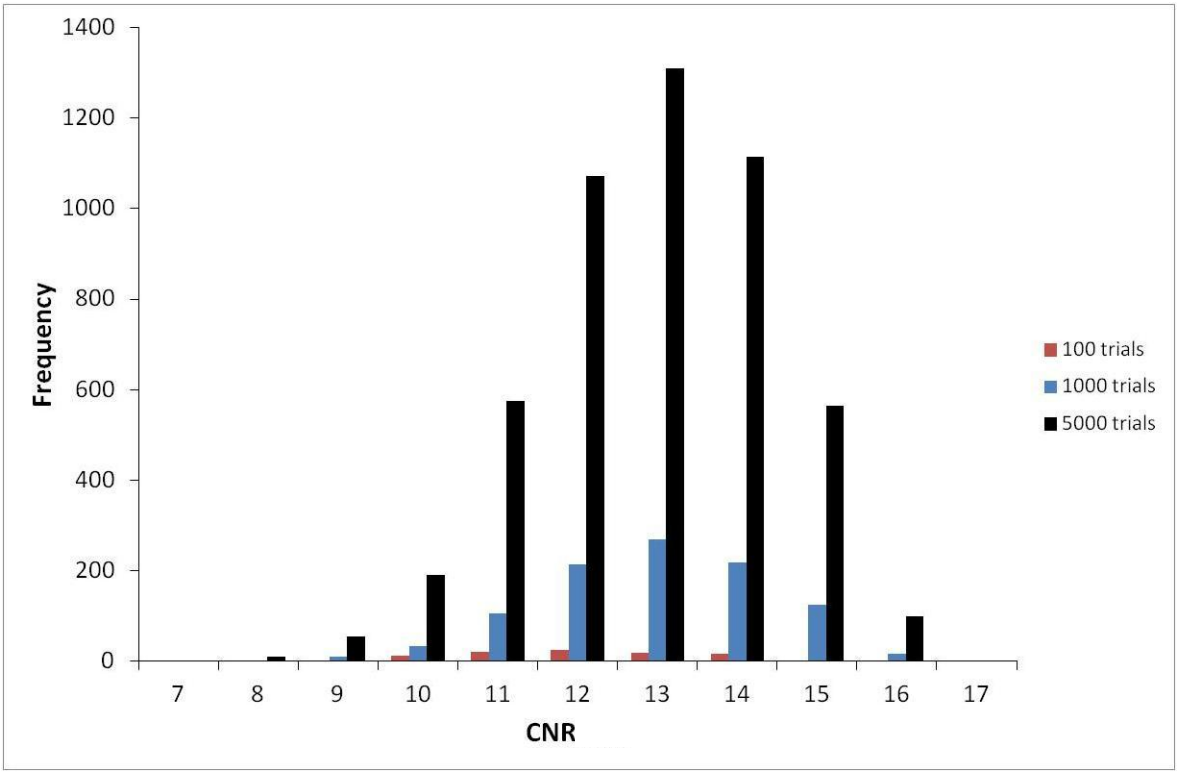

Figure 5.5: The CNR Gaussian distribution after 5000 trials.

The following results up to Figure 5.13 include the CNRs and weighting factors obtained after 100 trials.

5.3.1 Phantom 1

This phantom consisted of 89% glandular tissue and 11% adipose tissue as discussed in Chapter 4. In the Figure below 100 CNR_{tot} values with the maximum and minimum values are seen. Figure 5.8 shows the weighting factors for the maximum CNR and the minimum CNR after 100 trials. These weighting factors are used to scale the individual images obtained from projection data at the relevant energy bins and then summed to yield the image with either the lowest or the highest CNR.

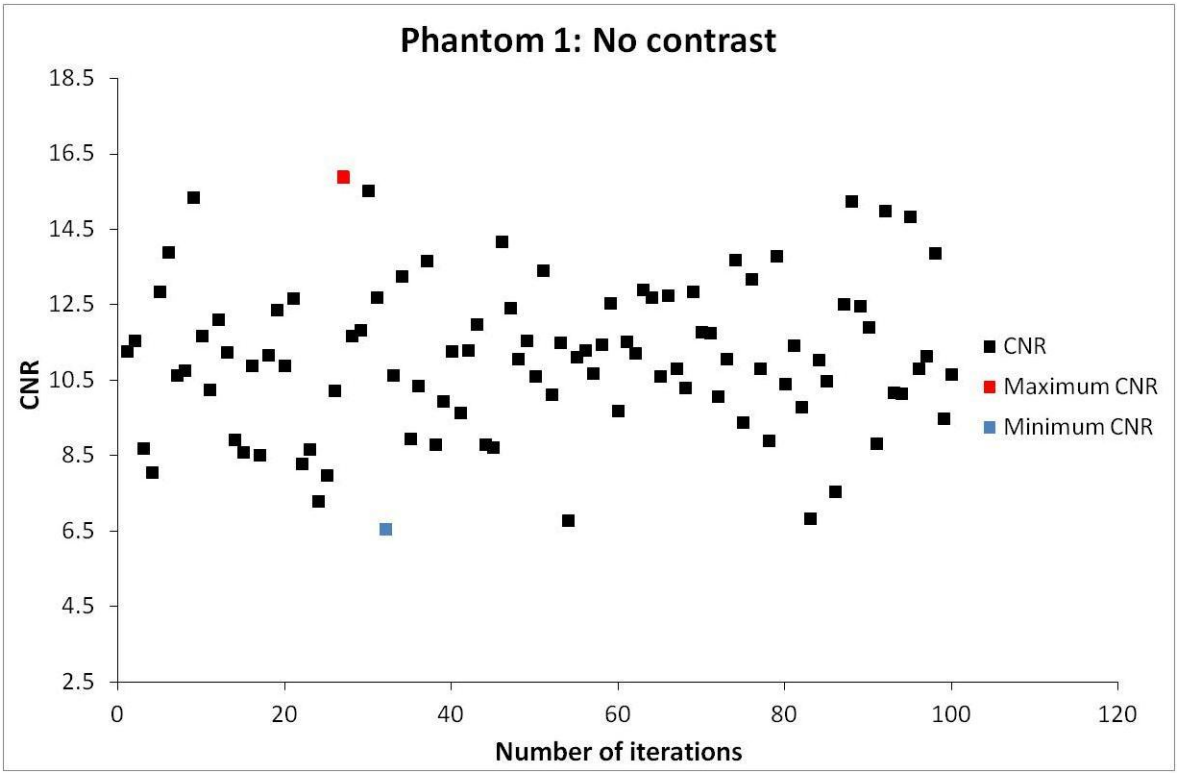

Figure 5.6: The combined CNRs obtained with 100 trials and 100 sets of weighting factors. The error bars for the CNRs are smaller than the symbol size.

The histogram of the CNR distribution is seen below in Figure 5.7.

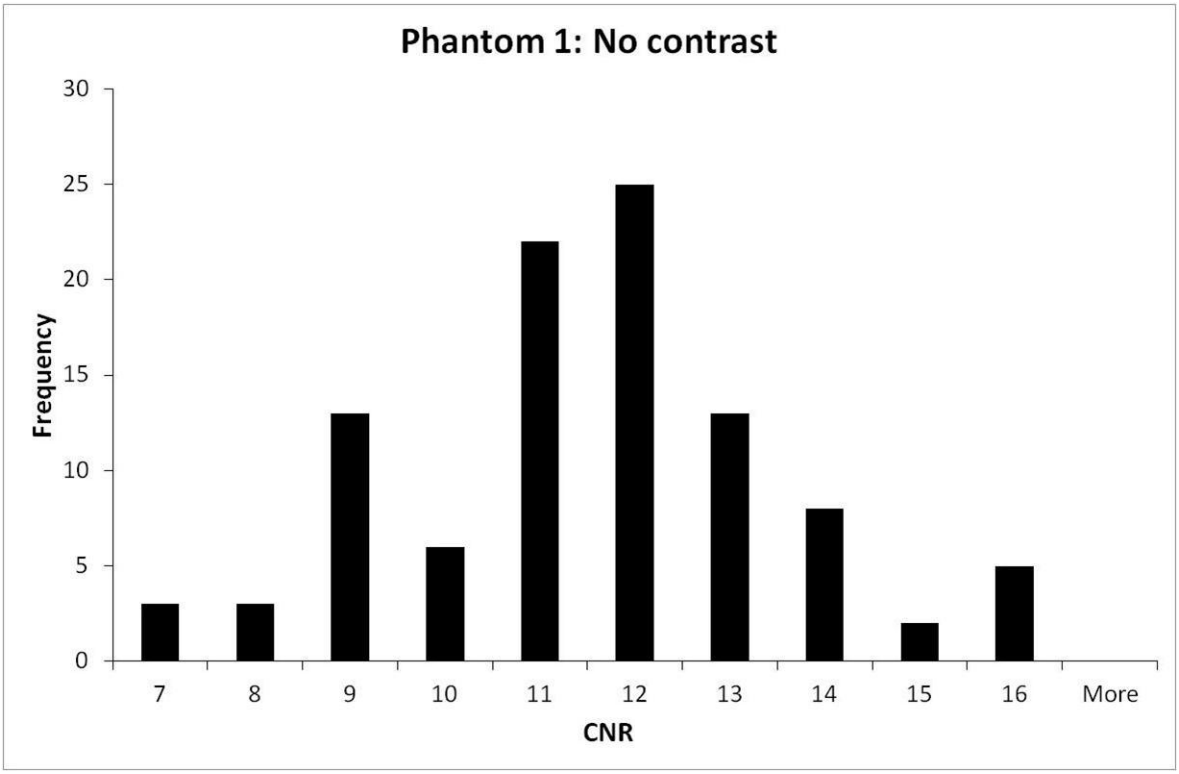

Figure 5.7: A histogram distribution of the CNRs.

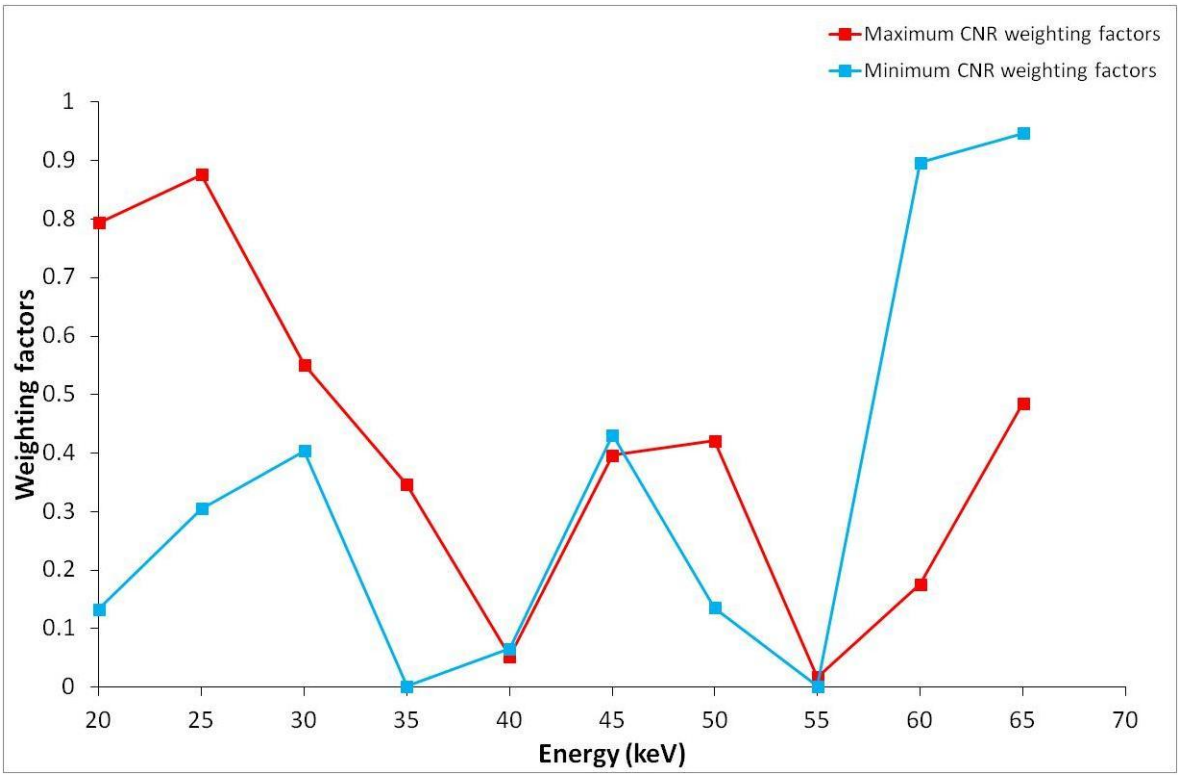

Figure 5.8: The weighting factors for the maximum CNR and the minimum CNR after 100 trials.

In Figure 5.6 the maximum CNR after 100 trials was 16.8 ± 0.125 and the minimum CNR was 6.57 ± 0.102. This was calculated in the resulting images from weighting factors obtained in Figure 5.8. For the maximum CNR, the highest weight was assigned to the second lowest energy. For the minimum CNR, the highest weight was assigned to the highest energy with the lowest CNR.

The following results were obtained for phantom 1 with 0.8mg/mL iodine contrast.

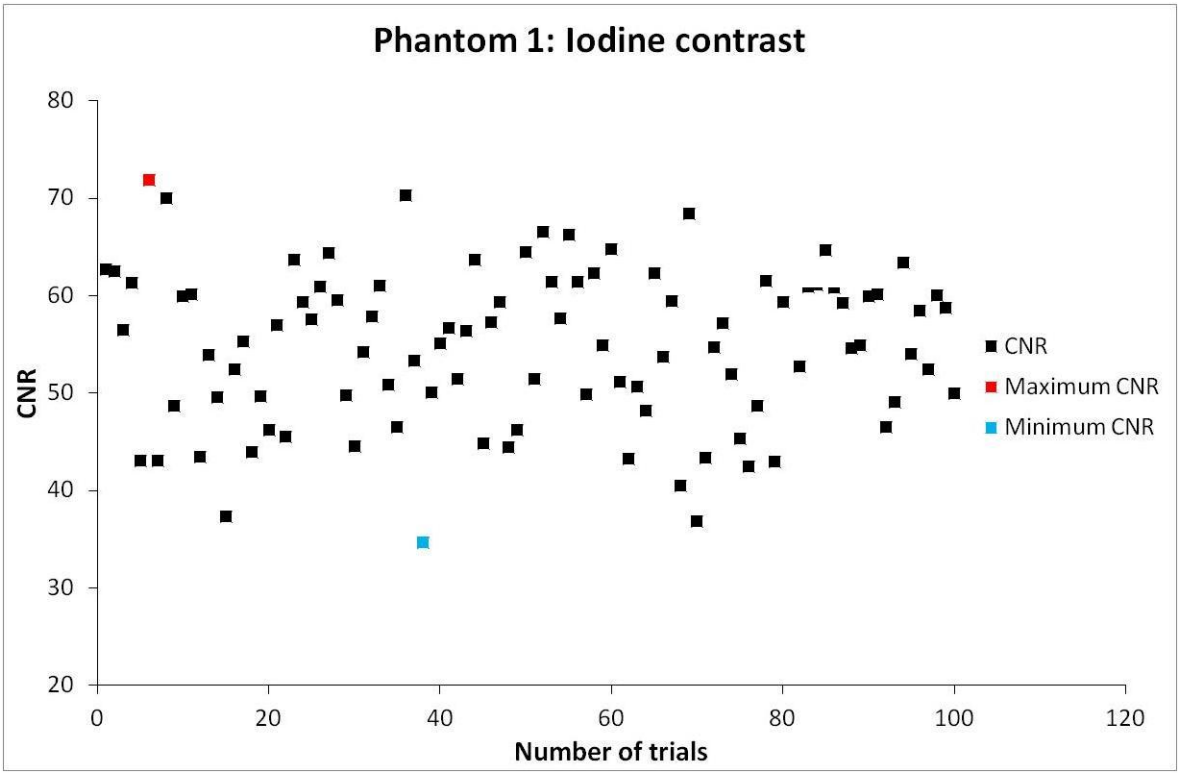

Figure 5.9: The combined CNRs obtained with 100 trials and 100 sets of weighting factors for the phantom containing iodine contrast. The error bars for the CNRs are smaller than the symbol size.

The histogram of the CNR distribution is seen below in Figure 5.10.

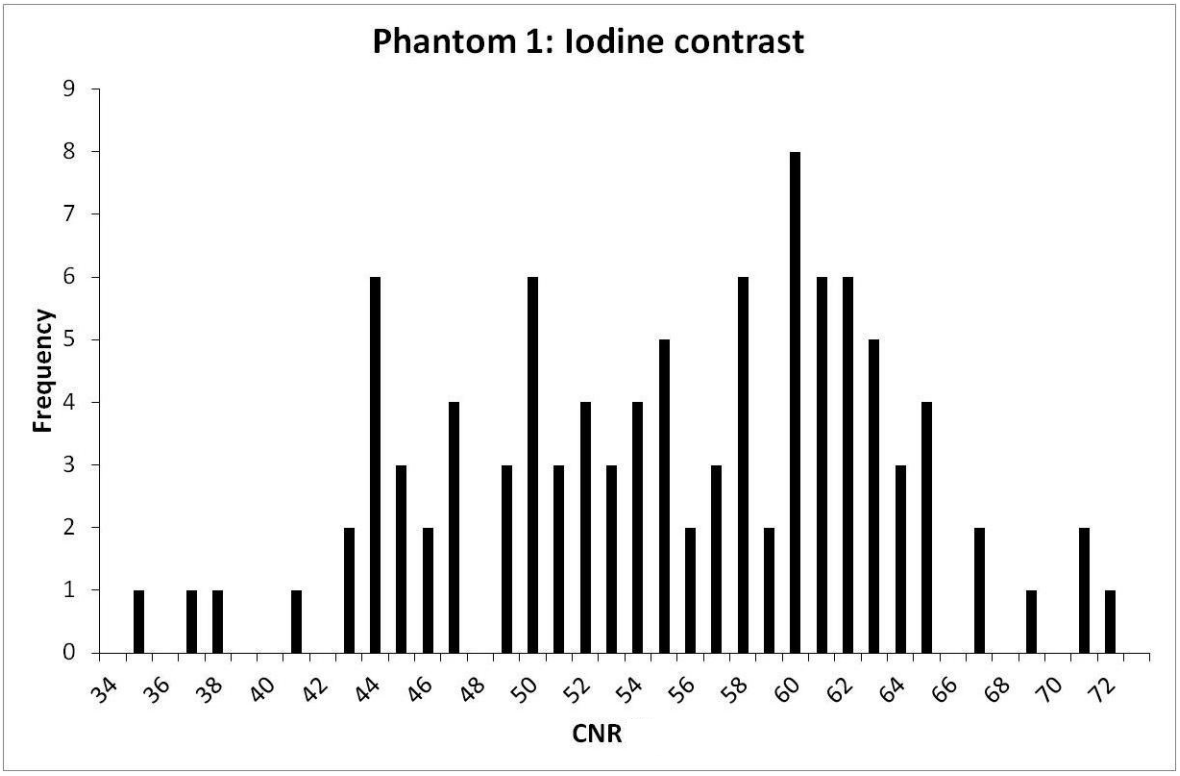

Figure 5.10: A histogram distribution of the CNRs.

Figure 5.11 shows the weighting factors that give rise to the maximum and minimum CNR images respectively.

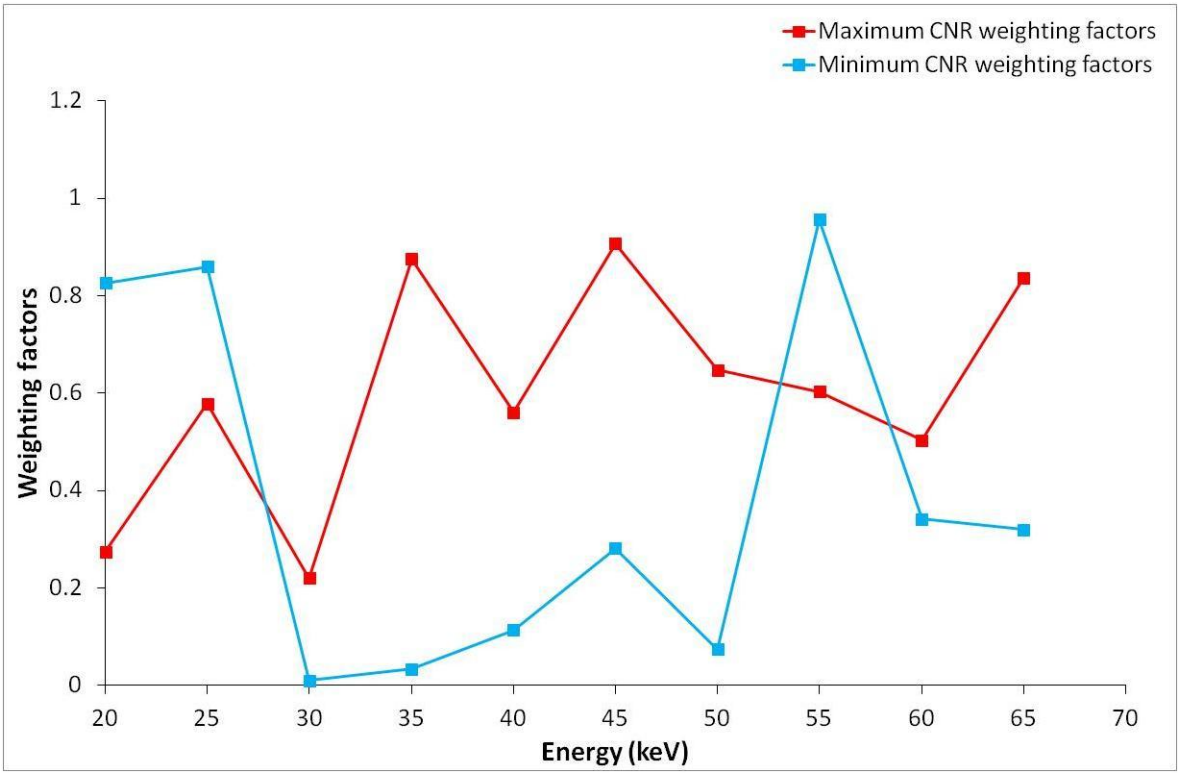

Figure 5.11: The weighting factors for the maximum CNR and the minimum CNR for the phantom containing iodine contrast.

For the maximum combined CNR of 71.87 ± 0.256, the highest weighting factor was obtained for the 35 keV slightly above the K-edge absorption peak and also in the 45 keV bin. For the minimum CNR of 34.72 ± 0.312, the 35 keV has a very low weighting factor that will result in an overall low CNR.

5.3.2 Phantom 2

This phantom consisted of 71% glandular tissue and 29% adipose tissue as discussed in Chapter 4. In the Figure below 100 CNR_{tot} values with the maximum and minimum values are seen. Figure 5.14 shows the weighting factors for the maximum CNR and the minimum CNR.

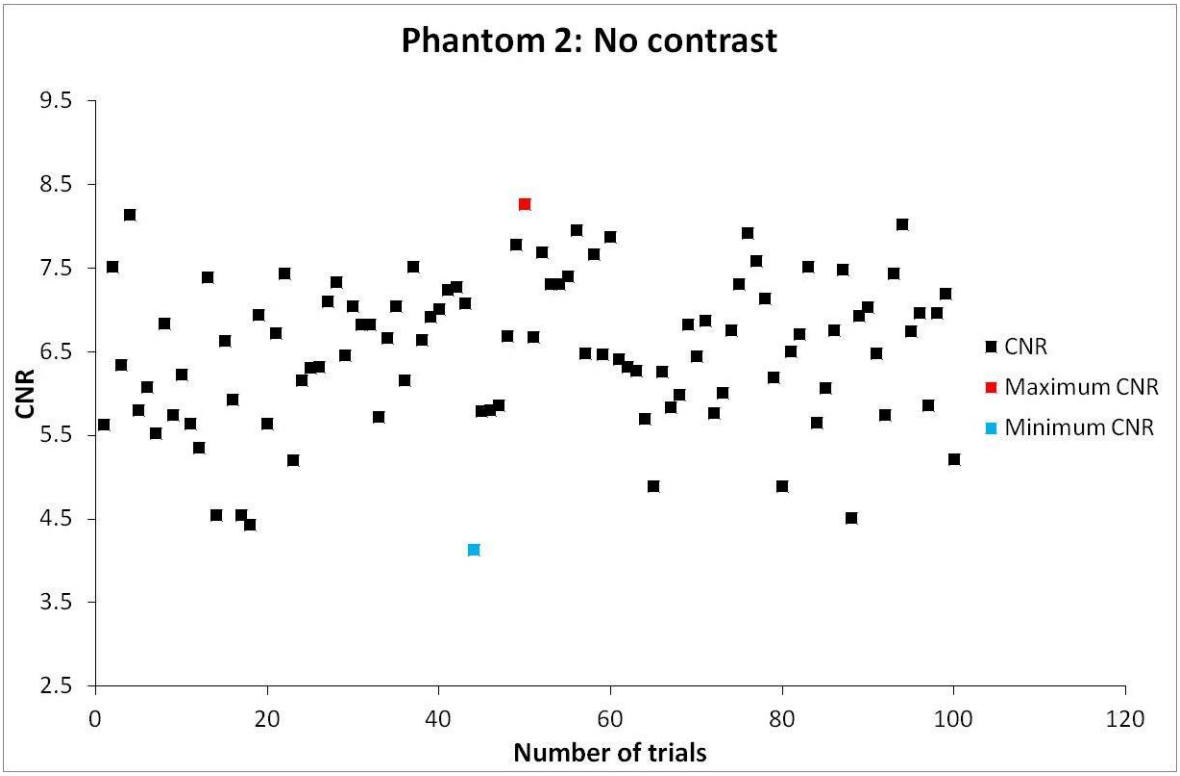

Figure 5.12: The combined CNRs obtained with 100 trials and 100 sets of weighting factors for Phantom 2. The error bars for the CNRs are smaller than the symbol size.

The histogram of the CNR distribution is seen below in Figure 5.13.

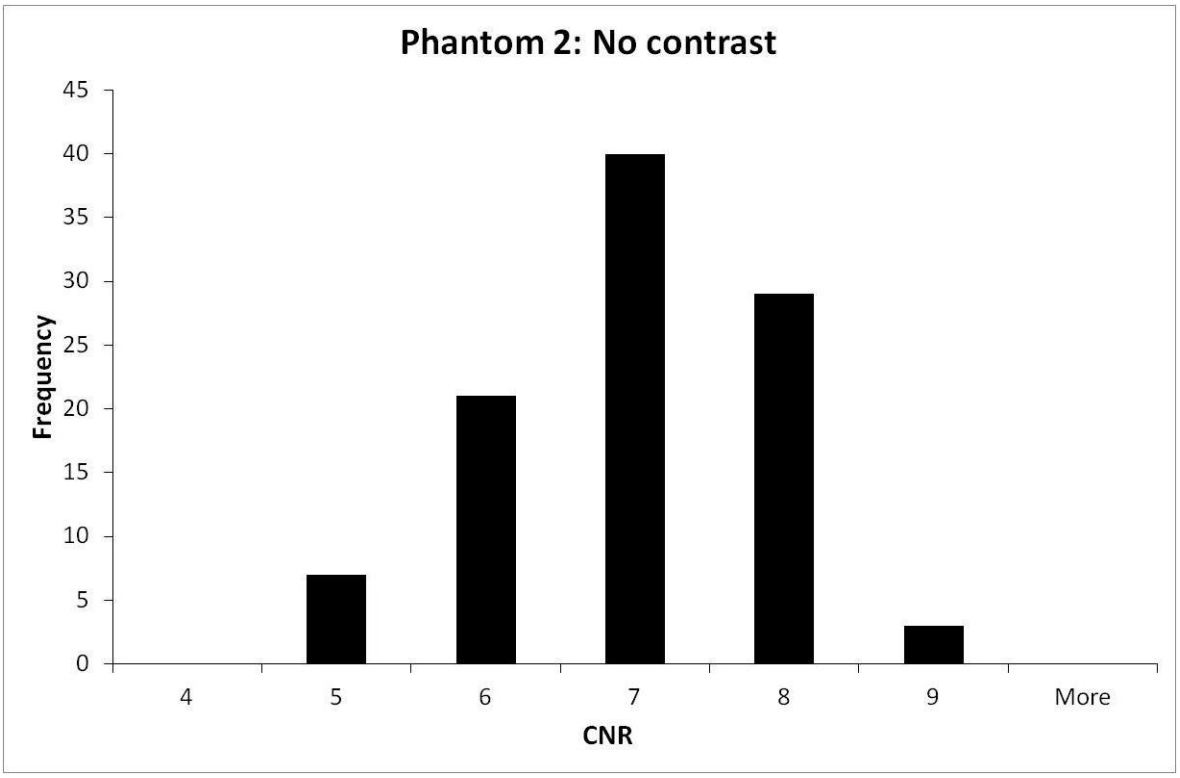

Figure 5.13: A histogram of the distribution of the CNRs.

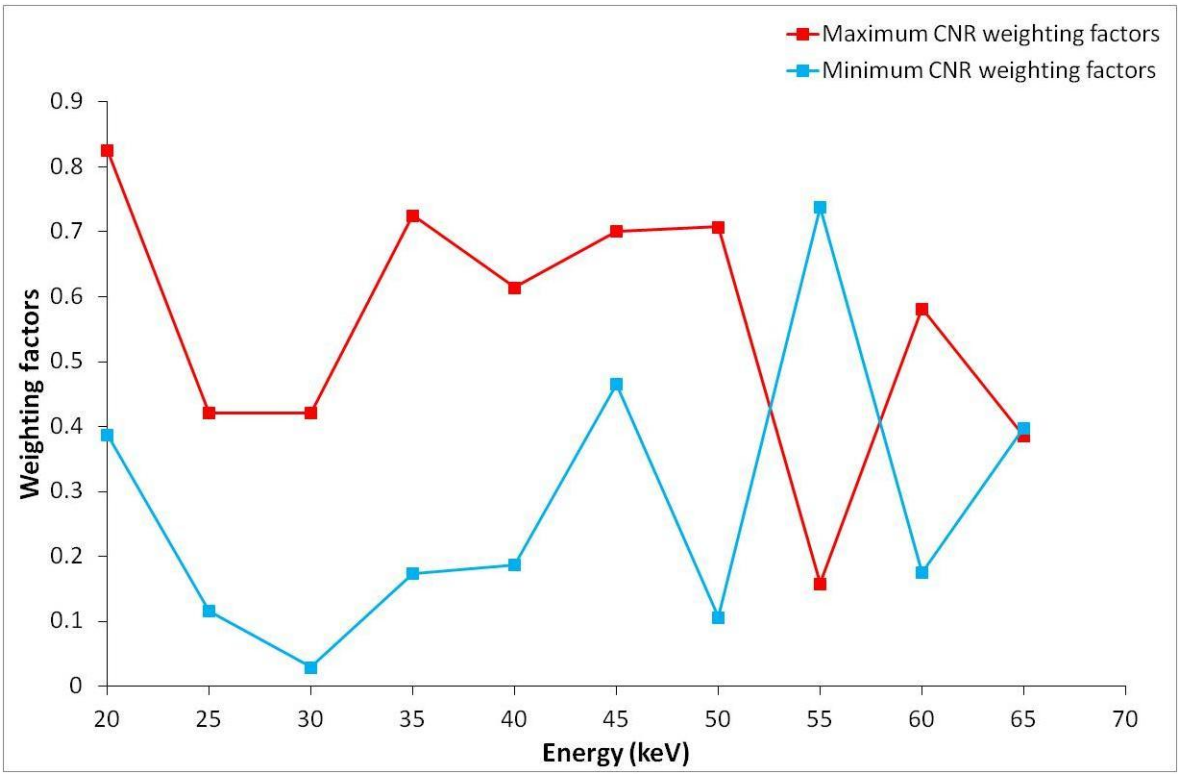

Figure 5.14: The weighting factors for the maximum CNR and the minimum CNR.

The maximum combined CNR after 100 trials were 15.63 ± 0.122 and the minimum combined CNR was 4.13 ± 0.145.

The following results were obtained for phantom 2 with 0.8mg/mL iodine contrast.

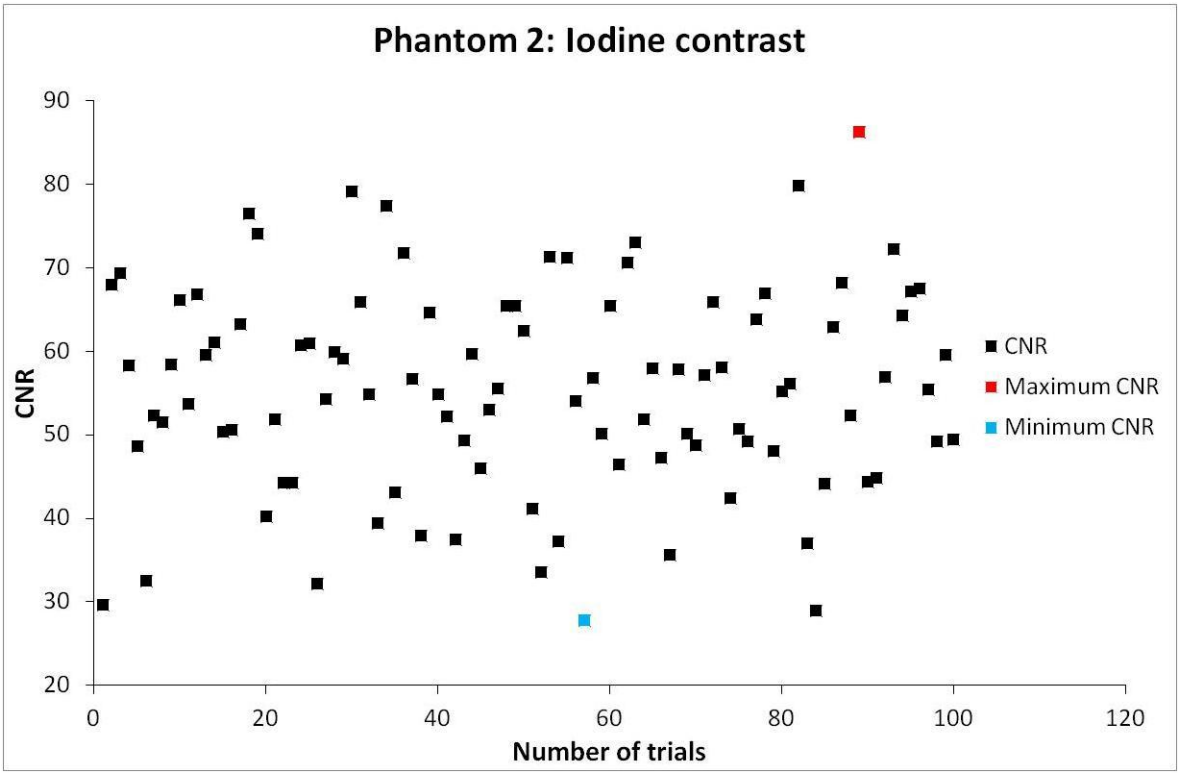

Figure 5.15: The combined CNRs obtained with 100 trials and 100 sets of weighting factors for the phantom containing iodine contrast. The error bars for the CNRs are smaller than the symbol size.

The histogram of the CNR distribution is seen below in Figure 5.16.

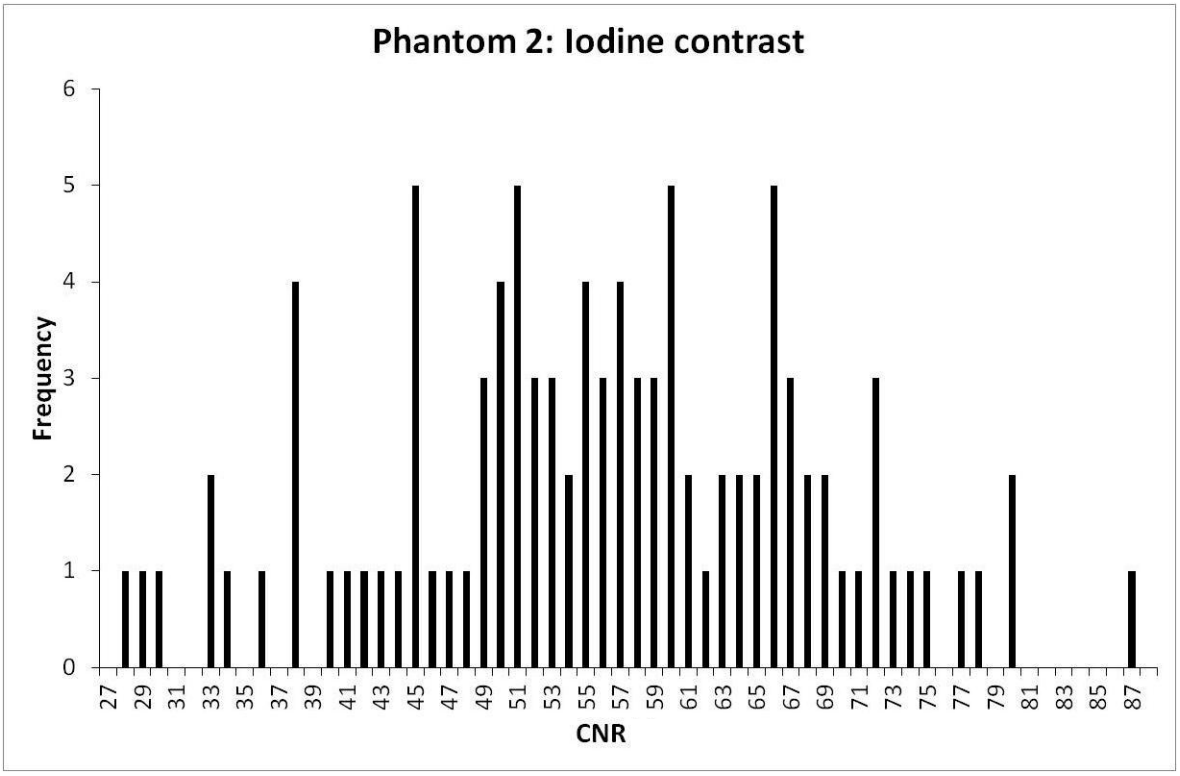

Figure 5.16: A histogram of the distribution of the CNRs.

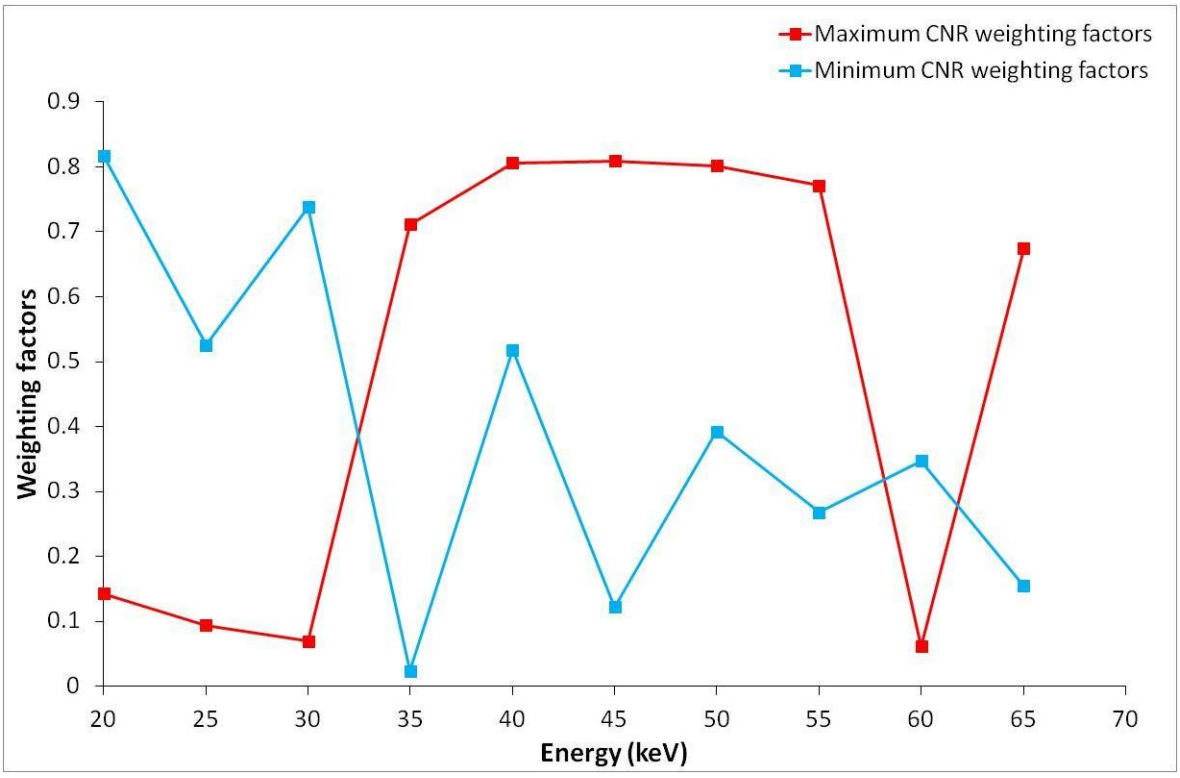

Figure 5.17: The weighting factors for the maximum CNR and the minimum CNR for the phantom containing iodine contrast.

For the minimum CNR of 27.84 ± 0.105, the lowest weighting factor occurs at the 35 keV just after the K-edge absorption peak. The highest CNR of 86.28 ± 0.201 has a high weighting factor at 35 keV and the lowest one at a high energy of 60 keV.

5.3.3 Phantom 3

This phantom consisted of 58% glandular tissue and 42% adipose tissue as discussed in Chapter 4. In Figure 5.18 below 100 CNR_{tot} values with the maximum and minimum values are seen. Figure 5.20 shows the weighting factors for the maximum combined CNR and the minimum combined CNR.

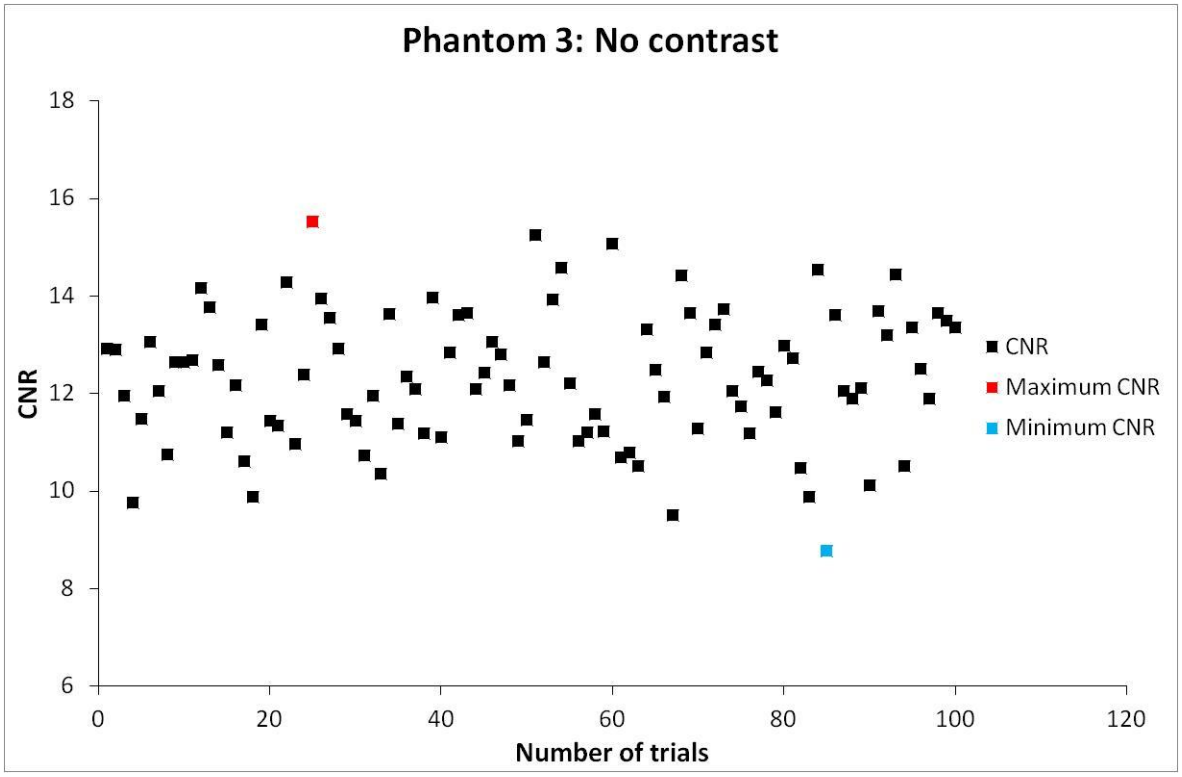

Figure 5.18: The combined CNRs obtained with 100 trials and 100 sets of weighting factors. The error bars for the CNRs are smaller than the symbol size.

The histogram of the CNR distribution is seen below in Figure 5.19.

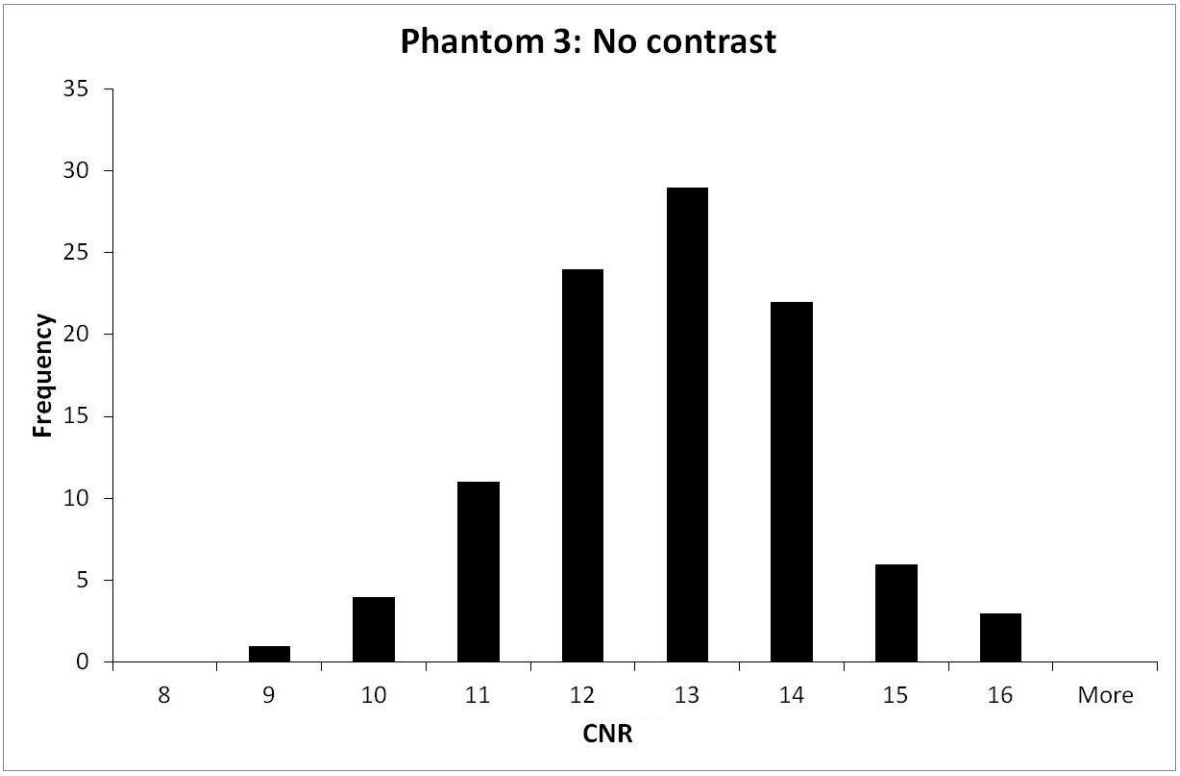

Figure 5.19: A histogram distribution of the CNRs.

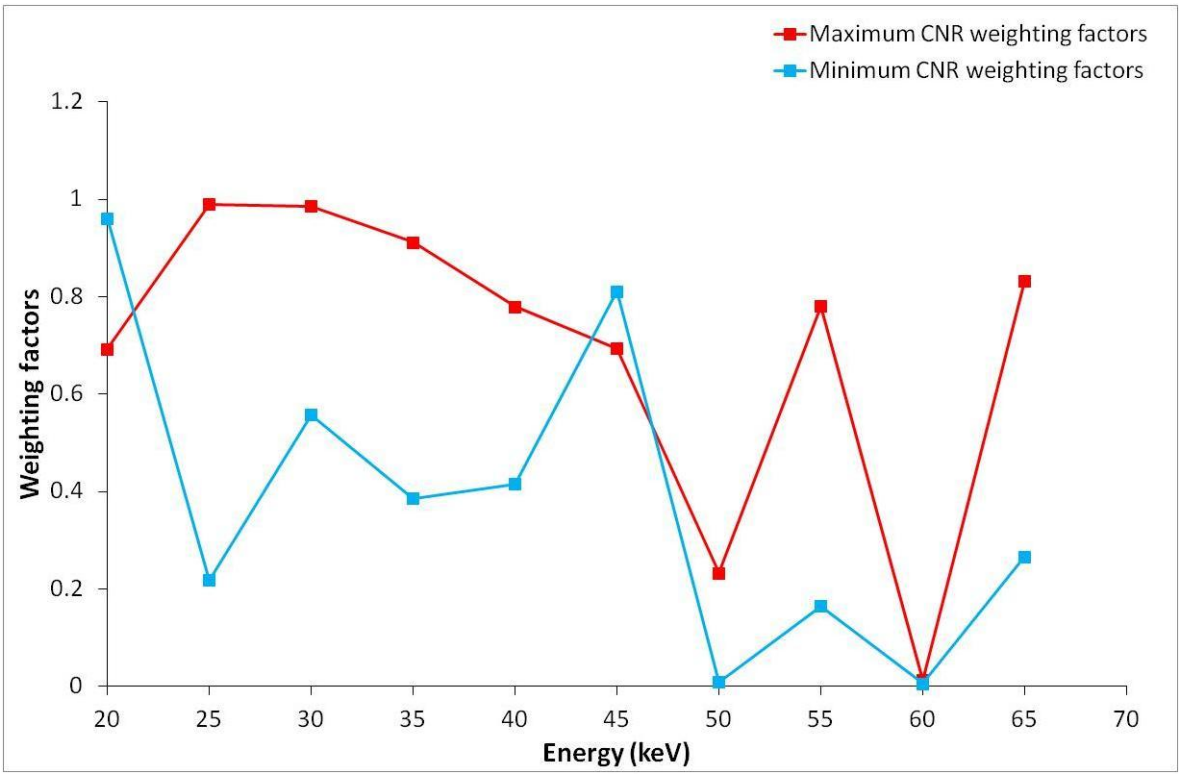

Figure 5.20: The weighting factors for the maximum CNR and the minimum CNR.

The maximum combined CNR after 100 trials were 15.53 ± 0.134 and the minimum combined CNR was 8.79 ± 0.215. The weightings factors for the maximum CNR correlate

well with that suggested in the literature except for the high weighting factors at 55 and 65 keV.

The following results were obtained for phantom 3 with 0.8mg/mL iodine contrast.

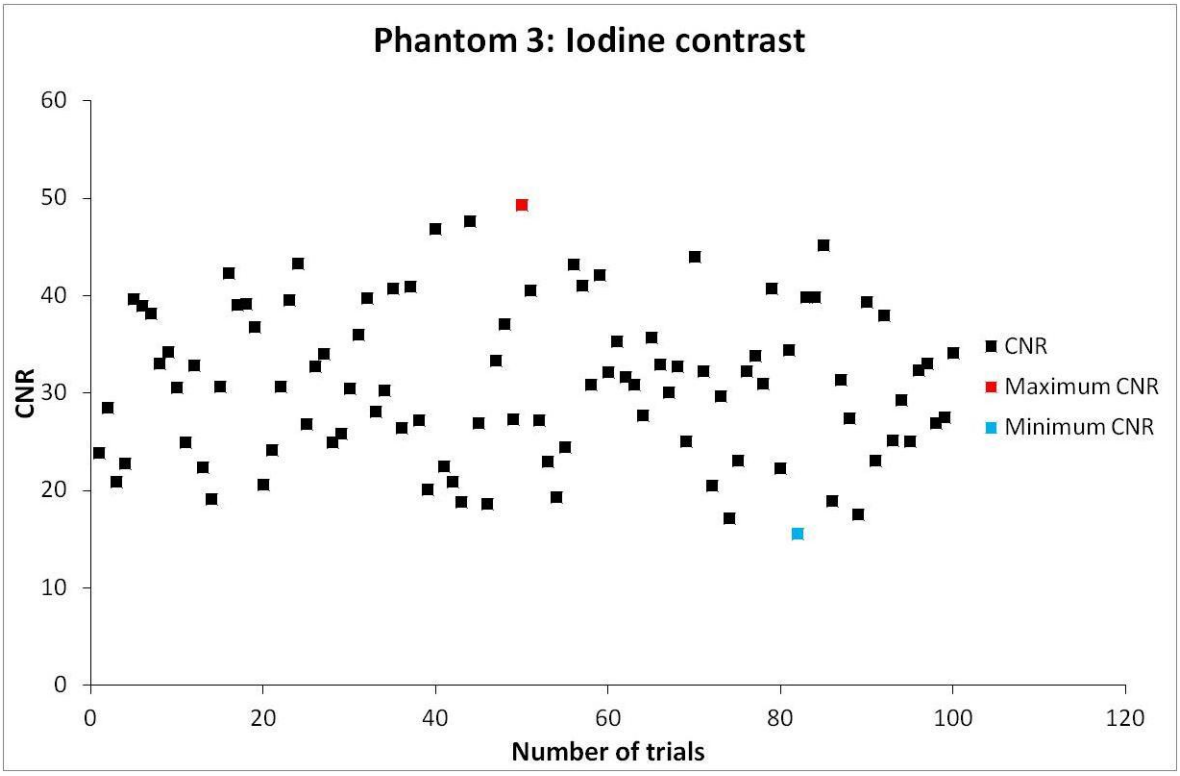

Figure 5.21: The combined CNRs obtained with 100 trials and 100 sets of weighting factors for the phantom containing iodine contrast. The error bars for the CNRs are smaller than the symbol size.

The histogram of the CNR distribution is seen below in Figure 5.22.

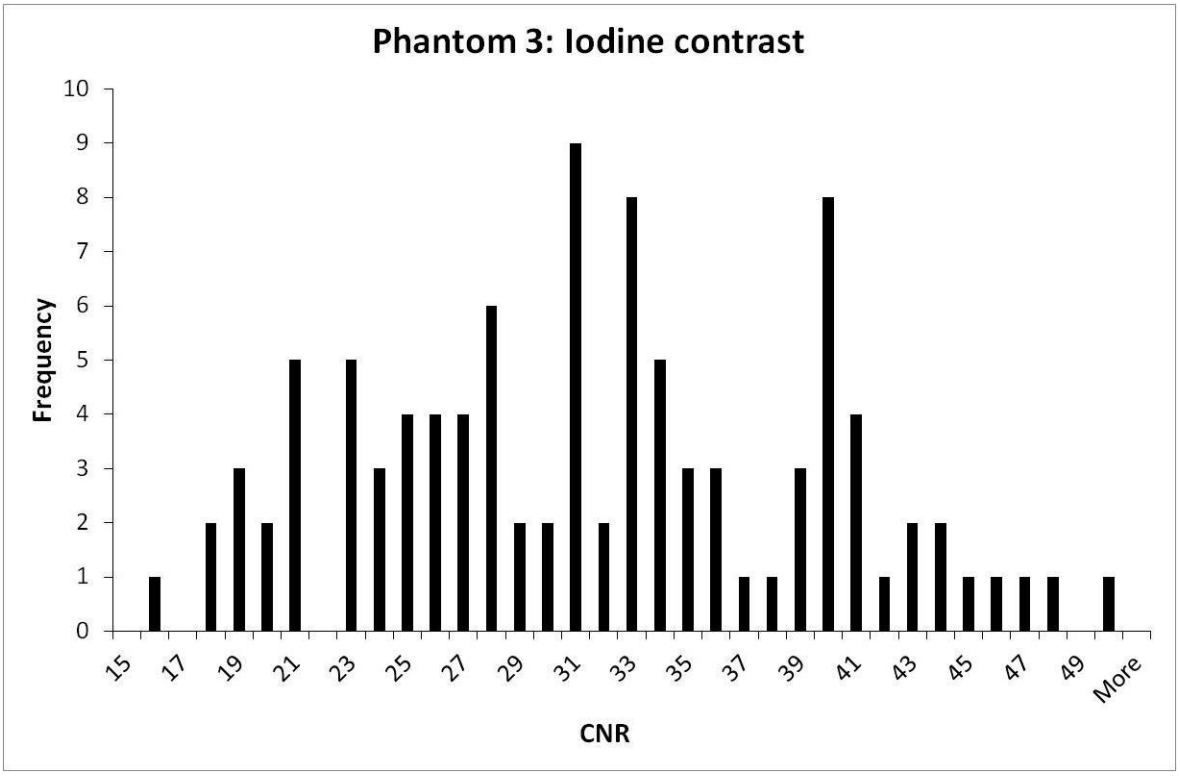

Figure 5.22: A histogram distribution of the CNRs.

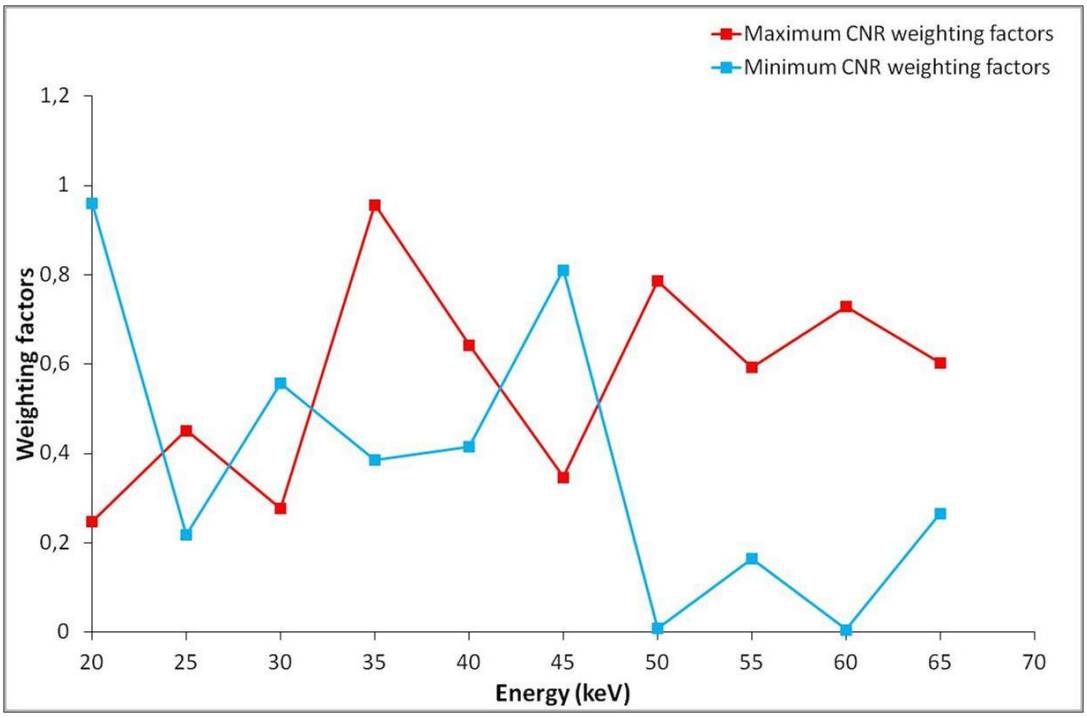

Figure 5.23: The weighting factors for the maximum CNR and the minimum CNR for the phantom containing iodine contrast.

The highest weighting factor for the maximum CNR of 49.31 ± 0.115 occurs just above the K-edge absorption peak. The highest weighting factors for the minimum CNR of 15.57 ± 0.238 are at the lower energy of 20 keV and 45 keV which will lead to a suppressed CNR.

The weighting factors after 10000 trials for the three phantoms are seen below in Figure 5.24.

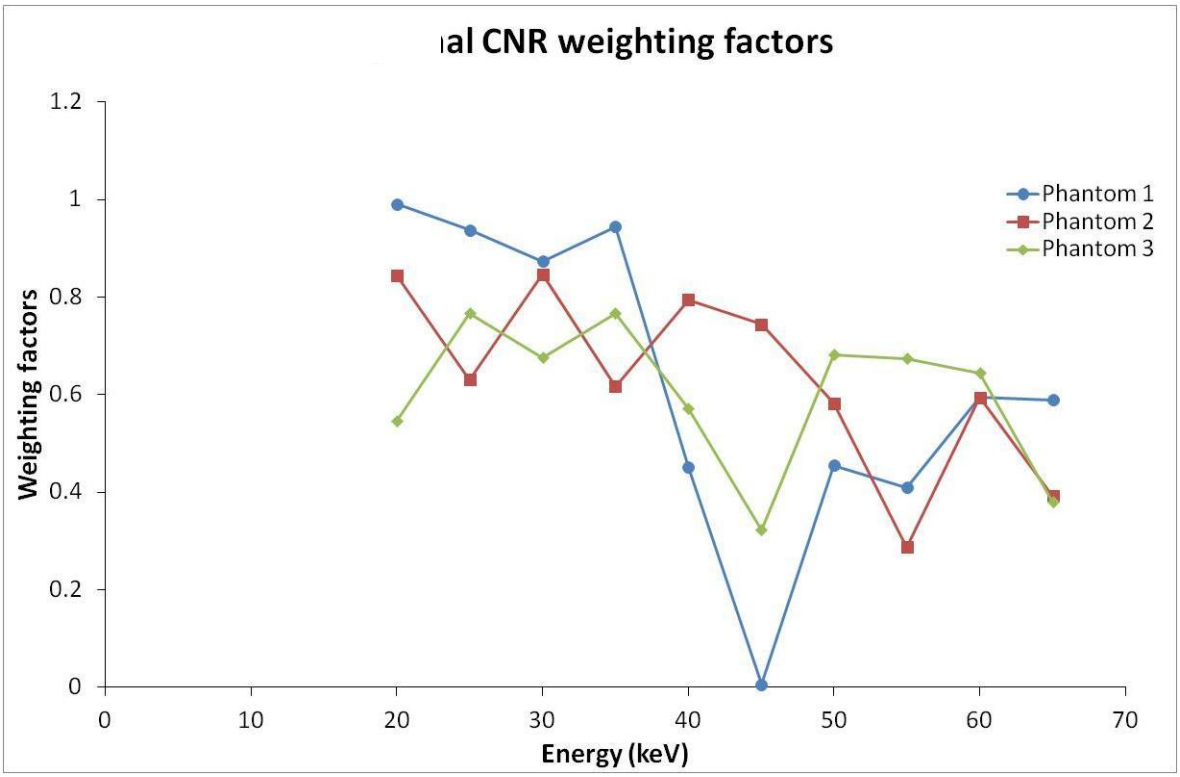

Figure 5.24: The optimal weighting factors after 10000 trials for the three phantoms.

It is seen in Figure 5.24 that for even a large number of trials large weights are sometimes given to higher energies as seen for phantom 3. This might lead to a less optimal CNR because the higher energies have smaller CNR.

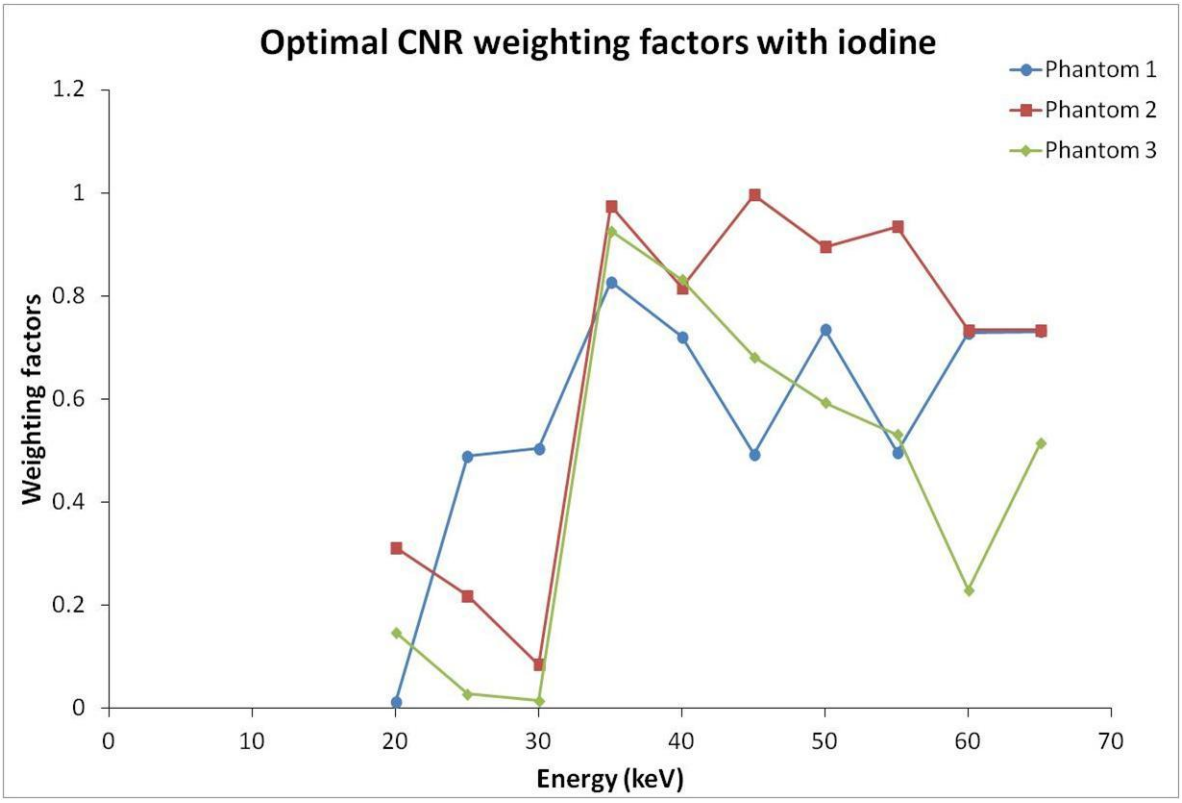

Figure 5.25: The optimal weighting factors for the iodine after 10000 trials for the three phantoms.

The maximum weighting factors are given to the 35 keV energy that is just above the K-edge of iodine. Lower weights are given to the lower energies, and the weighting factors decrease as the energy increases above 35 keV.

It can be seen from the above figures that if larger weights are applied to the lower energies, higher CNRs are obtained. The above method is however not ideal since low weights are sometimes applied to the lower energies and vice versa for the higher energies. Even though no prior information is needed for this method, the number of trials needed for an optimal solution is unclear. High or low CNRs are obtained with this iterative method. A further improvement on this method, as discussed in Section 5.2.2, is needed to make it more feasible to determine the optimal weighting factors.

5.3.4 Method 2: Results

The following weighting factors were obtained for the different phantoms by using Equation 5.3.

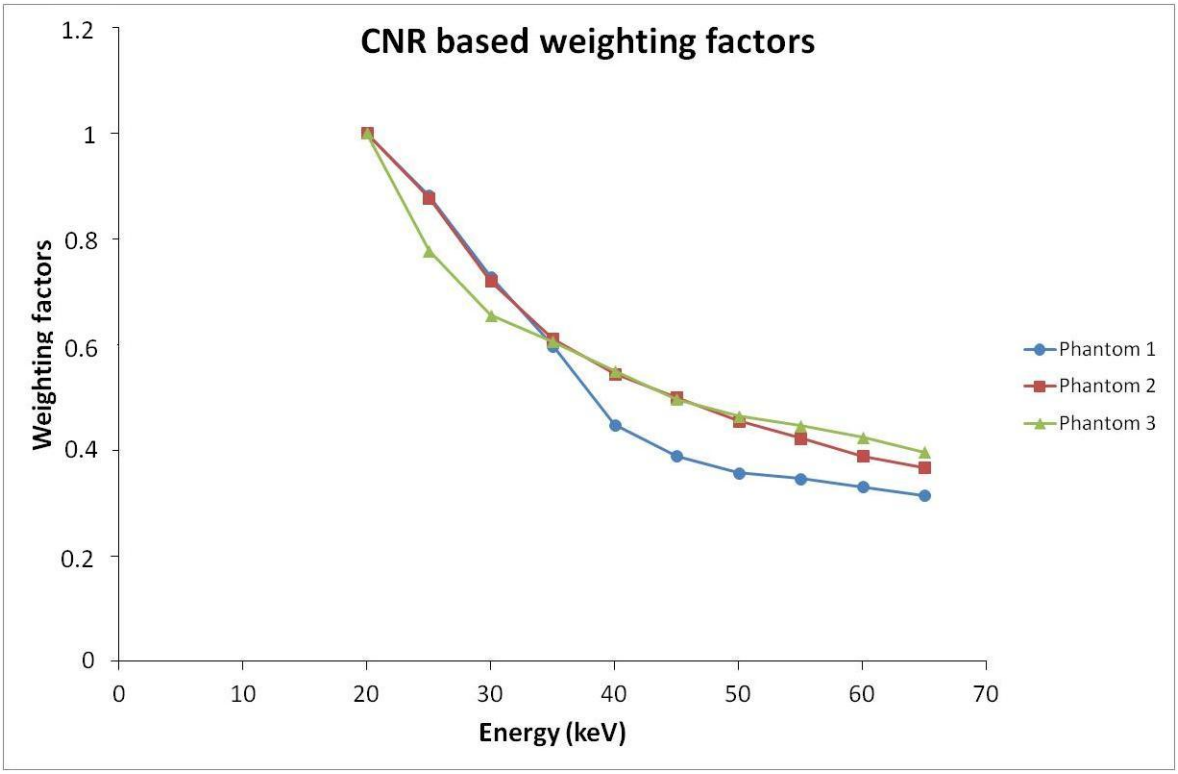

Figure 5.26: The weighting factors based on the CNRs

In comparison to Figure 5.24, the lowest energy with the highest CNR, now has the highest weighting factor. The CNRs decrease as the energy increases, so does the weighting factors according to Equations 5.3 and 5.4. This will lead to better CNRs as those seen in Figure 5.25.

For the iodine case, the maximum weight was given to 35 keV since this is the energy bin with the highest CNR. The 20 keV had the lowest CNR and weighting factor, gradually increasing up to 35 keV. For energies 40 keV to 65 keV, the weighting factors decreased as seen in Figure 5.23 below.

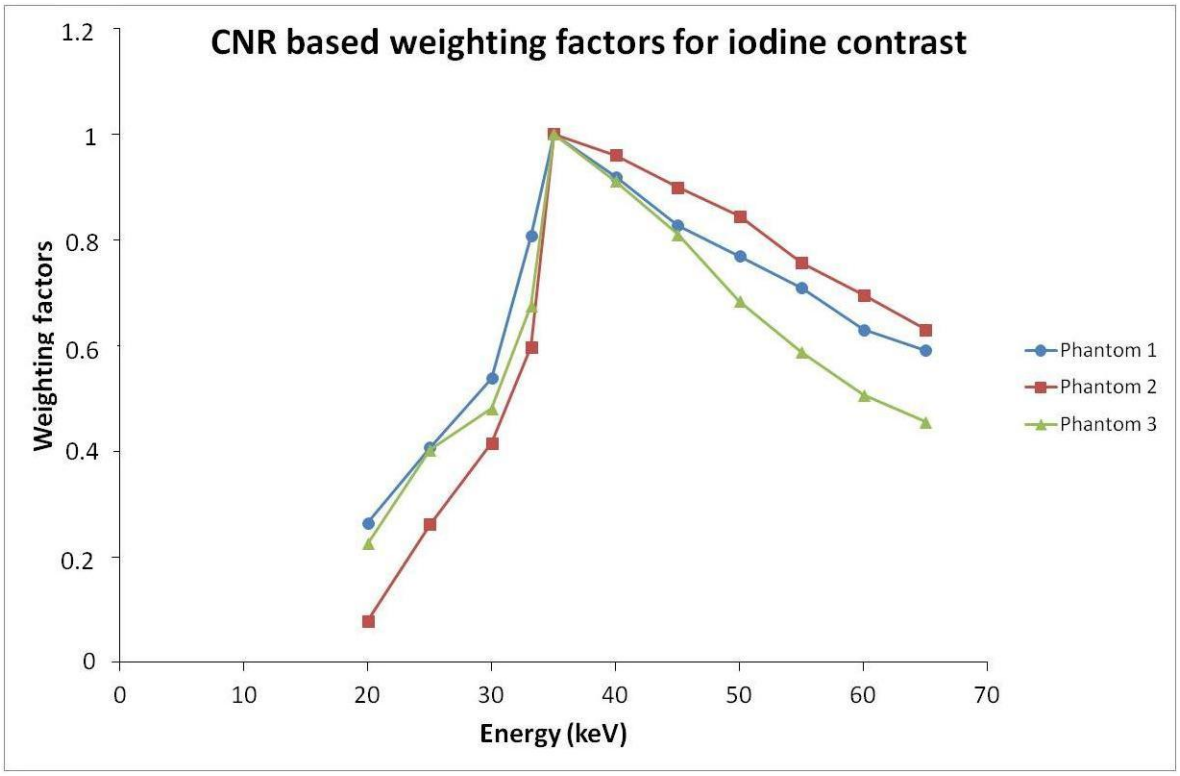

Figure 5.27: The weighting factors based on the CNRs for the iodine.

The lowest energy now has the lowest weighting factor, unlike phantom 2 and 3 in Figure 5.25.

The increase in the CNR for the three phantoms with the different methods is seen below in Figure 5.28. A higher CNR is obtained when utilising all the images and not just the 20 keV image. The weighting factors based on the CNRs yield the highest CNRs and correlate with that found in previous studies.[13,14]

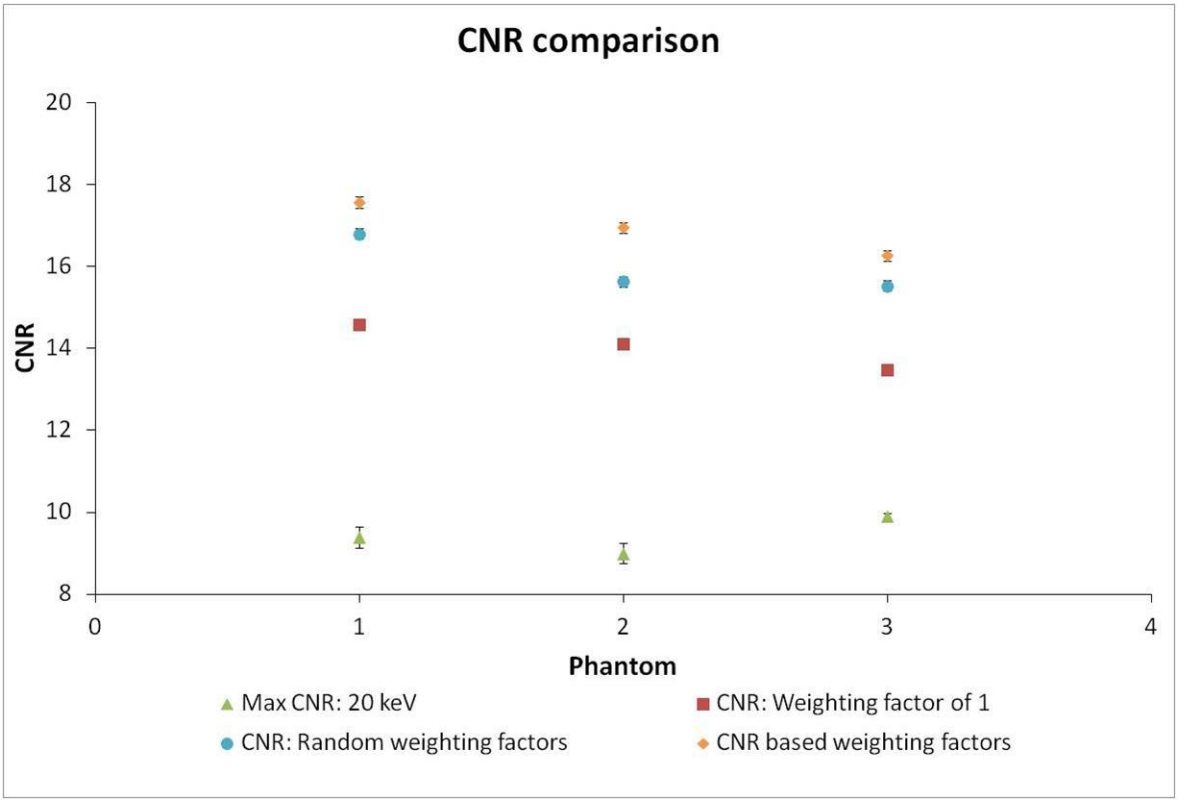

Figure 5.28: Comparison between the different CNRs obtained with the different methods. The uncertainties in the CNRs are indicated if they are larger than the symbol size.

An increase in the CNRs is found when the weighting factors are based on the CNRs of the different phantoms at the different energies.

All of the phantoms show a significant increase in the CNR when all of the images are added with a weighting factor of 1. This shows that better CNRs are obtained when all of the images are utilised and not just one at e.g. 20 keV. A further increase in the CNRs is seen when weighting factors with random numbers are applied. This is because images with high CNRs now contribute more to the final image and CNR. The CNRs are further increased when the weighing factors used are based on the CNRs of the different images obtained in Chapter 4.

Phantom 1 has an increase of 5.21 ± 0.102 when combining the images with a weighting factor of 1. The random weights increased the CNR with 2.21 ± 0.113 and the CNR based weighting factors increased the CNR with a further 0.77 ± 0.098.

Phantom 2 has an increase of 5.12 ± 0.312 when combining the images with a weighting factor of 1. The random weights increased the CNR with 1.51 ± 0.248 and the CNR based weighting factors increased the CNR with a further 1.32 ± 0.212.

Phantom 3 has an increase of 3.58 ± 0.101 when combining the images with a weighting factor of 1. The random weights increased the CNR with 2.05 ± 0.889 and the CNR based weighting factors increased the CNR with a further 0.74 ± 0.100.

The increase in the CNR for the three phantoms with the iodine after applying the different methods is seen below in Figure 5.29.

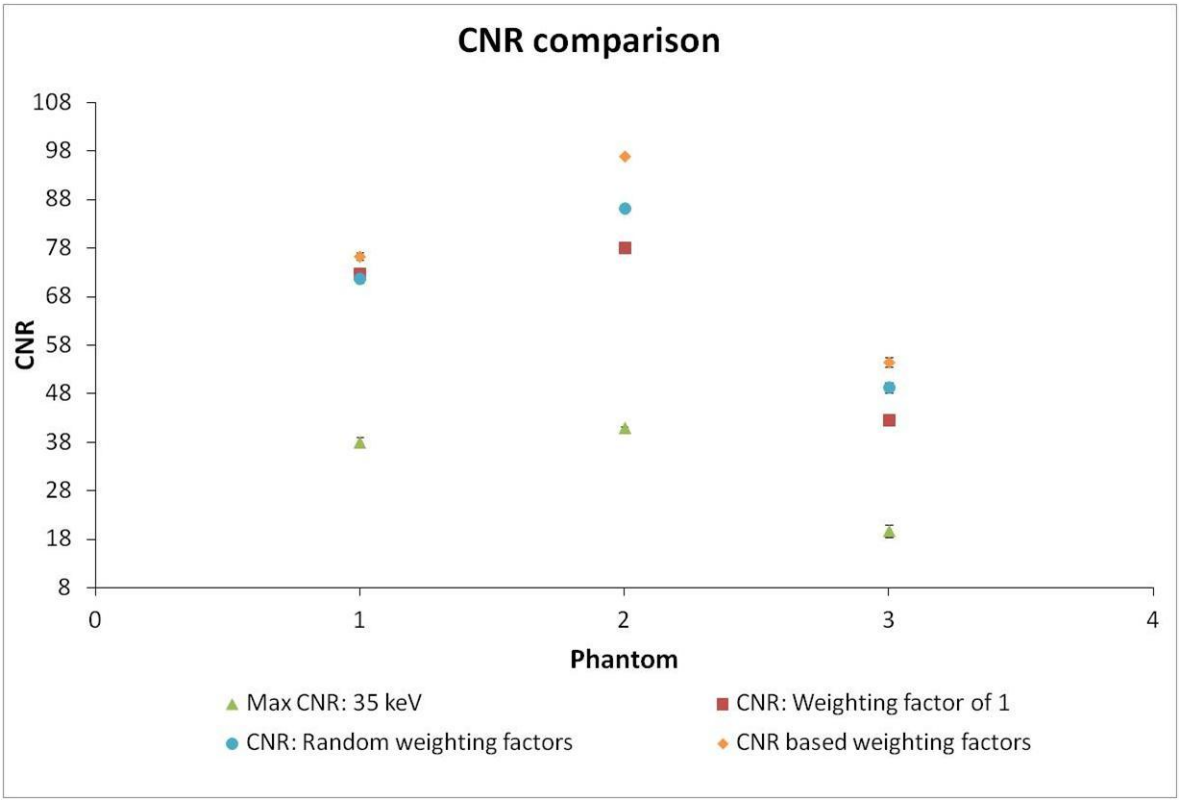

Figure 5.29: Comparison between the different CNRs with iodine obtained with the different methods. The uncertainties in the CNRs are indicated where they are bigger than the symbol size.

A big difference is seen when applying the weighting factors for all three the phantoms. As seen in Figure 5.27, all the phantoms have the highest weighting factor at 35 keV just above

the K-edge of iodine. Increases in the CNRs are seen when the weighting factors are based on the CNRs of the different phantoms at the different energies.

Combining all of the images yield a better CNR as seen in Figure 5.29. This shows that multi-energy CT is beneficial even when iodine contrast is used. When more weight is given to the 35 keV image, an increase in the CNR is seen. The highest CNRs are seen when the weighting factors are based on the CNRs of Chapter 4.

Phantom 1 has an increase of 34.74 ± 0.623 when combining the images with a weighting factor of 1. This significant increase shows the importance of utilising more than one image. The random weights increased the CNR with 1.06 ± 0. 0.715 and the CNR based weighting factors increased the CNR with 5.56 ± 0.801.

Phantom 2 has an increase of 37.22 ± 0.154 when combining the images with a weighting factor of 1. The random weights increased the CNR with 8.11 ± 0.201 and the CNR based weighting factors increased the CNR with 10.75 ± 0.258.

Phantom 3 has an increase of 22.94 ± 1.125 when combining the images with a weighting factor of 1. The random weights increased the CNR with 6.62 ± 1.04 and the CNR based weighting factors increased the CNR with 5.15 ± 1.110. Phantom 3 has lower CNRs than phantom1 and phantom 2 even though it has the least amount of glandular tissue. This can be due to the structures in the phantom that can lead to inaccurate ROI values as shown in Figure 4.33.

5.4 Conclusion

The CNRs of the different phantoms increase when more than one energy is utilised. This shows that multi-energy CT is a valuable technique that can be used to improve image quality. By applying random weights through a trial process, the CNRs are further improved. This is a valid method to use but the random nature of the weighting factors has its pitfalls since small weights are sometimes assigned to the lower energies and larger weights to the higher energies. A further improvement in this technique is proposed by using the CNRs of the images at different energies to determine appropriate weighting factors. This method correlates with what is suggested in previous studies but it has the advantage that no prior information regarding the images is needed. This method can therefore be used for more complex phantoms since no information regarding the effective linear attenuation coefficient or structural dimensions such as the length of the contrast element is needed. The increase of 1.2 - 1.3 fold for the CNRs obtained by using this method correlate well with that found in previous studies by Le *et al.* [14] and Schmidt *et al.* [13] and prove to be a valid method of energy weighting. Smaller increases in the CNRs can be expected because previous studies used simple phantoms and this study is based on a clinical phantom data with more variance in the structures.

The proposed method is easier to implement but the iterative method might be more time consuming depending on the number of trials and computing power.

5.5 References

1. Lindfors KK, Boone JM, Nelson TR, Yang K, Kwan ALC, Miller DF. Dedicated breast CT: initial clinical experience. Radiology. 2008 Mar;246(3):725–33.

2. Glick SJ. Breast CT. Annu Rev Biomed Eng. 2007;9(1):501–26.

3. Lai C-J, Shaw CC, Chen L, Altunbas MC, Liu X, Han T, et al. Visibility of microcalcification in cone beam breast CT: effects of X-ray tube voltage and radiation dose. Med Phys. 2007 Jul;34(7):2995–3004.

4. Schlomka JP, Roessl E, Dorscheid R, Dill S, Martens G, Istel T, et al. Experimental feasibility of multi-energy photon-counting K-edge imaging in pre-clinical computed tomography. Phys Med Biol. 2008;53(15):4031.

5. Shikhaliev PM. Energy-resolved computed tomography: first experimental results. Phys Med Biol. 2008;53(20):5595.

6. Shikhaliev PM. Computed tomography with energy-resolved detection: a feasibility study. Phys Med Biol. 2008 Mar 7;53(5):1475–95.

7. Shikhaliev PM. Energy-resolved computed tomography: first experimental results. Phys Med Biol. 2008 Oct 21;53(20):5595–613.

8. Shikhaliev PM. Tilted angle CZT detector for photon counting/energy weighting x-ray and CT imaging. Phys Med Biol. 2006 Sep 7;51(17):4267–87.

9. Shikhaliev PM. Beam hardening artefacts in computed tomography with photon counting, charge integrating and energy weighting detectors: a simulation study. Phys Med Biol. 2005;50(24):5813.

10. Giersch J, Niederlöhner D, Anton G. The influence of energy weighting on X-ray imaging quality. Nucl Instrum Methods Phys Res Sect Accel Spectrometers Detect Assoc Equip. 2004 Sep 21;531(1–2):68–74.

11. Niederlöhner D, Karg J, Giersch J, Firsching M, Anton G. Practical Aspects of Energy Weighting in X-ray Imaging. In: IEEE Nuclear Science Symposium Conference Record, 2004. (unpublished) Vol 5 pp. 3191-3194.

12. Niederlohner D, Nachtrab F, Michel T, Anton G. Using the Medipix2 detector for photon counting computed tomography. In: IEEE Nuclear Science Symposium Conference Record, 2005. 2005. p. 2327–31.

13. Schmidt TG. Optimal “image-based” weighting for energy-resolved CT. Med Phys. 2009 Jul;36(7):3018–27.

14. Le HQ, Ducote JL, Molloi S. Radiation dose reduction using a CdZnTe-based computed tomography system: Comparison to flat-panel detectors. Med Phys. 2010 Mar;37(3):1225–36.

15. Rupcich F, Gilat-Schmidt T. Experimental study of optimal energy weighting in energy-resolved CT using a CZT detector. In 2013 [cited 2017 Mar 7]. p. 86681X–86681X–8. Available from: http://dx.doi.org/10.1117/12.2008439

16. RANDOMU (IDL Reference) [Harris Geospatial Docs Center] [Internet]. [cited 2017 Mar 13]. Available from: https://www.harrisgeospatial.com/docs/randomu.html

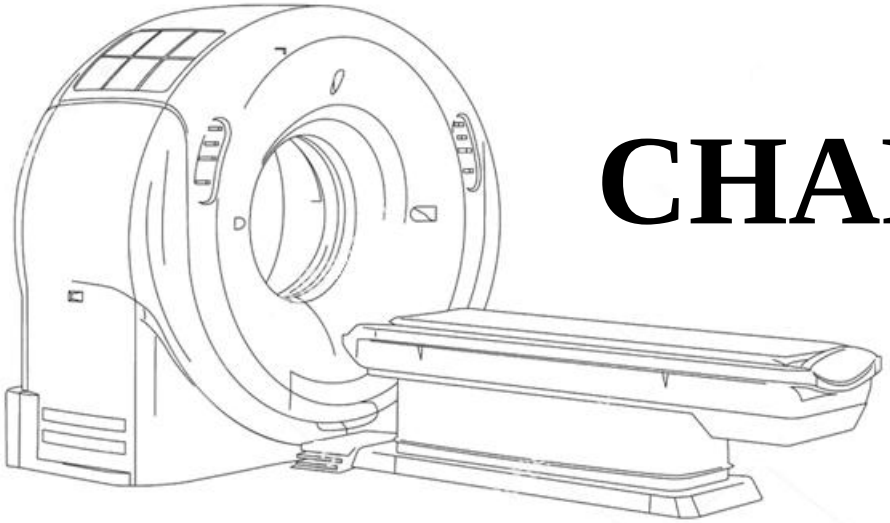

CHAPTER 6

Tissue differentiation with multi-energy CT simulations

Table of Contents

6.1 Introduction

In previous studies, elemental concentrations have been determined with dual-energy CT by using three-material decomposition algorithms.[1,2] Contrast agents such as iodine were used due to its K-absorption edge properties. In a study by Liu *et. al*[3], a three-material decomposition method based on the principle of mass conservation was proposed. By only using two energies a third condition was added to solve the three unknown materials. It was assumed that the sum of the volumes of the three materials equals the volume of the mixture. The study showed feasible results but depended on the dual-energy ratios of the two elements in the mixture.

An alternative method is to determine the effective atomic number and effective density of a material through the ρZ method. The density and atomic number are found with the help of subtraction and division of two linear attenuation coefficients.[4] This can be implemented before reconstruction[5], and in a more recent study, it was implemented after reconstruction.[4]

In another study by Schneider *et al*.[6] CT numbers were converted into mass density and elemental weights of tissues. Landry *et al*.[7] proposed an improved method with excellent conversion between the effective atomic number and the ratio of the linear attenuation coefficients at the two energies.

As seen in Chapter 4, the linear attenuation coefficients of materials are dependent on the X-ray beam energy. Different tissues have different mass attenuation coefficients when interacting with X-rays. This can be utilised to identify and extract elemental information from specific materials.[8]

The mass attenuation coefficient is used to define the rate of energy loss by a photon beam as it traverses a medium, independent of their state.[9] The attenuation depends therefore purely on the atomic structure of the tissue and the energy of the photon beam. Materials with the

same atomic structure will have the same mass attenuation coefficients e.g. vapour, water and ice. This coefficient is obtained by dividing the linear attenuation coefficient by the density, $\frac{\mu}{\rho}$.

A material with a higher mass attenuation coefficient and density will absorb more photons. Bone will, therefore, absorb more photons for the same thickness of soft tissue. This leads to the contrast that is seen in a CT image at kilovoltage beam energies. When these mass attenuation coefficients are close together, it is difficult to distinguish between them. This is seen in megavoltage imaging where poor contrast exists between the bone and soft tissue.

In Chapter 4, it was seen that a significant difference between the attenuation coefficients for the various tissues found in the breast exists at low energies. In this study, an alternative method was explored that uses the mass attenuation information from multiple energies to differentiate between different breast tissues. This technique shows promise in detecting malignant tissue by using a single egs_cbct simulation.

6.2 Methods & Materials

6.2.1 Overview

The method consists of using the mass attenuation coefficient information that is calculated from a single egs_cbct simulation to differentiate between different tissue types. The simulated tissue type consists of a specific elemental composition and density that is known before the simulation. The mass attenuation information for the different elements was obtained from the NIST database.[10] An in-house developed IDL code was used to determine the tissue type through a least squares optimisation method. Different tissue protocols are

used for the identification of these breast tissue types. Each consisting of a set of constraints that are derived from the chemical formula of the tissue type.

6.2.1 Tissue composition and mass attenuation coefficients

Suppose we have the phantom with an insert of known diameter and known tissue type. A profile can be obtained with egs_cbct at different energies that will contain information related to its linear attenuation coefficient. The linear attenuation coefficient information can be calculated from the profile data as shown in Chapter 4 Section 4.2.2. The mass attenuation coefficients for the specific tissue at different energies can be calculated by dividing the calculated linear attenuation coefficient (μ) by the density (ρ) of the material as seen in Equation 6.1.

$$\frac{\mu}{\rho} \text{ in g/cm}^2 \qquad 6.1$$

Where μ is the linear attenuation coefficient in cm^{-1} and ρ is the density in g/cm^3. Tabulated mass attenuation coefficients for the different elements in these tissues are available from NIST.[11,12]

The feasibility of differentiating between glandular and malignant tissue by means of their mass attenuation coefficients was explored. The three tissue types consist of the following elements that are used in Chapter 4 and listed in Table 6.1.

Table 6.1: The weight fractions of the elemental composition of the breast tissues.

Materials	H(%)	C(%)	N(%)	O(%)	Elements with Z>8
Adipose tissue	11.4	59.8	0.7	27.8	Na(0.1), S(0.1), Cl(0.1)
Glandular tissue	10.6	33.2	3.0	52.7	Na(0.1), P(0.1), S(0.2), Cl(0.1)
Malignant tissue	10	10.7	2.75	75	Cl(0.078)

A sum of least squares method was used to differentiate between the calculated mass attenuation coefficients and the NIST values for the corresponding breast tissues. This method minimises the sum of the squares of the differences between the true values and the ones calculated from the set of equations with calculated parameters.

$$S = \sum_{i=1}^{n} \left(t_i - o_i \right)^2 \qquad 6.2$$

The above data set consists of n number of equations where t_i is the true value for each equation and o_i is the calculated value with a set of parameters. This can also be written as

$$S = \sum_{i=1}^{n} r_i^2 \qquad 6.3$$

Where r_i^2 is the residual value which is the difference between the true value and the calculated value.

The mass attenuation coefficient of a compound, such as the breast tissues listed in Table 6.1, can be obtained by adding the mass attenuation coefficients of the various elements.[11]

$$\frac{\mu}{\rho} = \sum_i w_i \left(\frac{\mu}{\rho} \right)_i \qquad 6.4$$

Where w_i is the fraction by weight of the i^{th} atomic component. Therefore the following set of linear equations containing the mass attenuation coefficients of the tissue and elements were used.

Let's suppose each energy is represented by a bin e.g. 20 keV is bin1, 25 keV is bin2, etc.

$$\frac{\mu}{\rho_{bin1}} = \left(\frac{\mu}{\rho_H}\right)_{bin1} \times f_1 + \left(\frac{\mu}{\rho_C}\right)_{bin1} \times f_2 + \left(\frac{\mu}{\rho_O}\right)_{bin1} \times f_3 + \left(\frac{\mu}{\rho_N}\right)_{bin1} \times f_4 + \left(\frac{\mu}{\rho_{Cl}}\right)_{bin1} \times f_5$$

$$\frac{\mu}{\rho_{bin2}} = \left(\frac{\mu}{\rho_H}\right)_{bin2} \times f_1 + \left(\frac{\mu}{\rho_C}\right)_{bin2} \times f_2 + \left(\frac{\mu}{\rho_O}\right)_{bin2} \times f_3 + \left(\frac{\mu}{\rho_N}\right)_{bin2} \times f_4 + \left(\frac{\mu}{\rho_{Cl}}\right)_{bin2} \times f_5 .$$

$$\frac{\mu}{\rho_{bin3}} = \left(\frac{\mu}{\rho_H}\right)_{bin3} \times f_1 + \left(\frac{\mu}{\rho_C}\right)_{bin3} \times f_2 + \left(\frac{\mu}{\rho_O}\right)_{bin3} \times f_3 + \left(\frac{\mu}{\rho_N}\right)_{bin3} \times f_4 + \left(\frac{\mu}{\rho_{Cl}}\right)_{bin3} \times f_5$$

.
.

Where $\frac{\mu}{\rho_{bin1}}$ is the mass attenuation coefficient for each energy bin for the specific breast tissue derived from the simulated linear attenuation coefficient data (Section 4.2.2). The mass attenuation coefficients of the different elements are given by $\left(\frac{\mu}{\rho_H}\right)_{bin1}$ and are obtained from the NIST database for the different energies. The weight fraction of each element that is present in the material is given by f_i. The task at hand is to choose these weight fractions randomly over the unit interval [0,1] and to calculate each $\frac{\mu}{\rho_{bin\,i}}$. The set of weight fractions that minimises the difference between the calculated- and NIST mass attenuation coefficients at each energy bin, will be accepted as the solution to the set of linear equations.

A set of constraints based on the elemental compositions of the tissues were used to aid in the calculation mentioned above of the weight fractions.

6.2.2 Tissue-specific protocols

Three protocols were developed to distinguish between the main breast tissue types namely: a glandular-, adipose- and malignant mass tissue protocol. Each of these protocols has their

own set of constraints to determine the weight fractions of the elements present in the tissue type. These constraints will depend on the tissue type as well as the weight fractions of the different elements. A weight fraction of 0.5 can have a constraint of e.g. 0.4 to 0.6. As seen in Table 6.1, different tissue types can consist of the same elements, but the weight fractions differ. The selection of a specific protocol will depend on the tissue type that the user wants to identify. If one wants to determine if the simulated profile contains a malignant mass, then the malignant mass protocol will be selected. The same implies for the glandular and adipose tissues. A practical example is shown below.

Below we have a phantom with an insert of known diameter and known chemical composition and density. This information can be obtained from the PEGS4 file as explained in Section 4.2.1.

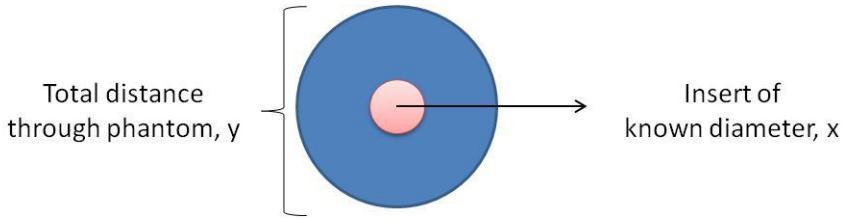

Figure 6.1: An example phantom for the determination of the linear attenuation coefficient of a specific tissue.

A single simulation in egs_cbct is done at multiple energies at a specific angle to obtain a set of profiles. The linear attenuation coefficients and the mass attenuation coefficients of the phantom and insert are then derived with the following equations.

$$\text{Primary signal} = -\ln\left(\frac{I_p}{I_0}\right) = \mu_1.x + \mu_2.(y - x) \qquad 6.5$$

Where x is the known diameter of the insert as shown in Figure 6.1. The mass attenuation coefficient is given by Equation 6.1.

$$\frac{\mu_1}{\rho} \text{ in g/cm}^2 \qquad 6.1$$

Since the chemical composition of the material is known, e.g. $C_{550}H_{104}O_6$, the mass attenuation coefficients of the various elements can be found in the NIST database. The mass attenuation coefficients obtained through the simulated profile are then used to differentiate the tissues by using different protocols. A detailed explanation is given in the next section.

6.2.2.1 Choosing a tissue-specific protocol

The main difference between the different protocols is the constraints that are used to determine the weight fractions of each element for each breast tissue type. For each protocol, the weight fraction of each element should be known for the given tissue type, which is not unreasonable given that this information is well known e.g. from NIST data.

The following steps are used to convert from a chemical compound to the weight per fraction of each element contained in it.

1. Firstly the molecular weight of the chemical compound (tissue type) is determined by multiplying the molar mass of each element by the number of atoms e.g. the molecular weight of water is shown below.

From the periodic table the mass number for hydrogen is 1.01 and for oxygen it is 16. This means the one mole of oxygen weighs in reality 16 g, and that for hydrogen 1 g. Since water contains two hydrogen atoms and one oxygen atom its molar mass is given by:

$M(H_2O) = (2 * 1.01 \text{ g/mol}) + (1 * 16.00 \text{ g/mol}) = 18.02 \text{ g/mol}$

2. The weight fraction of hydrogen will therefore be:

$[(2 * 1.01 \text{ g/mol}) / 18.02 \text{ g/mol}] = 0.1119$ and for oxygen :

$[(16.00 \text{ g/mol}) / 18.02 \text{ g/mol}] = 0.8879$

These weight fractions are now used as guide constraints in the tissue protocols.

The constraint on the weight fraction for hydrogen will then be a random number between 0.1 and 0.2 if the chemical compound is water. For oxygen, it will be between 0.8 and 0.9. An interval is chosen such that the different tissues cannot be misinterpreted.

It might be questioned as to why it is necessary to determine the weight fractions with random numbers if they are already known. The reason for this is that there exist variances between different malignant tissues and not all of them have the exact same elemental composition. By using this approach, a malignant mass with a slightly different composition can also be identified.

The tissue type is then determined by using a sum of least squares as described above and plotting the resulting mass attenuation coefficient curve on that of the known tissue. The complete method in the IDL code is shown in Appendix IV.

6.3 Results and Discussion

The following tissue protocols and their data inputs were used to test how accurately the proposed method could differentiate between a malignant mass and glandular tissue.

6.3.1 Malignant mass

This example is similar to the one seen in Section 6.2.2.2 above. A malignant mass was simulated, and the resulting mass attenuation coefficients were used with the different protocols to see if it can be identified. The resulting graphs of the mass attenuation coefficients are seen below.

The following mass attenuation coefficients were found for the malignant mass through egs_cbct simulations as described in Section 6.2.2. The uncertainties in the simulation are below 1%.

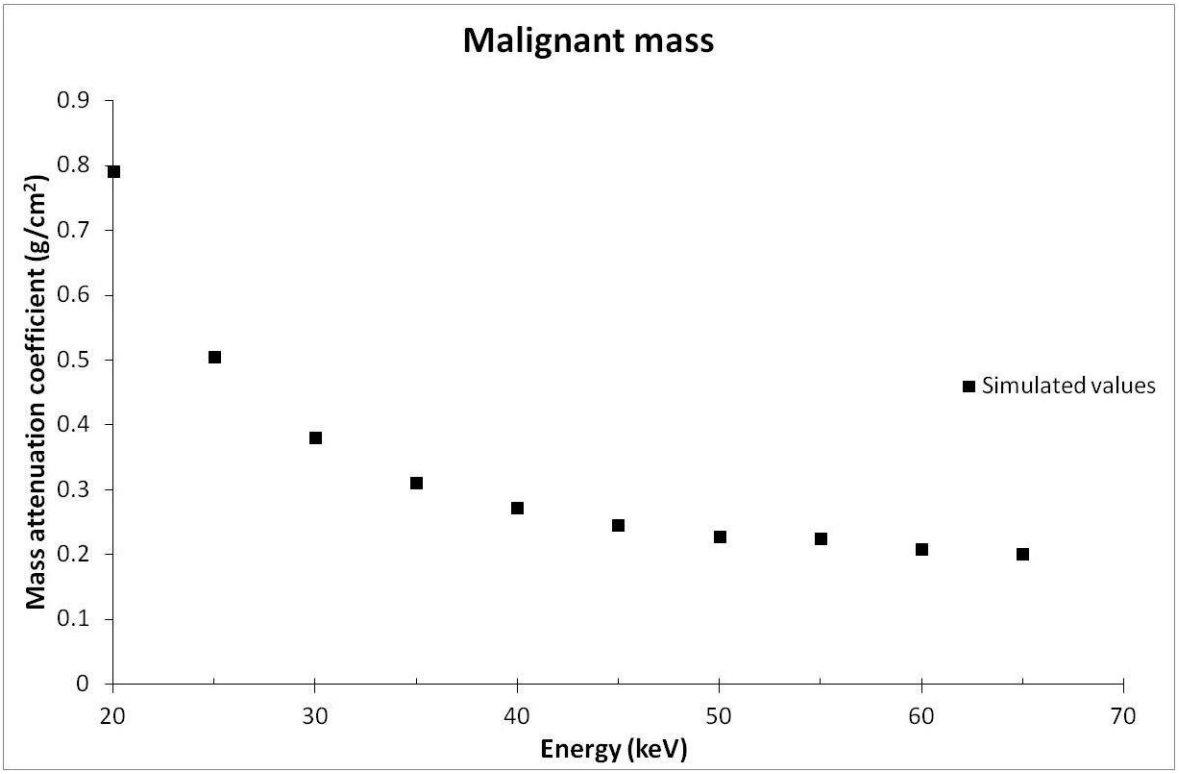

Figure 6.2: Simulated mass attenuation coefficients values for a malignant mass. The uncertainties are smaller than the symbol size.

The simulated values were compared with the adipose tissue protocol by using the sum of least squares method. The following results were obtained.

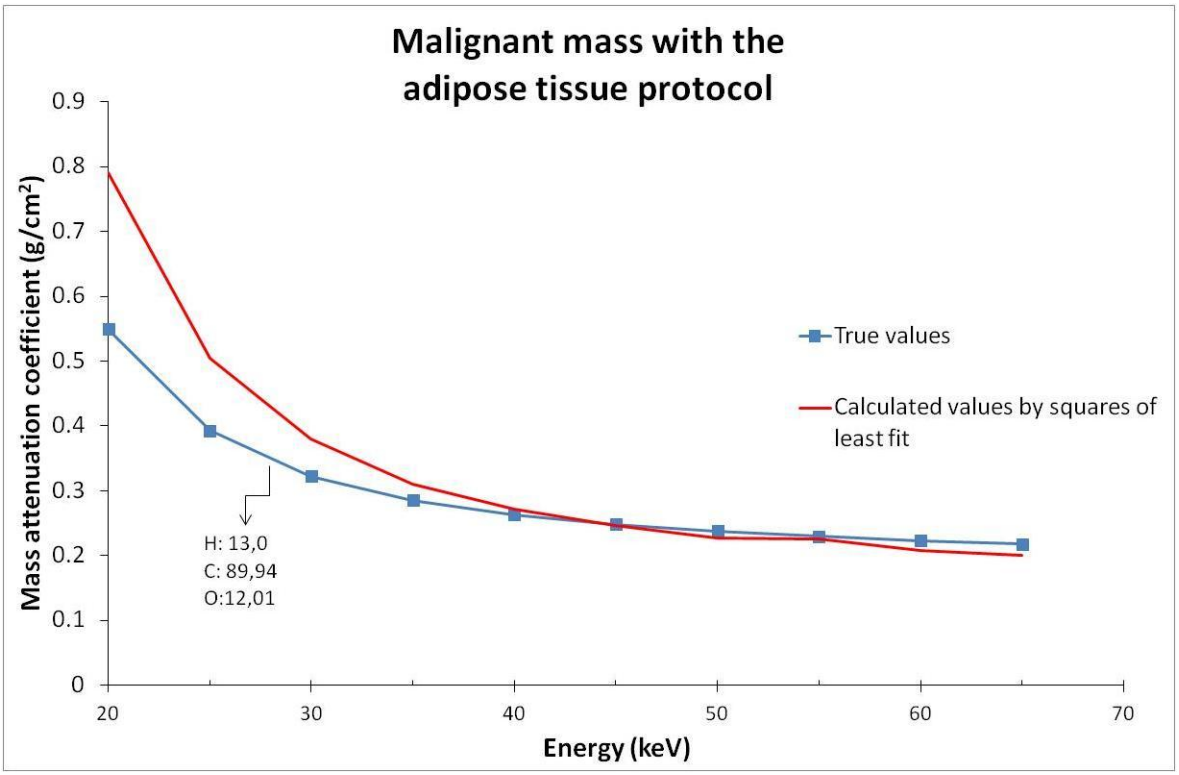

Figure 6.3: Malignant mass with the adipose tissue protocol. The calculated elemental composition is indicated on the graph. (The small amount of N was not included)

The maximum absolute difference between the two graphs was 0.241 at an energy of 20 keV. The calculated weight fraction for H was 1.60 % too low, for C it was 30.15 % too high and for O was 15.80 % too low in comparison with the weight fractions of adipose tissue. The significant difference in the C weight fraction shows that the simulated tissue could not be adipose tissue.

Secondly, the glandular tissue protocol was used to see if the simulated mass could be glandular tissue. The following results were obtained.

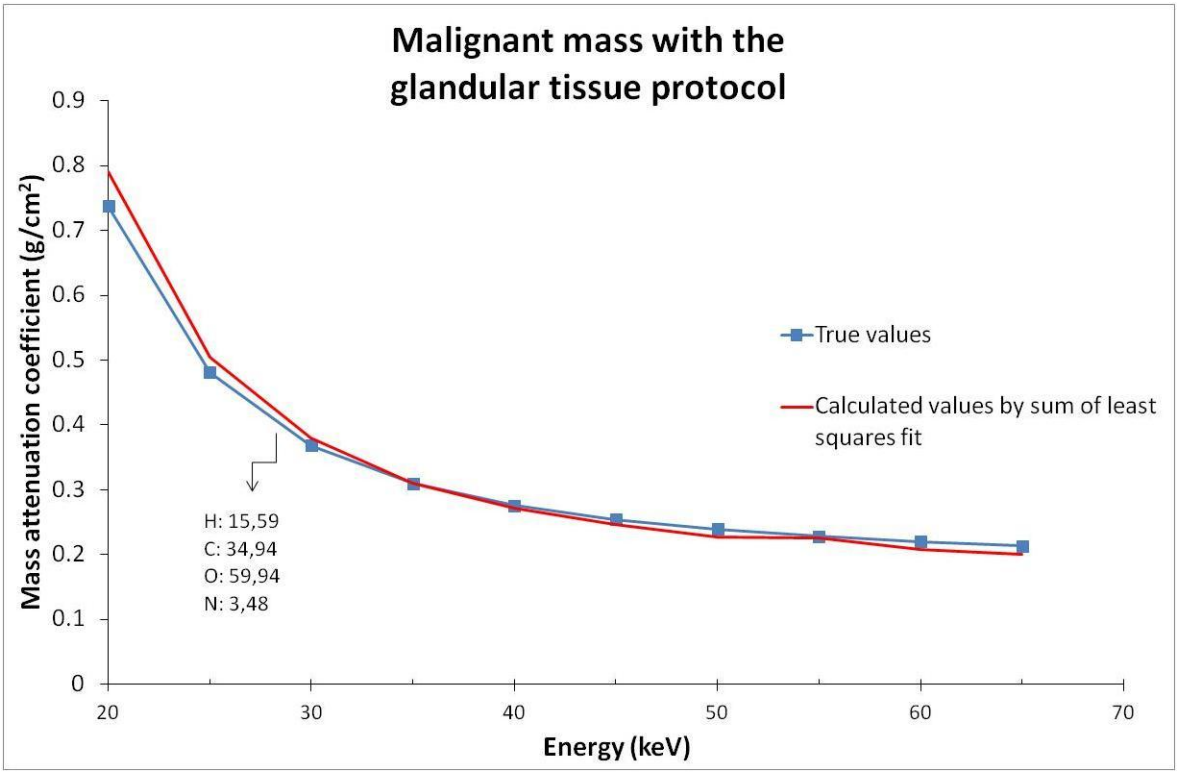

Figure 6.4: Malignant mass with the glandular tissue protocol. The calculated elemental composition is indicated on the graph.

The maximum absolute difference between the two graphs was 0.053 at an energy of 20 keV. The calculated weight fraction for H was 0.99 % too high, for C it was 1.74 % too high, for O was 7.24 % too high and for N it was 0.48 % too high in comparison with the weight

fractions of glandular tissue. These differences between the O weight fractions show that the simulated tissue could not be adipose tissue.

Lastly, the malignant tissue protocol was used to see if the simulated mass could be a malignant mass.

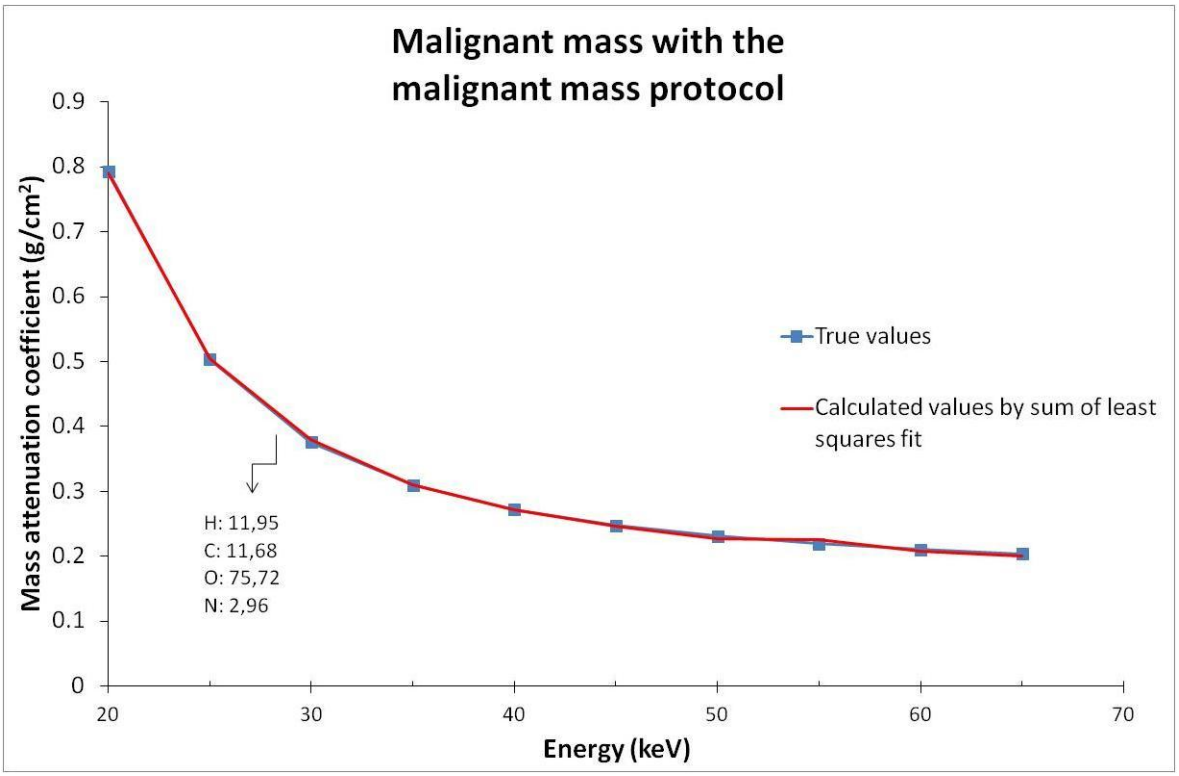

Figure 6.5: Malignant mass with the malignant mass protocol. The calculated elemental composition is indicated on the graph.

The maximum absolute difference between the two graphs was 0.006 at an energy of 55 keV. The calculated weight fraction for H was 1.95 % too high, for C it was 0.98 % too high, for O was 0.72 % too high, for N it was 0.21 % too high and for CL it was 0.24 % too high in comparison with the weight fractions of glandular tissue. These small differences and the small maximum absolute difference show that the tissue could be a malignant mass. The differences between the weight fractions are too small to represent a different tissue type

6.3.2 Glandular tissue

Glandular tissue was simulated, and the resulting mass attenuation coefficients were used with the different protocols to see if it can be identified. The resulting graphs of the mass attenuation coefficients are seen below.

The following mass attenuation coefficients were found for the glandular tissue through egs_cbct simulations as described in Section 6.2.2. The uncertainties in the simulation data are below 1%.

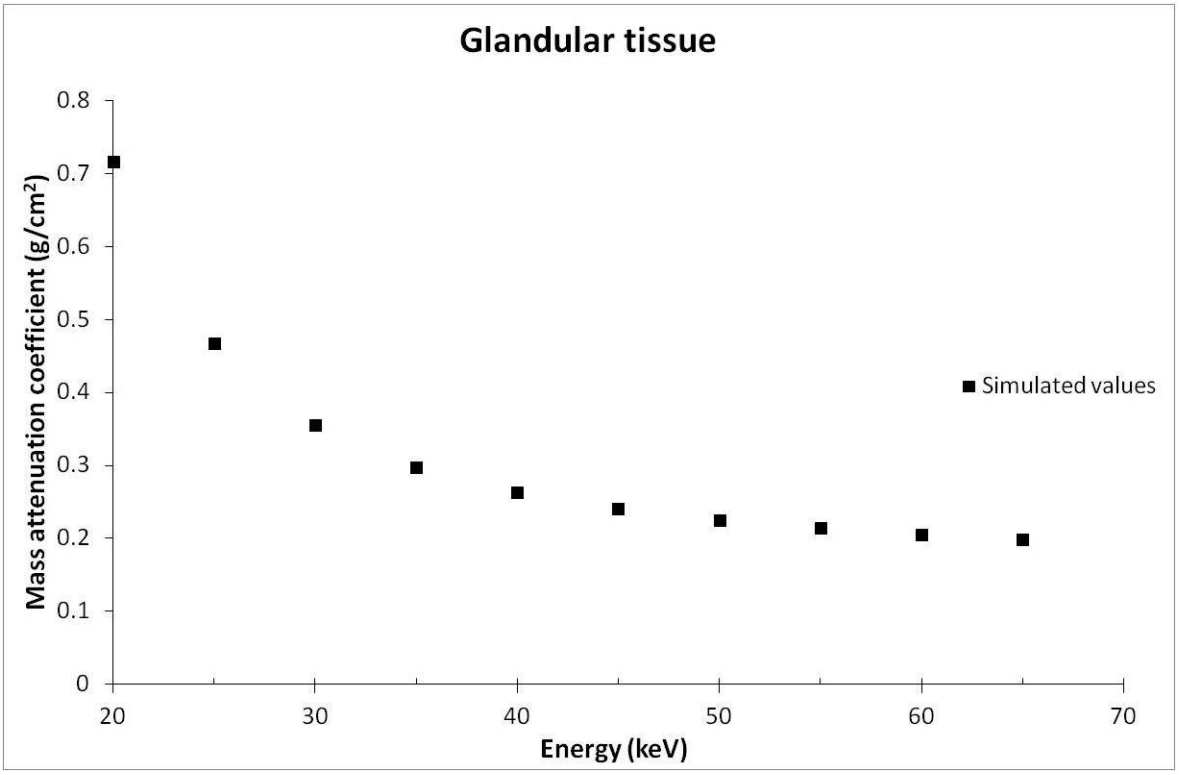

Figure 6.6: Simulated mass attenuation coefficients values for glandular tissue. The uncertainties are smaller than the symbol size.

The simulated values were compared with the adipose tissue protocol by using the sum of least squares method. The following results were obtained.

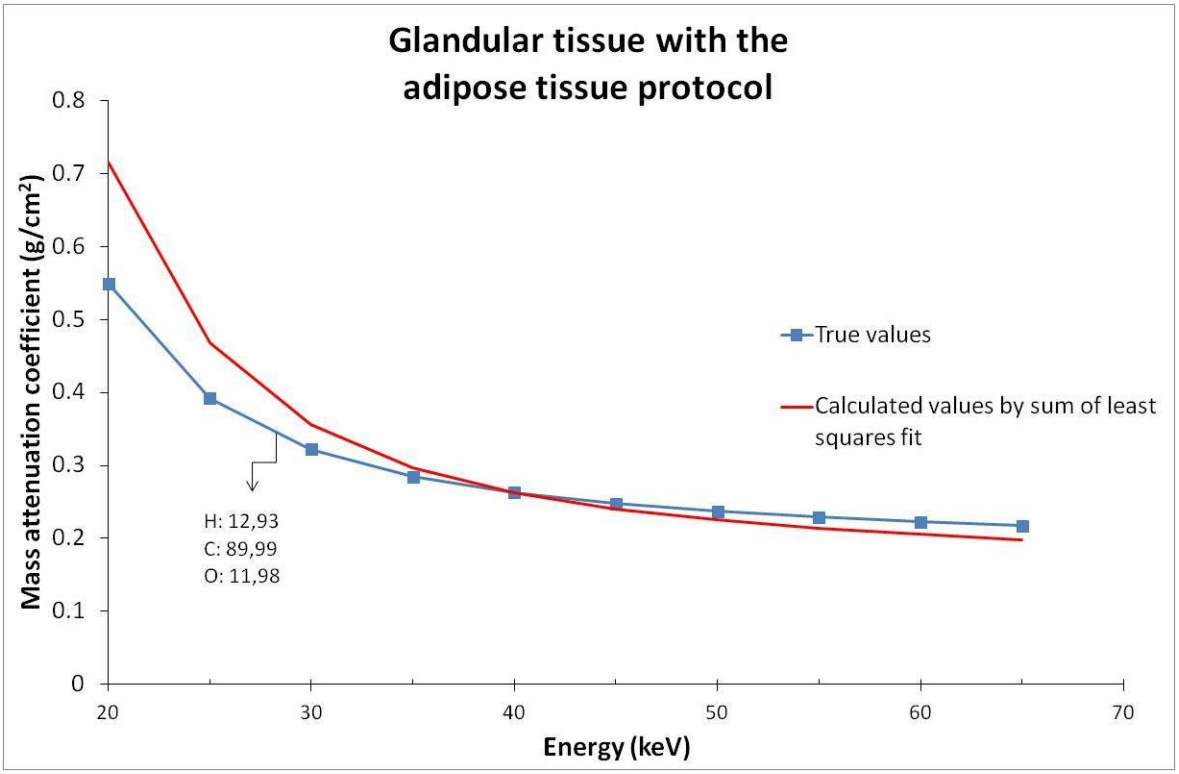

Figure 6.7: Malignant mass with the adipose tissue protocol. The calculated elemental composition is indicated on the graph. (The small amount of N was not included)

The maximum absolute difference between the two graphs was 0.167 at an energy of 20 keV. The calculated weight fraction for H was 1.52 % too low, for C it was 30.19 % too high and for O it was 15.82 % too low in comparison with the weight fractions of adipose tissue. The significant difference in the C weight fraction shows that the simulated tissue could not be adipose tissue.

Secondly, the glandular tissue protocol was used to see if the simulated mass could be glandular tissue. The following results were obtained.

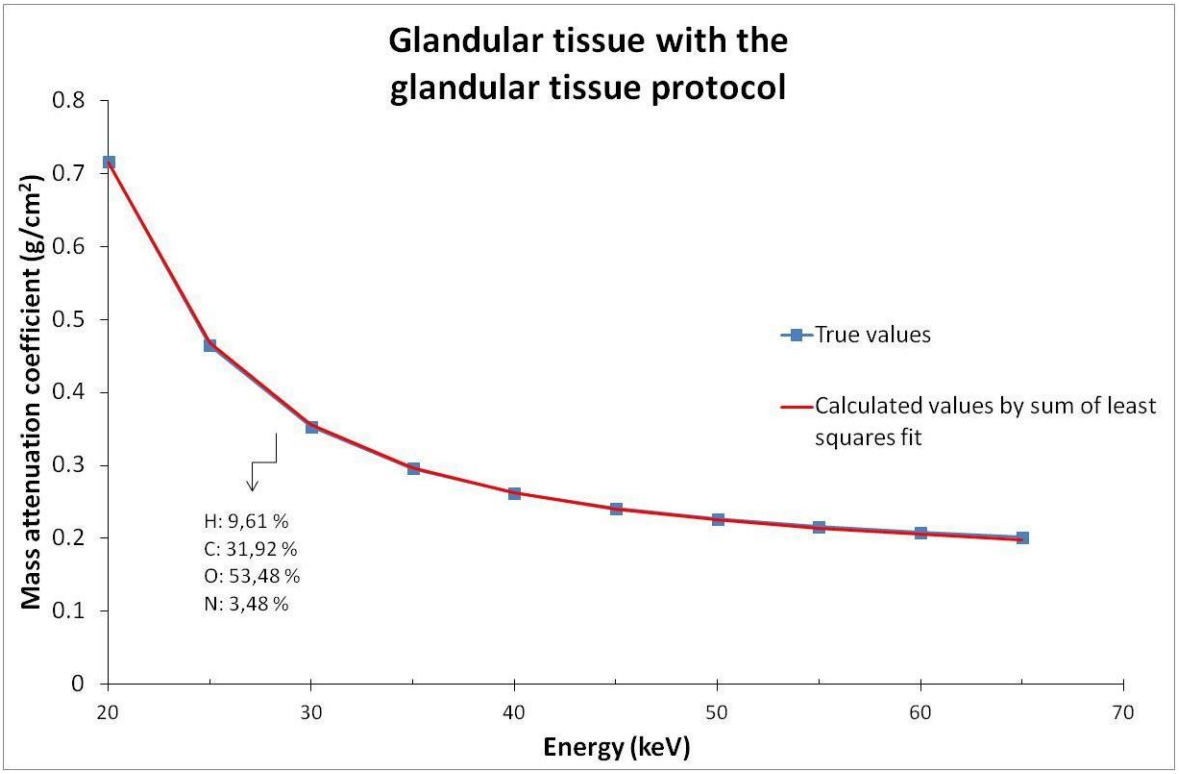

Figure 6.8: Glandular tissue with the glandular tissue protocol. The calculated elemental composition is indicated on the graph.

The maximum absolute difference between the two graphs was 0.003 at an energy of 25 keV. The calculated weigh fraction for H was 0.99 % too low, for C it was 1.28 % too high, for O was 0.78 % too high and for N it was 0.48 % too high in comparison with the weight fractions of glandular tissue. This small differences and the small maximum absolute difference show that the tissue could be glandular tissue. The differences between the weight fractions are too small to represent a different tissue type

Lastly, the malignant tissue protocol was used with the glandular tissue

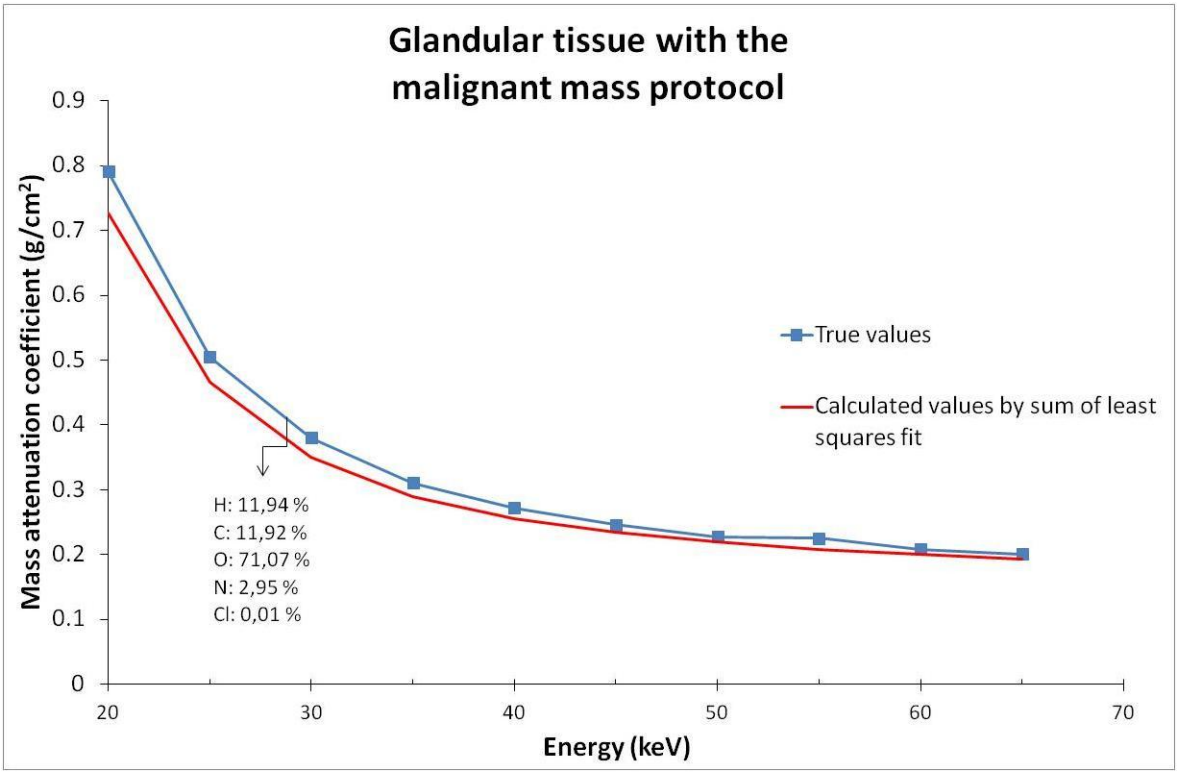

Figure 6.9: Glandular tissue with the malignant mass protocol. The calculated elemental composition is indicated on the graph.

The maximum absolute difference between the two graphs was 0.06 at an energy of 20 keV. The calculated weigh fraction for H was 1.94 % too high, for C it was 1.22 % too high, for O was 3.93 % too low, for N it was 0.20 % too high and for CL it was 0.06 % too high in comparison with the weight fractions of glandular tissue. The difference in the O weight fraction shows that the simulated tissue could not be glandular tissue.

From the above figures it can be seen that the protocols are able to differentiate between the two different tissue types. The maximum absolute difference and the difference between the weigh fractions give a quantitative evaluation of the graphs. This method shows promising results but further improvements are necessary to improve the accuracy. With the use of multiple-energies more information is available to use for differentiation between different tissues.

Before the chapter is concluded a brief discussion will now be presented for the case where the tissue under consideration is unknown. An alternative method is proposed for this case. The mass attenuation coefficients cannot be determined without the density information, and the constraints cannot be determined without the elemental weight per fraction or percentage weight information. In such a case a comparison can be made between the linear attenuation coefficients of the simulated tissue and a known tissue type. The linear attenuation coefficients of the different tissues found in the breast were determined in Chapter 4 and are shown again below.

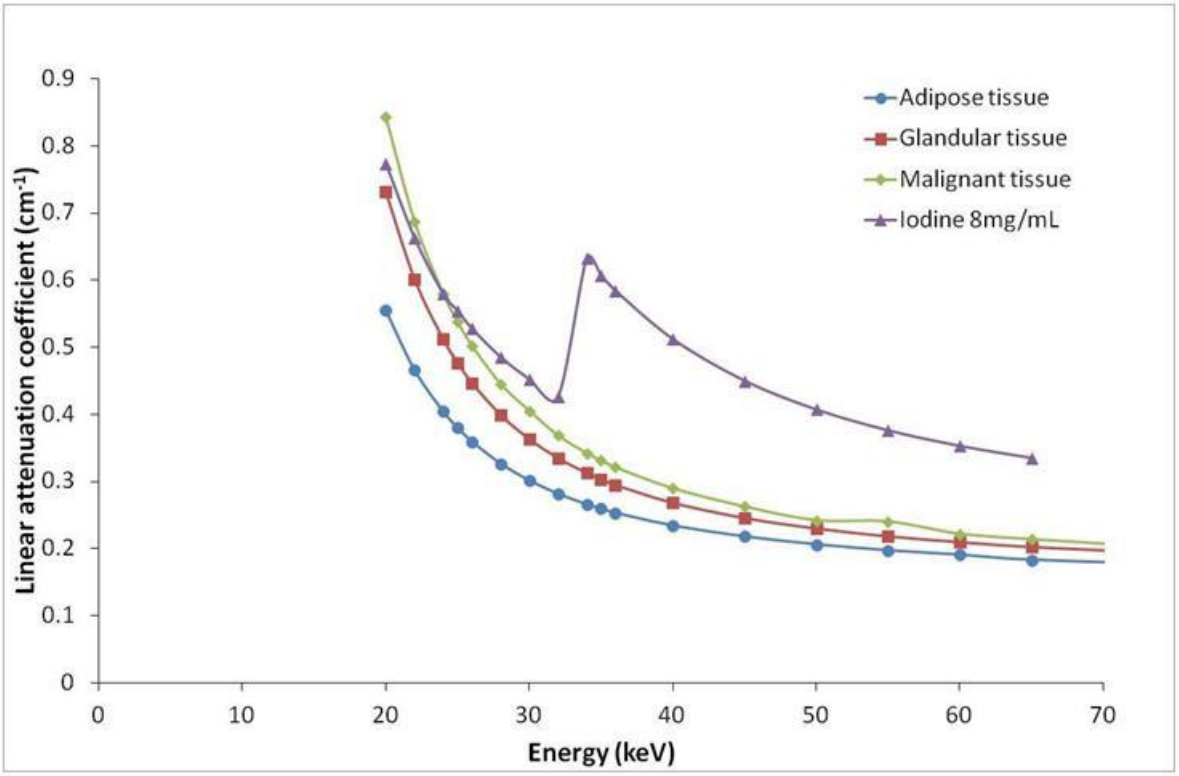

Figure 4.23: The linear attenuation coefficients for the different tissues for energies from 20 keV. The k-absorption edge of iodine can be seen at 34 keV.

There exist a clear difference between adipose, glandular and malignant tissue linear attenuation coefficients at low energies. The use of multiple energies provides a large range of linear attenuation coefficients that makes a simple comparison possible. This will not be possible if only two energies are used as with dual-source CT.

A single profile from a clinical phantom from Chapter 4 was obtained using egs_cbct simulation. The phantom slice consisted of adipose tissue, glandular tissue and an unknown mass. The complete phantom and simulation set-up is seen below in Figure 6.10. The unknown mass was positioned on the central axis to simplify the simulation and linear attenuation coefficient calculation.

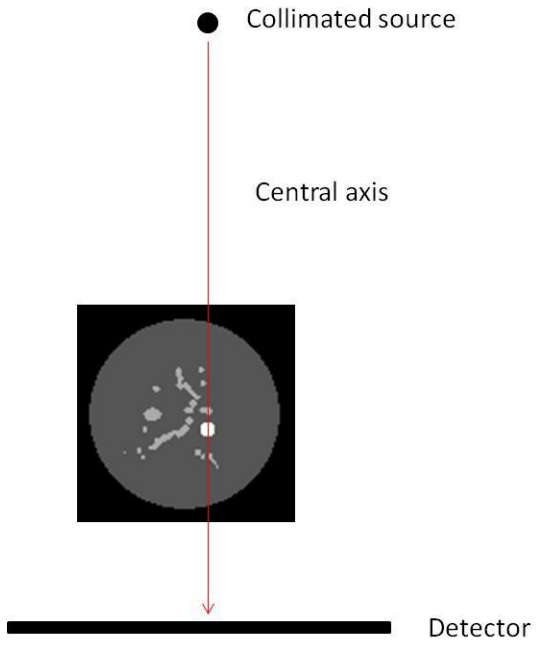

Figure 6.10: Clinical phantom used for tissue differentiation. The white object is the unknown mass, light grey structures are glandular tissue and the background is adipose tissue.

The dimensions of all the structures and the linear attenuation coefficients of the adipose and glandular tissue are available (Figure 4.23). The path length through all the structures was determined by using the *.egsphant file (Section 3.2.1.1) output. The linear attenuation coefficient from the unknown mass was calculated by using Equation 6.5 and the dimensions of the unknown mass. The linear attenuation coefficients of the unknown simulated tissue were plotted against known tissue linear attenuation coefficients.

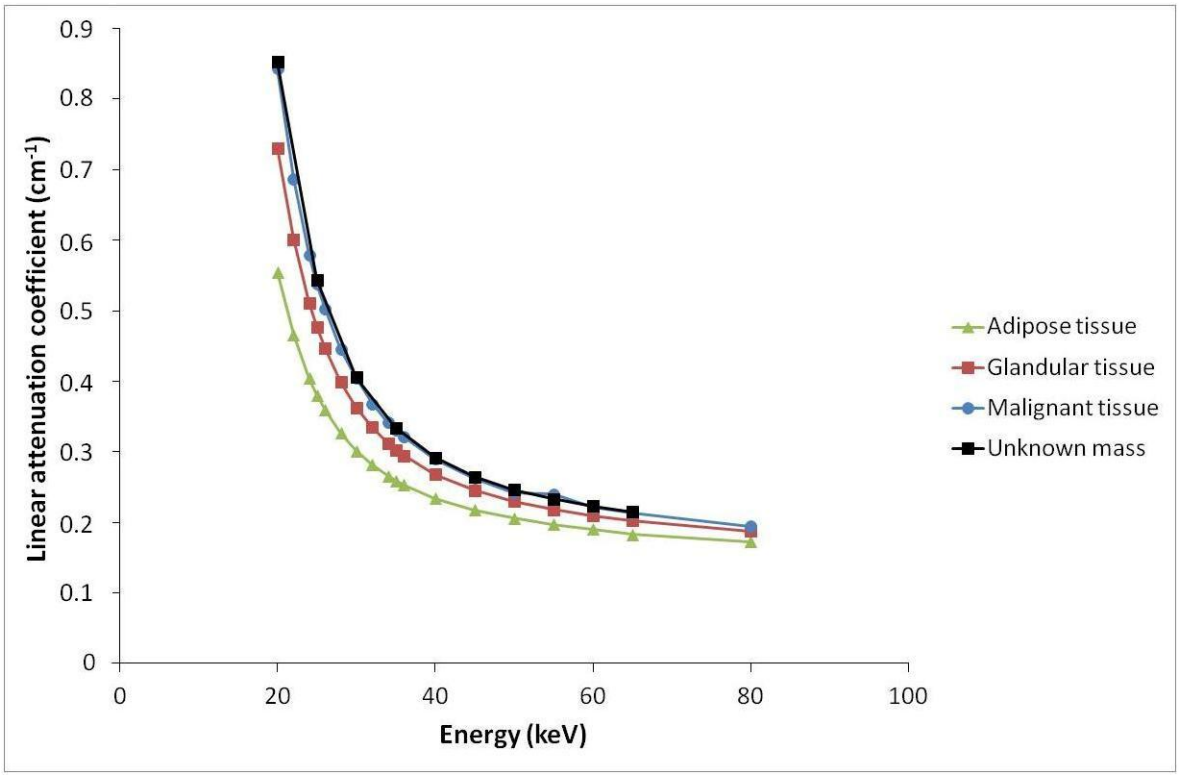

Figure 6.11: The comparison between the unknown mass and the known tissue linear attenuation coefficients.

From the above figure it can be seen that the unknown tissue is likely to be a malignant mass. The small deviation exists between the malignant mass linear attenuation coefficients and the linear attenuation coefficients of the unknown mass. This can be a result of a slight difference in the weight fractions or density of the two malignant masses. This method can be extended to a more quantitative analysis in future work.

6.4 Conclusion

Tissue differentiation is a valuable method that can be used to distinguish between different breast tissues. The method proposed in this chapter showed promising results if the simulated tissue type is known. The accuracy of the identification is highly depended on the given weight fractions as assigned in the tissue protocols. A drawback of this method is that it cannot be utilised if the simulated tissue type and density are not known. The alternative method proposed in the discussion can be used to overcome this problem if needed.

Further studies can be conducted that includes a method to identify a tissue type when another obscures it. This means that the simulated profile will contain information regarding two different tissue types. This will have a more relevant application on phantoms that represent clinical data. This method can also be extended and utilised for tissue types outside of the breast if they have significant differences in their linear attenuation coefficients.

What is encouraging about the approach used in the quest for tissue differentiation is that the study started off with a known breast phantom with known tissue compositions. The real stride forward was the ability to determine the attenuation information of the tissue from simulations and image information. From there a system of linear equations could be solved, and given the constraints assigned to the allowable values, breast tissue types could be identified. This can, in reality, take place provided that CT scanner detectors can resolve tube generated X-ray beams into smaller energy bins as was the approach used in this study.

6.5 References

1. Johnson TRC, Krauss B, Sedlmair M, Grasruck M, Bruder H, Morhard D, et al. Material differentiation by dual energy CT: initial experience. Eur Radiol. 2007 Jun;17(6):1510–7.

2. Fletcher JG, Takahashi N, Hartman R, Guimaraes L, Huprich JE, Hough DM, et al. Dual-energy and dual-source CT: is there a role in the abdomen and pelvis? Radiol Clin North Am. 2009 Jan;47(1):41–57.

3. Liu X, Yu L, Primak AN, McCollough CH. Quantitative imaging of element composition and mass fraction using dual-energy CT: three-material decomposition. Med Phys. 2009 May;36(5):1602–9.

4. Density and atomic number measurements with spectral x-ray attenuation method. J Appl Phys. 2003 Jul 18;94(3):2073–9.

5. Kalender WA, Perman WH, Vetter JR, Klotz E. Evaluation of a prototype dual-energy computed tomographic apparatus. I. Phantom studies. Med Phys. 1986 May 1;13(3):334–9.

6. Schneider W, Bortfeld T, Schlegel W. Correlation between CT numbers and tissue parameters needed for Monte Carlo simulations of clinical dose distributions. Phys Med Biol. 2000;45(2):459.

7. Landry G, Parodi K, Wildberger JE, Verhaegen F. Deriving concentrations of oxygen and carbon in human tissues using single- and dual-energy CT for ion therapy applications. Phys Med Biol. 2013 Aug 7;58(15):5029–48.

8. Alvarez RE, Macovski A. Energy-selective reconstructions in X-ray computerised tomography. Phys Med Biol. 1976 Sep 1;21(5):733.

9. Curry, III TS, Dowdey JE, Murray, JR. RC. Christensen's Physics of Diagnostic Radiology. Fourth edition. Philadelphia, London: Lea & Febiger; 1990. 522 p.

10. US Department of Commerce N. NIST: X-Ray Mass Attenuation Coefficients [Internet]. [cited 2015 Nov 24]. Available from: http://www.nist.gov/pml/data/xraycoef/

11. NIST: X-Ray Mass Attenuation Coefficients - Section 2 [Internet]. [cited 2017 Mar 9]. Available from: http://physics.nist.gov/PhysRefData/XrayMassCoef/chap2.html

12. Hubbell JH. Review and history of photon cross-section calculations. Phys Med Biol. 2006;51(13):R245.

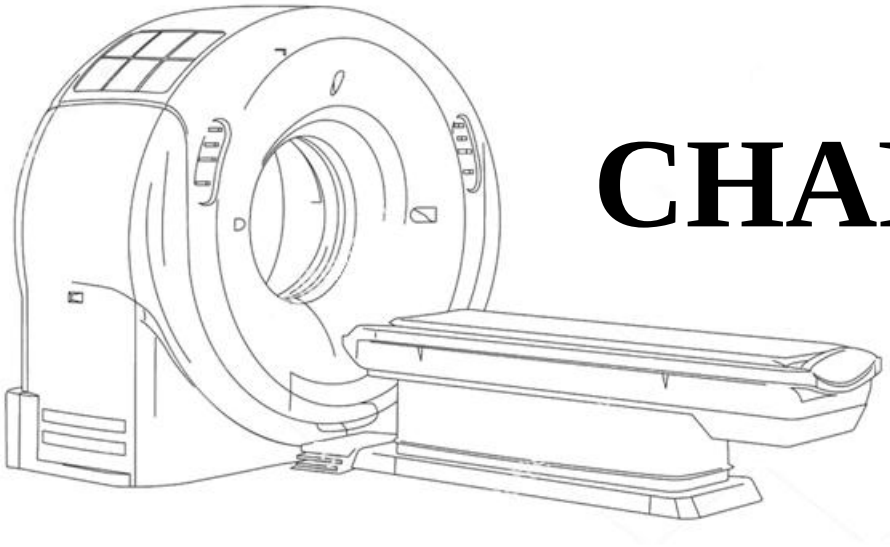

CHAPTER 7

Retrospective comments and future developments of this study

Table of Contents

7.1 Introduction

In this thesis, the feasibility of tissue differentiation by using multiple-energy CT was explored. This idea relies on the principle that the linear attenuation coefficients of materials are energy dependent. This is especially important in breast tissue where the difference between malignant and normal tissues become prominent below 31 keV.

Mammography is considered to be the golden standard for early breast cancer detection, but it has some pitfalls. In dense breasts, it becomes difficult to detect malignant lesions because of the overlapping of dense breast tissue. It is suggested that using a dedicated breast CT this problem can be overcome and fewer false-negatives will be detected.

Recent improvements in the technology make it possible to have energy discriminating detectors. This enables one to have a range of monoenergetic images resulting from different energies bins by doing a single image acquisition. The contrast in these images can be further improved through image-based energy weighting and by assigning different weights to each energy bin. The highest weighting factor is given to the energy bin with the highest CNR.

The possibility of having multiple energy bins also promotes the idea of tissue differentiation. Malignant tissues can be distinguished from normal tissue based on their response to these different energies.

These principles have been studied extensively by exploring different means of obtaining high CNRs and detecting malignant tissues.

7.2 Assumptions of this study

In this study, it was assumed that simulating monoenergetic energies will have the same outcome as that of a photon-counting detector. These simulations were conducted in egs_cbct without the use of a bowtie filter. All the simulations were conducted without simulating the scattered radiation. No additional corrections were applied for beam hardening artifacts or possible cupping effects. A normal Shepp-logan filter was used for all the reconstructions, assuming that it will produce sufficient image qualities.

7.3 Future developments

The work displayed in this thesis has a few shortcomings that can be improved with future studies and alternative methods.

In Chapter 2 the energy spectrum of the Toshiba aquilion 16 LB CT was approximated through HVL measurements. A more accurate representation of the CT can be obtained by creating a source model and using vendor specifications.

In Chapter 3 the RMI phantom was simulated with the use of egs_cbct code and a bowtie filter. The calculation of the bowtie filter thickness is a cumbersome task with room for potential errors. An alternative method of reducing the dynamic range on the detector can be explored and implemented. With the use of Monte Carlo simulations, studies like these are easy to conduct with endless possibilities.

In Chapter 4 the CNRs were determined for an energy range of 20 to 65 keV. The Breast Simulator software proved to be a very useful tool for the modelling of realistic breast phantoms. Dedicated breast CT is a very active field of research, and it is worthy of exploring more simulation studies based on realistic phantoms.

In Chapter 5 a new method for image-based energy weighting was proposed that is based on a random iterative method. Although it proved to be a valid method, CNR values are needed for the weighting factors to obtain an optimal image quality. Further improvements can be made on this method by using a more robust iterative regime that will follow the expected tendency.

In Chapter 6, the feasibility of tissue differentiation was explored based on the mass attenuation coefficients of various tissues and elements. This method showed promising results, but a few shortcomings were found. Prior to tissue differentiation, the elemental composition of the simulated tissue and its density need to be known. Further studies can involve conducting methods where an unknown mass can be easily identified by using the same principles proposed in this chapter.

ABSTRACT

Dedicated breast CT is a new innovative way of imaging breast tissue without the limitations of overlapping anatomical features. It has been shown that the dose received by the patient is comparable to that of conventional mammography techniques. Further developments have led to the idea of a photon-counting detector that can be utilised in conjunction with breast CT. This will produce images with higher CNRs and will improve the detection of malignant masses. Other applications of multi-energy CT include image-based energy weighting and the differentiation of different tissues.

The aim of this study was to explore the feasibility for tissue differentiation in breast tissue through the Monte Carlo simulation of a virtual multi-energy CT unit.

The EGSnrc Monte Carlo code was used to simulate a virtual CT unit, similar to the Toshiba Aquillion LB 16 CT. The radiation source modelling code, BEAMnrc, was used to model the different components of the virtual CT. These components include the X-ray tube, suitable filters and beam-defining components such as collimators. A phase-space file was obtained consisting of all the particles generated by the different components. The energy spectrum of the Toshiba Aquillion LB 16 CT was approximated by the virtual CT using HVL measurements.

The RMI electron density CT phantom was used to benchmark the virtual CT against the Toshiba Aquillion LB 16 CT. The phantom consists of several inserts with known electron densities that produce different CT numbers. A similar phantom was modelled with an in-house developed IDL program and used for the simulations. The reconstructed images were then used for the benchmarking of the HUs. This benchmarking ensured that the method used in this study produces a realistic model of a CT unit.

Breast simulator software was used to model three breast phantoms consisting of different glandularities. The composition of the different breast tissues was taken from literature. The three phantoms were simulated at 20 keV up to 65 keV in 5 keV increments. All of the image reconstructions in this study was done with a filtered backprojection algorithm by using the OSCar reconstruction software. The CNRs of the different images obtained at different energies were assessed.

Image-based energy weighting was investigated to further enhance the CNRs of the images by multiplying each energy bin with a specific weighting factor. The weighting factors were determined by a random number generator in an in-house developed IDL code. Good results were obtained with a 1.2-1.3 fold increase in the CNR. Further improvements were made by applying constraints to the weighting factors of the different energy bins.

A new method was proposed to differentiate between different breast tissues by using the mass attenuation information from multiple energies. This technique showed promising results and can detect malignant tissue by using a single egs_cbct simulation.

In conclusion, it is feasible to differentiate between different breast tissue types when using a multiple-energy CT unit. Better CNRs are obtained when utilising the information of the entire energy spectrum. This will lead to better tumour detection, even in dense breasts consisting of 89% glandular tissue.

Keywords: Multiple-energy CT, breast CT, Monte Carlo, egs_cbct, image-based energy weighting, tissue differentiation

OPSOMMING

Toegewyde bors RT is ‘n nuwe innoverende manier om borsweefsel te beeld sonder die beperkinge van oorvleuelende anatomiese kenmerke. Dit het getoon dat die dosis wat die pasiënt ontvang, vergelykbaar is met dié van konvensionele mammografie tegnieke. Verdere ontwikkelings het gelei tot die idee van ‘n foton-tel detektor wat gebruik kan word in samewerking met die bors RT. Dit sal beelde met ‘n hoër kontras-tot-ruis verhouding produseer en sal die opsporing van kwaadaardige massas verbeter. Ander gebruike van multi-energie RT, sluit beeld-gebaseerde energie beelding en die differensiasie van verskillende weefsels in.

Die doel van hierdie studie was om die haalbaarheid vir weefsel differensiasie in borsweefsel te verken deur die Monte Carlo simulasie van ‘n virtuele multi-energie RT-eenheid.

Die EGSnrc Monte Carlo-kode is gebruik om ‘n virtuele RT-eenheid, soortgelyk aan die Toshiba Aquillion LB 16 RT na te boots. Die bestraling bron modellerings kode, BEAMnrc, is gebruik om die verskillende komponente van die virtuele RT te modelleer. Hierdie komponente sluit in die X-straalbuis, geskikte filters en veldgrootte definieer komponente soos kollimators in. ‘n Fase-ruimte lêer is verkry uit al die deeltjies gegenereer deur die verskillende komponente. Die energie spektrum van die Toshiba Aquillion LB 16 RT was benader deur die virtuele RT deur middel van half-waarde laag metings.

Die RMI elektrondigtheid RT fantoom is gebruik om die virtuele RT teen die Toshiba Aquillion LB 16 RT te maatstaf. Die fantoom bestaan uit verskeie insetsels met ‘n bekende elektron digthede wat verskillende RT getalle te produseer. ‘n Soortgelyke fantoom is ontwikkel met ‘n self ontwikkelde IDL kode, wat gebruik was vir die simulasies. Die gerekonstrueerde beelde is dan gebruik vir die maatstaf van die Hounsfield eenhede. Die

maatstaf verseker dat die metode wat gebruik word in hierdie studie, ‘n realisitiese model van ‘n RT-eenheid kan lewer.

Bors simuleerder sagteware is gebruik om drie bors fantome te modelleer wat bestaan uit verskillende digthede. Die samestelling van die verskillende bors weefsel is geneem uit die literatuur. Die drie fantome is gesimuleer met 20 keV tot 65 keV in inkremente van 5 keV. Al die beeld rekonstruksies in hierdie studie is gedoen met ‘n gefilterde terug-projeksie algoritme deur gebruik te maak van die OSCaR rekonstruksie sagteware. Die kontras-tot-ruis verhouding van die verskillende beelde, by verskillende energieë was beoordeel.

Beeld-gebaseerde energie beelding was ondersoek om die kontras-tot-ruis verhouding verder te versterk deur elke beeld by ‘n spesifieke energie te vermenigvuldig met ‘n spesifieke gewig faktor. Die gewig faktore word bepaal met ‘n ewekansige getal genereerder in ‘n self ontwikkelde IDL kode. Goeie resultate is verkry met ‘n 1,2-1,3 voudige toename in die kontras-tot-ruis verhouding. Verdere verbeterings is gemaak deur die toepassing van beperkings om die gewig faktore van die verskillende energie te bepaal.

‘n Nuwe metode is voorgestel om te onderskei tussen verskillende bors weefsel deur gebruik te maak van die massa attenuasie inligting uit verskeie energie. Hierdie tegniek het belowende resultate en kan kwaadaardige weefsel op spoor deur die gebruik van ‘n enkele egs_cbRT simulasie.

Ten slotte, dit is moontlik om te onderskei tussen verskillende tipes borsweefsel deur die gebruik van ‘n multi-energie RT-eenheid. Beter kontras-tot-ruis verhoudings word verkry wanneer die inligting van die hele energie spektrum gebruik word. Dit sal lei tot ‘n beter gewas opsporing, selfs in digte borste wat bestaan uit 89% klierweefsel.

Sleutelwoorde: multi-energie RT, bors RT, Monte Carlo, egs_cbct, beeld-gebaseerde energie beelding, weefsel differensiasie

Acknowledgements

This research project was funded by the South African Medical Research Council with funds from National Treasury under its Economic Competitiveness and Support Package. This research and the publication thereof is the result of funding provided by the South African Medical Research Council in terms of the MRC's Flagships Awards Project SAMRC-RFA-UFSP-01-2013/HARD.

"I Can Do All Things Through Christ Who Strengthens Me" - Philippians 4:13

Endless gratitude and appreciation towards my promoter, Dr FCP du Plessis. Thank you for your willingness to have taken on this project with me. Your positivity and words of encouragement carried me through this journey. Your immense knowledge and passion is something to strive for.

I would like to thank my colleagues and Head of Department, Prof, W.I.D Rae, for their support and valuable advice.

Albert van Eck at the High-Performance Computing Cluster at the University, for always being willing to help with hours of installing software and solving problems. Without his assistance and devotion, this study wouldn't have been possible.

My loving husband for going on this journey with me and supporting me all the way. Without his encouragement and devotion to our family, it would have been impossible. Thank you for being the best father to our Danielle and supporting me through my roller coaster of emotions during my second pregnancy and the birth of our Alexander.

Physica
Medica
European Journal
of Medical Physics

APPENDIX

I

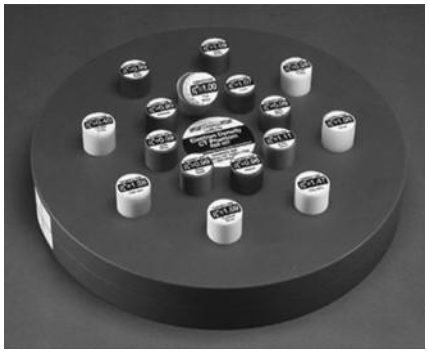

APPENDIX

II

```
pro rmi1_egscbct_bow

xcenter=fltarr(1)
ycenter=fltarr(1)
gdiameter=fltarr(1)
FOV=fltarr(1)

;Size of phantom

resx = 0.1
resy = 1.0
resz = 0.1

degree = 0

xrange = 600

yrange = 10

zrange= 421

;zrange = 4

phantom = fltarr(xrange,yrange,zrange)
finalphantom = fltarr(xrange,yrange)
rotatedphantom = fltarr(xrange,yrange)

;-------------------------------------------------------------------------
-----------------
;EGSPHANT

nmed = 9

media = strarr(nmed)

;_____________________________________________________________________________
_____________________

;FIRST SIMULATION ; 1-7
;_____________________________________________________________________________
_____________________

media(0) = 'AIR700ICRU'
media(1) = 'H2O700ICRU'
media(2) = 'Breast'
media(3) = 'SB3'
media(4) = 'Adipose'
media(5) = 'LN-450'
media(6) = 'CB4'
media(7) = 'Poly'
media(8) = 'AL700ICRU'

estepe = fltarr(nmed)

estepe(*) = 1.0

dimxyz = intarr(3)

for k=0,zrange-1 do begin

for i =0,xrange-1 do begin
```

```
;;
for j = 0,yrange-1 do begin

phantom(i,j,k) = 1

endfor
endfor
endfor

;_____________________________________________________________________________
__________________

;CO-ORDINATES OF BOWTIE FILTER
;_____________________________________________________________________________
________

File = filepath('bow_idl.txt', subdirectory =
['egs_cbct','Breast','FINAL','bow_FINAL'])
openr, l, file, /get_lun
result=file_lines(file)
vector=fltarr(2,result)
a=fltarr(result)
b=fltarr(result)
;
readf,l,vector
;
for i=0,result-1 do begin
a(i) = vector(0,i) & b(i) = vector(1,i)
endfor

maks=max(a)
mini=min(a)

for i=0,result-1 do begin
phantom(a(i),*,10:b(i)) = 9.0
endfor

h=0

hier:

print,h

kk =h+90

hoek =kk * !dtor       ;90 IS 0

;POSITIONS OF INSERTS

hoek2 = hoek -(45 * !dtor)
hoek3= hoek- (90 * !dtor)
hoek4= hoek- (135 * !dtor)
hoek5= hoek- (180 * !dtor)
hoek6= hoek- (225 * !dtor)
hoek7= hoek- (270 * !dtor)
hoek8= hoek- (315 * !dtor)

hoek9= hoek
hoek10 = hoek -(22.5 * !dtor)
hoek11 = hoek -(67.5 * !dtor)
hoek12 = hoek3
```

```
hoek13 = hoek -(112.5 * !dtor)
hoek14 = hoek -(157.5 * !dtor)
hoek15 = hoek5
hoek16 = hoek -(202.5 * !dtor)
hoek17 = hoek -(247.5 * !dtor)
hoek18 = hoek7
hoek19 = hoek -(292.5 * !dtor)
hoek20 = hoek -(337.5 * !dtor)

;-------------------------------------------------------------------------
-----------------
;Cylinder

;Radius of cylinder in cm
radius =(8.25/resz)

;Center on x-axis:
xcenter =xrange/2

;Center on y-axis:
ycenter =330

;Cylinder height in cm
cylinderh = 5/resx

diameter = 2*radius
;-------------------------------------------------------------------------
----------------
;Cylinder 1

x1center=round(xcenter + (2.7/resx) * cos (hoek))
y1center=round(ycenter + (2.7/resz) * sin (hoek))

;Radius of cylinder
radius1 =0.7/resx

;-------------------------------------------------------------------------
----------------

;Cylinder 2

x2center=round(xcenter + (2.7/resx) * cos (hoek2))
y2center=round(ycenter + (2.7/resz) * sin (hoek2))

;Radius of cylinder
radius2 =0.7/resx

;-------------------------------------------------------------------------
---------------
;Cylinder 3

x3center=round(xcenter + (2.7/resx) * cos (hoek3))
y3center=round(ycenter + (2.7/resz) * sin (hoek3))

;Radius of cylinder
radius3 =0.7/resx

;-------------------------------------------------------------------------
---------------

;Cylinder 4
```

```
x4center=round(xcenter + (2.7/resx) * cos (hoek4))
y4center=round(ycenter + (2.7/resz) * sin (hoek4))

;Radius of cylinder
radius4 =0.7/resx

;-------------------------------------------------------------------------
----------------

;Cylinder 5

x5center=round(xcenter + (2.7/resx) * cos (hoek5))
y5center=round(ycenter + (2.7/resz) * sin (hoek5))

;Radius of cylinder
radius5 =0.7/resx

;-------------------------------------------------------------------------
---------------
;Cylinder 6

x6center=round(xcenter + (2.7/resx) * cos (hoek6))
y6center=round(ycenter + (2.7/resz) * sin (hoek6))

;Radius of cylinder
radius6 =0.7/resx

;-------------------------------------------------------------------------
---------------

;Cylinder 7

x7center=round(xcenter + (2.7/resx) * cos (hoek7))
y7center=round(ycenter + (2.7/resz) * sin (hoek7))

;Radius of cylinder
radius7 =0.7/resx

;-------------------------------------------------------------------------
----------------
;Cylinder 8

x8center=round(xcenter + (2.7/resx) * cos (hoek8))
y8center=round(ycenter + (2.7/resz) * sin (hoek8))

;Radius of cylinder
radius8 =0.7/resx

;-------------------------------------------------------------------------
---------------
;Cylinder 9

x9center=round(xcenter + (7.175/resx) * cos (hoek9))
y9center=round(ycenter + (7.175/resz) * sin (hoek9))

;Radius of cylinder
radius9 =0.7/resx

;-------------------------------------------------------------------------
---------------
```

```
;Cylinder 10

x10center=round(xcenter + (5.269843451/resx) * cos (hoek10))
y10center=round(ycenter + (5.269843451/resz) * sin (hoek10))

;Radius of cylinder
radius10 =0.7/resx

;-------------------------------------------------------------------------
----------------
;Cylinder 11

x11center=round(xcenter + (4.968400145/resx) * cos (hoek11))
y11center=round(ycenter + (4.96840014/resz) * sin (hoek11))

;Radius of cylinder
radius11 =0.7/resx
;-------------------------------------------------------------------------
---------------
;Cylinder 12

x12center=round(xcenter + (7.715/resx) * cos (hoek12))
y12center=round(ycenter + (7.715/resz) * sin (hoek12))

;Radius of cylinder
radius12 =0.7/resx

;-------------------------------------------------------------------------
---------------
;Cylinder 13

x13center=round(xcenter + (4.968400145/resx) * cos (hoek13))
y13center=round(ycenter + (4.96840014/resz) * sin (hoek13))

;Radius of cylinder
radius13 =0.7/resx

;-------------------------------------------------------------------------
----------------
;Cylinder 14

x14center=round(xcenter + (5.2698434519/resx) * cos (hoek14))
y14center=round(ycenter + (5.2698434519/resz) * sin (hoek14))

;Radius of cylinder
radius14 =0.7/resx

;-------------------------------------------------------------------------
---------------
;Cylinder 15

x15center=round(xcenter + (7.179/resx) * cos (hoek15))
y15center=round(ycenter + (7.179/resz) * sin (hoek15))

;Radius of cylinder
radius15 =0.7/resx

;-------------------------------------------------------------------------
---------------
;Cylinder 16
```

```
x16center=round(xcenter + (5.269843451/resx) * cos (hoek16))
y16center=round(ycenter + (5.2698434519/resz) * sin (hoek16))

;Radius of cylinder
radius16 =0.7/resx

;-------------------------------------------------------------------------
----------------
;Cylinder 17

x17center=round(xcenter + (4.96840014/resx) * cos (hoek17))
y17center=round(ycenter + (4.968400145/resz) * sin (hoek17))

;Radius of cylinder
radius17 =0.7/resx

;-------------------------------------------------------------------------
---------------
;Cylinder 18

x18center=round(xcenter + (7.715/resx) * cos (hoek18))
y18center=round(ycenter + (7.7155/resz) * sin (hoek18))

;Radius of cylinder
radius18 =0.7/resx

;-------------------------------------------------------------------------
---------------
;Cylinder 19

x19center=round(xcenter + (4.968400149/resx) * cos (hoek19))
y19center=round(ycenter + (4.968400145/resz) * sin (hoek19))

;Radius of cylinder
radius19 =0.7/resx

;-------------------------------------------------------------------------
----------------
;Cylinder 20

x20center=round(xcenter + (5.269843451/resx) * cos (hoek20))
y20center=round(ycenter + (5.269843451/resz) * sin (hoek20))

;Radius of cylinder
radius20 =0.7/resx

;-------------------------------------------------------------------------
-----------
cylradius = ycenter + (radius/resx)

minx = xcenter - radius ;(begin by minimum vir kringe)
maxx = xcenter + radius

miny = ycenter - radius
maxy = ycenter + radius

miny1 = y1center - radius1
maxy1 = y1center + radius1

miny2 = y2center - radius2
maxy2 = y2center + radius2
```

```
miny3 = y3center - radius3
maxy3 = y3center + radius3

miny4 = y4center - radius4
maxy4 = y4center + radius4

miny5 = y5center - radius5
maxy5 = y5center + radius5

miny6 = y6center - radius6
maxy6 = y6center + radius6

miny7 = y7center - radius7
maxy7 = y7center + radius7

miny8 = y8center - radius8
maxy8 = y8center + radius8

miny9 = y9center - radius9
maxy9 = y9center + radius9

miny10 = y10center - radius10
maxy10 = y10center + radius10

miny11 = y11center - radius11
maxy11 = y11center + radius11

miny12 = y12center - radius12
maxy12 = y12center + radius12

miny13 = y13center - radius13
maxy13 = y13center + radius13

miny14 = y14center - radius14
maxy14 = y14center + radius14

miny15 = y15center - radius15
maxy15 = y15center + radius15

miny16 = y16center - radius16
maxy16 = y16center + radius16

miny17 = y17center - radius17
maxy17 = y17center + radius17

miny18 = y18center - radius18
maxy18 = y18center + radius18

miny19 = y19center - radius19
maxy19 = y19center + radius19

miny20 = y20center - radius20
maxy20 = y20center + radius20

dimxyz(0) = xrange & dimxyz(1) = yrange & dimxyz(2) = cylinderh

finaltotphantom = fltarr(xrange+1,yrange+1,cylinderh+1)
;_____________________________________________________________________________
__________________
```

```
for k=ycenter-radius,ycenter+radius do begin

for i =xcenter-radius,xcenter+radius do begin
;;
for j = 0,yrange-1 do begin

x = -xcenter + i & z = -ycenter + k

    r=sqrt(x^2 + z^2)

    if (r le radius) then begin

    phantom(i,j,k) = 2

    endif

    x = -x1center + i & z = -y1center + k

    r=sqrt(x^2 + z^2)

    if (r le (radius1)) then begin

    phantom(i,j,k) = 3

    endif

    x = -x2center + i & z = -y2center + k

    r=sqrt(x^2 + z^2)

    if (r le (radius2)) then begin

    phantom(i,j,k) = 4

    endif

    x = -x3center + i & z = -y3center + k

    r=sqrt(x^2 + z^2)

    if (r le (radius3)) then begin

    phantom(i,j,k) = 5

    endif

    x = -x4center + i & z = -y4center + k

    r=sqrt(x^2 + z^2)

    if (r le (radius4)) then begin

    phantom(i,j,k) = 6

    endif

    x = -x5center + i & z = -y5center + k

    r=sqrt(x^2 + z^2)

    if (r le (radius5)) then begin
```

```
    phantom(i,j,k) = 7

    endif

    x = -x6center + i & z = -y6center + k
;
    r=sqrt(x^2 + z^2)

    if (r le (radius6)) then begin

    phantom(i,j,k) = 8

    endif

endfor
endfor
endfor

phantom(*,*,187:239) = 1.0

;VIEW PHANTOM

window,1
tvscl,phantom(*,0,*)

dimxyz(0) = xrange & dimxyz(1) = yrange & dimxyz(2) = zrange


;WRITING EGSPHANT FILE

xbound = fltarr(xrange+1)
ybound = fltarr(yrange+1)
zbound = fltarr(zrange+1)
;
File = filepath('xbound.txt', subdirectory = ['egs_cbct'])
openr, l, file, /get_lun
readf,l,xbound
free_lun,l

File = filepath('ybound.txt', subdirectory = ['egs_cbct'])
openr, l, file, /get_lun
readf,l,ybound
free_lun,l

File = filepath('zbound_bow0.txt', subdirectory = ['egs_cbct'])
openr, l, file, /get_lun
readf,l,zbound
free_lun,l

filename = 'RMI1_bow_t_'+strcompress(h)+'.egsphant'

    filename1 = strcompress(filename)

    filename1 = strmid(filename,0,11)

    filename2 =strmid(filename, 12, 25)

    filename3 = filename1 + filename2
```

```
File = filepath(filename3, subdirectory =
['egs_cbct','Breast','FINAL','bow_FINAL'])
openw, 1, file, /get_lun
printf,1,format='(I1)',nmed
;
for m = 0, nmed-1 do begin
    printf,1, media(m)
endfor
;
printf,1,format='(9(f8.6," "," "," "," "," "))', estepe

if (cylinderh le 100) then begin

    printf,1, format='((2(I5)),I4)',dimxyz     ;groter as 90 = (3(I5))

    endif else begin

    printf,1, format='(3(I5))',dimxyz

endelse

printf,1, format = '(603(f16.7," "))',xbound
printf,1, format = '(11(f16.7," "))',ybound
printf,1, format = '(422(f16.7," "))',zbound

rhoq=fltarr(xrange+1)

rho = fltarr(xrange)
den = fltarr(xrange)

xrange2 = xrange-1

;writing media data

    for k=0,zrange-1 do begin
    for j = 0,yrange-1 do begin
    for i = 0,xrange2  do begin

    rho(i) =phantom(i,j,k)

    endfor

    printf,1,format='($,601(I0))',rho
    printf,1,' '

    endfor

    printf,1,' '

    endfor

    for k=0,zrange-1 do begin
    for j = 0, yrange-1 do begin
    for i = 0, xrange2  do begin

    den(i) = phantom(i,j,k)

    if (den(i) eq 1) then den(i) = 0.0012048
    if (den(i) eq 2) then den(i) = 1.000
    if (den(i) eq 3) then den(i) = 0.980
    if (den(i) eq 4) then den(i) = 1.820
```

```
    if (den(i) eq 5) then den(i) = 0.940
    if (den(i) eq 6) then den(i) = 0.450
    if (den(i) eq 7) then den(i) = 1.870
    if (den(i) eq 8) then den(i) = 0.920
    if (den(i) eq 9) then den(i) = 2.7020
    endfor

    printf,1,format='(601(f16.7))',den
    printf,1,' '

    endfor

    printf,1,' '

    endfor
;
print,'Completed writing media densities'

print,'Completed writing EGS4PHANT file'

free_lun,1
stop

h=h+1

if (h eq 360) then begin

stop

endif

goto,hier


                                                                    end
```

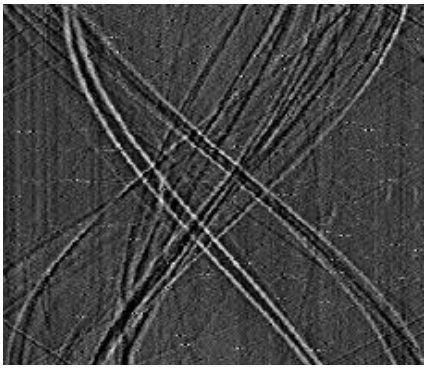

APPENDIX

III

```
pro sinogram_ring

x=350.0
y=200.0

nrows=360.0

sino = fltarr(350,360)

File =
filepath('values_glandular.txt',subdirectory=['egs_cbct','Breast','FINAL','
TESIS BREAST'])

values = File
openr, unit, values, /get_lun
einde=file_lines(values)
values=fltarr(einde)
readf, unit, values

free_lun,unit

for e = 40,65,5 do begin

for zz=0,3 do begin

jj=fix(values(zz))

for z=0,nrows-1 do begin

filename = 'glandular_mass_tesis_'+strcompress(e)+'_'+strcompress(z)+'.txt'

    filename1 = strcompress(filename)

    filename1 = strmid(filename,0,21)

    filename2 = strcompress(filename)

    filename2 =strmid(filename,22,22)

    filename3 = filename1 + filename2

    filename4 = strcompress(filename3)

    filename5 = strmid(filename3,0,24)

    filename6= strmid(filename3,25,26)

    filename7 = filename5 + filename6

    filenamen = 'glandular_'+strcompress(e)


    filenamen1 = strcompress(filenamen)

    filenamen1 = strmid(filenamen,0,10)

    filenamen2 = strmid(filenamen,11,20)

    filefolder = filenamen1 + filenamen2
```

```
File = filepath(filename7,subdirectory=['egs_cbct','Breast','FINAL','TESIS
BREAST',filefolder])

beeld = File
openr, unit, beeld, /get_lun
einde=file_lines(beeld)
beeld=fltarr(einde)
readf, unit, beeld

free_lun,unit

beeldfinal=fltarr(350,200)
beeldfinal(*,*) = 0.0

for j=0,y-1 do begin
xx = (j*350.0)
xx2 = xx+349.0

beeldfinal(*,j) = beeld(xx:xx2)
endfor

sino(*,z) = beeldfinal(*,jj)

endfor

sino2 = fltarr(350,360)

diff = fltarr(360)

ave = fltarr(360)

;RING ARTIFACT CORRECTION

ave = total(sino,2)

ave1=ave/nrows

diff = ave1 - smooth(ave1,9,/edge_truncate)

for r =0,359 do begin
sino2(*,r) = (sino(*,r) - diff(*))
endfor

;DISPLAY UNCORRECTED AND CORRECTED SINOGRAM

window,1,xsize=350,ysize=360
tvscl,sino

window,2,xsize=350,ysize=360
tvscl,sino2

;WRITE BACK TO PHANTOM SLICE

slice = fltarr(512,512)


for hh=0,359 do begin
for j=0,511 do begin
slice(81:430,j) = sino2(*,hh)
endfor
window,1,xsize=512,ysize=512
```

```
tvscl,slice
write_jpeg,'C:\Program
Files\MATLAB\OSCar\'+filefolder+'\ring\slice_'+strcompress(jj)+'_'+strcompr
ess(hh)+'.jpg',tvrd()
endfor

endfor
endfor

print,'end'

end
```

APPENDIX

IV

```
pro least_sum_squared_malignant

  x=fltarr(5)
  y=fltarr(5)
  z=fltarr(5)
  q=fltarr(5)
  r=fltarr(5)
  b=fltarr(5)
  d=fltarr(10)

;Mass attenuation coefficients
  a =
[0.790844,0.504831,0.380131,0.310741,0.27167,0.246163,0.227026,0.225263,0.2
08068,0.200432]

m=100000000
  c = fltarr(100,10)
  seed=10.0*(randomu(seed))

  for i=0,999999 do begin

 b=randomu(seed,5)

;Random number generator

  b(0)=0.08+0.04*randomu(seed)
  b(1)=0.08+0.04*randomu(seed)
  b(2)=0.7+0.1*randomu(seed)
  b(3)=0.02+0.01*randomu(seed)
  b(4)=0.02*randomu(seed)

  eqn1=0.36950*b(0)+ 0.44200*b(1)+  0.86530*b(2)+  0.61790*b(3)+  7.74000*b(4)
  eqn2=0.36310*b(0)+ 0.31360*b(1)+  0.52650*b(2)+  0.40190*b(3)+  4.06600*b(4)
  eqn3=0.35700*b(0)+ 0.25620*b(1)+  0.37790*b(2)+  0.30660*b(3)+  2.42600*b(4)
  eqn4=0.35130*b(0)+ 0.22580*b(1)+  0.30190*b(2)+  0.25740*b(3)+  1.58800*b(4)
  eqn5=0.34580*b(0)+ 0.20760*b(1)+  0.25850*b(2)+  0.22880*b(3)+  1.11700*b(4)
  eqn6=0.34060*b(0)+ 0.19570*b(1)+  0.23140*b(2)+  0.21050*b(3)+  0.83130*b(4)
  eqn7=0.33550*b(0)+ 0.18710*b(1)+  0.21330*b(2)+  0.19800*b(3)+  0.64830*b(4)
  eqn8=0.33070*b(0)+ 0.18050*b(1)+  0.20040*b(2)+  0.18880*b(3)+  0.52530*b(4)
  eqn9=0.32600*b(0)+ 0.17530*b(1)+  0.19070*b(2)+  0.18170*b(3)+  0.43940*b(4)
  eqn10=0.32160*b(0)+ 0.17100*b(1)+ 0.18320*b(2)+  0.17610*b(3)+  0.37750*b(4)


E1 =(eqn1-a(0))^2
E2 =(eqn2-a(1))^2
E3=(eqn3-a(2))^2
E4=(eqn4-a(3))^2
E5=(eqn5-a(4))^2
E6 =(eqn6-a(5))^2
E7 =(eqn7-a(6))^2
E8=(eqn8-a(7))^2
E9=(eqn9-a(8))^2
E10=(eqn10-a(9))^2

diff_squared=(E1+E2+E3+E4+E5+E6+E7+E8+E9+E10)
```